



HAL
open science

Time reversal for mobile networks

Dinh-Thuy Phan Huy

► **To cite this version:**

Dinh-Thuy Phan Huy. Time reversal for mobile networks. Signal and Image processing. INSA de Rennes, 2015. English. NNT : 2015ISAR0026 . tel-01303767

HAL Id: tel-01303767

<https://theses.hal.science/tel-01303767>

Submitted on 18 Apr 2016

HAL is a multi-disciplinary open access archive for the deposit and dissemination of scientific research documents, whether they are published or not. The documents may come from teaching and research institutions in France or abroad, or from public or private research centers.

L'archive ouverte pluridisciplinaire **HAL**, est destinée au dépôt et à la diffusion de documents scientifiques de niveau recherche, publiés ou non, émanant des établissements d'enseignement et de recherche français ou étrangers, des laboratoires publics ou privés.

Thèse



THESE INSA Rennes
sous le sceau de l'Université européenne de Bretagne
pour obtenir le titre de
DOCTEUR DE L'INSA DE RENNES
Spécialité : Electronique et Télécommunications

présentée par
Dinh Thuy PHAN HUY

ECOLE DOCTORALE : MATISSE
LABORATOIRE : IETR

Retournement Temporel: application aux réseaux mobiles

Thèse soutenue le 14.12.2015
devant le jury composé de :

Marion Berbineau

Directrice de Recherche, IFSTTAR, Lille / Présidente du jury

Julien De Rosny

Directeur de Recherche CNRS, Institut Langevin, Paris / Rapporteur

Martine Liénard

Professeur, Université de Lille 1 / Rapporteur

Geneviève Baudoin

Professeur, ESIEE, Paris / Examinatrice

Matthieu Crussière

Maître de Conférences, INSA de Rennes / Examineur

Joe Wiat

Directeur de la chaire C2M, Institut Mines Telecom, Paris / Examineur

Maryline Hélard

Professeur, INSA de Rennes / Directrice de thèse

Retournement Temporel : application aux réseaux mobiles

Dinh Thuy PHAN HUY



En partenariat avec



Table of Contents

Table of Contents	1
Acknowledgements	6
Abstract	7
Résumé étendu en Français des travaux de la thèse	9
I. Introduction.....	9
II. Etat de l'art sur le retournement temporel dans les réseaux sans fil.....	9
III. Evaluation de la performance du retournement temporel dans les Réseaux mobiles à l'intérieur des bâtiments.....	12
A. Cartes montrant le ratio entre le débit atteint par un 'récepteur idiot' et le débit atteint par un 'récepteur parfait' en fonction de la position.....	12
B. Caractérisation de la confidentialité d'une communication verte par retournement temporelle: mesure expérimentale du puits de taux d'erreur binaire.....	14
IV. Conception de leviers pour la focalisation par retournement temporel dans des scénarios difficiles typiques des réseaux mobiles.....	16
A. Retournement temporel pour le mode de duplexage en fréquence.....	17
B. Retournement temporel en mobilité.....	19
V. Conception de nouveaux systèmes de communication et de nouvelles applications basées sur le retournement temporel.....	21
A. Modulation spatiale pour communications par retournement temporel.....	21
B. Précodeurs "Make-It-Real" pour MIMO OFDM/OQAM.....	22
C. Navigation et guidage par retournement temporel.....	23
D. DFT-SM-MRT pour 'large MIMO' et ondes millimétriques.....	24
VI. Conclusion.....	26
List of contributions	27
List of figures	29
List of tables	36
General mathematical notations	41

Mathematical notations for single-carrier studies.....	43
1 Chapter 1 - Introduction.....	45
2 Chapter 2 - State-of-the-art on time reversal for wireless communications	46
2.1 Matched filter and maximum ratio transmission beamformer.....	48
2.1.1 The transmit 'matched filter': a time compression technique.....	48
2.1.2 Maximum ratio transmission (MRT) beamforming: a spatial focusing technique	52
2.1.3 Conclusion.....	57
2.2 Time reversal space-time focusing.....	58
2.2.1 Time reversal and space-time focusing.....	58
2.2.2 Time reversal versus other space-time filters.....	61
2.2.3 Conclusion.....	61
2.3 Time reversal for wireless communications in multiple scattering medium	62
2.3.1 Time reversal in MIMO wireless communications.....	62
2.3.2 Taking advantage of multiple scattering to perform wireless communication using Time reversal	67
2.3.3 Conclusion.....	68
2.4 Recent time reversal techniques for wireless communications	69
2.4.1 Low complexity single carrier receivers.....	69
2.4.2 Low complexity single carrier transceivers	71
2.4.3 Low transmit power.....	72
2.4.4 Low complexity multi-carrier transceivers and receivers.....	73
2.5 Conclusion on the state-of-the art and introduction to our contributions	73
3 Chapter 3 - Performance evaluation of time reversal in indoor mobile networks .75	75
3.1 Dumb-to-perfect receiver throughput ratio maps of femto/small cell using TR.....	75
3.1.1 Introduction.....	75
3.1.2 System description.....	76
3.1.3 Post receiver SINR computation.....	78
3.1.4 Simulation assumptions	80
3.1.5 Results	82
3.1.6 Conclusion and next steps	84
3.2 Characterization of the Confidentiality of a Green Time reversal Communication System: Experimental Measurement of the Spy BER Sink.....	84

3.2.1	<i>Introduction</i>	84
3.2.2	<i>The spy bit error rate metric</i>	88
3.2.3	<i>Experimental method</i>	91
3.2.4	<i>Measurements results</i>	98
3.2.5	<i>Conclusion</i>	99
4	Chapter 4 - Design of enablers for time reversal focusing in challenging scenarios which are typical from mobile networks	100
4.1	Frequency division duplex time reversal (FDD TR)	100
4.1.1	<i>Introduction</i>	100
4.1.2	<i>System description</i>	101
4.1.3	<i>Post receiver SINR computation</i>	104
4.1.4	<i>Feedback analysis</i>	105
4.1.5	<i>Simulation results</i>	105
4.1.6	<i>Conclusion</i>	112
4.2	Time reversal in mobility	112
4.2.1	<i>Introduction</i>	112
4.2.2	<i>Common system model</i>	115
4.2.3	<i>Systems specific models</i>	121
4.2.4	<i>Initial comparison of the studied schemes</i>	129
4.2.5	<i>Performance comparison</i>	130
4.2.6	<i>Conclusion</i>	134
5	Chapter 5 - Design of new communication schemes and applications based on time reversal for mobile networks	135
5.1	Receive Antenna Shift Keying for time reversal wireless communications.....	135
5.1.1	<i>Introduction</i>	135
5.1.2	<i>Introduction to receive antenna shift keying</i>	136
5.1.3	<i>Generic system model and expression of the output of the single tap receiver</i>	137
5.1.4	<i>PAM and RASK Modulation Schemes</i>	140
5.1.5	<i>Simulation Results</i>	141
5.1.6	<i>Conclusion</i>	144
5.1.7	<i>Annex</i>	144
5.2	“Make-It-Real” precoders for MIMO OFDM/OQAM without inter carrier interference	146

5.2.1	<i>Introduction</i>	146
5.2.2	<i>System model</i>	148
5.2.3	<i>Precoders</i>	154
5.2.4	<i>Performance evaluation methodology</i>	156
5.2.5	<i>Results</i>	156
5.2.6	<i>Conclusion</i>	158
5.3	Time reversal for ant trails in wireless networks	159
5.3.1	<i>Introduction</i>	159
5.3.2	<i>System model</i>	163
5.3.3	<i>Performance evaluation methodology</i>	166
5.3.4	<i>Simulation results</i>	168
5.3.5	<i>Conclusion</i>	173
5.3.6	<i>Details</i>	174
5.4	Discrete Fourier transform based spatial multiplexing and MRT for millimetre wave large MIMO 174	
5.4.1	<i>Introduction</i>	174
5.4.2	<i>Common system model</i>	179
5.4.3	<i>Studied systems</i>	181
5.4.4	<i>Performance evaluation methodology</i>	182
5.4.5	<i>Results</i>	184
5.4.6	<i>Conclusion</i>	188
6	Chapter 6 - Conclusion and future works	190
6.1	Conclusions	190
6.2	Future works.....	190
7	Annex	192
7.1	Details on OFDM/OQAM with time reversal	192
7.2	Details on separate receive and training antenna system.....	193
7.2.1	<i>Introduction</i>	193
7.2.2	<i>Generic system model</i>	195
7.2.3	<i>Classical MISO or Reference System (RS)</i>	196
7.2.4	<i>Separate receive and training antennas (SRTA)</i>	197
7.2.5	<i>Performance evaluation</i>	201

7.2.6	<i>Conclusion</i>	204
8	References	206

Acknowledgements

I thank my dear family, Mathieu, Lila, Iris and my parents for their daily support.

I thank my Thesis Director, Prof. Maryline H elard for all these years of support and advice. I thank the reporters of the Thesis, Prof. Martine Li enard and Mr. Julien De Rosny, for their precious comments on the manuscript: they have been taken into account in this improved and last version. I thank Mrs Marion Berbineau for the presidency of the jury and all other members of the jury, Prof. Genevi eve Baudoin, Mr. Matthieu Crussiere and Mr. J. Wiart, for their sharp questions and comments during the PhD defence: I will keep these in mind in my future work. I very warmly thank my co-authors and colleagues, inside and outside Orange, for their precious help: Ahmed Saadani, Antti T olli, Azeddine Gati, Berna Sayrac, Bernadette Villeforceix, Bernard Le Floch, Bruno Jahan, Christian Gallard, C ecile Germond, Christian Leray, Daniel Mustaki, Dorra Ben Cheikh, Elisabeth De Carvalho, Fadi Abi Abdallah, Fatima Karim, Hacene Azzouz, Isabelle Siaud, Jean-Christophe Pr evotet, Jean-Marc Kelif, Joe Wiart, Julien De Rosny, Jean-Marie Chaufray, Jean-Philippe Desbat, Laurence Delaunay, Laurent Lab egu erie, Matthieu Cruss iere, Mikael Sternad, Nandana Rajatheva, Nadine Malhouroux-Gaffet, Olivier Simon, Philippe Du Reau, Pascale Jeune, Patrice Pajusco, Pierre Siohan, Patrick Tortelier, Roxana Burghelea, Rodolphe Legouable, Rapha el Visoz, Sana Ben Jemaa, Slim Ben Halima, Thierry Dubois, Thierry Sarrebourg, Tommy Svensson, Wolfgang Zirwas, Youmni Ziade, Zwi Altman, Yvan Kokar ... I thank the entire Wireless Technology Evolution department, in Orange.

This work has been done partially in the framework of Agence Nationale de la Recherche (ANR) VERSO 2010 TRIMARAN project, with "P ole Images et R eseaux" and "P ole SYSTEMATIC" and partially in the framework of the FP7 project ICT-317669 METIS, which is partly funded by the European Union.

Abstract

This thesis studies the time reversal technique to improve the energy efficiency of future mobile networks and reduce the cost of future mobile devices.

Time reversal technique consists in using the time inverse of the propagation channel impulse response (between a transceiver and a receiver) as a pre-filter. Such pre-filtered signal is received with a stronger power (this is spatial focusing) and with a strong main echo, relatively to secondary echoes (this is time compression). During a previous learning phase, the transceiver estimates the channel by measuring the pilot signal emitted by the receiver. Space-time focusing is obtained only at the condition that the propagation remains identical between the learning phase and the data transmission phase: this is the ‘channel reciprocity’ condition.

Numerous works show that spatial focusing allows for the reduction of the required transmit power for a given target received power, on the one hand, and that time compression allow for the reduction of the required complexity at the receiver side to handle multiple echoes, on the other hand.

However, studies on complexity reduction are limited to ultra wideband. Some works of this thesis (based on simulations and experimental measurements) show that, for bands which are more typical for future networks (a carrier frequency of 1GHz and a spectrum of 30 MHz to 100 MHz), thanks to time reversal, a simple receiver and a mono-carrier signal are sufficient to reach high data rates.

Moreover, the channel reciprocity condition is not verified in two scenarios which are typical from mobile networks. Firstly, in most European mobile networks, the frequency division duplex mode is used. This mode implies that the transceiver and the receiver communicate on distinct carriers, and therefore through different propagation channels. Secondly, when considering a receiver on a moving connected vehicle, the transceiver and the receiver communicate one with each other at distinct instants, corresponding to distinct positions of the vehicles, and therefore through different propagation

channels. Some works of this thesis propose solutions to obtain space-time focusing for these two scenarios.

Finally, some works of this thesis explore the combination of time reversal with other recent signal processing techniques (spatial modulation, on the one hand, a new multi-carrier waveform, on the other hand), or new deployment scenarios (millimeter waves and large antenna arrays to inter-connect the nodes of an ultra dense network) or new applications (guidance and navigation) which can be envisaged for future mobile networks.

Résumé étendu en Français des travaux de la thèse

I. Introduction

Les réseaux mobiles se sont développés de manière spectaculaire durant les dernières décennies. La 5ème génération (5G) des réseaux mobiles sera déployée dans les années 2020. Ces futurs réseaux devront supporter mille fois plus de trafic que ne le font les réseaux actuels, et plus de cinquante milliards d'objets connectés. Parallèlement, la consommation d'énergie des Réseaux mobiles ainsi que le coût des équipements de réseau et les coûts des terminaux mobiles deviennent des sujets de plus en plus préoccupants. Il est donc important de commencer à investiguer des techniques de traitement de signal qui ont la particularité d'être quasi optimales quand elles sont implémentées dans des réseaux basse puissance et des terminaux à bas coût. La technique de focalisation spatio-temporelle des ondes dite de 'Retournement Temporel' est une solution candidate. Le but de cette thèse est d'investiguer cette solution.

II. Etat de l'art sur le retournement temporel dans les réseaux sans fil

De nombreux travaux ont été menés sur la technique de retournement temporel dans le cadre des réseaux de communication sans fil. Un émetteur émet le signal radio de manière focalisée vers un récepteur cible grâce à une méthode très simple. Il utilise une ou plusieurs antenne(s). Le récepteur émet d'abord un signal d'apprentissage (par exemple une séquence pilote connue de l'émetteur et normalisée). L'émetteur réceptionne le signal d'apprentissage et estime la réponse impulsionnelle du canal de propagation entre le récepteur et lui-même. Il effectue cette tâche pour chacune de ses antennes. Dans un second temps, l'émetteur calcule un filtre de 'retournement temporel' (pour chacune de ses antennes): la réponse impulsionnelle du canal estimée, renversée temporellement. Enfin, l'émetteur transmet son signal de données, filtré par le filtre de retournement temporel (pour chacune de ses antennes).

Sous certaines conditions dites de 'réciprocité du canal', l'onde obtenue converge sur la cible (le point focal) avec une très forte puissance : c'est le phénomène de « focalisation spatiale ».

Un canal de propagation est 'réciproque' si la réponse impulsionnelle de la propagation du point A au point B est identique à celle de la propagation du point B au point A. C'est le cas quand l'environnement est statique et quand A et B utilisent la même bande de fréquence. Dans les réseaux sans fil, cela implique d'utiliser le mode de duplexage en temps ou 'time division duplex' (TDD) mode. En revanche, lorsque le milieu varie, ou lorsque le mode de duplexage en fréquence ou 'frequency division duplex' (FDD) mode, est utilisé, le canal n'est pas réciproque et le retournement temporel ne s'applique pas.

Dans un milieu de propagation diffusif, le canal de propagation est « multi-écho » et « multi-trajet ». C'est le cas, par exemple dans milieu urbain dense ou à l'intérieur de bâtiments. Un signal focalisé, en revanche est presque dénué d'échos : c'est le phénomène de « compression temporelle ».

En remontant aux années 1950, on montre que deux techniques plus anciennes précèdent le retournement temporel : le filtre adapté et la technique de formation de faisceau dite 'maximum ratio transmission' (MRT beamforming). Ce filtre a été utilisé pour ses propriétés de compression temporelle pour réduire les échos. La technique de formation de faisceau MRT a été introduite pour faire de la focalisation spatiale, avec une propagation en vue directe (sans multi-trajet). Les deux manières les plus courantes d'implémenter le retournement temporel dans une communication sans fil utilisent le filtre adapté et le MRT beamforming:

- pour une forme d'onde mono-porteuse : on applique un filtre adapté distinct pour chaque antenne de transmission de l'émetteur ; pour que le résultat corresponde au retournement temporel il faut que les puissances des filtres des diverses antennes conservent les mêmes rapports que les puissances des réponses impulsionnelles des diverses antennes ;
- pour une forme d'onde multi-porteuse : on applique un 'maximum ratio transmission beamformer' au réseau d'antennes de l'émetteur, distinct pour chaque sous-porteuse ; pour que le résultat corresponde au retournement temporel il faut que les puissances des beamformers des diverses sous-porteuses conservent les mêmes rapports que les puissances des canaux des diverses sous-porteuses. L'ensemble des beamformers pris sur toutes les sous-porteuses, est souvent appelé '**précodeur**'.

La plupart des travaux précédents sur les communications sans fil par retournement temporel étudient l'ultra large bande. En ultra large bande, à cause de la taille de la bande, le nombre d'échos est très élevé. Les récepteurs sont donc complexes. Ces travaux montrent que grâce au retournement temporel, la complexité des récepteurs peut être réduite. A faible rapport signal sur bruit, comme illustré dans la Fig. 1, grâce à la « compression temporelle », les interférences entre symboles consécutifs sont noyées dans le bruit. La quantité de traitement de signal dans le terminal peut alors être réduite. Ces travaux

montrent aussi que le niveau d'émission d'onde du réseau peut être réduit. En concentrant l'énergie sur le récepteur, l'émetteur peut réduire son émission pour délivrer la puissance juste nécessaire pour atteindre le débit souhaité. De plus, à faible rapport signal sur bruit, les lobes secondaires sont noyés dans le bruit (comme illustré dans la Fig. 2). On peut alors envisager de focaliser sur une seconde antenne, un second flux tout en limitant l'interférence entre flux. Dans ce cas une communication dite MIMO (multiple-input multiple-output) est établie.

Les travaux précédents montrent que le retournement temporel est optimal à faible rapport signal sur bruit, même quand le récepteur est simple. Le récepteur le plus simple est le 'récepteur à un écho' ou 'récepteur idiot' ('dumb receiver' en anglais). Ce récepteur détecte l'écho de plus grande énergie. Les autres échos génèrent une interférence qui n'est pas supprimée. Le 'récepteur idiot' ne peut donc être optimal que dans un milieu sans écho.

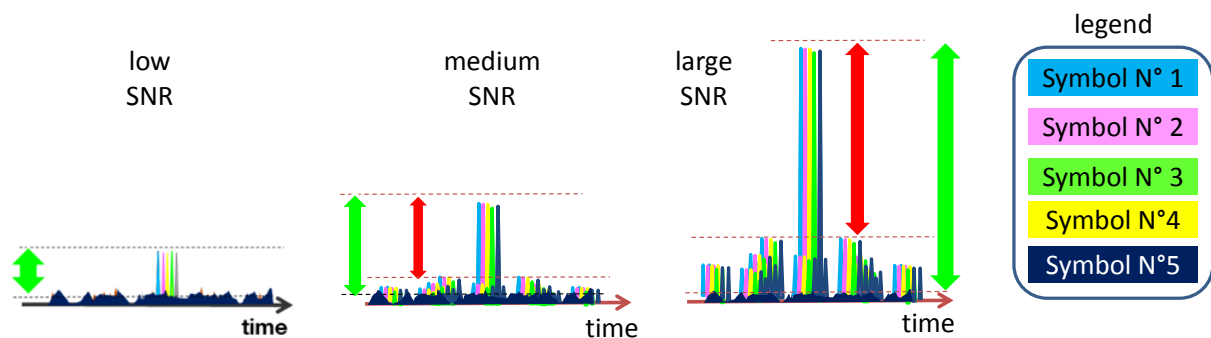


Fig. 1 Signal focalisé en fonction du rapport signal sur bruit (SNR)

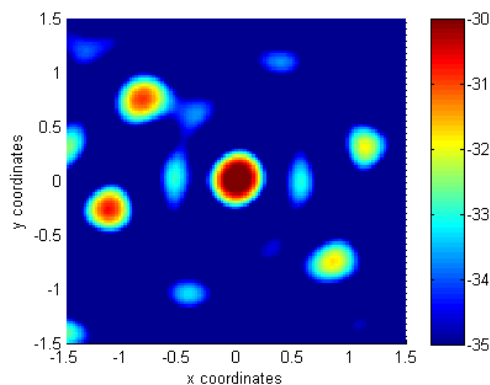


Fig. 2 Focalisation spatiale pour un rapport signal sur bruit faible

Les études précédentes n'adressent pas spécifiquement le scénario des réseaux mobiles. Les bandes mobiles sont plus petites (1 à 100MHz) pour une fréquence porteuse autour du GHz. De plus, le retournement temporel ne s'applique aux systèmes de duplexage en fréquence (fréquent en Europe) ni aux hautes mobilités. Ces limitations rendent l'usage de cette technique pour les réseaux mobiles difficile.

Cette thèse apporte trois contributions décrites dans les sous-sections suivantes.

- nous apportons de nouveaux résultats permettant d'évaluer l'intérêt du retournement temporel dans les réseaux mobiles à l'intérieur des bâtiments (femtos/small cells) ;
- la seconde contribution propose des leviers pour permettre à la focalisation par retournement temporel de fonctionner dans les réseaux mobiles même dans les scénarios difficiles: le mode duplex en fréquence et les fortes mobilités ;
- la dernière contribution propose de nouveaux systèmes de communication et de nouvelles applications reposant toutes sur le retournement temporel.

III. Evaluation de la performance du retournement temporel dans les Réseaux mobiles à l'intérieur des bâtiments

Cette contribution comporte deux études de communication à l'intérieur des bâtiments utilisant une fréquence porteuse (1 GHz) et un spectre (30 MHz à 100 MHz) typiques pour des réseaux mobiles 4G ou 5G. La première étude est basée sur des simulations. La seconde étude utilise des résultats expérimentaux.

A. Cartes montrant le ratio entre le débit atteint par un 'récepteur idiot' et le débit atteint par un 'récepteur parfait' en fonction de la position

Le retournement temporel est optimal avec le 'dumb receiver' à faible rapport signal sur bruit. Il est donc un candidat intéressant pour des réseaux 'verts' opérant à faible rapport signal sur bruit et à faible puissance. Cependant, la probabilité que les conditions d'optimalité soient réunies, de manière pratique, à l'intérieur d'un bâtiment typique, est inconnue. Pour la première fois, nous proposons d'établir une carte montrant le ratio entre le débit atteint par un 'récepteur idiot' et le débit atteint par un 'récepteur parfait' en fonction de la position du récepteur dans un bâtiment typique. Contrairement aux travaux précédents, nous utilisons des simulations 'systèmes', permettant de collecter des résultats statistiques (sur une zone de bâtiment entière), et nous utilisons l'expression exacte (non simplifiée) du rapport signal sur bruit et interférence (SINR) mesuré après le récepteur. Cette démarche nous permet de mesurer de manière précise la distance entre la performance du 'récepteur idiot' et du 'récepteur parfait'. Le 'récepteur parfait' est un récepteur qui annule parfaitement les interférences inter-symboles. Les formules de rapport signal sur bruit et interférence incluent l'exacte expression des termes d'interférence inter-symbole et d'interférence entre flux. Un modèle de canal de propagation sophisti-

qué issu du projet européen Winner II est utilisé, pour fournir un maximum de réalisme à la simulation. Nos simulations montrent qu'avec un émetteur équipé de 16 antennes et émettant à une puissance aussi faible que -10 dBm (0.1 mW) sur une bande de 100 MHz, le récepteur idiot reçoit 100 Mbit/s à 500 Mbit/s, et atteint au moins 80% du débit du récepteur parfait sur au moins 60% des positions dans le bâtiment. La Fig. 3 décrit l'environnement simulé. La Fig. 4 donne la carte de débit atteint par le récepteur idiot. La Fig. 5 donne la carte du ratio entre débit du récepteur idiot et débit du récepteur parfait.

En comparant la Fig. 4 et la Fig. 5, on constate que c'est lorsque le débit est le plus faible (c'est-à-dire à bas rapport signal sur bruit) que le récepteur idiot est quasi parfait.

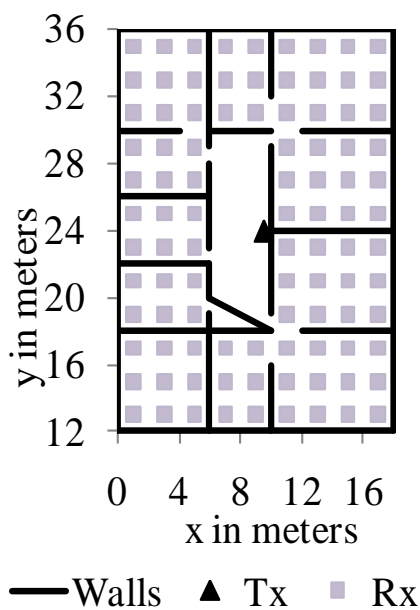


Fig. 3 Etage d'un bâtiment, avec position de l'antenne émettrice (Tx) dans le couloir, les murs ('Walls') et les positions successives de mesure du récepteur dans les bureaux

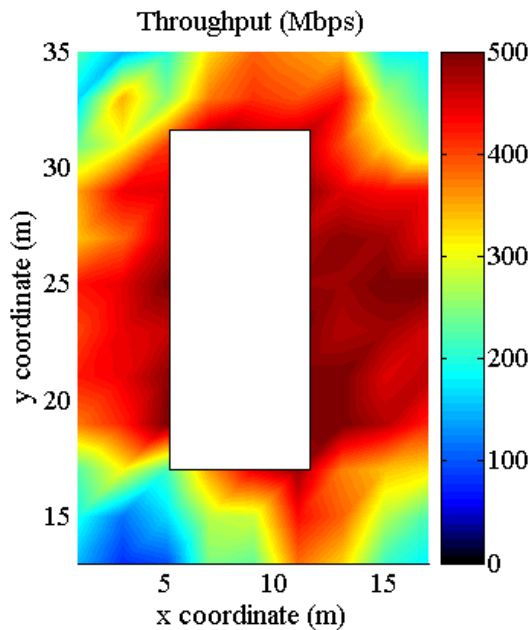


Fig. 4 Carte de débit du récepteur idiot

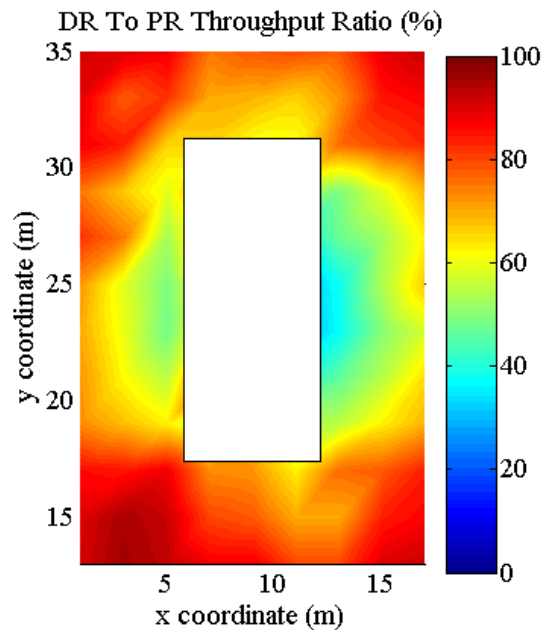


Fig. 5 Carte du ratio entre débit du récepteur idiot et débit du récepteur parfait.

B. Caractérisation de la confidentialité d'une communication verte par retournement temporelle: mesure expérimentale du puits de taux d'erreur binaire

Le retournement temporel permet de focaliser le signal sur un récepteur cible. Si la focalisation est suffisante, et la puissance autour de la cible suffisamment, ce système peut empêcher les écoutes indiscrètes. Pour la première nous vous présentons une mesure expérimentale caractérisant le niveau de confidentialité d'un système de communication par retournement temporel à l'intérieur d'un bâtiment. Un flux de données est émis, sur une bande de 30 MHz (centrée sur 1 GHz) avec une modulation à 256 états (256QAM), et focalisé sur une antenne cible. Un débit de 240 Mbits/s est donc atteint en pratique.

L'émetteur est équipé de 16 antennes distribuées dans la pièce. Le signal reçu est démodulé par une antenne dite 'espion' utilisant un 'récepteur idiot'. Le taux d'erreurs binaire atteint par l'antenne espion est ensuite évalué pour de multiples positions entourant la cible. Le taux d'erreur binaire de l'espion 'spy BER' est ensuite tracé en fonction de la distance cible-espion. La Fig. 6 montre le montage expérimental utilisé. La Fig. 7 montre l'environnement de mesure. Les mesures sont effectuées suivant quatre axes. La Fig. 8 montre la puissance mesurée par l'espion (normalisée par rapport à la puissance reçue par la cible), pour les quatre axes. Une forme de 'cloche' apparaît clairement. La Fig. 9 montre le taux d'erreurs binaire de l'espion 'spy BER' pour les quatre axes. Le taux d'erreur binaire mesuré varie plus rapidement dans l'espace que la longueur d'onde. Ceci est dû en partie à une mesure imparfaite de la position du récepteur.

Cette expérience met clairement en évidence un 'puits de taux d'erreur binaire de l'espion' centré sur la cible. Ceci montre que l'espion est très désavantagé par rapport à la cible pour intercepter le message envoyé. Cette étude montre aussi qu'un très haut débit peut être atteint avec un 'récepteur idiot'.

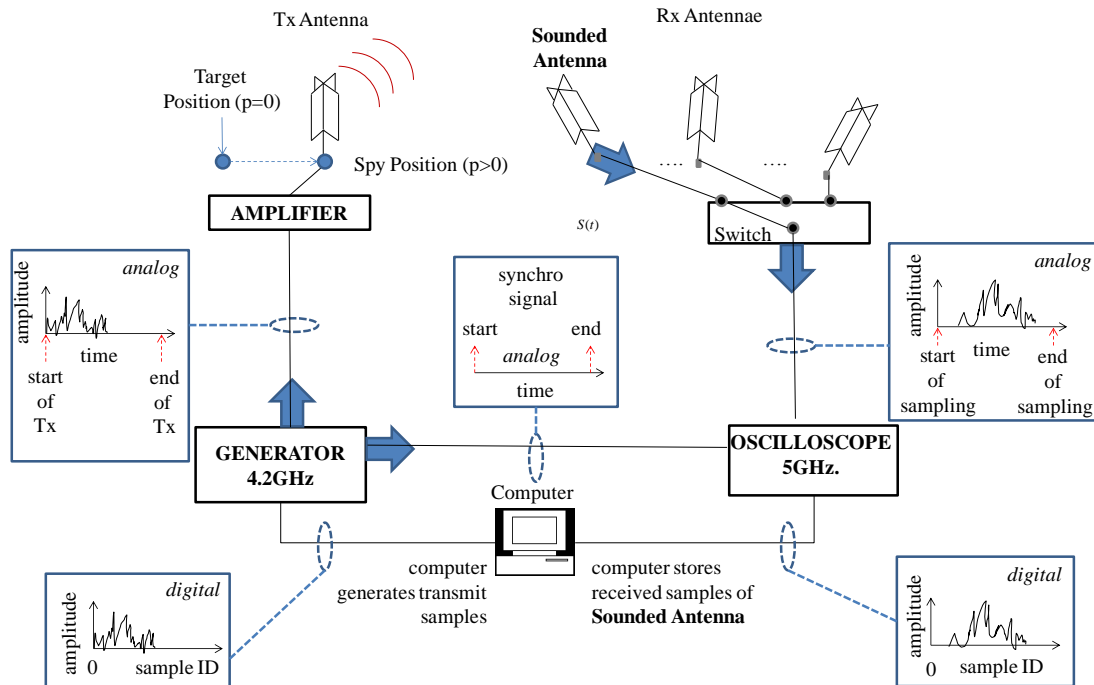


Fig. 6 Montage expérimental

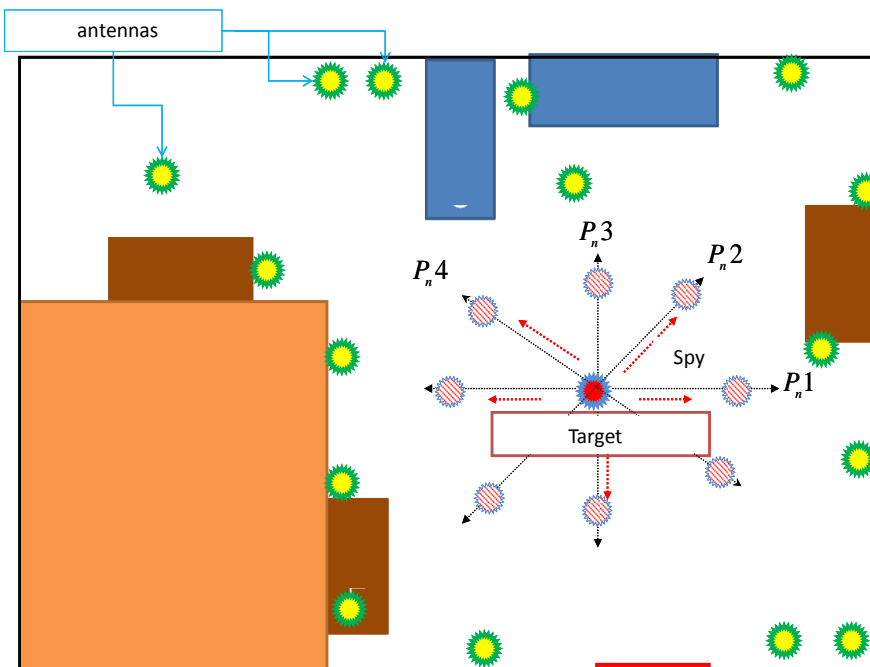


Fig.7 Environnement expérimental, et position des antennes et des mesures

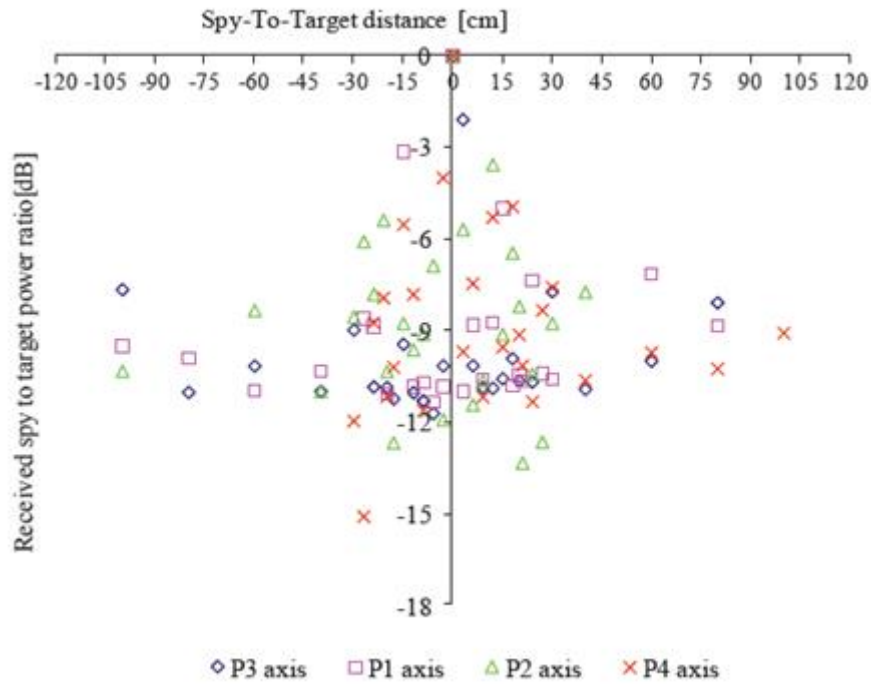


Fig. 8 Received spy to target power ratio

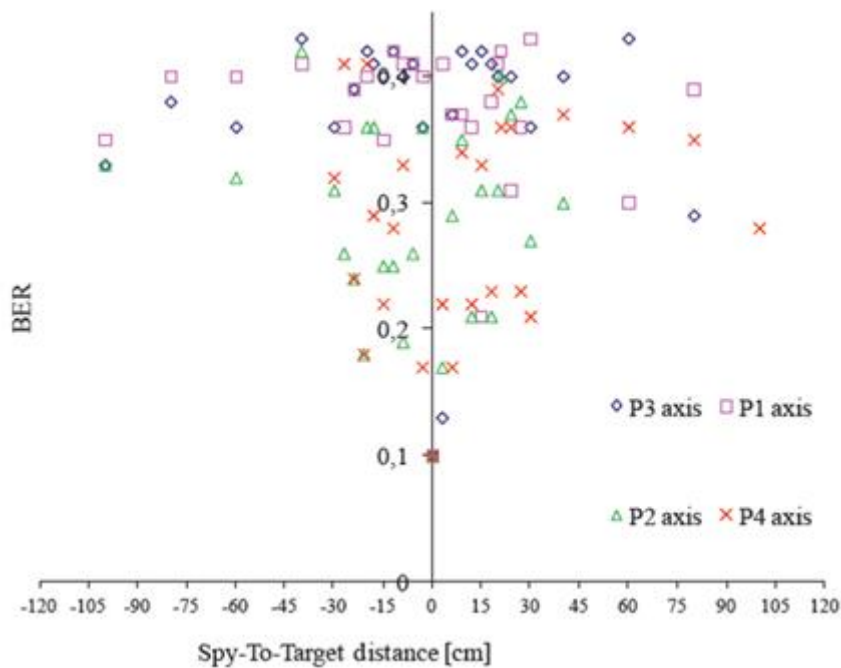


Fig. 9 Spy BER

IV. Conception de leviers pour la focalisation par retournement temporel dans des scénarios difficiles typiques des réseaux mobiles

Cette contribution se compose de deux études. La première étude propose une technique pour focaliser par retournement temporel en mode de duplex en fréquence. La seconde étude propose une technique pour focaliser sur une cible se déplaçant rapidement (un véhicule connecté par exemple).

A. Retournement temporel pour le mode de duplexage en fréquence

Cette étude propose une nouvelle technique de précodage pour le mode de duplexage en fréquence et pour des communications sans fil MIMO. De ce mode de duplexage, la voie montante et la voie descendante utilisent des fréquences différentes.

Conventionnellement, l'émetteur émet un signal pilote qui permet au récepteur d'estimer le canal de propagation dans le sens descendant. Puis, le récepteur compresse le canal en le quantifiant. Dans la technique de 1bit time reversal (1bit TR), le canal est quantifié sur 1 bit : le signe de la partie réelle et le signe de la partie imaginaire de chaque élément de la réponse du canal est utilisé. Puis le récepteur remonte l'information du canal quantifié vers l'émetteur en l'encodant dans un message de signalisation. Le poids de la signalisation dépend donc du niveau de compression. Sur la base de cette information quantifiée et encodée, l'émetteur calcule un précodeur. Ce dernier est donc grossièrement adapté au canal de propagation de la voie descendante.

Nous proposons ici un nouveau précodeur, le 'frequency division duplex time reversal' ('FDD TR'), basé sur une méthode de remontée 'analogique' du canal de propagation, sans quantification et ni encodage. Comme le montre la Fig. 10. L'émetteur émet des pilotes, le récepteur estime la réponse impulsionnelle du canal de propagation descendant. Puis le récepteur émet des pilotes, l'émetteur estime le canal de propagation montant. Puis le récepteur émet à nouveau des pilotes, préfiltré par la réponse impulsionnelle du canal descendant précédemment déterminée. Ceci permet à l'émetteur d'estimer la réponse impulsionnelle d'un canal 'combiné', équivalent à la propagation dans le sens montant puis le sens descendant successivement. L'émetteur pourrait estimer le canal descendant à partir du canal combiné, en le convoluant par l'inverse temporel du canal montant, puis utiliser l'inverse temporel de canal descendant estimé comme filtre d'émission. Le signal résultant est focalisé en temps et en espace. Afin d'obtenir un filtre d'émission mathématiquement identique en moins d'étapes, l'émetteur construit le filtre de FDD TR comme la convolution de deux filtres : l'inverse temporel du canal 'combiné' et le canal montant. Les données sont envoyées préfiltrées par ce filtre de FDD TR.

En termes de signalisation, le FDD TR nécessite moins de bande passante que le 1 bit TR. Des simulations utilisant les expressions exactes du SINR en sortie du récepteur sont utilisées. La Fig. 11 illustre le SINR pour le FDD TR, le 1bit TR et le TR, en fonction du rapport signal sur bruit (SNR). 32 an-

tennes sont utilisées à l'émission. Lorsque la propagation comporte des multi-trajets tout en étant dominée par un écho (scenario 'LOS'), le 1bit TR rehausse les échos multiples par rapport à la réalité puisqu'il attribue une même puissance identique à tous les échos, contrairement au FDD TR. Le 1bit TR dégrade donc la focalisation temporelle. Les simulations montrent effectivement que le FDD TR est plus performant que le 1bit TR en environnement de propagation indoor à faible nombre d'échos (scenario 'LOS') et de performance similaire en environnement de propagation indoor avec beaucoup de multi-trajets (scenario 'NLOS').

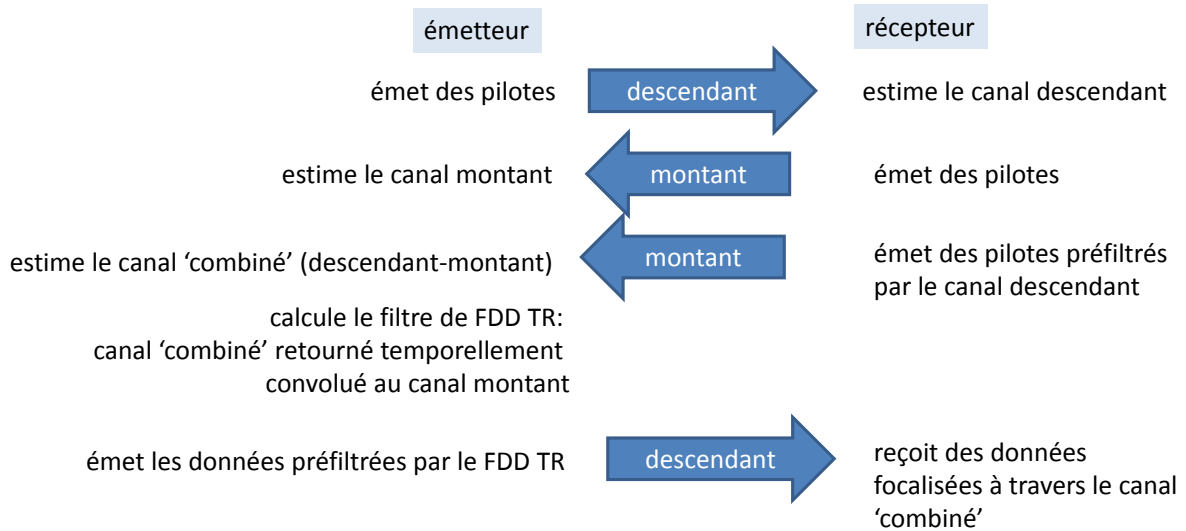


Fig. 10 Principe du FDD TR

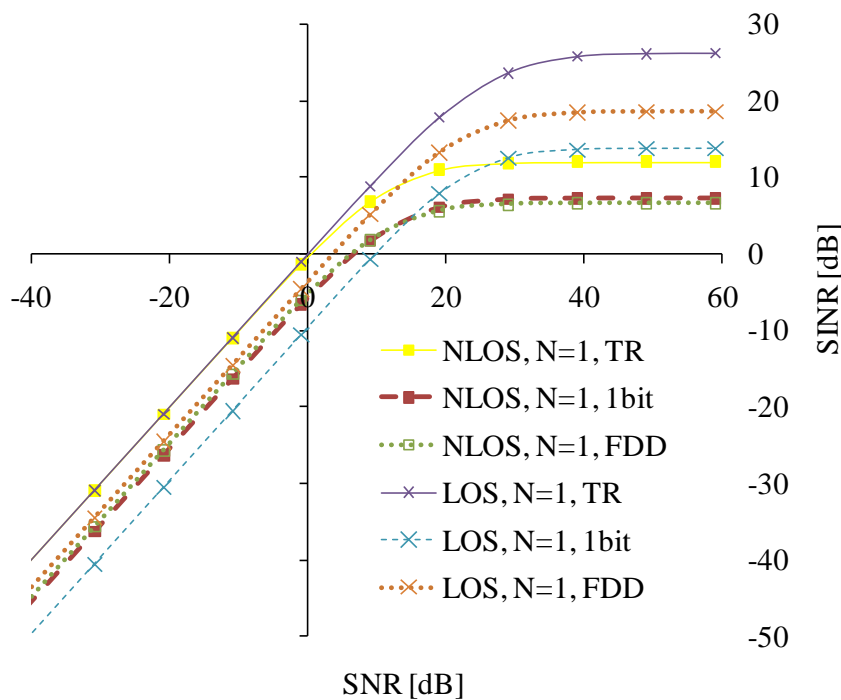


Fig. 11 rapport signal sur bruit et interférence en sortie du récepteur en fonction du rapport signal sur bruit

B. Retournement temporel en mobilité

Dans cette étude, on considère une station de base en extérieur équipée de 64 antennes (telle les stations de base dites ‘Massive MIMO’ proposées pour la 5G). Le précodeur MRT est utilisé pour focaliser sur un véhicule connecté. Ce véhicule est équipé d’une antenne sur le toit. Le mode de duplexage en temps est utilisé.

Dans un système conventionnel, que nous appelons ‘système de référence’ ou ‘reference system’ (RS) en anglais, le véhicule émet des pilotes pendant la trame montante afin de permettre la station de base d’estimer le canal de propagation. La station de base utilise cette estimée pour calculer le précodeur MRT. Durant la trame descendante, la station de base focalise vers le véhicule en utilisant ce précodeur. Malheureusement, à cause du délai entre le sens montant et le sens descendant et à cause du déplacement de ce véhicule dans ce laps de temps, la station de base ‘manque sa cible’.

Nous proposons une nouvelle technique appelée ‘separate receive and training antenna’ (SRTA) permettant de résoudre ce problème. Nous disposons plusieurs antennes sur le véhicule connecté, comme illustré dans la Fig. 12.

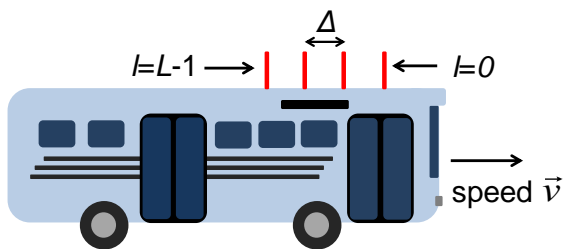


Fig. 12 antennes sur le véhicule

Nous donnons un rôle particulier à l’antenne en amont du véhicule. Nous appelons cette antenne : ‘antenne d’apprentissage’ (‘training antenna’) ou ‘antenne prédictive’ (‘predictor antenna’). L’antenne prédictive émet les pilotes durant la trame montante pour permettre à la station de base d’estimer le canal. La station de base focalise vers le véhicule en utilisant cette estimée. Une antenne de réception reçoit les données pendant la trame descendante. Cette fois-ci, l’antenne de réception est choisie distincte de l’antenne prédictive. Elle est choisie dynamiquement en fonction de la vitesse du véhicule et de l’écartement des antennes sur le toit. L’objectif est que l’antenne de réception soit le plus au centre possible de la tâche focale, comme illustré dans la Fig. 13.

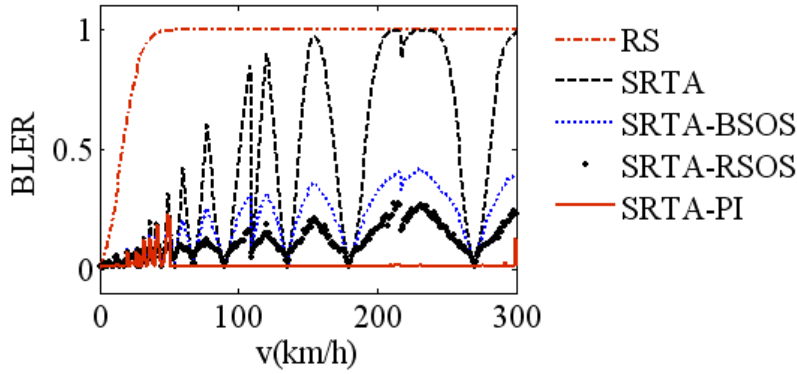


Fig. 14 BLER versus speed

V. Conception de nouveaux systèmes de communication et de nouvelles applications basées sur le retournement temporel

Nous proposons quatre nouvelles utilisations du retournement temporel.

A. Modulation spatiale pour communications par retournement temporel

Dans un milieu multi-diffusant, à fort rapport signal sur bruit, les interférences entre symboles sont élevées. Les modulations à grand nombre d'états (et à forte efficacité spectrale) tels que la 16 Quadrature Amplitude modulation (16QAM) ne peuvent pas être utilisées. Nous proposons de combiner le concept récent de 'modulation spatiale' avec le retournement temporel, pour améliorer le débit d'une communication par retournement temporel avec 'récepteur idiot', sans accroître considérablement la complexité du récepteur. Nous proposons un nouveau système, appelé 'receive antenna shift keying' (RASK) illustré par la Fig. 15. On considère dans cet exemple, un émetteur avec un nombre quelconque P d'antennes. Le récepteur a 16 antennes. A chaque temps symbole, l'émetteur focalise sur une antenne du récepteur parmi les 16. L'identité de cette antenne code pour une information binaire sur 4 bits : l'information est codée spatialement. Le récepteur retrouve l'information binaire en déterminant laquelle des antennes est prise pour cible de la focalisation.

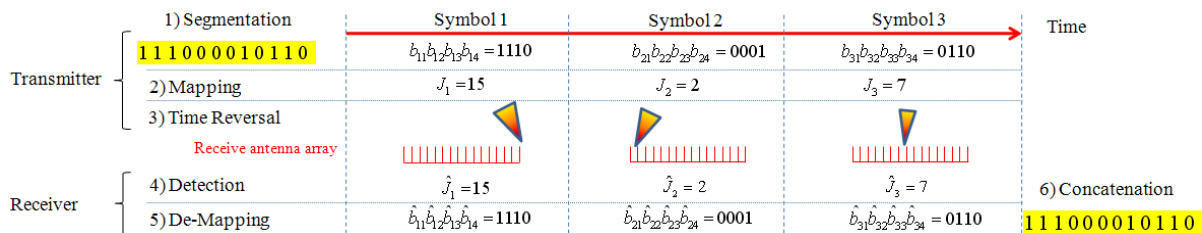


Fig.15 Example of RASK with 16 receive antennas and 3 symbol periods

Le RASK à 16 antennes est comparé à un système de communication par retournement utilisant une modulation conventionnelle de même efficacité spectrale (la 16QAM). Les résultats de simulation illustrés dans la Fig. 16 montrent que le RASK a un meilleur taux d'erreurs binaire que la 16QAM.

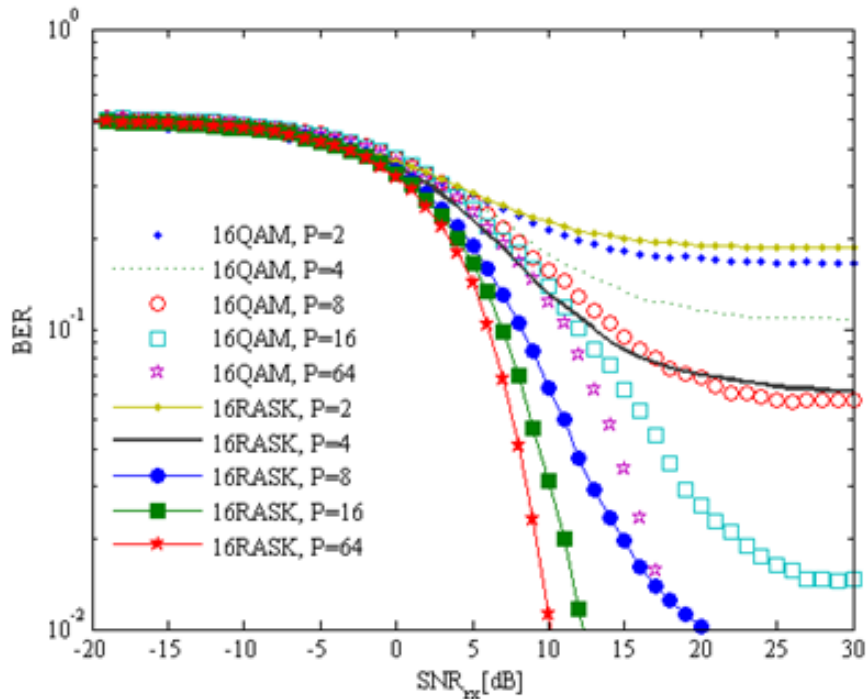


Fig. 16 TR, K=15 taps, P=2, 4, 8, 16 or 64 transmit antennas

B. Précodeurs "Make-It-Real" pour MIMO OFDM/OQAM

Nous considérons un système multi-porteuse utilisant la modulation 'orthogonal frequency division multiplex' (OFDM) et MIMO. Pour ce système, les précodeurs de faible complexité tels que le MRT, le minimum mean square error (MMSE) ou le zero forcing (ZF) peuvent être utilisés pour focaliser plusieurs flux simultanément vers plusieurs antennes. Ces précodeurs ne détruisent pas l'orthogonalité entre porteuse des sous-porteuses de l'OFDM.

Pour la 5G, une modulation multi-porteuse alternative, appelée 'OFDM/OQAM' (Offset QAM) est proposée. En effet, son encombrement spectral est plus faible que celui de l'OFDM. Cependant, la combinaison de l'OFDM/OQAM avec les précodeurs MRT et MMSE introduit des interférences entre sous-porteuses. Nous proposons ici une nouvelle famille de précodeurs appelés 'make-it-real' (MIR) précodeurs. Ces précodeurs sont construits à partir du MRT et du MMSE. Ils sont légèrement modifiés afin que le canal équivalent résultant du précodage et de la propagation n'introduise plus d'interférences entre symboles pour l'OFDM/OQAM.

Des simulations illustrées dans la Fig. 17 montrent que les précodeurs MIR associés avec l'OFDM/OQAM permettent d'obtenir une meilleure efficacité spectrale que les précodeurs originels associés à l'OFDM.

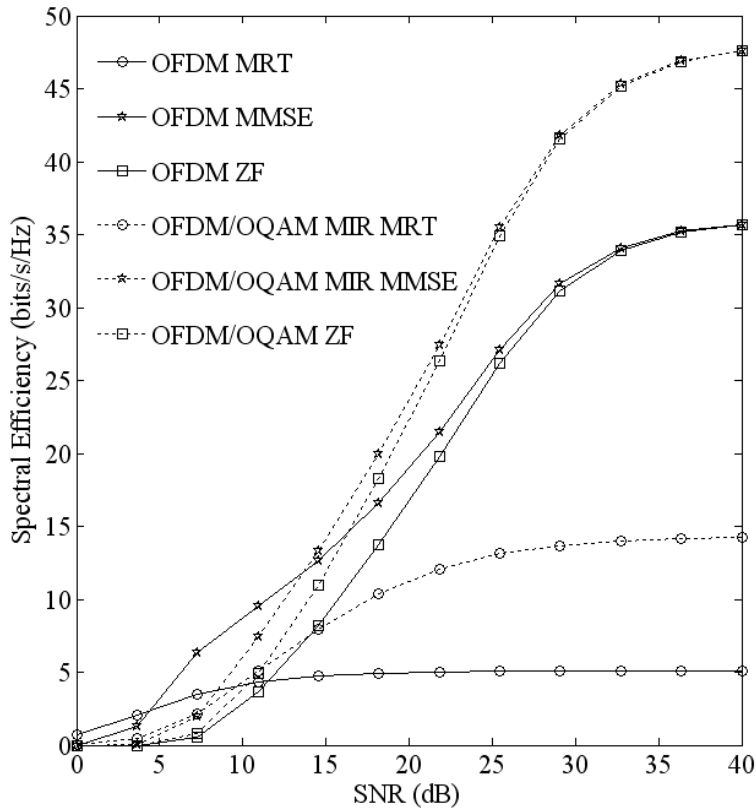


Fig. 17 Spectral efficiencies for 8x8 MIMO

C. Navigation et guidage par retournement temporel

Nous proposons d'utiliser les réseaux mobiles et la focalisation par retournement temporel pour faire un système de navigation et de guidage que nous appelons 'time reversal for ant trails' (TRAT). Le TRAT imite les fourmis. Une fourmi 'exploratrice' à la recherche de nourriture laisse des traces de phéromones le long de son parcours. Les autres fourmis retrouvent la piste de l'exploratrice en détectant les phéromones et arrivent à destination (nourriture). Dans notre système, un explorateur émet des signaux pilotes par voie radio régulièrement pendant son exploration. Un réseau estime et enregistre les réponses impulsionnelles. Dans un second temps, le réseau génère des balises spatio temporelles électromagnétiques en retournant temporellement les réponses impulsionnelles enregistrées. Un 'navigateur' remonte la piste de l'explorateur en détectant et en suivant les balises.

La Fig. 18 illustre le résultat du TRAT (obtenu par simulation) dans le cas d'un parcours 'labyrinthe'. Plusieurs paramètres peuvent empêcher le navigateur d'arriver à destination : lorsque les

balises sont trop éloignées les unes des autres ; lorsqu'il ne scanne pas l'espace de manière suffisante pour détecter la balise ; lorsque le réseau n'a pas suffisamment d'antennes pour générer une balise bien localisée spatialement ; lorsque la longueur d'onde est trop courte par rapport à la longueur totale du parcours.

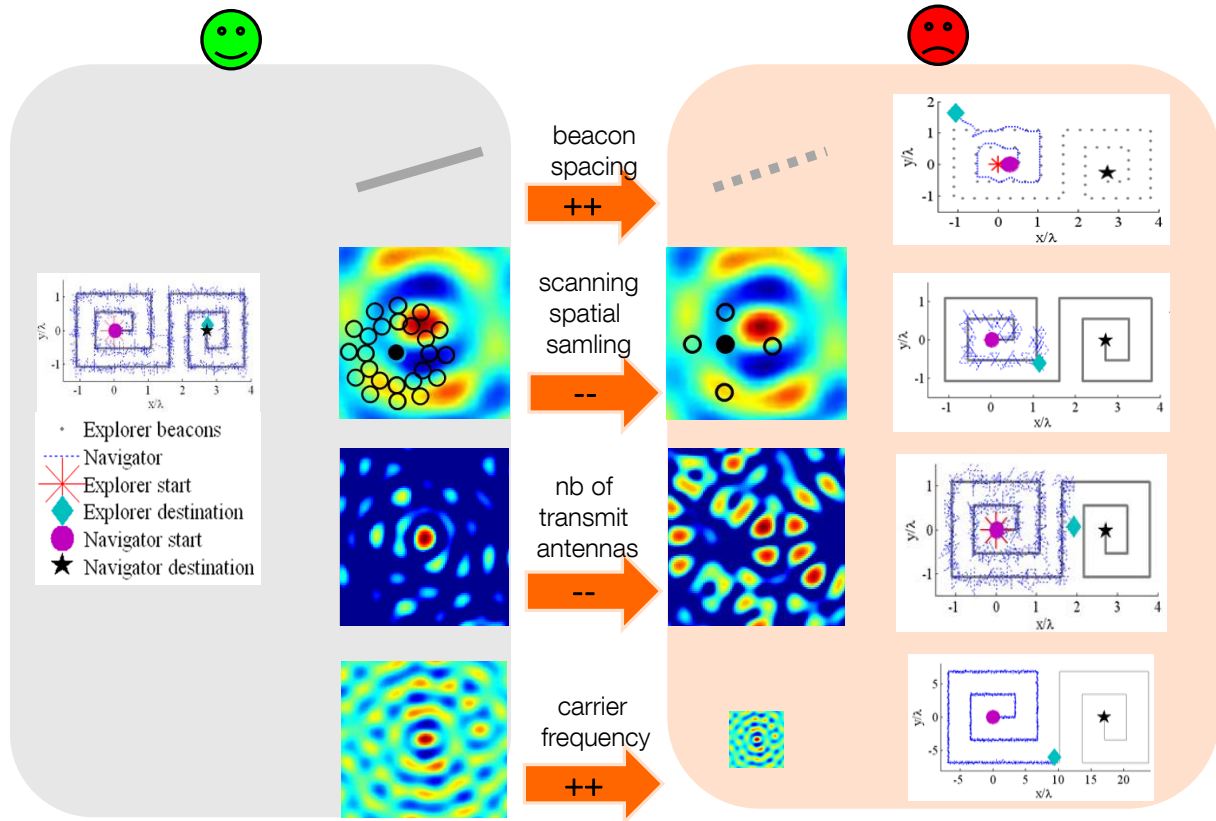


Fig. 18 Performance du TRAT dans un parcours labyrinthique et influences de divers paramètres (de l'espace entre balises, de la précision de la détection de balise, du nombre d'antennes d'émission et de la fréquence porteuse)

D. DFT-SM-MRT pour 'large MIMO' et ondes millimétriques

Avec la 5G, des réseaux très denses de points d'accès (espacés de 10 à 100 mètres) seront potentiellement déployés. Ceci pourrait permettre de satisfaire une grande demande de trafic. Des solutions de backhaul sans fil, très haut débit et de courte portée seront nécessaires pour relier, en partie, ce réseau très dense.

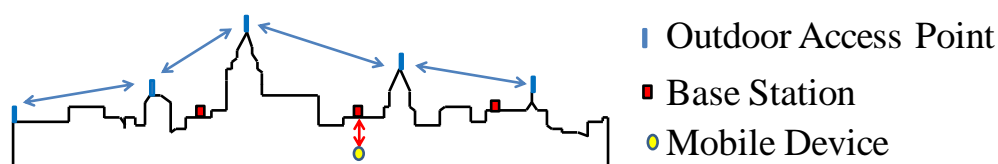


Fig. 19 Example of outdoor wireless meshed network

Nous proposons d'utiliser les ondes millimétriques (de courte portée) et des systèmes 'large MIMO' (comportant des centaines d'antennes à l'émetteur et au récepteur) pour fournir du très haut débit. Nous proposons de multiplexer spatialement des centaines de flux. La décomposition en valeurs singulières ou singular value decomposition (SVD) est la solution optimale. Cependant, la complexité de cette technique est proportionnelle au cube du nombre d'antennes, et devient rédhibitoire pour des systèmes 'large MIMO'. Nous proposons de combiner le MRT avec un multiplexage spatial par transformée de Fourier discrète spatiale (DFT-SM). Le DFT-SM consiste à utiliser une DFT et une DFT inverse dans le domaine spatial, comme précodeurs et décodeurs. Quand deux réseaux d'antennes linéaires se font face, le DFT-SM envoie/détecte les flux de données suivant des angles distincts (voir la Fig. 20). Quand deux réseaux d'antennes circulaires se font face (voir Fig. 21), le DFT-SM envoie/détecte les flux de données sur des ondes en hélices de vitesses distinctes. Le MRT sert à compenser les non-alignements. Notre schéma s'appelle donc le DFT-SM-MRT (SM : spatial multiplexing).

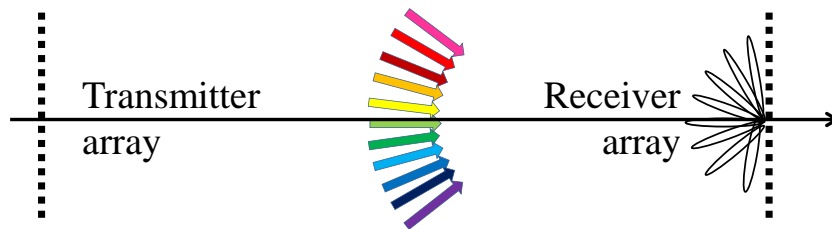


Fig. 20 DFT-SM for aligned linear arrays

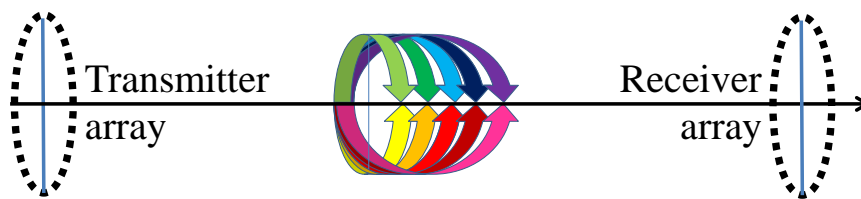


Fig. 21 DFT-SM for aligned circular arrays

Le ratio entre la complexité de la SVD beamforming et la complexité du schéma proposé est tracé dans la Fig. 22. Le ratio explose pour les systèmes 'large MIMO'.

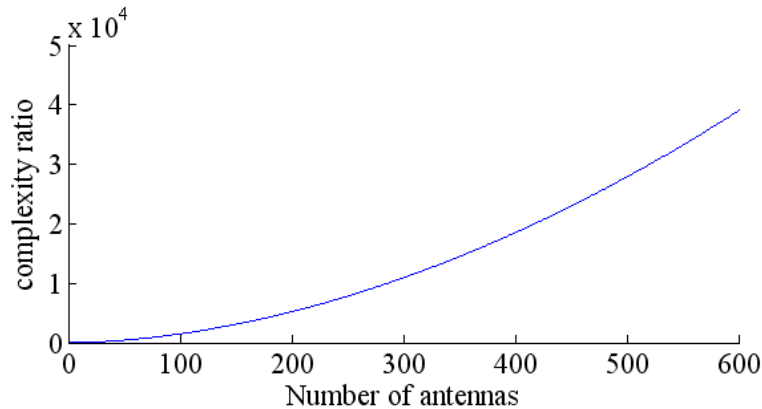


Fig. 22 Complexity ratio versus number of antennas

Des résultats de simulations montrent que le schéma proposé, avec 512 antennes, permet d'atteindre des efficacités spectrales de 100 bits/s/Hz à 1000 bits/s/Hz. Le DFT-SM-MRT atteint 1/3 à 5/7 de la performance de la SVD avec une complexité 10,000 fois moindre.

VI. Conclusion

Le retournement temporel a été clairement identifié lors de travaux ultérieurs comme avantageux pour l'ultra large bande. Il permet d'obtenir une performance optimale avec un récepteur très simple. Grâce à nos simulations et nos études expérimentales, nous savons désormais que les mêmes avantages peuvent être tirées dans les bandes typiques pour des réseaux mobiles, à condition d'utiliser un nombre d'antennes suffisant (16 antennes typiquement).

La plupart des travaux précédents sur le retournement temporel ignorent les scénarios suivants: le mode de duplexage en fréquence et les hautes mobilités. La condition de réciprocité du canal n'est en effet pas vérifiée dans ces deux cas. Dans les réseaux mobiles, le mode de duplexage en fréquence et les véhicules connectés sont incontournables. Nous proposons de nouvelles techniques permettant de focaliser en FDD et en mobilité : le FDD TR et le SRTA.

Nous proposons aussi de nouveaux systèmes de communication et de nouvelles applications utilisant un réseau mobile focalisant par retournement temporel.

La suite de nos travaux se focalisera sur ce dernier volet de la thèse.

List of contributions

Magazine

1. Phan-Huy, D.-T. ; Sternad, M. ; Svensson, T. , “Making 5G Adaptive Antennas Work for Very Fast Moving Vehicles,” *IEEE Intelligent Transportation Systems Magazine*, vol.7, no.2, pp.71,84, Summer 2015.

Conference

1. **Phan-Huy, D.-T.**; Ben Halima, S.; Helard, M., "Dumb-to-perfect receiver throughput ratio maps of a time reversal wireless indoor system," in *Proc. 2013 20th International Conference on Telecommunications (ICT)*, pp. 1,5, May 2013.
2. **Phan-Huy, D.-T.**; Ben Halima, S.; Hélar, M., "Frequency division duplex Time reversal," in *Proc.2011 IEEE Global Telecommunications Conference (GLOBECOM 2011)*, pp.1,5, Dec. 2011.
3. **Phan-Huy, D.-T.**; Hélar, M., "Receive antenna shift keying for time reversal wireless communications," in *Proc.2012 IEEE International Conference on Communications (ICC)*, pp.4852,4856, June 2012.
4. **Phan-Huy, D.-T.**; Sarrebourg, T.; Gati, A.; Wiart, J.; Hélar, M., “Characterization of the confidentiality of a green time reversal communication system: Experimental measurement of the spy BER sink,” in *Proc. 2013 IEEE Wireless Communications and Networking Conference (WCNC)*, pp.4783,4788, April 2013.
5. **Phan-Huy, D.-T.** and Hélar, M., “Large MISO Beamforming For High Speed Vehicles Using Separate Receive & Training Antennas”, in *Proc. 2013 IEEE VTC 2013*, pp. 1,5.
6. **Phan-Huy, D.-T.**; Siohan, Pierre; Hélar, Maryline, « “Make-It-Real” precoders for MIMO OFDM/OQAM without inter carrier interference », in *Proc. 2013 IEEE Global Telecommunications Conference (GLOBECOM 2013)*, pp. 3920,3924, december 2013.

7. **Phan Huy, D.-T.**; Sternad, M., Svensson, T., “Adaptive Large MISO Downlink with Predictor Antennas Array for very fast moving vehicles”, in *Proc. ICCVE*, pp. 331,336, december 2013.
8. **Phan Huy, D. T.**; Tölli, A.; Rajatheva, N.; De Carvalho, E., "DFT based spatial multiplexing and maximum ratio transmission for mm-wave large MIMO", in *Proc. IEEE WCNC 2014*, pp. 913,918, April 2014.
9. **Phan-Huy, D.-T.**, Malhouroux-Gaffet, N.; Hélard, M., “Time reversal for Ant Trails in wireless networks”, in *Proc. 2014 IEEE Global Telecommunications Conference (GLOBECOM)*, december 2014.

Other contributions on time reversal not presented in the PhD thesis:

1. **Phan-Huy, D.-T.**; Siohan, P.; Hélard, M., “Make-It-Real-And-Anticirculating Orthogonal Space-Time Coding for MIMO OFDM/OQAM”), in *Proc. 2015 IEEE 16th International Workshop on Signal Processing Advances in Wireless Communications (SPAWC)*, June 2014.
2. **Phan-Huy, D.-T.**; Kokar, Y.; Sarrebourg d'Audeville, T.; Malhouroux Gaffet, N.; Pajusco, P.; Leray, C.; Gati, A.; Wiart, J., “On the human exposure to radio frequency radiations expected from future small connected objects”, in *Proc. 2014 IEEE Global Telecommunications Conference (GLOBECOM)*, December 2014.

List of figures

Fig. 2.1.1 Two identical networks having a system function $H(f)$ separated by a time reversal device. Figure based on [1].....	49
Fig. 2.3.1 Multi-Antenna TR.....	63
Fig. 2.3.2 Multi-antenna TR equivalent channel.....	64
Fig. 3.1.1 System model.....	76
Fig. 3.1.2 Building floor.....	81
Fig. 3.1.3 Throughput CCDF, $E=0$ dBm	82
Fig. 3.1.4 DR To PR Throughput Ratio, $E=0$ Bm	82
Fig. 3.1.5 Throughput CCDF, $E=-10$ dBm.....	83
Fig. 3.1.6 DR To PR Throughput Ratio, $E=-10$ dBm.....	83
Fig. 3.1.7 TR, 1 stream.....	83
Fig. 3.1.8 TR, 2 streams	83
Fig. 3.1.9 TR, DPRTR.....	83
Fig. 3.1.10 1bit TR, 1 stream.....	83
Fig. 3.1.11 1bit TR, 2 streams	83
Fig. 3.1.12 1bit TR, DPRTR.....	83
Fig. 3.2.1 Spy BER evaluation.....	88

Fig. 3.2.2 Room and positions of antennas.	89
Fig. 3.2.3 Experimental Setup: focusing phase, for spy position p and antenna i.....	91
Fig. 3.2.4 Spy BER.....	98
Fig. 3.2.5 Spy to target received power ratio[dB]	99
Fig. 4.1.1 System Model	101
Fig. 4.1.2 FDD TR scheme.....	102
Fig. 4.1.3 32x1 M Tap	106
Fig. 4.1.4 32x1 Winner II	107
Fig. 4.1.5 16x2 Winner II	108
Fig. 4.1.6 16x1 M Tap	109
Fig. 4.1.7 16x1 Winner II	110
Fig. 4.1.8 16x2 Winner II	111
Fig. 4.2.1 Adaptive downlink beamforming towards a vehicle, LOS propagation scenario	112
Fig. 4.2.2 Adaptive downlink beamforming towards a vehicle, NLOS propagation scenario.	113
Fig. 4.2.3 Vehicle antennas.....	116
Fig. 4.2.4 RS and SRTA systems. Distinct beamformers are computed for distinct times during the downlink frame. Each beamformer is based on a distinct channel measurement performed during the uplink frame. All channel measurements go through the same procedure and undergo the same processing delay before being converted into beamformers. a) In the RS system, during the delay between the channel measurement and the data transmission, the vehicle moves by a displacement $v t_0$. This causes beamforming mis-pointing to occur. b) In the SRTA system, during	

the during the delay between the channel measurement and the data transmission the vehicle moves by a displacement which is $v t_{av}$) compensated by the use of a predictor antenna which is distinct from the receive antenna. In this case, mispointing is avoided.	119
Fig. 4.2.5 SRTA and SRTA-BSOS systems. a) in SRTA system, residual beamforming mispointing occurs for the considered speed. The target antenna receives the data with a weak power. b) in the SRTA-BSOS system, multiple side lobes are strengthened to give more opportunities for the target antenna to receive the data with a high power.....	124
Fig. 4.2.6 SRTA and SRTA-PI systems. a) In SRTA system, for the considered speed, residual beamforming mis-pointing occurs and the beamformer ‘misses’ the receive antenna (the first antenna behind the front antenna). b) in the SRTA-PI system, several channel measurements collected over a duration of $t_a(v)$, and coming from several predictor antennas are collected and interpolated to predict the channel and beamform over the exact position of the new receive antenna (the second antenna behind the front antenna).....	126
Fig. 4.2.7 SRTA-PI, one channel realization at 240kmph. The real part of the channel measurements, cumulated over predictor antennas and measurement times, are plotted. Each measurement is plotted as a function of the corresponding sensed position in space. The exact values of the channel coefficients of five antennas of the vehicles at the data transmission time are also plotted. One can observe that the channel predicted for the 5th antenna obtained by interpolation of the measurements, perfectly matches the exact value.	127
Fig. 4.2.8 Selected antennas	131
Fig. 4.2.9 Extended frame versus speed	132
Fig. 4.2.10 SNR versus speed.....	132
Fig. 4.2.11 BLER versus speed	132
Fig. 4.2.12 Transmit active antennas versus speed.....	133

Fig. 4.2.13 Energy Saving versus speed.....	133
Fig. 4.2.14 BLER versus speed, strong LOS.....	134
Fig. 5.1.1 Example of RASK with 16 receive antennas and 3 symbol periods.....	137
Fig. 5.1.2 System Model for PAM and RASK	137
Fig. 5.1.3 TR, K=1tap.....	142
Fig. 5.1.4 1bit TR, K=1tap	142
Fig. 5.1.5 TR, K=15taps	143
Fig. 5.1.6 1bit TR, K=15taps.....	143
Fig. 5.2.1 MIR Precoder OFDM/OQAM Transmitter architecture.....	151
Fig. 5.2.2 OFDM/OQAM Receiver architecture.....	152
Fig. 5.2.3 Peak spectral efficiencies, 8x8 MIMO.....	157
Fig. 5.2.4 Spectral efficiencies with $TuTsOFDM = 0.75$ and $TuTsOQAM = 1$, 8x8 MIMO.....	158
Fig. 5.3.1 two examples of ‘exploration-followed-by-navigation’ process.....	159
Fig. 5.3.2 Time reversal focusing	160
Fig. 5.3.3 TRAT procedure.....	163
Fig. 5.3.4 ‘Navigation’ phase	165
Fig. 5.3.5 Positions of ‘virtual’ antennas depending on the scanning method	166
Fig. 5.3.6 Example of implementation of the rotation-based scanning.....	166
Fig. 5.3.7 Labyrinth-type trajectory, with total $L=49a$	168

Fig. 5.3.8 Reference simulation.....	169
Fig. 5.3.9 $\delta = 0.3 > \delta_{ref}$	169
Fig. 5.3.10 $N_{rx} = 4 < N_{rx,ref}$	170
Fig. 5.3.11 $N_{tx} = 6 < N_{tx,ref}$	170
Fig. 5.3.12 Scanning: grid-based instead of rotation-based	170
Fig. 5.3.13 $f_0 = 5GHz > f_{0,ref}$	171
Fig. 5.3.14 CDF of D_{max} with $NMPC = NMPC, ref$ and varying N_{tx}	172
Fig. 5.3.15 CDF of D_{max} with $N_{tx} = N_{tx,ref}$ and varying $NMPC$	172
Fig. 5.3.16 Grid-based scanning.....	173
Fig. 5.3.17 Rotation-based scanning	173
Fig. 5.4.1 Example of outdoor wireless meshed network	174
Fig. 5.4.2 DFT-SM for aligned linear arrays	176
Fig. 5.4.3 DFT-SM for aligned circular arrays	176
Fig. 5.4.4 System model.....	180
Fig. 5.4.5 Complexity ratio versus number of antennas	182
Fig. 5.4.6 Model for translated, rotated circular array with reflection	183
Fig. 5.4.7 Model for translated, rotated linear array with reflection	183
Fig. 5.4.8 Circular array, translation effect only.....	185
Fig. 5.4.9 Circular array, rotation effect only	185

Fig. 5.4.10 Circular array, reflection effect only	185
Fig. 5.4.11 Circular array, rotation, translation and reflection effects	186
Fig. 5.4.12 Circular array, rotation, translation and reflection (Zoom)	186
Fig. 5.4.13 Linear array, translation effect only	187
Fig. 5.4.14 Linear array, rotation effect only	187
Fig. 5.4.15 Linear array, reflection effect only	187
Fig. 5.4.16 Linear array, translation, rotation and reflection effects.....	187
Fig. 5.4.17 Linear array, translation, rotation and reflection effects (Zoom)	188
Fig. 7.1.1 OFDM/OQAM modulator and de-modulator	192
Fig. 7.1.2 Transmitter architecture, TR implementation	192
Fig. 7.1.3 Transmitter architecture, Maximum Ratio Transmission implementation	193
Fig. 7.2.1 Vehicle antenna(s) for RS and SRTA systems	200
Fig. 7.2.2 Vehicle Antennas in SRTA	201
Fig. 7.2.3 Impact of number of transmit antennas K and vehicle speed v on SNR , for classical (RS) scheme	203
Fig. 7.2.4 Impact of number of transmit antennas K and vehicle speed v on $BLER$ for classical (RS) scheme	203
Fig. 7.2.5 Impact of vehicle speed v on SNR , for classical (RS) and SRTA schemes, for $K=64$, over random channel model	203

Fig. 7.2.6 Impact of v on BLER for classical (RS) and SRTA with different d values, for $K=64$, over random channel model	203
Fig. 7.2.7 Adaptive Frame Duration vs vehicle speed v	204
Fig. 7.2.8 Receive Antenna index versus vehicle speed v	204
Fig. 7.2.9 Results with Winner II C1 Channel Models.....	205

List of tables

Table 4.2.1 Parameters and expected ordering	129
Table 4.2.2 BLER For 64 QAM, rate $\frac{3}{4}$, Turbo code, with block length of 6000 bits	131
Table 5.4.1 DFT-SM-MRT performance at $m=40$	188
Table 7.2.1 Look Up Table	201

Acronyms

1-bit TR	one bit time reversal
AMC	adaptive modulation and coding
AWGN	additive white gaussian noise
BER	bit error rate
BF	beamforming
BLER	block error rate
BS	base station
BSOS	border switch off scheme
CCDF	complementary cummulative distribution Function
CSIR	channel state information at the receiver
CSIT	channel state information at the transmitter
DFT	discrete fourier transform
DFT-SM-MRT	discrete fourier transform based spatial multiplexing with maximum ratio transmission
DL	downlink
DPRTR	dumb to perfect receiver throughput ratio
DR	dumb receiver
FDD	frequency division duplex

FDD TR	frequency division duplex time reversal
FFT	fast fourier transform
IDFT	inverse discrete fourier transform
IFFT	inverse FFT
LOS	line of sight
MCS	modulation and coding scheme
MIMO	multiple input multiple output
MIR	make-it-real
MISO	multiple input single output
MMSE	minimum mean square error
MRT	maximum ratio transmission
MS	mobile station
NLOS	non line of sight
OFDM	orthogonal frequency division multiplex
OQAM	offset quadrature amplitude modulation
PA	predictor antenna
PAM	phase and amplitude modulation
QAM	quadrature amplitude modulation
QPSK	quadrature phase shift keying

RASK	receive antenna shift keying
RS	reference system
RSOS	random switch off scheme
SIMO	Single Input Multiple Output
SINR	Signal to noise and interference ratio
SISO	Single Input Single Output
SM	spatial modulation
SNR	signal-to-noise ratio
SRTA	separate receive and training antenna
SSK	space shift keying
STBC	space time block code
STC	space time coding
STR	single tap receiver
SVD	singular value decomposition
TDD	time division duplex
TR	time reversal
TRAT	time reversal for ant trails
UL	uplink
UWB	ultra wideband

WLAN wireless local area network

ZF zero forcing beamforming

General mathematical notations

H	A straight capital letter in bold is a matrix
I	Identity matrix
$\mathbf{H}_{i,j}$	Element of the line number i and the column number i of H
v	A straight small letter in bold is a vector
\mathbf{v}_i	\mathbf{v}_i is the element number i of v
H *	Conjugate of H
H ^H	Transpose conjugate of H
$h(t)$	An italic letter is a function of one or several variables, depending on the context
$\delta(t)$	is the value of the Dirac function at t
$\cos(t)$	is the value of the the cosine function at t
$\log(t)$	is the value of the the Neperian logarithme function at t
$\log_2(t)$	is the value of the the binary logarithm function at t
$\sin(t)$	is the value of the the sine function at t
$ \cdot $	is the module operation
$E[\cdot]$	expectation operation
$\Re(\cdot)$	real part extraction. If z is a complex number, then $Real(z)$ is its real part.
$\Im(\cdot)$	imaginary part extraction. If z is a complex number, then $Imag(z)$ is its imaginary part.
$\lceil \cdot \rceil$	$\lceil t \rceil$ is the ceil of t .
$\ \cdot\ $	If $\mathbf{H} \in \mathbb{C}^{N \times M}$, then, $\ \mathbf{H}\ ^2 = \sum_{n=0}^{N-1} \sum_{m=0}^{M-1} \mathbf{H}_{nm} ^2$.
$sign(\cdot)$	gives the sign
*	Convolution product
J	complex number verifying $J^2 = -1$. If z is a complex number, then $z = Real(z) + J.Imag(z)$

σ_z^2 If z is a complex variable, σ_z^2 denotes the variance of z .

$\max_x(y(x))$ is the max operation

Mathematical notations for single-carrier studies

For sum particular studies (section 3.1, section 4.1 and section 5.1), we use the following specific set of mathematical notations:

- $A_{n,j} \in \mathbb{C}$ is the n^{th} symbol;
- $E_{i,j} \in \mathbb{R}^+$ is the power allocated to the transmit antenna number i and the data stream targeted to the antenna number j ;
- $f(t)$ is the transmit pulse shape filter; it is the square raised root cosine filter with roll-off factor of 0.22;
- $f^{1bit}(\cdot) = \text{sign}(\Re(\cdot)) + J \cdot \text{sign}(\Im(\cdot))$;
- $F \in \mathbb{R}^+$ is the receiver noise figure;
- $h_{i,j}(t)$ is the response impulse of the channel between the transmit antenna number i and the receive antenna number j ;
- $h_{i,j,k} \in \mathbb{C}$ is the gain of the tap number k of $h_{i,j}(t)$
- $i, i' \in \mathbb{N}$ are transmit antennas indexes;
- $j, j' \in \mathbb{N}$ is receive antennas indexes;
- $k, k', k_1 \in \mathbb{N}$ are tap indexes;
- M is the number of channel taps;
- N is the number of receive antennas;
- $n_j(t)$ is the noise at antenna number j and time t ;
- $N_0 \in \mathbb{R}^+$ is the noise power spectral density;
- $p_{i,j}(t)$ is the prefilter (function of time t) at the transmit antenna number i and targeting the antenna number j ;
- $p_{i,j,k} \in \mathbb{C}$ is the gain of the tap number k $p_{i,j}(t)$

-
- P is the number of transmit antennas;
 - $Pu_j \in \mathbb{R}^+$ is the useful power at the receive antenna j ;
 - $Pisi_j \in \mathbb{R}^+$ is the inter-symbol interference power at the receive antenna j ;
 - $Pisi_j \in \mathbb{R}^+$ is the multi-stream interference power at the receive antenna j ;
 - $P_N \in \mathbb{R}^+$ is the noise power;
 - $q(t)$ is the receive filter;
 - $S_{i,j}(t)$ (function of time t) is the signal transmitted by the antenna number j and targeting the receive antenna number j .
 - $SINR_j \in \mathbb{R}^+$ is the signal-to-interference-and-noise ratio at the receive antenna j ;
 - $t \in \mathbb{R}$ is the time;
 - $T \in \mathbb{R}^+$ is the symbol period;
 - If $v(t) = 1$ then, $t > 0$, and $v(t) = -1$, otherwise.
 - $\alpha_{i,j} \in \mathbb{R}^+$ is the gain of the channel between the transmit antenna number i and the data stream targeted to the antenna number j (due to path loss);
 - $\varepsilon_{K n k k'} = (K - n)T + \tau_{k k'}$.
 - $\delta(t)$ denotes the Dirac function;
 - $\lambda_{i,j} \in \mathbb{R}^+$ is a normalising factor;
 - $\rho_f(t) = f(t) * f^*(-t)$;
 - $\tau_k \in \mathbb{R}^+$ is the delay of the k^{th} tap.
 - $\tau_{k k'} = \tau_{k'} - \tau_k$.

Chapter 1 - Introduction

Mobile networks have been developing tremendously during the last decades. The 5th generation of mobile network will be deployed in the 2020's. These future networks will have to support 1000 times more traffic than today, and more than 50 billions of connected objects. In parallel, the concern for energy consumption of mobile networks is growing. The concern for network equipment and mobile devices cost is growing. It is therefore important to start investigating signal-processing techniques that are near to optimum when considering low power networks and low cost devices. 'Time reversal' space-time focusing technique is one candidate solution. The purpose of this PHD thesis is to investigate this solution. This PhD thesis is organised as follows:

Chapter 2 is a state-of-the art on time reversal for wireless communications. It presents the time reversal technique and relates it to the matched filter and the maximum ratio transmission beamformer. Previous works on time reversal in wireless local area networks and ultra wideband communication systems are summarised. They show that thanks to TR, the complexity of devices and the network transmit power can be lowered. However, these studies do not specifically address mobile networks. The chapter also raises issues and challenges which are specific to mobile networks.

Next chapters describe our contributions and answer the questions raised by Chapter 2:

- Chapter 3 provides new results enabling to evaluate the interest of time reversal indoor mobile networks such as femtos/small cell networks;
- Chapter 4 describes new enablers for time reversal focusing in mobile networks in challenging scenarios listed in chapter 2;
- Chapter 5 describes new communication schemes and new applications based on time reversal and mobile networks.

Chapter 6, chapter 7, 8 and 9 are the conclusion, the annex, the list of references and the list of acronyms, respectively.

Chapter 2 - State-of-the-art on time reversal for wireless communications

This chapter provides a state-of-the-art on time reversal techniques for wireless communications:

- sub-section 2.1 summarises early works on matched filter and maximum ratio transmission beamformer;
- sub-section 2.2 introduces the time reversal space-time technique and relates it to the matched filter and the maximum ratio transmission beamformer;
- sub-section 2.3 summarises the first works on time reversal for wireless communications and explains the role of the wireless propagation;
- sub-section 4 summarises recent techniques exploiting time reversal.

The following notations are used throughout this chapter:

- L is the number of sub-carriers, if a multi-carrier system is considered;
- N is the number of transmit antennas;
- M is the number of receive antennas.

In this chapter, different notations are used to denote the propagation channel, depending on the context:

- $h(t)$ is a channel impulse response of a single-carrier and single-input single-output (SISO) communication system and $H(f)$ is the corresponding frequency response;
- $h_{n,m}(t)$ is the channel response impulse between transmit antenna n and receive antenna m in a single-carrier and multiple-input multiple-output (MIMO) $N \times M$ communication system;
- $\mathbf{h} \in \mathbb{C}^{1 \times N}$ is the vector of channel coefficients between the receiver and the transmitter in a single-carrier and $N \times 1$ multiple-input single-output (MISO) communication system, in line-of-sight (LOS) propagation.
- $\mathbf{H} \in \mathbb{C}^{M \times N}$ is the channel matrix in a single-carrier and $N \times M$ MIMO communication system, in LOS propagation;

- $\mathbf{H}^{(l)} \in \mathbb{C}^{M \times M}$ is the channel matrix for a multicarrier and MIMO $N \times M$ communication system, for sub-carrier l .

In this chapter, the following filters are studied in a **single carrier and SISO** communication system:

- $p_{TR}(t) = h(-t)$ is the time reversal filter of $h(t)$;
- $p_{MF}(t)$ is the matched filter of $h(t)$;
- $p_{IF}(t)$ is the time inverse filter of $h(t)$.

In this chapter, the following notations are used to study a **single carrier and $N \times M$ MIMO** communication system:

- $x_m(t)$ is the data stream intended to antenna m ;
- $p_{n,m}(t)$ is the matched filter (and time reversal filter) for $h_{n,m}(t)$;
- $s_n(t)$ is the signal sent by antenna n ;
- $y_m(t)$ is the signal received by antenna m ;
- $h_{m,m'}^{eq}(t)$ is the equivalent channel after prefiltering and propagation between receive antenna m and transmit data stream m' .

In this chapter, the following notation is used to study a **single carrier and $N \times M$ MIMO communication system in LOS propagation**: $\mathbf{p}_{MRT} \in \mathbb{C}^{N \times 1}$ is the vector of optimum beamforming coefficients in a MISO $N \times 1$ link.

In this chapter, the following notations are used to study a **single carrier and $N \times M$ MIMO communication system in LOS propagation**:

- $\mathbf{P}_{MRT} \in \mathbb{C}^{M \times N}$ is maximum ratio transmission precoder (beamformer) in a MIMO $N \times M$ link, in LOS propagation;
- $\mathbf{P}_{ZF} \in \mathbb{C}^{M \times N}$ is zero forcing precoder (beamformer) in a MIMO $N \times M$ link, in LOS propagation;
- $\mathbf{x} \in \mathbb{C}^{M \times 1}$ is the vector of M transmitted data symbols;

- $\mathbf{s} \in \mathbb{C}^{N \times 1}$ is the vector of N transmitted symbols;
- $\mathbf{y} \in \mathbb{C}^{M \times 1}$ is the vector of M received data symbols.
- $\mathbf{u} \in \mathbb{C}^{M \times 1}$ is the useful part of the received signal;
- $\mathbf{v} \in \mathbb{C}^{M \times 1}$ is the inter-symbol interference part of the received signal;
- $\mathbf{w} \in \mathbb{C}^{M \times 1}$ is the multi-stream interference part of the received signal;
- $\mathbf{n} \in \mathbb{C}^{M \times 1}$ is the noise part of the received signal;

In this chapter, the following notations are used to study a **multi-carrier and $N \times M$ MIMO** communication system:

- $\mathbf{H}^{eq,(l)} \in \mathbb{C}^{M \times M}$ is the equivalent channel matrix apres precoding and propagation for an MIMO $N \times M$ link, for sub-carrier l .
- $\mathbf{P}_{MRT}^{(l)} \in \mathbb{C}^{M \times N}$ is maximum ratio transmission precoder (beamformer), for sub-carrier l ;
- $\mathbf{x}^{(l)} \in \mathbb{C}^{M \times 1}$ is the vector of M transmitted data symbols, for sub-carrier l ;
- $\mathbf{s}^{(l)} \in \mathbb{C}^{N \times 1}$ is the vector of N transmitted symbols, for sub-carrier l ;
- $\mathbf{y}^{(l)} \in \mathbb{C}^{M \times 1}$ is the vector of M received data symbols, for sub-carrier l ;
- $\mathbf{u}^{(l)} \in \mathbb{C}^{M \times 1}$ is the useful part of the received signal;
- $\mathbf{v}^{(l)} \in \mathbb{C}^{M \times 1}$ is the inter-symbol interference part of the received signal;
- $\mathbf{n}^{(l)} \in \mathbb{C}^{M \times 1}$ is the multi-stream interference part of the received signal.

2.1 Matched filter and maximum ratio transmission beamformer

This sub-section presents the works that have preceeded the birth of the Time reversal space-time focusing technique.

2.1.1 The transmit ‘matched filter’: a time compression technique

In this sub-section, we will show that very early, the time inverses of recorded signals have been exploited for telecommunications in environments with multiple echoes. Echoes degrade the quality of the communication. As further explained in the following sub-sections, the inverse of the signal can be

used render the propagation nearly echo-free. This can be seen as a ‘time compression’ or ‘time focusing’ technique.

We will also show that these works ignored the spatial domain.

2.1.1.1 A first Time reversal experiment on the telephone network in 1957

To our knowledge, the first time **time reversal (TR)** is mentioned in telecommunications, is in 1957, in [1]. In this paper, Bogert proposes to transmit pictures and television over the standard telephone circuits. Telephone circuits can reliably transport a narrow band signal such as voice. However, a large band signal such as video is subject to what he Bogert calls the “delay distortion” phenomenon. In other words, multiple echoes of the signal are received after propagation through the telephone circuits. Consequently, the quality of the received image is degraded.

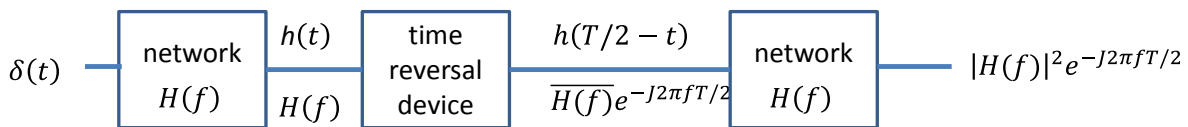


Fig. 2.1.1 Two identical networks having a system function $H(f)$ separated by a time reversal device. Figure based on [1]

To compensate the aforementioned delay distortion phenomenon, Bogert proposes to place a “Time reversal device” exactly at half way between the transmitter and the receiver, as illustrated by Fig. 2.1.1. He assumes that the telephone line is somewhat uniform. He also assumes that the propagation between the transmitter and the time reversal device on one hand, and the propagation between the time reversal device and the receiver on the other hand, are identical. It models these two propagation channels with the same filter $h(t)$ in the time domain and the same corresponding filter $H(f)$ in the frequency domain. The time reversal device first records the received signal over a magnetic tape during a period T . In a second phase, the time reversal device replays the recorded signal time reversely: $h(T/2 - t)$. The observed received signal is compared to the signal that is received without the time reversal device. As illustrated in the figure below, in the presence of the time reversal device, the signal is received through an equivalent filter with the following frequency response: $|H(f)|^2 e^{-j2\pi f T/2}$.

In the absence of the time reversal device, the signal is received through an equivalent filter with the following frequency response: $H(f)e^{-j2\pi f T/2}$.

One could imagine the same experiment with the true ‘time reversal’ prefilter $p_{TR}(t)$:

$$p_{TR}(t) = h(-t).$$

Then the equivalent filter would become simply $|H(f)|^2$.

The paper does not explain why, in theory, this should be better. The paper only relies on experimental results. First experiments are conducted with the transmission of an impulse. The results show that the received impulse response with the time reversal device is more compressed in time than without the time reversal device. Other experiments involve the transmission of pictures. Again, the results show that the received picture has a better quality with the time reversal device than without.

The author acknowledges that putting a time reversal device half way of a network cannot be used in practice. Nevertheless, this work is in fact a very early discovery of the ‘matched filter’. It is also a very early experimental demonstration of one of the properties of the ‘matched filter’: it mitigates the effect of multiple echoes by compressing in time the propagation channel. It renders the propagation channel near to a ‘single echo’ channel, or ‘single tap’ channel. The next sub-section briefly summarizes the matched filter concept.

2.1.1.2 The matched filter

According to Turin, in its “introduction to matched filters” [2] in 1960, if $h(t)$ is any physical waveform, then a filter $p_{MF}(t)$ which is matched to $h(t)$ is, by definition, one with the impulse response:

$$p_{MF}(t) = kh(T - t),$$

where k and T are arbitrary constants. If we take $k = 1$ and $T = 0$, we obtain, again the time reversal filter:

$$p_{MF}(t) = h(-t) = p_{TR}(t).$$

For the purpose of comparison with the “matched filter”, the paper also introduces the “inverse filter” $p_{IF}(t)$ as:

$$(p_{IF} * h)(t) = \delta(t),$$

where δ is the dirac function and $*$ is the product of convolution.” Note that **the “matched filter” is proportional to the inverse in the time domain of a waveform, whereas the inverse filter is not. The “matched filter” and the “inverse filter” are therefore distinct filters.**

In this paper, Turin explains that this matched filter can have many interesting properties for two applications: radar and communications applications.

In the case of radar, Turin explains that if one wants to detect the presence/absence of a known waveform $h(t)$ in a received signal $x(t)$ affected with an additive white noise $n(t)$, then one method

consists in filtering $x(t)$ by the matched filter $h(-t)$, then to sample it at time $t = 0$, and finally to compare the result to a threshold λ . The main idea is that, as shown in the figure below, the output signal of the matched filter is very strong at time $t = 0$ and very weak for times around $t = 0$, when $h(t)$ is present in $x(t)$. Note that in presence of $x(t)$ as most of the energy is received at $t = \Delta$, the received signal is nearly echo-free (as observed earlier in [1]). This simple radar system is illustrated by Fig. 2.1.2 and Fig. 2.1.3.

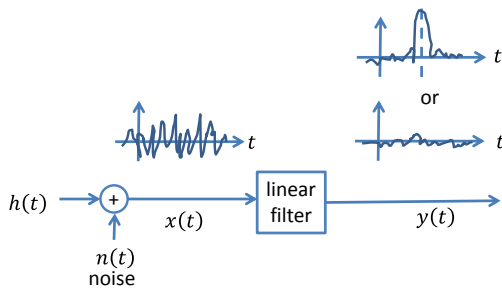


Fig. 2.1.2 Principle of radar. Figure based on [2]

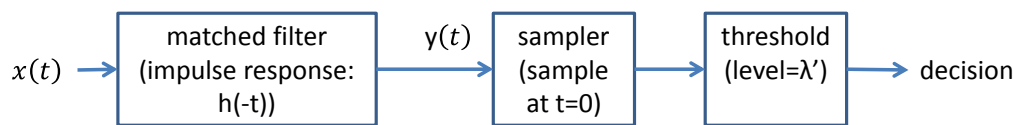


Fig. 2.1.3 Simple radar detection system. Figure based on [2]

The paper explains that this method can also be used in data communication. In this case, one waveform among K different possible waveforms (namely $h_1(t), h_2(t), \dots, h_K(t)$) is transmitted. The receiver detects which of K possible signals was transmitted as follows. The received signal passes through K parallel matched filters, each of them being matched to one of the K known waveforms. Then the output of each matched filter is sampled at the same time, and diminished by biased threshold (which depends on the energy of the transmit signal). In the case, all the waveforms have the same probability; this test is called the 'Maximum-Likelihood' test. A decision circuit collects the K parallel outputs. The decision circuit determines the index m of the transmitted waveform $s_m(t)$ that corresponds to the greatest output among the K collected outputs. The K-ary communication system is illustrated by Fig. 2.1.4.

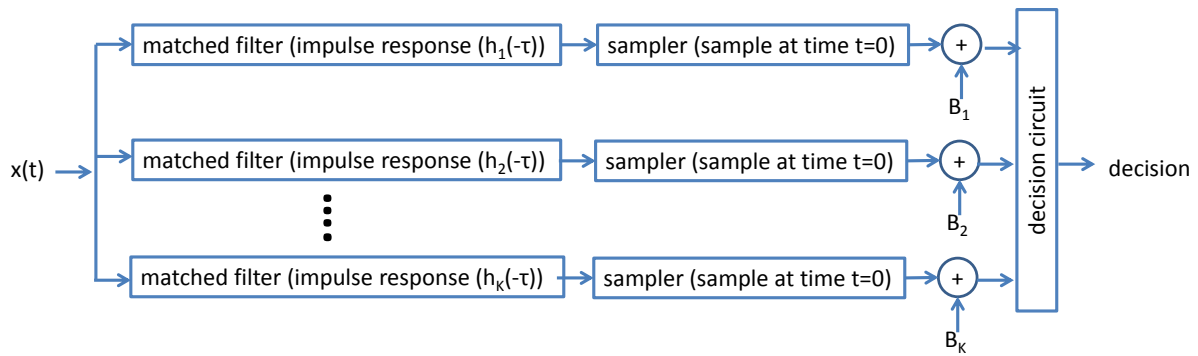


Fig. 2.1.4 Simple K-ary receiver. Figure based on [2]

In this paper, it is shown that, under certain conditions, the optimal filter (for both the radar and M-ary communication problems) is the matched filter. The optimality is true only if the Signal-to-noise ratio is low. In this case only, the matched filtering and sampling operations generate a very high output useful signal power without amplifying the noise. The inverse filter, on the contrary is not recommended for low Signal-to-noise ratio as amplifies the noise. A third filter, the **Minimum Mean Square Error (MMSE) filter** [10] can be considered. It is optimum for every signal-to-noise ratio. It is equal to the matched filter at low signal-to-noise ratio and equal to the inverse filter at high signal-to-noise ratio.

Later on, Turin has described solutions for digital matched filters in [3][4]. Finally, in [4], Turin has shown that a bank of tapped delay line matched filters (also known as ‘rake receiver’ of [5]) enables to perform data communications with spread spectrum with multi-path environment. This was the based for the physical layer of 3G cellular networks as explained in [6].

Again, as in [1], studies on the matched filter only focused on reducing the number of echoes, i.e. reducing the effect of the propagation in the domain. None of these studies did show any property of the matched filter linked to spatial domain.

2.1.2 Maximum ratio transmission (MRT) beamforming: a spatial focusing technique

In this sub-section, we will show that very early, the time inverse of recorded signals has been used to focus a wireless signal in space and perform beamforming. We will also show that these works ignored the time domain.

2.1.2.1 Beamforming in Line-of-sight (LOS) and far field

In [7], “The term beamforming derives from the fact that early spatial filters were designed to form pencil beams in order to receive a signal radiating from a specific location and attenuate signals from

other locations. ‘Forming beams’ seems to indicate radiation of energy; however, beamforming is applicable to either radiation or reception of energy.”

For the particular case of arrays constituted of several elements that are either sensors or transmitters, the propagation between a target point in space and each element, assuming far field and planar waves, is given by:

$$\mathbf{h} = [1 \quad e^{-J2\pi f\tau_1} \quad e^{-J2\pi f\tau_2} \quad \dots \quad e^{-J2\pi f\tau_N}],$$

where \mathbf{h} is a column vector parameterised by the angle θ of the direction of arrival (or departure) of the planar wave and τ_i is the delay with which the planar wave hits the array element i . In such context, beamforming into the direction θ consists in applying a beamforming weight on the received signal at each array element and for each frequency f is a column vector \mathbf{p}_{BF} . The paper shows that if the vector \mathbf{h} can be estimated accurately by the array through (thanks to the use of pilots sent by the target and known by the array), then the optimum beamformer in terms of receive Signal-to-noise ratio is $\mathbf{p}_{BF} = \mathbf{h}^H$. We therefore have:

$$\mathbf{p}_{BF} = \begin{bmatrix} 1 \\ e^{J2\pi f\tau_1} \\ e^{J2\pi f\tau_2} \\ \dots \\ e^{J2\pi f\tau_N} \end{bmatrix} = \begin{bmatrix} 1 \\ e^{-J2\pi f(-\tau_1)} \\ e^{-J2\pi f(-\tau_2)} \\ \dots \\ e^{-J2\pi f(-\tau_N)} \end{bmatrix}.$$

We observe that \mathbf{p} is indeed here equal to the time inverse of \mathbf{h} .

In this case, if the array transmits the data symbol x the received symbol is:

$$y = \mathbf{h}\mathbf{p}_{BF}x + n = Nx + n,$$

where n is the sampled noise. The received signal is multiplied by the beamforming gain of N in amplitude and N^2 in power. Note, that if the power of the beamformer were constrained to be unitary ($\|\mathbf{p}^H\|^2=1$), then **the beamforming gain would be \sqrt{N} in amplitude and N in power.**

Fig. 2.1.5 illustrates the beamforming pattern obtained with a linear phased array of N equal to 10 antenna elements. Free space path loss propagation is modelled. The array is pointing successively towards to distinct targets. The field power is computed numerically and plotted (in dB and colour scale) as a function of the spatial coordinates (in wavelength unit). A high power is observed in the direction of the target.

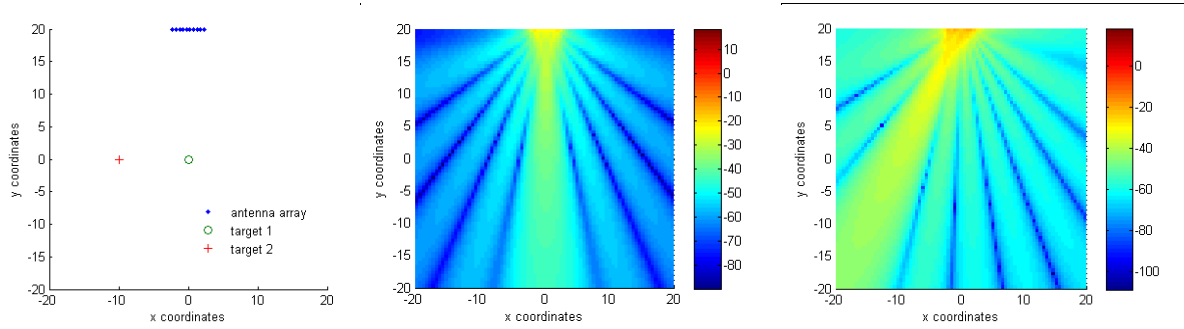


Fig. 2.1.5 Beamforming pattern with 10 antenna elements. The figure on the left illustrates the positions of the transmit antenna array, and the positions of ‘target 1’ and ‘target 2’ with Cartesian coordinates x and y . The figure in the middle, and on the right; illustrate the beamforming pattern (the field power in dB and colorscale as a function of the Cartesian coordinates x and y) created by the transmit antenna array when it beamforms towards ‘target 1’ and ‘target 2’, respectively.

Therefore, this beamforming technique is equivalent to using the **time inverse of the channel**. This beamforming technique is implicitly using TR.

2.1.2.2 Maximum Ratio Transmission (MRT) beamforming in LOS

In [8] the authors propose to transmit several distinct data streams to several distinct antennas, simultaneously and using the same transmit antenna array. LOS propagation is considered. In this paper, the transmitter has N transmit antennas and the receiver has M receive antennas. The transmitter sends M data symbols. Let $\mathbf{x} \in \mathbb{C}^M$ be a vector of size M . \mathbf{x}_m is the data symbol intended to the target receive antenna number m , with $1 \leq m \leq M$. The transmitter sends N signals over its N antennas. Let $\mathbf{s} \in \mathbb{C}^N$ be the vector of size N of transmitted signals. \mathbf{s}_n is the signal transmitted by the transmit antenna number n , with $1 \leq n \leq N$. The channel can be modelled by a MIMO matrix $\mathbf{H} \in \mathbb{C}^{M \times N}$. $\mathbf{H}_{m,n}$ is the coefficient of the channel between the receive antenna number n and the transmit antenna number m . The receiver receives M distinct signals over its M antennas. The paper proposes to use the following signal:

$$\mathbf{s} = \mathbf{P}_{MRT} \mathbf{x},$$

where $\mathbf{P}_{MRT} \in \mathbb{C}^{N \times M}$ and $\mathbf{P}_{MRT} = \mathbf{H}^H$ is the maximum ratio transmission (MRT) beamformer.

Consequently, the received signal \mathbf{y} is therefore:

$$\mathbf{y} = \mathbf{H} \mathbf{H}^H \mathbf{x} + \mathbf{n},$$

where $\mathbf{n} \in \mathbb{C}^M$ is the vector of noise samples. Each receive antenna m receives a signal:

$$\mathbf{y}_m = \mathbf{u}_m + \mathbf{v}_m + \mathbf{n},$$

where:

- $\mathbf{u}_m \in \mathbb{C}^M$ and $\mathbf{u}_m = \sum_{n=1}^N |\mathbf{H}_{m,n}|^2 \mathbf{x}_m$ is the **useful** part of the received signal;
- $\mathbf{v}_m \in \mathbb{C}^M$ and $\mathbf{v}_m = \sum_{n=1}^N \sum_{m'=1, m' \neq m}^M \mathbf{H}_{m,n} \mathbf{H}_{m',n}^* \mathbf{x}_{m'}$ is the **multi-stream interference** part of the signal.

In [9], the author explains that this technique is indeed a beamforming scheme creating one distinct beam per distinct receive antenna. The beam intended towards a given antenna is considered as a useful signal by the target antenna and an interfering signal by all other neighbouring antennas. Due to the design of the transmitted signal, the useful signal is strong whereas the interfering signal is weak. Let us consider the data stream number m . The expression of the channel between the receive antenna number i and the transmit antenna array is the line number m of the global channel matrix \mathbf{H} :

$$\mathbf{h} = [\mathbf{H}_{m,1} \quad \dots \quad \mathbf{H}_{m,L}].$$

As we consider LOS propagation, one can express the channel coefficient $\mathbf{H}_{m,n}$ as follows:

$$\mathbf{H}_{m,n} = \alpha_{m,n} e^{-j(2\pi f \tau_{m,n})},$$

where $\alpha_{m,n}$ and $\tau_{m,n}$ are the amplitude and the delay of the channel, and f is the frequency. Therefore, we have:

$$\mathbf{h} = [\alpha_{m,1} e^{-j(2\pi f \cdot \tau_{m,1})} \quad \dots \quad \alpha_{m,N} e^{-j(2\pi f \cdot \tau_{m,N})}].$$

The MRT beamformer \mathbf{p}_{MRT} for this particular data stream is the column number m of the global beamformer \mathbf{P}_{MRT} :

$$\mathbf{p}_{MRT} = \begin{bmatrix} \mathbf{H}_{m,1}^* \\ \dots \\ \mathbf{H}_{m,N}^* \end{bmatrix} = \begin{bmatrix} \alpha_{m,1} e^{j(2\pi f \cdot \tau_{m,1})} \\ \dots \\ \alpha_{m,N} e^{j(2\pi f \cdot \tau_{m,N})} \end{bmatrix} = \begin{bmatrix} \alpha_{m,1} e^{-j(2\pi f \cdot (-\tau_{m,1}))} \\ \dots \\ \alpha_{m,N} e^{-j(2\pi f \cdot (-\tau_{m,N}))} \end{bmatrix}.$$

Therefore, again, the MRT beamformer \mathbf{H}^H is equivalent to the time inverse of the channel. This beamforming technique is implicitly using TR.

Note that in the time domain a beamformer called ‘zero forcing’ (ZF) beamformer has been introduced [10]. It is equivalent to applying the inverse filter presented in 2.1.1.2 in the spatial domain instead of the time domain. The ZF beamformer aims at nulling the signal destined to antenna m on all other antennas: only antenna m will receive its dedicated signal. The expression of the **ZF beamformer \mathbf{P}_{zf}** is given by:

$$\mathbf{P}_{zf} = \mathbf{H}^H (\mathbf{H}\mathbf{H}^H)^{-1}.$$

In this case, the received signal becomes:

$$\mathbf{y} = \mathbf{H}\mathbf{p}_{zf}\mathbf{x} + \mathbf{n} = \mathbf{x} + \mathbf{n}.$$

In sub-section 2.1.1.2, the inverse filter was found to be less performant than the TR filter when the signal-to-noise ratio is low. Identically, in the spatial domain, the MRT beamformer outperforms the ZF beamformer at low signal-to-noise ratio. Here is a simple example illustrated by Fig. 2.1.6, to show the differences between the two beamformers. We consider free space propagation. 20 transmit antennas are randomly positioned over a circle of 10 wavelengths of radius. A target source is positioned at the centre of the cell. 5 control points are randomly positioned over a circle with a radius of 0.5 wavelength around the target source. The MRT beamformer and the ZF beamformer are considered. The same total transmit power is considered in both cases. In this case, normalised beamformers $\mathbf{p}_{MRT}/\sqrt{\|\mathbf{p}_{MRT}\|^2}$ and $\mathbf{p}_{ZF}/\sqrt{\|\mathbf{p}_{ZF}\|^2}$ are considered.

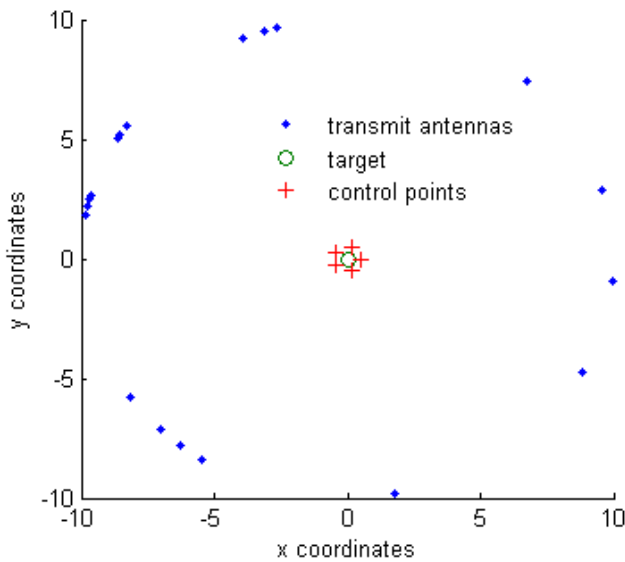


Fig. 2.1.6 transmit antennas, source antenna and control points

The field power is then computed numerically over a region of 3 by 3 wavelengths around the source and plotted as a function of spatial coordinates in Fig. 2.1.7. In Fig. 2.1.7 a) and b) the power for the MRT and the ZF beamformers are plotted respectively. It is assumed that there is no noise. One can observe that ZF guarantees a low power around the target at the expense of the power at the source. With ZF, the transmitters must spend a part of their power budget on creating the 5 nulls in space. Figure 2.1.7 c) and d) illustrate the received power, when a noise floor of -35 dB is considered, for MRT and ZF respectively. In this case, only for MRT the useful signal strength exceeds the noise floor.

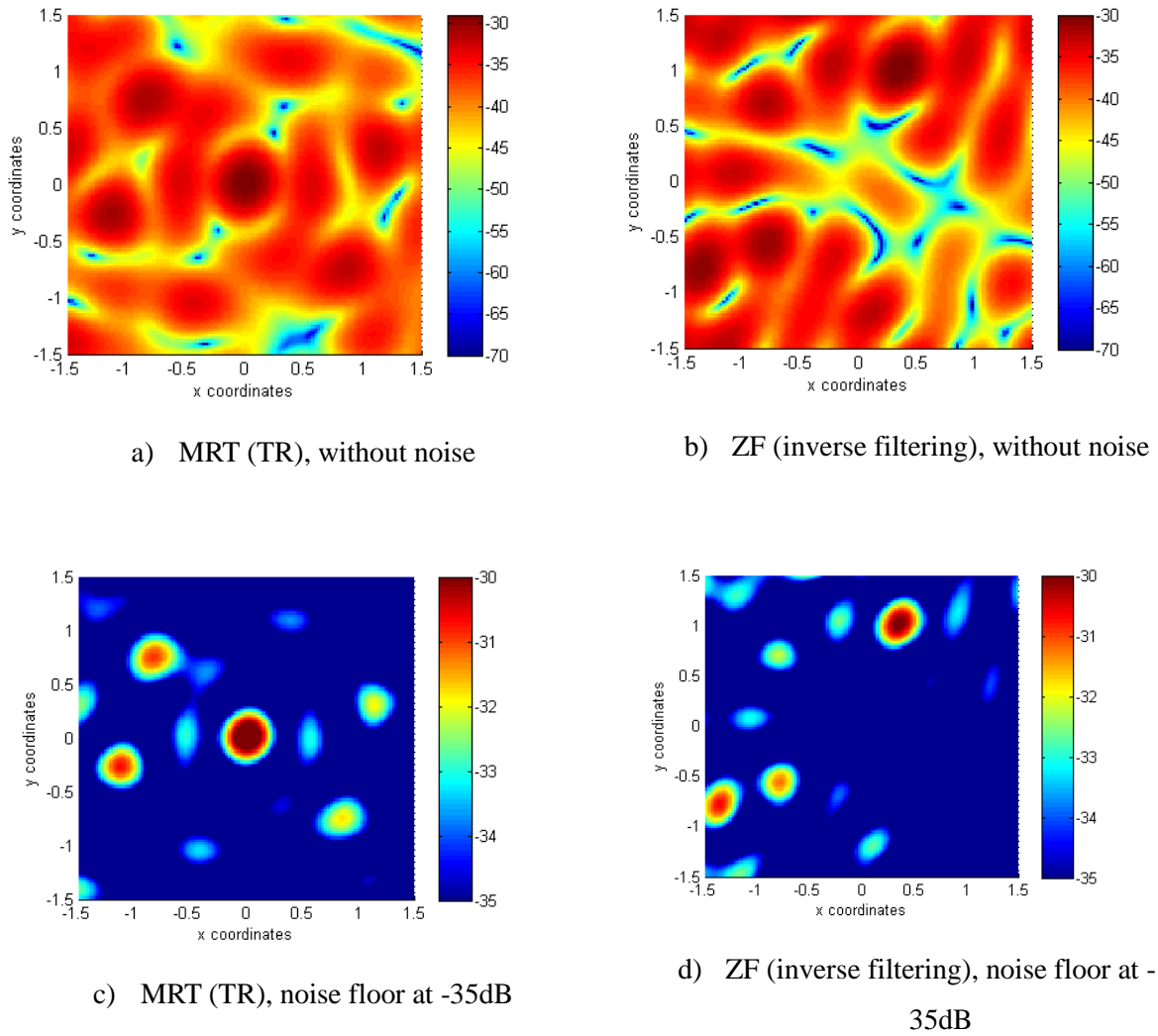


Fig. 2.1.7 maximum ratio transmission versus zero forcing

A third beamformer, the **Minimum Mean Square Error beamformer** [10] can be considered. It is optimum for every signal-to-noise ratio. It is equal to the MRT beamformer at low signal-to-noise ratio and equal to the ZF beamformer at high signal-to-noise ratio. Its expression is given by:

$$\mathbf{P}_{mmse} = y\mathbf{H}^H(\mathbf{H}\mathbf{H}^H + x\mathbf{I})^{-1},$$

where \mathbf{I} is the identity matrix, where x is the inverse of the signal to noise ratio and y is a normalising factor ensuring that the transmitter always transmit with the same power whatever the radio conditions. At high SNR, the MMSE beamformer is equal to the ZF beamformer. At low SNR, the beamformer is equal to the MRT beamformer (if normalised beamformers are considered).

2.1.3 Conclusion

This sub-section shows that for a long period, there have been two separate works:

- On one hand, the time inverse of recorded signals was used to mitigate multipath propagation, which typically occurs in non line-of-sight (NLOS) propagation. This technique was best known as the matched filter. This technique compresses the channel in the time domain. It renders the channel nearly ‘echo-free’ or ‘single tap’. It has been compared to the inverse filter, which perfectly nulls echoes. It outperforms the inverse filter at low signal-to-noise ratio.
- On the other hand, the time inverse of recorded signals was used (implicitly) to perform MRT beamforming in LOS. This technique focuses the signal in the spatial domain. It has been compared to the ZF beamforming, which perfectly nulls the power in pre-defined points in space. It outperforms ZF at low signal-to-noise ratio.

To our knowledge, none of these separated works discovered that the same technique (time reversal) was indeed mitigating multipath propagation and performing focusing in the spatial domain, simultaneously, in all propagation conditions (both LOS and NLOS propagation).

2.2 Time reversal space-time focusing

2.2.1 Time reversal and space-time focusing

One has to wait for the works of Prof. M. Fink [11][12] to understand that TR is indeed a space-time focusing technique. In a lossless and static propagation medium (without absorbers), the wave propagation equation is invariant by the TR operation. In other words, the two following waves are solutions of the same Maxwell equations:

- a wave generated by a source and propagating through a given lossless medium with the time increasing;
- The same wave, ‘played’ time reversely.

Note that, as time goes by, the first wave diverges, fading away in space and generating more echoes and multi-paths each time that it hits an obstacle. On the contrary, as time goes by, the second wave converges back to the source. An echo-free signal with maximum power is hitting the source. The second wave is focused in the space and the time domain, simultaneously.

In theory, one can imagine a continuous convex surface of sensors enclosing the source and recording the first wave, as illustrated by Fig. 2.2.1. The second wave could be generated by the same surface, with the sensors emitting their recorded field, simply time reversed. The source would need to absorb the received signal perfectly, as illustrated by Fig. 2.2.2.

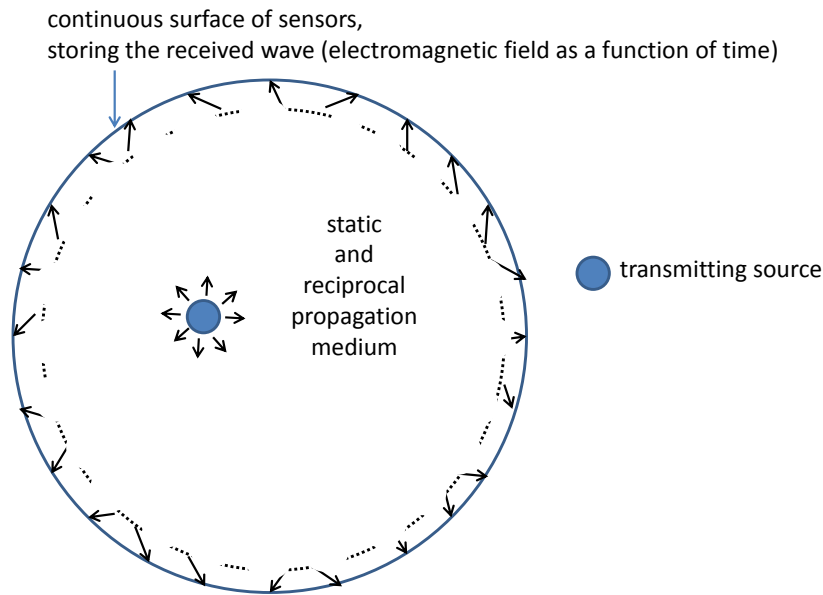


Fig. 2.2.1 Recording phase

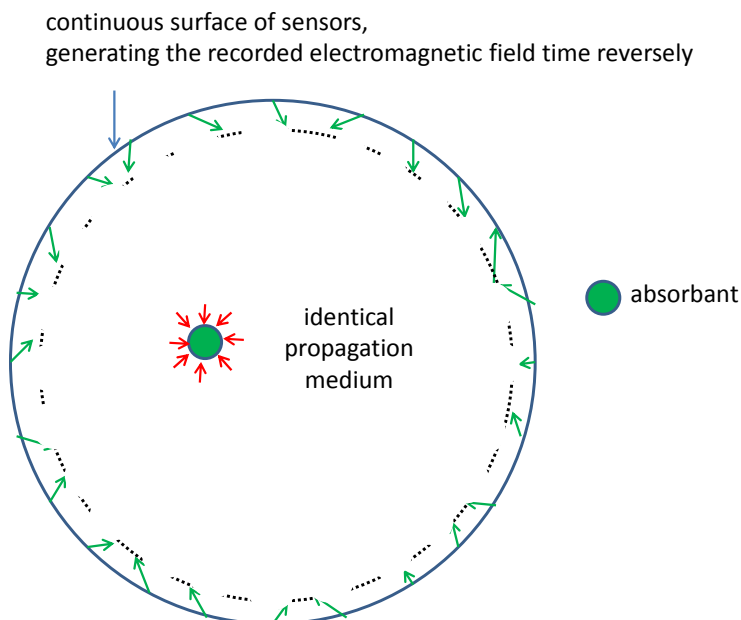


Fig. 2.2.2 Transmitting phase

In many practical situations, the wavefield radiated by the source is partially recorded (in space). This loss of information generates irreversibility. The same difficulty arises for an absorbing medium. One cannot reverse the wave propagation. Nevertheless, one can still achieve space-time focusing. The quality of the focusing depends on the level of information (on the propagation) available at the transmitter. In [11][12] a finite number of sensors (instead of a continuous surface) are used. During the recording phase, illustrated by Fig. 2.2.3 a source transmits one pulse. The sensors record the channel impulse response. During the transmission phase, illustrated by Fig. 2.2.4, the sensors transmit the recorded channel impulse responses, reversed in time. The resulting wave **nearly** 'propagates back' to the source with a strong power at a given time and on the source: space-time focusing is achieved.

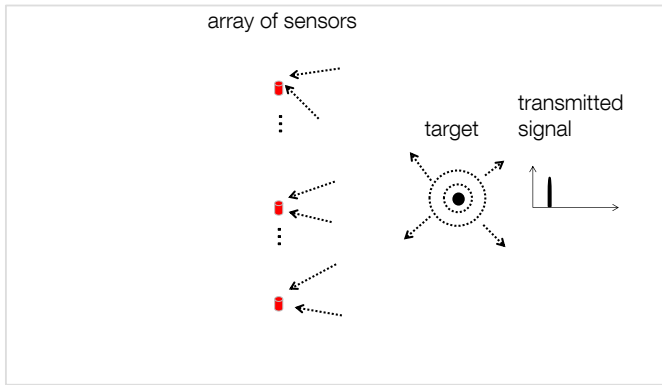


Fig. 2.2.3 Recording phase

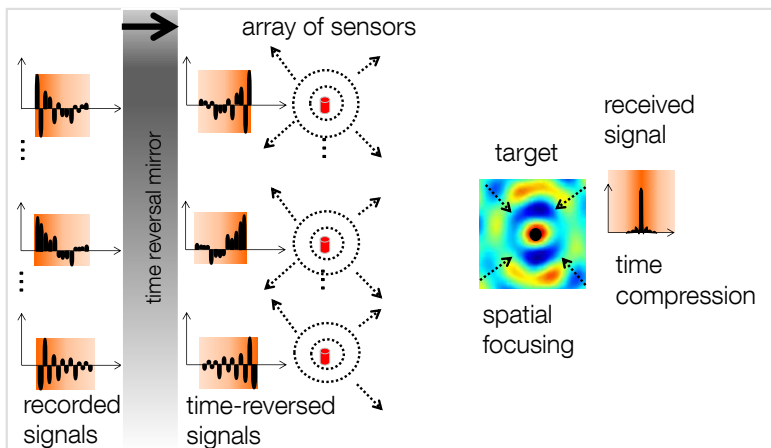


Fig. 2.2.4 Transmitting phase in time reversed mode

The property of echoes mitigation discovered in the case of a single antenna source during early works described in sub-section 2.1.1, is also observed in the case of a multi-antenna source. The property of spatial focusing of TR discovered in the case of LOS propagation during early works described in sub-section 2.1.2, can also be observed in NLOS propagation. TR focuses in the spatial and the time domains simultaneously, in NLOS propagation and with multi-antenna array. Less obviously, spatial focusing can also be obtained with a single antenna system if there is a lot of scattering and a large bandwidth [12]. This will be discussed in section 2.3.

Note that TR space-time focusing technique has been mainly studied in static environments. However, as shown in [13] and [14], in some varying environments with some particular symmetric properties, the invariance principle can still be observed. TR technique might also be applicable in such environment.

In practice, space-time filters (TR, inverse filter and MMSE) can be implemented with filters and beamformers:

- using a single-carrier modulation and applying distinct filters (matched filter, inverse filter and MMSE filter, respectively) to distinct transmit antennas;

- Using a multi-carrier modulation and applying distinct beamformers (MRT beamformer, ZF beamformer and MMSE beamformer, respectively) to each sub-carrier. In this case, the resulting set of beamformers is often called ‘precoder’.

2.2.2 Time reversal versus other space-time filters

In [15] and [16] the authors compare two space-time filtering techniques in ultra sound: TR and the inverse filtering. The same conclusions can be drawn for electromagnetic waves. Similar conclusions as for the comparison between the matched filter and the inverse filter in the time domain, and the MRT beamformer and the ZF beamformer in the spatial domain:

- The TR space-time filtering technique is less performant than the ZF space-time filtering to guarantee a low power around the source at a target time.
- The TR space-time filtering technique outperforms the ZF space-time filtering technique to provide the highest power possible at the source, under a transmit power constrain.

In a strongly noisy environment, at low SNR, TR is therefore expected to be preferable to inverse filtering.

2.2.3 Conclusion

In wireless networks, we are considering a medium **with loss of information**, as transmit antennas cannot be put everywhere in space. Therefore, TR does not ‘reverse wave propagation’. Nevertheless, it focuses the energy in the space and time domains. The focusing is improved when the number of transmit antennas in different locations increases.

The TR space-time filter can be implemented with filters and beamformers. When one transmit antenna and a medium of multi-echoes (typically in a NLOS propagation) are considered, the TR space-time filter equals the transmit matched filter. When several transmit antennas and a medium without multipath (typically a LOS medium) are considered, the TR space-time filter equals the MRT beamformer. When several antennas and a medium with multi-path and multi-echoes (typically a NLOS medium) are considered, the TR space-time filter can be implemented in two different ways:

- using a single-carrier modulation and distinct TR filters for distinct transmit antennas;
- Using a multi-carrier modulation and distinct MRT beamformers for distinct sub-carriers.

This is also valid for other space-time filters such as the inverse filter (ZF beamformer) and the MMSE filter (MMSE beamformer).

Regarding the performance of TR space-time filter relatively to others:

- TR space-time filter (MRT beamforming) gets the maximum of energy on the target, and therefore particularly interesting at low SNR especially when the transmit power is limited; however it does not guarantee low power around the source;
- Inverse filtering (ZF beamforming) outperforms TR to send simultaneous several beams towards several receive antennas with minimum interference between beams, at high SNR and when the available transmit power is high.
- MMSE filtering (MMSE beamforming) is tracking the SNR, it is equal to TR at low SNR, equal to ZF at high SNR, and outperforms the two filters at medium SNR.

2.3 Time reversal for wireless communications in multiple scattering medium

This sub-section briefly recalls why TR has been proposed for in a multiple input multiple output (MIMO) wireless communications. In particular, it analyses the relationship between space-time focusing performance and multiple scattering.

2.3.1 Time reversal in MIMO wireless communications

We consider a MIMO wireless communication system. We consider M receive antennas and N transmit antennas. When TR is used at the transmission, we can define a received equivalent MIMO channel. As explained in section 2.2, there are two main ways to implement time reversal: either using matched filters or maximum ratio transmission beamformers.

2.3.1.1 Using a set of matched filters

Let $h_{n,m}(t)$ be the channel response impulse between transmit antenna n and receive antenna m , where $1 \leq n \leq N$ and $1 \leq m \leq M$. Let $x_m(t)$ be the data stream intended to antenna m . Assuming per stream and per antenna pre-filtering $p_{n,m}(t)$, the signal transmitted by antenna n is:

$$s_n(t) = \left(\sum_{m=1}^M p_{n,m} * x_m \right)(t),$$

where, $p_{n,m}(t)$ is the ‘**matched filter**’ for the channel $h_{n,m}(t)$:

$$p_{n,m}(t) = h_{n,m}^*(-t).$$

The overall system is illustrated by Fig. 2.3.1.

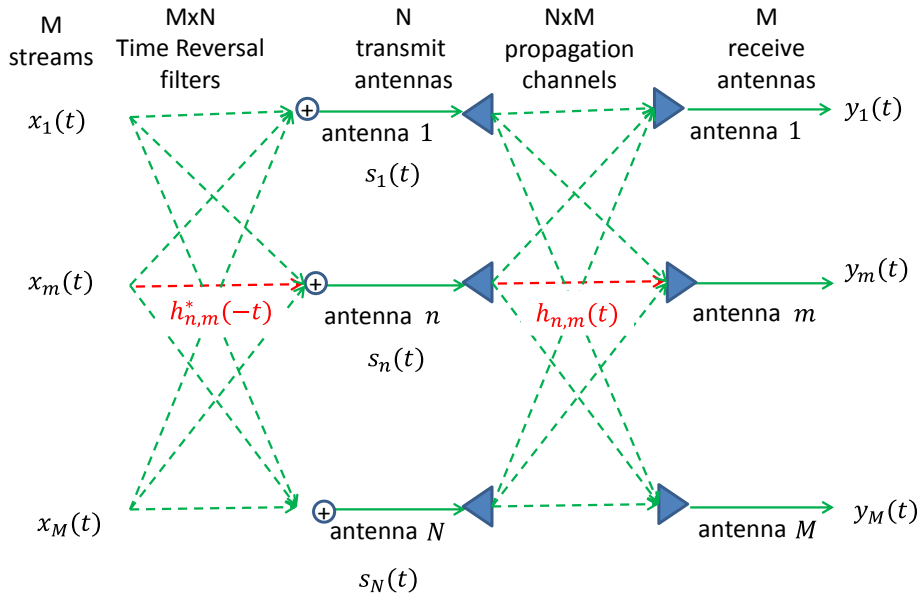


Fig. 2.3.1 Multi-Antenna TR

The received signal at the antenna m is (without considering noise):

$$y_m(t) = \left(\sum_{n=1}^N h_{n,m} * s_n \right)(t).$$

By replacing s_n by its definition, one obtains:

$$y_m(t) = \left(\sum_{m'=1}^M h_{m',m}^{eq} * x_{m'} \right)(t),$$

where, $h_{m',m}^{eq}$ is the equivalent channel between the equivalent virtual antenna m' (transmitting the data stream m') and the receive antenna m . $h_{m',m}^{eq}$ is given by:

$$h_{m',m}^{eq}(t) = \left(\sum_{n=1}^N h_{n,m} * p_{n,m'} \right)(t).$$

$$h_{m',m}^{eq}(t) = \left(\sum_{n=1}^N h_{n,m} * p_{n,m} \right)(t) = \sum_{n=1}^N h_{n,m}(t) * h_{n,m}^*(-t)$$

The overall equivalent system is illustrated below.

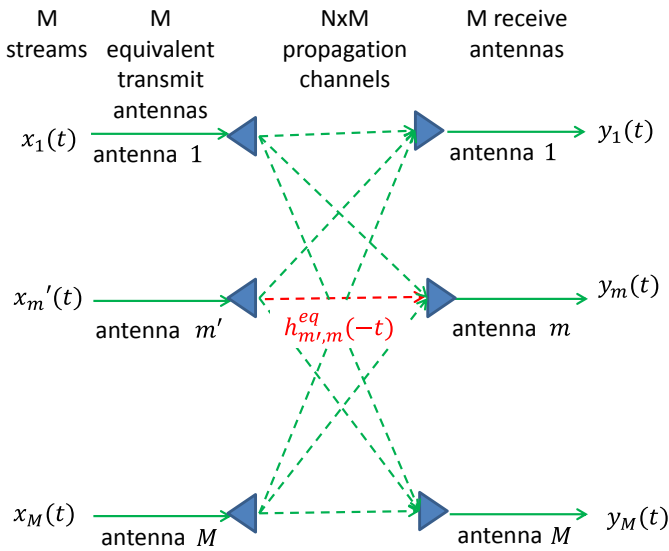


Fig. 2.3.2 Multi-antenna TR equivalent channel

$h_{m,m}^{eq}(t)$ is a sum of auto-correlation products. For all n 's, the auto-correlation product $h_{n,m}(t) * h_{n,m}^*(-t)$ is positive at the focusing time (i.e. at $t = 0$). Therefore, $h_{m,m}^{eq}(0) > 0$ and $h_{m,m}^{eq}(0)$ increases with the number of transmit antennas N . Out of the focusing time (non zero t), the value of $h_{m,m}^{eq}(t)$ depends on the propagation conditions. $h_{m',m}^{eq}(t)$ is a sum of cross-correlation products. Its value also depends on the propagation conditions.

Each antenna m , receives the sum of a desired signal $u_m(t)$, an inter-symbol interference $v_m(t)$, and an inter-stream interference $w_m(t)$. Thus, we can write:

$$y_m(t) = u_m(t) + v_m(t) + w_m(t),$$

where,

$$u_m(t) = h_{m,m}^{eq}(0)x_m(t),$$

$$v_m(t) = h_{m,m}^{isi}(t) * x_m(t),$$

$$w_m(t) = \sum_{m'=1, m' \neq m}^M h_{eq,m',m}(t) * x_{m'}(t),$$

and where,

$$h_{m,m}^{isi}(t) = h_{m,m}^{eq}(t) \text{ for } t \neq 0 \text{ and } h_{m,m}^{isi}(0) = 0.$$

Under certain propagation conditions (identified later in sub-section 2.3.2), time compression (i.e. focusing in the time domain) can be observed. This would translate into the following inequality:

$$|h_{m,m}^{eq}(0)| \gg |h_{m,m}^{eq}(t \neq 0)|.$$

This has the following consequence:

$$|u_m(t)| \gg |v_m(t)|.$$

In other terms, time compression reduces the inter-symbol interference.

Under certain propagation conditions (identified later in sub-section 2.3.2), spatial focusing can be observed. This would translate into the following inequality:

$$|h_{m,m}^{eq}(0)| \gg |h_{m',m}^{eq}(t)|.$$

This has the following consequence:

$$|u_m(t)| \gg |w_m(t)|.$$

In other terms, time compression reduces the multi-stream interference (or MIMO spatial interference).

2.3.1.2 Using a set of maximum ratio transmission beamformers

This time, we consider a multi-carrier system with L sub-carriers. Let $\mathbf{H}^{(l)} \in \mathbb{C}^{M \times N}$ be the response in frequency of the channel response impulse between transmit antenna n and receive antenna m , for a given sub-carrier l , where $1 \leq l \leq L$, $1 \leq n \leq N$ and $1 \leq m \leq M$. Let $\mathbf{x}^{(l)} \in \mathbb{C}^{M \times 1}$ be the vector of M data symbols, with $\mathbf{x}_m^{(l)} \in \mathbb{C}$ being intended to antenna m and sub-carrier l . Let $\mathbf{s}^{(l)} \in \mathbb{C}^{N \times 1}$ be the vector of N symbols transmitted on sub-carrier l and over the N transmit antennas. $\mathbf{s}_m^{(l)} \in \mathbb{C}$ is the signal intended to receive antenna number m and sent from the transmit antenna n , on sub-carrier l . The expression of $\mathbf{s}^{(l)}$ is given by:

$$\mathbf{s}^{(l)} = \mathbf{P}_{MRT}^{(l)} \mathbf{x}^{(l)},$$

where $\mathbf{P}_{MRT}^{(l)}$ is the MRT beamformer for sub-carrier number l only:

$$\mathbf{P}_{MRT} = (\mathbf{H}^{(l)})^H.$$

$\mathbf{y}^{(l)} \in \mathbb{C}^{M \times 1}$ is vector of M data symbols received on sub-carrier l and by the M receive antennas. $\mathbf{y}_m^{(l)} \in \mathbb{C}$ is the signal received on the receive antenna number m , on sub-carrier l . The expression of $\mathbf{y}^{(l)}$ is given by:

$$\mathbf{y}^{(l)} = \mathbf{H} \mathbf{P}_{MRT}^{(l)} \mathbf{x}^{(l)} + \mathbf{n} = \mathbf{H}^{(l)} (\mathbf{H}^{(l)})^H \mathbf{x}^{(l)} + \mathbf{n}^{(l)},$$

where $\mathbf{n}^{(l)}$ is the vector of noise samples, on sub-carrier l . One can define an equivalent channel

$\mathbf{H}^{(l),eq} \in \mathbb{C}^{M \times N}$ as follows:

$$\mathbf{H}^{(l),eq} = \mathbf{H}^{(l)} (\mathbf{H}^{(l)})^H.$$

The useful data symbol m is received at antenna m through the following equivalent channel coefficient:

$$\mathbf{H}_{m,m}^{(l),eq} = \sum_{n=1}^N \left| \mathbf{H}_{m,n}^{(l)} \right|^2.$$

$\mathbf{H}_{m,m}^{(l),eq}$ is a sum of N positive variables. It is therefore positive and its value increases with the number of antennas N .

The interfering data symbol m' is received at antenna m through the following equivalent channel coefficient:

$$\mathbf{H}_{m,m'}^{(l),eq} = \sum_{n=1}^N \sum_{m'=1, m' \neq m}^M \mathbf{H}_{m,n}^{(l)} \left(\mathbf{H}_{m',n}^{(l)} \right)^*.$$

This $\mathbf{H}_{m,m'}^{(l),eq}$ is a sum of different variables.

On each receive antenna m , on sub-carrier l , the received signal can be written as follows:

$$\mathbf{y}_m^{(l)} = \mathbf{u}_m^{(l)} + \mathbf{v}_m^{(l)} + \mathbf{n}_m^{(l)},$$

where:

- $\mathbf{u}_m^{(l)} = \mathbf{H}_{m,m}^{(l),eq} \mathbf{x}_m^{(l)}$ is the **useful** part of the received signal;
- $\mathbf{v}_m^{(l)} = \sum_{m'=1, m' \neq m}^M \mathbf{H}_{m,m'}^{(l),eq} \mathbf{x}_{m'}^{(l)}$ is the **multi-stream interference** part of the signal.

Under certain propagation conditions (identified later in sub-section 2.3.2), **time compression** (i.e. focusing in the time domain) can be observed. This would translate into the following mathematical observation: $\mathbf{H}_{m,m}^{(l),eq}$ is independent from l , i.e., it is frequency flat.

Under certain propagation conditions (identified later in sub-section 2.3.2), spatial focusing can be observed. This would translate into the following mathematical observation:

$$\mathbf{H}_{m,m'}^{(l),eq} \ll \mathbf{H}_{m,m}^{(l),eq}.$$

2.3.1.3 Conclusion

In conclusion, TR has the two following effects on a MIMO wireless communication:

- **Time compression reduces inter-symbol interference;**
- **Spatial focusing reduces multi-stream interference.**

The strength of these effects depends on the propagation conditions. The next sub-section analyses the advantages which can be drawn from such effects. It also analyses in which propagation conditions these effects are strong enough to bring an advantage.

2.3.2 Taking advantage of multiple scattering to perform wireless communication using Time reversal

Many studies show that TR takes advantage from scattering. In [17][18], the authors explain that a MIMO system as the one described in sub-section 2.3.1 can be seen as an adaptive ‘lens’ focusing several data streams on to several receive antennas. Scattering creates additional virtual transmit antennas (‘reflections’) in different locations. Scattering therefore extends the “aperture” of the lens. Scattering therefore improves the system focusing and its capacity. In [19], the authors analyse TR space-time focusing in random fields. This study shows that TR spatial focusing quality, (i.e. the ratio between the main lobe and the secondary lobe), increases with the product **bandwidth** \times **delay spread**, i.e. with the channel selectivity, or equivalently with scattering, even in a Single Input Single Output (SISO) configuration. [20] shows experimentally that better focusing is achieved, when the wave propagates through a forest of parallel steel rods with high density, than through an homogeneous medium. However, one can note that this scattering medium was almost not absorbing.

[21] is, to our knowledge, the first experimental demonstration of TR concept in a wireless communication, in realistic propagation conditions. This study uses acoustic waves for underwater communications (between sub-marines for instance).

In [22][23], the authors study the use of TR for wireless communications using electromagnetic waves. These studies explain that in a richly scattering environment (modelled with several independent and identically distributed Gaussian taps in the channel impulse response), **TR is near to optimal, i.e. it almost achieves Water-Filling solution, in low SNR region, with a single tap receiver.** In

[22][23], the authors also observe that the outage probability decreases with the number of taps, for both TR and Water Filling.

Numerous studies try to measure the space-time focusing performance alone as in [24], without quantifying the benefits of this focusing on the efficiency of the communication link. As TR focusing increases with multiple scattering, the best focusing is obtained in a reverberating chamber or in indoor (in NLOS preferably). In [25][26], the spatial focusing is measured in a reverberating chamber and in indoor. As a better focusing is obtained with large bandwidth \times delay spread products, many measurements are performed in the context of ultra wideband (UWB). In [22][23][27], the authors analyse the TR space-time focusing performance in indoor, based on measurements, for a bandwidth spanning 2-8GHz. These measurements show that about seven wavelengths from the target the signal power reduces by at least 10dB. In [28][29][30], the authors characterise experimentally the spatial focusing properties of TR in UWB using a circular array and measure that at 9 wavelengths from the target, the received signal is reduced by 10dB, in NLOS condition. In [31], the authors study the impact of the bandwidth on the robustness of TR in terms of space-time focusing. Many other studies based on UWB channel measurements in indoor or intra-vehicular conditions confirm the existence of spatial focusing and time compression and a focusing gain of around 10dB [32][33][34][35][36][37][38][45].

Numerous studies try to measure the data communication enhancement brought by the use of TR, in terms of signal-to-interference-and-noise ratio (SINR), Bit Error Rate (BER), or spectral efficiency (in bits per seconds and per Hertz). Most studies are focused on UWB. In the references [39][40][41][42][43][44], UWB wireless links in SISO, MISO and MIMO configurations are studied, through simulations, experiments and test beds. Regarding WLAN, a performance study analysing the outage probability based on an analytical post receiver SINR has been held in [45]. Finally, a BER evaluation has been done for a non-impulsive waveform [46].

One can note that most studies use conventional antennas. However, in [47], the authors have managed a sub-wavelength spatial focusing using TR and new microstructured antennas.

Finally, even when the bandwidth \times delay spread product is small (for instant a medium with low scattering), spatial focusing and time compression can be obtained by using a large number of antenna elements at the transmitter side.

2.3.3 Conclusion

To conclude this sub-section, experimental studies confirm that pure TR enables to achieve spatial focusing and time compression, in large bandwidth systems (like UWB) and multiple scattering propagation media (like NLOS links). This space-time focusing property can be translated into an im-

provement in terms of BER or capacity, in SISO mode at least. One can observe that indoor mobile networks such as femtos/small cell networks (described in [48][49]) do naturally offer richly scattering environments, although their bandwidth is smaller (in the order of 1 MHz-100 MHz). However, previous works do not address these specific scenarios.

The next sub-section is an overview recent techniques improving wireless communication systems and going beyond a mere use of TR.

2.4 Recent time reversal techniques for wireless communications

This sub-section is an overview of the new techniques for wireless communications that have been developed recently based on TR:

- Sub-sections 2.4.1, 2.4.2 and 2.4.3 present single-carrier communications with low cost receivers (such as single tap receivers), low complexity transceivers and strong power constrains, respectively.
- Sub-section 2.4.4 presents low complexity and green multi-carrier communications.

2.4.1 Low complexity single carrier receivers

As explained in sub-sections 2.2 and 2.3, TR compresses the channel in the time domain and reduces echoes and inter-symbol interference. At low SNR, these echoes (inter-symbol interferences) are below the noise floor, as illustrated in Fig. 2.4.1. This is the origin of several potential simplifications of the receiver. Several approaches have been studied.

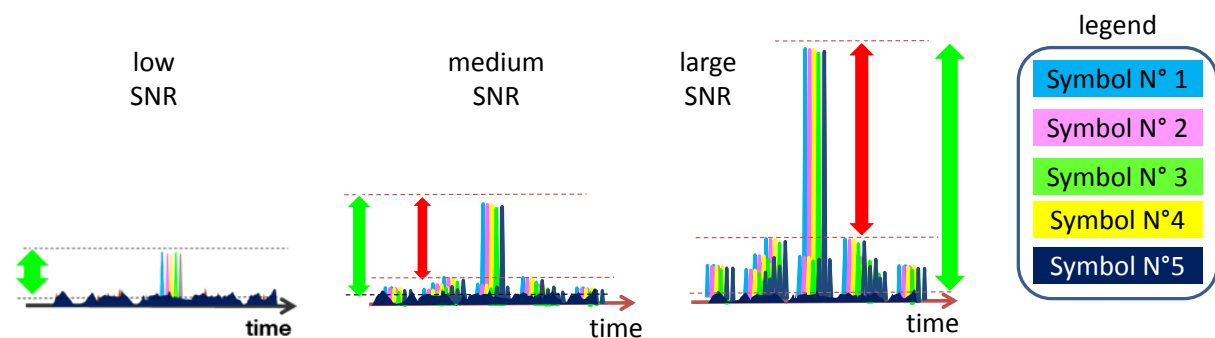


Fig. 2.4.1 Echoes in TR received signal for various SNR values

In [50] the authors investigate data transmission over channels with a huge number of taps, typically UWB channels. They propose to report the complexity from the receiver to the transmitter. A single tap receiver instead of a complex MMSE receiver is used. A single tap receiver simply detects the strongest tap in the channel and performs channel equalisation assuming there is this only tap in the channel. A single tap receiver is therefore best suited for a single tap channel and is very sensitive to

inter-symbol interference. At the transmitter side, TR is used. Thanks to time compression the inter-symbol interference is reduced. At low signal-to-noise ratio, the interference is below the noise floor and **the single tap receiver provides optimum performance**, as illustrated by Fig. 2.4.2. At higher signal-to-noise ratio, rate back-off (i.e. spacing in time of symbols) is necessary to limit inter-symbol interference.

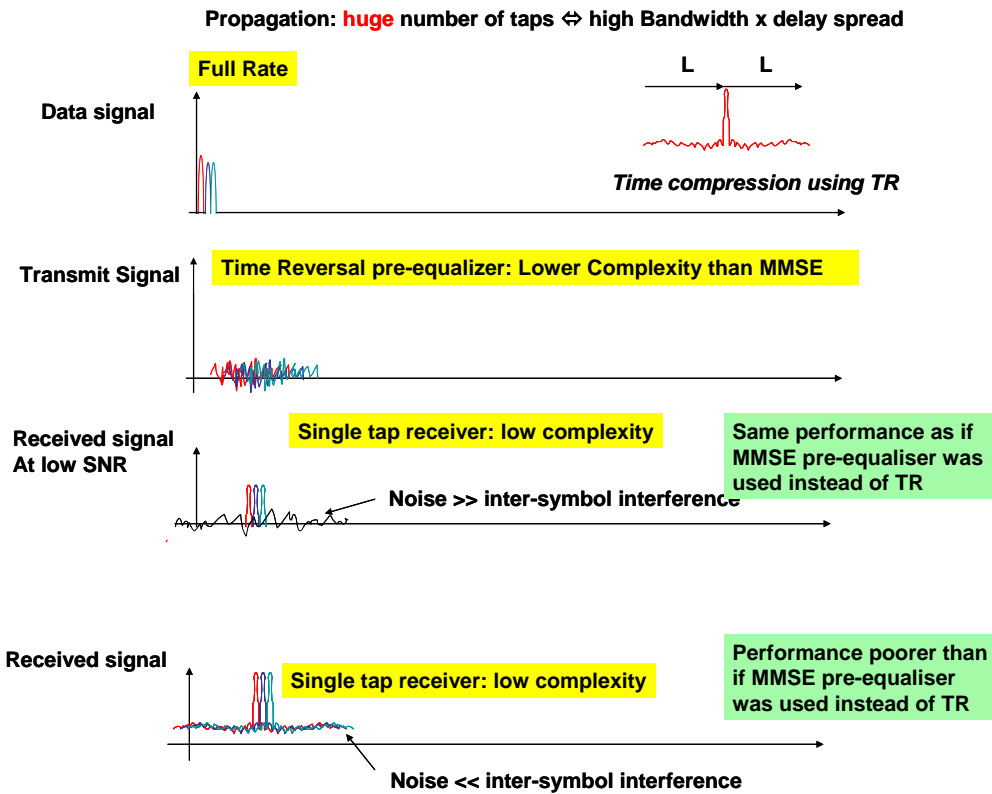


Fig. 2.4.2 Using TR instead of MMSE pre-filter in full rate mode

Even in the cases of multi-user transmission, a simple receiver can be kept, in UWB MISO [51]. However, the multi-user interference is high and the solutions to mitigate it are not straightforward. In [51] the interference is minimised by determining distinct time offsets to distinct users. In [53][54], users do not fully overlap in the frequency domain. Partial frequency overlaps between users are determined. The objective is to maximise the sum capacity. In [55][56][57], some sophisticated transmit power allocation, or a modification of the beamformer is necessary to reduce the multi-user interference.

Many studies involve low complexity receivers, which are slightly more complex than the single tap receiver. In [58], the authors combine TR and a ‘reduced’ rake receiver. The number of fingers of the rake receiver is reduced. This system attains a better performance in environments with very high interference than the single tap receiver does. In [59], the authors show that TR pre-filtering significantly reduces the number of taps that the MMSE receiver needs to estimate in order to achieve a certain tar-

get BER. In [60], joint TR and ZF filtering for multi-stream interference mitigation are proposed. TR spatial focusing properties are used to minimise multi-stream interference. ZF deletes the residual inter-symbol interference left by TR.

In [61], the authors propose to compensate for Doppler effect at the transmitter in addition to using TR. The Delay-Doppler spread function is estimated at the receiver and pre-compensated.

As summarised in [62][63][64], TR is the optimum transmission technique at low SNR even with a low complexity receiver. Multi-user communications with low complexity receivers are more challenging. The multi-stream interference is high. Nevertheless, with larger antenna arrays this should also be feasible.

2.4.2 Low complexity single carrier transceivers

TR implies perfect knowledge of the channel impulse response at the transmitter, perfect transmission of the time-reversed channel impulse response. In Time division duplex (TDD) mode, thanks to channel reciprocity, perfect channel state knowledge is achievable but it requires the following step: the target (receiver) first sends pilots; the transmitter based on received pilots estimates the channel.

In Frequency division duplex (FDD) mode, more steps are required: the focusing antenna array sends pilots to the target; the target estimates the channel for each transmit antenna; the target sends the channel information (in a quantized and compressed manner) to the transmitter. The last step degrades the focusing quality, as huge compression is required to limit the overhead.

Many simplified TR pre-filters have been built. They use an imperfect knowledge of the channel impulse response. They are designed to perform focusing in FDD or to lower the complexity of UWB focusing transceivers. Most of these studies rely on the works of [65]. In [65], the authors present a simplified form of TR, referred as to “one-bit Time reversal” or “1bit time reversal” (1Bit TR), for ultrasound. The method consists in transmitting the sign of the time reversed channel impulse response instead of the time reversed channel impulse response itself. In other words, the transmitter sends $sign(h(-t))$ instead of $h(-t)$. Experimental results in [39] show that one-bit TR achieves an improved spatial focusing (surprisingly) and a degraded time compression compared to conventional TR. [66][67] applied one-bit TR to WLAN transmission, and also proposed it for frequency division duplex mode. The study confirms spatial focusing and (degraded) time compression are obtained with 1bit TR. In [68] and [69], the authors show that one-bit TR can be used for UWB multi-user communication. Recently, a quantized TR pre-filter has been studied in [70].

2.4.3 Low transmit power

TR has been extensively proposed for communications with transmitters subjects to extreme power constrains. Indeed, in a conventional system, the energy is radiated in all directions, independently from the traffic location. Using antennas adaptively to focus the energy in the busy areas or on busy users. Thanks to the beamforming gain (which is linear with the number of transmit antennas [71]), the network can transmits with a lower power and still deliver the same data rate. Energy can be saved in the network. The general level of human exposure to waves and eavesdroppers can also be reduced.

In [71], cooperative TR transmission has been studied in wireless sensors networks. Sensors do not need to send a huge amount of data with a large data rate. They therefore operate at low spectral efficiency and low signal-to-noise ratio target. Sensors are very contrained in transmission power as they work on a battery. As already explained in sub-section 2.4.1, TR is optimum at low signal-to-noise ratio. In [62], one source node transmits data towards a sink node, using all other nodes as relays. The relays are synchronised and focus together towards the target node using TR pre-filters. The study shows that TR is optimum.

In [72], the authors use several access points in indoor to transmit towards several users. The access points are synchronised and controlled by a central entity. The access points transmit jointly and beam-form towards the users simultaneously. Several beamforming schemes are studied: ZF and TR. TR outperforms ZF at low signal-to-noise ratio and is outperformed by ZF at high signal-to-noise ratio. TR is therefore more suited for a system operating at low SNR and being extremely constrained in transmit power.

In [73] TR is claimed to be a new paradigm for green and low complexity wireless communications systems. Many studies suggest using TR for “green communications”, in various scenarios and for various types of services. [74] and [75] addresses the context of the standardised WIFI system. [76] shows that the level of human exposure to electromagnetic waves generated by small cells can be reduced thanks to TR. [73] proposes to use TR as a green technique for confidential and secure communications. If the spatial focusing is strong, the signal received out of the target position is low. Therefore, in theory, it should be more difficult for an eavesdropper to intercept the communication. Recent studies demonstrate the advantages of TR in the domain of physical layer security using experimental measurements in [77][78][79]. Recently, [80] has claimed that TR is a new paradigm for green internet of things. Indeed. Many connected objects are very constrained in energy, rely on a battery, do not require high data rates, and need to be low cost. As already explained, TR is optimum at low signal-to-noise ratio and allows for the use of low complexity transmission and reception techniques. It is therefore a good candidate technique for the internet of things.

2.4.4 Low complexity multi-carrier transceivers and receivers

Most mobile and wireless standards today are using multi-carrier waveforms. Even for future 5G networks, new multicarrier waveforms are being proposed. OFDM is more robust to inter-symbol interference than single tap receivers are, however, studies show that it can still benefit from TR.

TR has been proposed for OFDM. [81] has used this technique for underwater communications. [82] studies OFDM and MISO transmission with TR and shows that it is optimum. Dubois has studied thoroughly TR with multi-carrier modulations. Dubois started by studying non impulsive waveforms in [83]. In a SISO context, in [84], Dubois analyses the benefits in terms of synchronization process complexity reduction and the guard interval reduction, that can be obtained by using TR in OFDM. In a MISO context, the combination of TR and orthogonal space-time block codes, and adaptive modulation and coding, has been studied in [85]. [86] shows that if a very large number of transmit antenna (i.e. a ‘massive’ MIMO system) is used, then the required length of the guard interval is near to zero. In other terms, the channel becomes ‘single tap’. In [87], TR is combined with a new multi-carrier waveform known as ‘OFDM/OQAM’. MISO (details on OFDM/OQAM with TR are provided in the annex) transmission is considered. Two channel estimation algorithms for multicarrier systems are proposed in [88] for an OFDM system using TR. Finally, TR does bring a benefit to OFDM: the MRT beamforming gain. As already mentioned in sub-section 2.4.3, the beamforming gain enables the transmitter to deliver the same rate with lower radiated power. Potentially, some energy can be saved in the network.

2.5 Conclusion on the state-of-the art and introduction to our contributions

TR provides time compression, spatial focusing in high bandwidth x delay spread environments. Studies on TR, in UWB and WLAN, have shown that TR can be exploited to lower transmission/reception complexity in single carrier and multi-carrier transmissions, and for green communications. However, there are still some remaining questions regarding the interest of using time reversal in mobile networks:

- Is TR advantageous for indoor mobile networks such as femtos/small cells networks? What is the performance of TR when one takes into account the carrier frequency, the spectrum bandwidths, the propagation, and advanced signal-processing models, for such networks?
- Can TR be used in scenarios, which are challenging for TR but which are also typical from mobile networks (frequency division duplex mode and high mobility)?

- Are there any opportunities for new applications or communication systems using mobile networks, thanks to TR?

Our contributions focus on providing answers to these questions.

Chapter 3 - Performance evaluation of time reversal in indoor mobile networks

Previous works presented in sub-section 2.4 claim that TR is suitable for **low complexity and green** wireless communications in indoor and mainly for UWB and WLAN, with simplified signal processing models. In this sub-section, we present new results (obtained by simulation in sub-section 3.1 and experimentally in sub-section 3.2) for indoor mobile networks such as femtos/small cells. Our studies aim at providing the most realistic possible performance assessment for such indoor mobile networks by using the right carrier frequencies and spectrum bandwidths, sophisticated channel models (or real channel measurements) and advanced and new signal processing models.

3.1 Dumb-to-perfect receiver throughput ratio maps of femto/small cell using TR

3.1.1 Introduction

The concern for energy consumption in wireless networks is growing, and some studies show that a large part of the consumption comes from the power amplifier [89]. Systems operating at ultra-low output power, in the low SNR region, are thus becoming an important subject. In addition, in the particular case of mobile networks (small cells or femtos) deployed inside public buildings, like schools or hospitals, extremely low complexity, cheap and replaceable devices would be beneficial.

As explained in section 2, one good candidate technique for such application is TR as it allows for the use of simple receivers. Most of papers (those mentioned in section 2 and [90]) have evaluated the performance of TR based on UWB indoor channel measurements, thus assessing the performance for a limited number of measured positions of the transmitter and receiver. Recently, [45] has proposed a statistical study of TR performance for an indoor with lower bandwidth than UWB and larger coverage. However, in order to derive a closed form of the outage probability, many simplifying assumptions have been taken.

Until now, the performance of TR schemes over an entire indoor coverage area such as a building floor, for a given transmit power, has never been performed. Especially, no study has evaluated in which parts of the coverage area a low complexity receiver is sufficient and optimum, and whether this part is large, when the transmitter operates at a very low output power.

In this study, we complete the performance evaluation of TR and 1bit TR techniques for indoor environments, by providing for the first time the achieved throughput in all positions inside a typical building floor, of a 16x2 system. The transmitter is deployed in the corridor and has a very low trans-

mitted power value (0 dBm). Our methodology is based on post receiver Signal-to-interference ratio analytical formulas, taking inter-symbol interference and multi-stream interference into account, and allows the performance of a ‘Dumb Receiver’ (i.e. a single tap receiver) to be compared with the one of a ‘Perfect Receiver’ (i.e. an interference free receiver), for each position in the building. We use Winner II MIMO channel model [91] for a bandwidth of 100 MHz (such large bandwidths are expected to be available with 5G networks), in order to generate the channel in an entire building floor, taking into account spatial correlation between antennas, and walls penetration losses.

Sub-section 3.1.2 sets the system model; sub-section 3.1.3 derives the post receiver SINR formulas, sub-section 3.1.4 presents our simulations results and sub-section 3.1.5 concludes this study.

3.1.2 System description

Sub-section 3.1.2.1 lists the notations used through this study. Sub-section 3.1.2.2 provides an overview of the system model. Sub-section 3.1.2.3 recalls TR and 1bit TR pre-filters.

3.1.2.1 Notations

In this study, we use the ‘mathematical notations for single carrier transmissions studies’. With these notations, we set:

- $\rho_f(t) = f(t) * f^*(-t)$;
- $\tau_{kk'} = \tau_{k'} - \tau_k$.
- $\varepsilon_{Knk'k'} = (K - n)T + \tau_{kk'}$.

3.1.2.2 System Overview

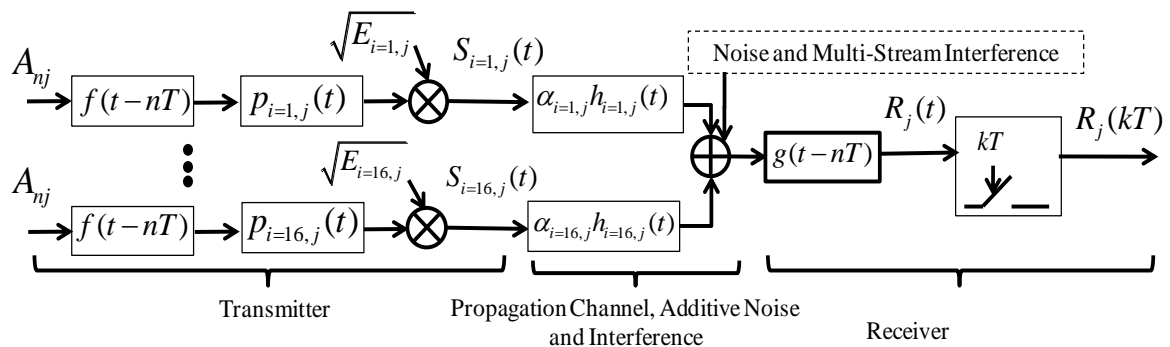


Fig. 3.1.1 System model illustrated for receive antenna j

A communication between a wireless network and N receive antennas is considered. Each receive antenna j is served by P transmit antennas. Fig. 3.1.1 illustrates our system model. Assuming per antenna and per user pre-filtering $p_{i,j}(t)$ and power allocation $E_{i,j}$, the expression of the signal $S_{i,j}(t)$ transmitted by antenna i (with $1 \leq i \leq N$) to receive antenna j (with $1 \leq j \leq P$) is:

$$S_{i,j}(t) = \sqrt{E_{i,j}} \sum_n A_{n,j} f(t - nT) * p_{i,j}(t), \quad \text{Eq. 3.1.1}$$

where $A_{n,j}$ is the n^{th} symbol, T is the symbol period, $f(t)$ is a pulse shape filter occupying a bandwidth of $1/T$ and verifying:

$$\frac{1}{T} \int_{-\infty}^{+\infty} |f(t)|^2 dt = 1. \quad \text{Eq. 3.1.2}$$

The fast fading channel impulse response $h_{i,j}(t)$ between antenna i and user j is modeled with M taps:

$$h_{i,j}(t) = \sum_{k=1}^M h_{i,j,k} \delta(t - \tau_k), \quad \text{Eq. 3.1.3}$$

where $h_{i,j,k}$ and τ_k are the gain and the delay of the k^{th} tap, respectively. The gain due to path loss is $\alpha_{i,j}$. The fast fading channel coefficients $h_{i,j,k}$ are assumed constant for the duration of the post receiver SINR computation and can vary due to the receiver mobility, however in the average fast fading channel power is assumed equal to 1:

$$E \left[\sum_{k=1}^M |h_{i,j,k}|^2 \right] = 1, \quad \text{Eq. 3.1.4}$$

Based on Eq. 3.1.1 and Eq. 3.1.3, the signal received at user j and filtered by $q(t)$ is derived:

$$R_j(t) = \sum_{i \in \Omega_j} \alpha_{i,j} (S_{i,j} * h_{i,j} * q)(t) + \sum_{j' \neq j} \sum_{i \in \Omega_{j'}} \alpha_{i,j'} (S_{i,j'} * h_{i,j'} * q)(t) + (n_j * q)(t), \quad \text{Eq. 3.1.5}$$

where $n_j(t)$ is an additive white Gaussian noise process of zero mean and spectral density N_0 . Assuming $q(t)$ is matched to the pulse shape filter, we have:

$$q(t) = f^*(-t), \quad \text{Eq. 3.1.6}$$

Finally, the signal is sampled at time $t = KT$ (assuming perfect synchronization).

3.1.2.3 TR and 1bit TR prefilters

This sub-section provides the expression of $p_{ij}(t)$. M -tap pre-filtering is considered:

$$p_{i,j}(t) = \sum_{k=1}^M p_{i,j,k} \delta(-t - \tau_k). \quad \text{Eq. 3.1.7}$$

The $p_{i,j,k}$ coefficients are updated periodically to track the fading variations, i.e. the variations of the $h_{i,j,k}$ coefficients. Two pre-filters based on the inversed channel impulse response $h_{i,j}^*(-t)$ are studied successively: TR and 1bit TR, namely. For TR, we set:

$$p_{i,j}(t) = h_{i,j}^*(-t) / \sqrt{\lambda_{i,j}}, \quad \text{Eq. 3.1.8}$$

thus $p_{i,j,k} = h_{i,j,k}^*$. If instantaneous normalization is applied, i.e.

$$\lambda_{i,j} = \sqrt{\sum_{k=1}^M |h_{i,j,k}|^2}. \quad \text{Eq. 3.1.9}$$

For 1bit TR, we set:

$$p_{i,j}(t) = f^{1bit}(h_{i,j}^*(-t)) / \sqrt{2M}, \quad \text{Eq. 3.1.10}$$

thus $p_{i,j,k} = y(h_{i,j,k}^*) / \sqrt{2M}$.

3.1.3 Post receiver SINR computation

To compute the SINR formula, the following assumptions are taken: $A_{n,j}$ are independent variables,

$$E[|A_{n,j}|^2] = 1 \text{ and } E[A_{n,j}] = 0.$$

Two receivers are considered: ‘Perfect Receiver’ and ‘Dumb Receiver’, namely. For the Dumb Receiver, the sampled signal is simply processed by a one tap maximum ratio combining. The only difference between the Dumb Receiver and the Perfect Receiver is that the Perfect Receiver is interference free.

3.1.3.1 Dumb Receiver

Based on Eq. 3.1.5-Eq. 3.1.10 for both TR and 1bit TR (with their specific $p_{i,j,k}$ values), the received signal sampled at $t=KT$ can be written as:

$$R_j(KT) = \begin{aligned} & A_{K,j} \sum_{i \in \Omega_j} \alpha_{i,j} \sqrt{E_{i,j}} \sum_{k,k'=1}^M h_{i,j,k} p_{i,j,k'} \rho_f(\tau_{k,k'}) + \\ & \sum_{n \neq K} A_{n,j} \sum_{i \in \Omega_j} \alpha_{i,j} \sqrt{E_{i,j}} \sum_{k,k'=1}^M h_{i,j,k} p_{i,j,k'} \rho_f(\varepsilon_{K,n,k,k'}) + \\ & \sum_{j' \neq j} \sum_n A_{n,j'} \sum_{i \in \Omega_{j'}} \alpha_{i,j'} \sqrt{E_{i,j'}} \sum_{k,k'=1}^M h_{i,j,k} p_{i,j',k'} \rho_f(\varepsilon_{K,n,k,k'}), \end{aligned} \quad \text{Eq. 3.1.11}$$

with $\tau_{k,k'}$ and $\varepsilon_{K,n,k,k'}$ defined in 3.1.2.1.

Assuming that multi-stream interference and inter-symbol interference are Gaussian and independent, the expression of the post receiver SINR of user j can be derived as:

$$SINR_j = Pu_j / (Pis_j + Pi_j + P_N), \quad \text{Eq. 3.1.12}$$

where Pu_j is the useful power, Pis_j is the inter-symbol interference power, Pi_j is the multi-stream interference and P_N is the noise power.

The expressions of Pu_j , Pis_j , Pi_j and P_N are:

$$Pu_j = \left| \sum_{i \in \Omega_j} \alpha_{i,j} \sqrt{E_{i,j}} \sum_{k,k'=1}^M h_{i,j,k} p_{i,j,k'} \rho_f(\tau_{k,k'}) \right|^2, \quad \text{Eq. 3.1.13}$$

$$Pis_j = \sum_{n \neq 0} \left| \sum_{i \in \Omega_j} \alpha_{i,j} \sqrt{E_{i,j}} \sum_{k,k'=1}^M h_{i,j,k} p_{i,j,k'} \rho_f(\tau_{k,k'} + nT) \right|^2, \quad \text{Eq. 3.1.14}$$

$$Pi_j = \sum_{j' \neq j} \sum_n \left| \sum_{i \in \Omega_{j'}} \alpha_{i,j'} \sqrt{E_{i,j'}} \sum_{k,k'=1}^M h_{i,j,k} p_{i,j',k'} \rho_f(\tau_{k,k'} + nT) \right|^2, \quad \text{Eq. 3.1.15}$$

$$P_N = FN_0/T. \quad \text{Eq. 3.1.16}$$

where F is the receiver noise figure.

3.1.3.2 Perfect Receiver

For both TR and 1bit TR (with their specific p_{ijk} values), the Perfect Receiver post receiver SINR of receive antenna j is simply:

$$SINR_j = P u_j / P_N. \quad \text{Eq. 3.1.17}$$

3.1.3.3 Throughput

The achieved throughput is deduced from the post receiver SINR. The system maximum theoretical throughput is given by:

$$\text{Throughput} = \sum_{j=1}^N \log(1 + SINR_j) / (T \times \log(2)). \quad \text{Eq. 3.1.18}$$

3.1.4 Simulation assumptions

In this sub-section, we use the post receiver SINR formulas derived in sub-section 3.1.3 to study TR performance in a typical indoor environment illustrated by Fig. 3.1.2. Channel coefficients $h_{i,j,k}$ and $\alpha_{i,j}$ are generated through simulation using Winner II channel model. A first advantage of Winner II model is to account for spatial correlation, which is necessary to assess MIMO techniques. A second advantage is to account for penetration loss due to walls, which is necessary for indoor. The ‘cluster delay line model for indoor small office A1’ is used to generate fast fading. The fast fading channel is normalized so that in average, its power is 1 as in Eq. 3.1.4. Two different models are used for fast fading coefficients: NLOS and LOS. NLOS model is used when there is no obstacle on the direct path between the transmitter and the receiver, and LOS model is used when a wall is in between. The ‘A1 indoor corridor to room’ model is used for path loss computation.

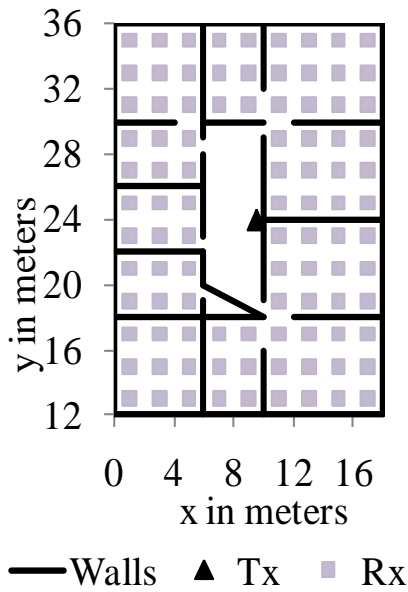


Fig. 3.1.2 Building floor

We simulate a MIMO system with a linear array of 16 transmit antennas (spaced by half of the wavelength) and two receive antennas. Thus, $P = 16$. The two receive antennas are spaced by 0.875 of the wavelength as it corresponds to the second zero of the Bessel function (the first one being slightly lower than half of the wavelength). This antenna spacing is selected because in the A1 NLOS fast fading channel model, angles of departure and arrival of propagating rays have a large distribution, and thus the spatial correlation function of the channel is similar to the one that is obtained with the Jakes channel model, i.e. the Bessel function.

A bandwidth of 100 MHz (corresponding to $T = 10^{-8}$ seconds). The carrier frequency is 2 GHz. Assuming $N_0 = -174$ dBm/Hz and $F = 9$ dB.

Equal power allocation per stream and per antenna is assumed. A total power allocation of $E = 0$ dBm and -10 dBm is assumed. Regarding the number of streams (or receive antennas), $N = 1$ and 2 are assessed. Thus, we set $E_{ij} = 10^{\frac{E-30}{10}} / (16N)$ watts. Finally, the pulse shape filter $f(t)$ is the square raised root cosine filter with roll-off factor of 0.22.

As illustrated in Fig. 3.1.2, the position of the transmitter is fixed in the corridor, while a large number of positions in the surrounding rooms are used for the receiver. For each position of the receiver, the path loss gain is computed and a large number of fast fading samples are generated. For each sample, the post receiver SINR formulas in Eq. 3.1.12 and Eq. 3.1.17 are applied for Dumb Receiver and Perfect Receiver respectively. The corresponding throughputs are computed according to Eq. 3.1.18. Finally, for each position, the average throughput over all samples is computed.

3.1.5 Results

The complementary cumulative distribution function (CCDF) of the achieved throughput is plotted in Fig. 3.1.3, where $G(x)$ is the percentage of positions with a throughput larger than x . TR and 1bit TR, one stream and two stream transmissions are compared, under the assumption that the Dumb Receiver is used. Though the transmit output power is very low (0 dBm), the entire building floor is covered, with all schemes. With TR and one stream, for instance, 50 to 400 Mbps are achieved depending on the position. The corresponding spectral efficiency is 0.5 to 4 bps/Hz. As expected, two streams transmission increases the throughput, allowing to achieve 100 Mbps to 500 Mbps, and 1bit TR is less efficient than TR.

To evaluate whether a Dumb Receiver is optimum, the CCDF of the dumb to perfect receiver throughput ratio (DPRTR), i.e. the ratio between the throughput obtained with the dumb receiver and the throughput obtained with the perfect receiver, is plotted in Fig. 3.1.4. In this figure, $Z(x)$ is the percentage of positions with a DPRTR larger than x . For both TR and 1bit TR, considering one stream, this ratio already equals 50 to 100% depending on the position. If we focus, on 50% of the “best” positions, the DPRTR lies between 70 and 100%. If we reduce the output power to minus 10dBm instead of 0dBm, the DPRTR is 80% for 80% of the covered area (Fig. 3.1.5 and Fig. 3.1.6), i.e. the Dumb Receiver is near to optimum in the entire covered area. However, with such low power, the throughput lies between only 9 Mbps and 500 Mbps (i.e. a spectral efficiency between 0.09 bps/Hz and 5 bps/Hz).

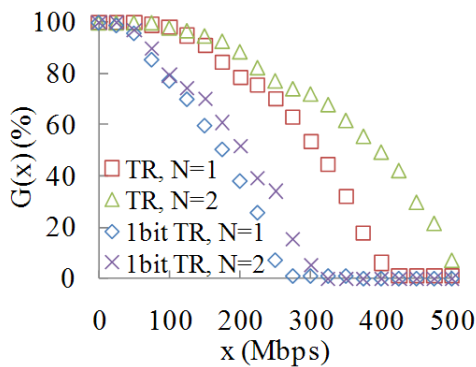


Fig. 3.1.3 Throughput CCDF, E=0 dBm

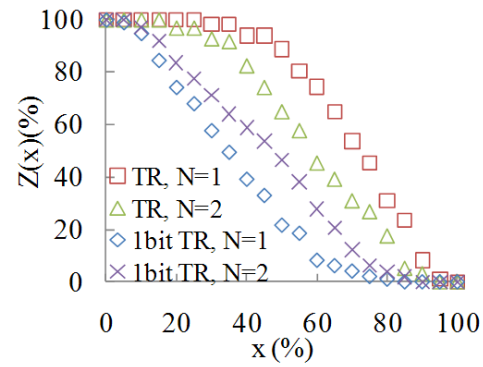


Fig. 3.1.4 DR To PR Throughput Ratio, E=0Bm

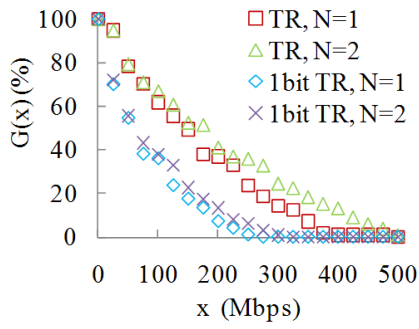


Fig. 3.1.5 Throughput CCDF, $E=-10$ dBm

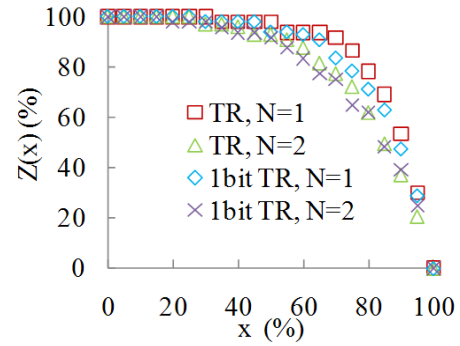


Fig. 3.1.6 DR To PR Throughput Ratio, $E=-10$ dBm

To visualize the regions of high and low throughputs, the throughput is plotted in colour scale as a function of the Cartesian coordinates of the in Fig. 3.1.7 and Fig. 3.1.8, for one stream and two streams respectively. For these figures, 0dBm output power, TR and Dumb Receiver are considered. Using two streams instead of one brings enhancements in a large region near the transmitter.

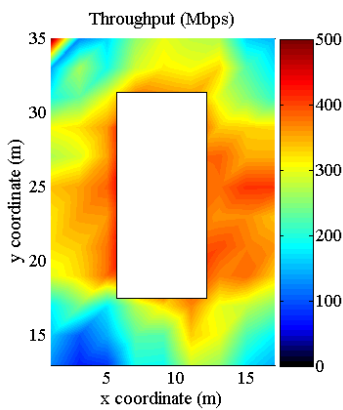


Fig. 3.1.7 TR, 1 stream

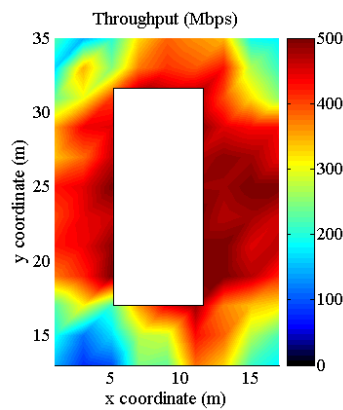


Fig. 3.1.8 TR, 2 streams

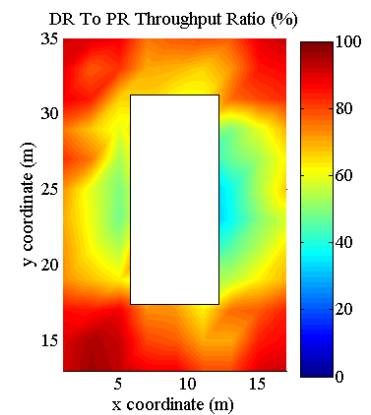


Fig. 3.1.9 TR, DPRTR

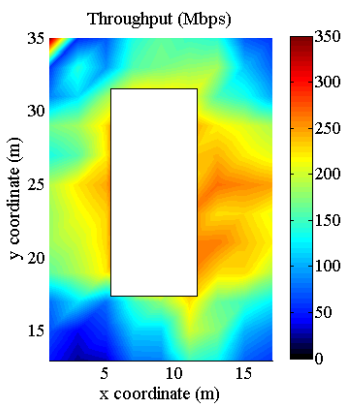


Fig. 3.1.10 1bit TR, 1 stream

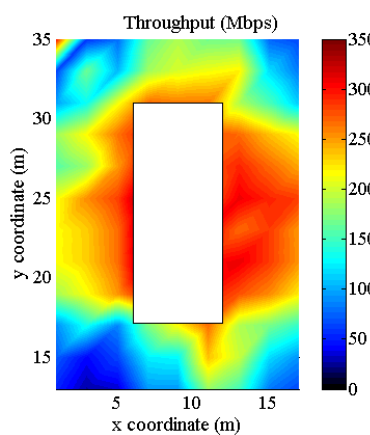


Fig. 3.1.11 1bit TR, 2 streams

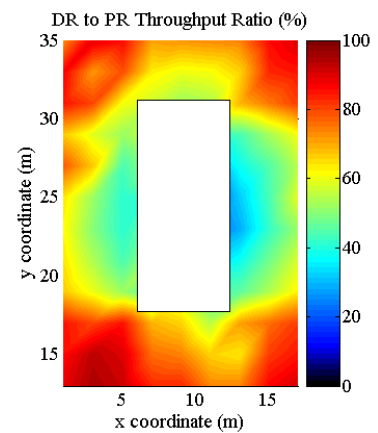


Fig. 3.1.12 1bit TR, DPRTR

To visualize the regions where the Dumb Receiver is optimum, Fig. 3.1.9 plots the DPRTR in colour scale as a function of the position. The Dumb Receiver is optimum in a large region far from the transmitter.

Fig. 3.1.10, Fig. 3.1.11 and Fig. 3.1.12 are the equivalent of Fig. 3.1.7, Fig. 3.1.8 and Fig. 3.1.9, with 1bit TR instead of TR this time. The same observations can be made for 1bit TR as for TR. However, TR outperforms 1bit TR. Indeed, 1bit TR allocates the same power to all echoes, whatever their true power is. This increases the effect of low power echoes compared to the reality. 1bit TR therefore worsens the inter-symbol interference.

3.1.6 Conclusion and next steps

Our system level performance evaluation study shows that with an output power as low as 0dBm, a system bandwidth as large as 100 MHz, and a Dumb Receiver, an entire building floor is covered with throughput values from 100 to 500 Mbps when two streams are transmitted, and from 50 to 400 Mbps even with one stream. Moreover, the Dumb Receiver achieves at least 50% of the Perfect Receiver throughput, and up to 100%. To conclude, this performance assessment confirms that TR techniques are good candidates for systems operating at very low output power in wireless indoor networks, as they manage to provide satisfactory coverage and capacity even with a Dumb Receiver.

3.2 Characterization of the Confidentiality of a Green Time reversal Communication System: Experimental Measurement of the Spy BER Sink

3.2.1 Introduction

In TDD wireless MISO communication systems, high spectral efficiency can be achieved by using channel knowledge at the transmitter to pre-filter the signal. As explained in section 2, TR is an excellent candidate for green, low complexity and confidential communications. As already mentioned in section 2, many very complete experimental studies on TR (especially on UWB) [63][40][37][36][44][34][48] have been held to assess the performance of time reversal at the target receive antenna: from signal-to-noise-and-interference ratio computations up to real over-the-air data transmission using FPGA platforms [39]. However, up to now, no study has assessed the confidentiality of time reversal, i.e. the fact that the signal can be demodulated at the target, and not around the target.

In this study, we propose to perform the first study that characterizes the confidentiality of a time reversal indoor communication, between a network of distributed antennas and a target antenna. We introduce a new metric: the bit error rate (BER) achieved by a spy antenna nearby the target. Sub-section 3.2.2 defines the spy BER metric. Sub-section 3.2.3 describes our experimental method to

measure the spy BER. Sub-section 3.2.4 analyses our spy BER experimental measurements. Sub-section 3.2.5 concludes this study.

The following notations are used in this study.

- a_n is the symbol coefficient sent of the cosine part of the carrier;
- \hat{a}_n^p is the estimate of a_n^p ;
- b_n is the symbol coefficient sent of the sine part of the carrier;
- \hat{b}_n^p is the estimate of b_n^p ;
- B is the system bandwidth;
- BER^p is the bit error rate measured at position p ;
- C is the size of the quadrature amplitude modulation;
- $co(t) = \cos(2\pi F_C t)$;
- d_i is the data bit number i ;
- \hat{d}_i^p is the detected bit number i ;
- $f(t)$ is the square raised root cosine filter with roll off factor β ;
- F_C is the carrier frequency;
- F_G is the sampling frequency of the generator;
- F_O is the sampling frequency of the oscilloscope;
- Γ is the target peak power;
- $h^{p,i}(t)$ is the channel impulse response between transmit antenna i and spy antenna at position p ;
- i is the transmit antenna index;
- j is the bit index;

- k is the sample index; depending on the context this is the index of an oscilloscope sample, a generator sample, or a data symbol;
- $k_{synchrono}^p$ index of the sample corresponding to the detected ‘single tap’, for synchronisation;
- λ_k^p synchronised and time inversed received signal;
- $m^i(t)$ is the time reversal prefilter applied to the transmit antenna i ;
- M is the number of transmit antennas;
- n is the symbol index;
- N_{bits} is the number of data bits;
- N_u is the number of data symbols;
- N_1 is the number of symbol periods corresponding to a guard period preceding data transmission;
- N_2 is the number of symbol periods corresponding to a guard period following data transmission;
- p is the position index;
- p_n^p real part of the detected symbol (data or synchronisation symbol);
- P is the number of positions;
- q_n^p imaginary part of the detected symbol(data or synchronisation symbol);
- r_k is the received data sample number k in generator sample unit;
- s_k is the normalised received data sample number k in generator sample unit;
- $S_{symbols}$ is the set of symbol indexes corresponding to actual transmission and the guard periods preceding and following data transmission;
- S_{time} is the interval in time corresponding to $S_{symbols}$;
- S_G is the interval in generator sample units corresponding to $S_{symbols}$;

- $S_k^{0,i}$ sample number k obtained after normalisation and time inversion of the $y_k^{0,i'}s$;
- S_0 is the interval in oscilloscope sample units corresponding to $S_{symbols}$;
- $si(t) = \sin(2\pi F_c t)$;
- t is the time;
- $u(t)$ is the analog training signal sent from position $p = 0$;
- $U^{0,i}(t)$ signal sent by generator and received at antenna i ;
- $v^{0,i}(t)$ analog signal after propagation of $u(t)$ through the wireless channel $h^{0,i}(t)$;
- $V^{p,i}(t)$ signal received by the oscilloscope after propagation of $U^{0,i}(t)$ through wireless channel $h^{p,i}$;
- $w_k^{0,i}$ oscilloscope sample number k of analog signal $v^{0,i}(t)$;
- $W_k^{p,i}$ oscilloscope sample number k of the analog signal $V^{p,i}(t)$;
- $x_k^{0,i}$ oscilloscope sample number k of noise;
- $X_k^{p,i}$ oscilloscope sampled noise in sample $W_k^{p,i}$;
- $y(t) = 1$ if $0 \leq t < 1$, $t = 0$ otherwise;
- $y_k^{0,i}$ generator sample number k (obtained after processing of the $x_k^{0,i'}s$);
- y_k^p sum over the antennas i of the $Y_k^{p,i'}$ s ;
- $Y_k^{p,i}$ generator sample number k (obtained after processing of the $X_k^{p,i'}s$);
- $\theta^p(t)$ is the signal received by the spy antenna at the position p and at time t ;
- ϑ_k^p sample number k after demodulation on the sin part of the carrier, for position number; for position p ;
- Θ^p is the maximum of $|\theta^p(t)|$;
- ε_n^a is the noise sample on the cosine part of the carrier, for the sample number n ;

- ε_n^b is the noise sample on the sine part of the carrier, for the sample number n ;
- ζ^p normalisation factor;
- $\xi_k^{p'}$'s time inverse of $\gamma_k^{p'}$'s;
- $\varphi(t)$ transmit signal (without time reversal prefiltering);
- $\psi^i(t)$ is the signal transmitted by antenna i (without time reversal prefiltering);
- ω_k^p sample number k after demodulation on the cosine part of the carrier, for position number p .

3.2.2 The spy bit error rate metric

This sub-section proposes a characterization method and a spy BER metric to assess the confidentiality of a Time reversal communication, as illustrated in Fig. 3.2.1.

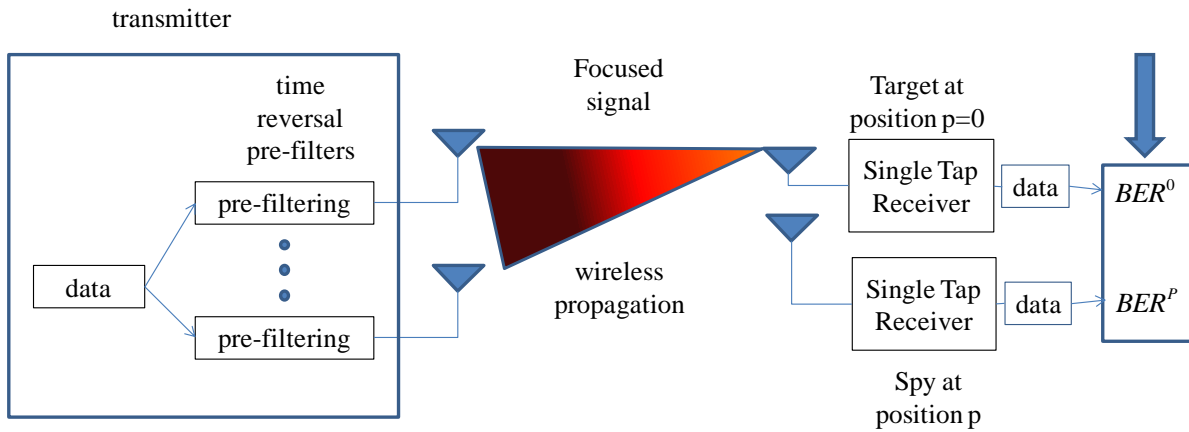


Fig. 3.2.1 Spy BER evaluation

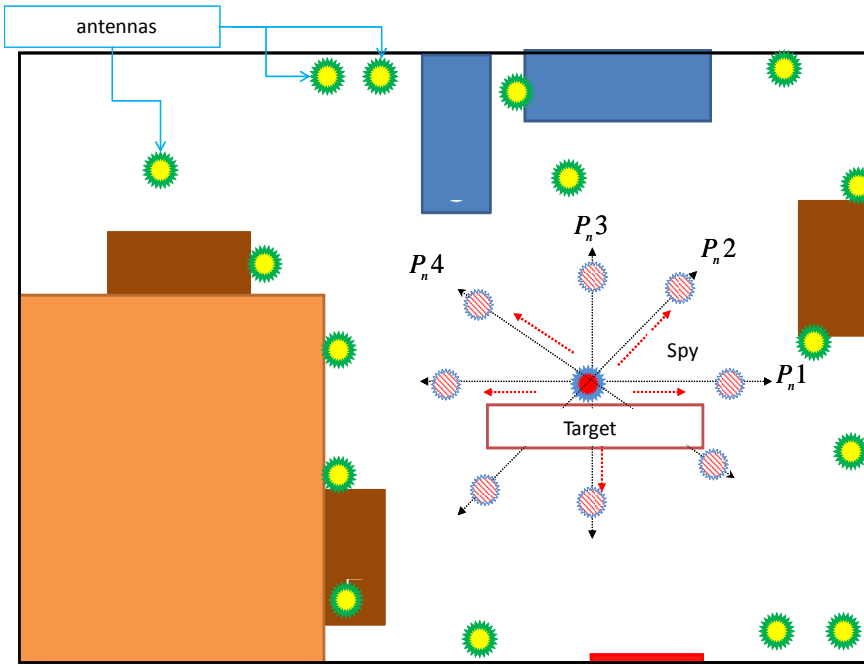


Fig. 3.2.2 Room and positions of antennas.

A first basic definition can be provided. Downlink data transfer from a transmitter with M distributed transmit antennas (numbered with indices $i = 0 \dots M - 1$), and a receiver with 1 target receive antenna is considered. The target receive antenna is set at position number $p = 0$. The bit error rate BER^0 achieved by the target antenna is assessed. A spy antenna is positioned nearby the target antenna. Variable positions, numbered with indices $p = 0 \dots P - 1$, are tested. For each position p , the spy antenna achieved Bit Error Rate BER^p , i.e. the “spy BER” is assessed. We propose to evaluate this BER^p versus p spatial function, to characterize the confidentiality of the data transmission. The larger is BER^p for positions $p > 0$ far from the target position $p = 0$, the more confidential the communication is.

The following paragraphs further mathematically define the BER^p metric.

Let $h^{p,i}(t)$ be the channel impulse response (in the system band B centered on the carrier frequency F_C) between transmit antenna i and spy antenna at position p . $h^{p,i}$ includes antenna gains, path loss, shadowing, and fast fading.

The transmitter sends N_{bits} data bits d_j ($0 \leq j \leq N_{bits} - 1$) using a Quadrature Amplitude Modulation with constellation size C . We define the number of symbols $N_u = N_{bits} / \log_2(C)$. For each symbol number n , with ($0 \leq n \leq N_u - 1$), the coefficients a_n and b_n are sent over the cosine and sine parts of the carrier, respectively. These a_n and b_n are associated to bits $d_{\log_2(C)n+i}$ with $i = 0 \dots \log_2(C) - 1$. Assuming filtering by $f(t)$ and a bandwidth of B , the data signal $\varphi(t)$ to be transmitted is given by:

Eq. 3.2.1

$$\varphi(t) = \sum_{n=0}^N (a_n \cos(t) + b_n \sin(t)) f\left(t - \frac{n}{B}\right).$$

For each antenna i , assuming per antenna time reversal pre-filtering $m^i(t) = h^{0,i}(-t)$, the signal $\psi^i(t)$, transmitted by antenna i , and normalized to ensure a peak power equal to Γ , is given by:

Eq. 3.2.2

$$\psi^i(t) = \sqrt{\Gamma} \frac{(\varphi * m^{0,i})(t)}{\max_{\tau} (|\sum_{i=0}^{M-1} (\varphi * m^{0,i})(\tau)|)}.$$

The signal $\theta^p(t)$, received at the position p , and coming from all transmit antennas after propagation through $h^{p,i}$ is given by:

Eq. 3.2.3

$$\theta^p(t) = \sqrt{\Gamma} \sum_{i=0}^{M-1} (\psi^i * h^{p,i})(t).$$

Assuming a single tap receiver, with perfect synchronization, perfect peak amplitude estimation of $\theta^p = \max_{\tau} (|\theta^p(t)|)$, with noise ε_n^a and ε_n^b over the cosine and sine parts, the output of the single tap receiver, \hat{a}_n^p (for the cosine part) and \hat{b}_n^p (for the sine part) are given by:

Eq. 3.2.4

$$\hat{a}_n^p = \frac{1}{\theta^p} (\theta^p * \cos * f)\left(\frac{n}{B}\right) + \varepsilon_n^a.$$

Eq. 3.2.5

$$\hat{b}_n^p = \frac{1}{\theta^p} (\theta^p * \sin * f)\left(\frac{n}{B}\right) + \varepsilon_n^b.$$

The de-mapping is then performed to estimate the bits $\hat{d}_{\log_2(C)n+j}^p$ based on \hat{a}_n^p and \hat{b}_n^p , with $j = 0 \dots \log_2(C) - 1$. The bit error rate BER^p achieved by the spying antenna at position p is given by

Eq. 3.2.6

$$BER^p = \frac{1}{N_{bits}} \sum_{i=0}^{N_{bits}} |\hat{d}_j^p - d_j|,$$

where \hat{d}_j^p is the estimation of d_i for position p .

3.2.3 Experimental method

3.2.3.1 Overview

The metric described in sub-section 3.2.2 cannot be easily assessed experimentally, as it requires the development of analog and digital communications modules at the transmitters and the receiver. Also, simultaneous transmission of M transmit antennas requires to have M frequency heads and amplifiers.

To perform experimental measurements of BER^p , we propose an experimental methodology, which has a low complexity, but still, evaluates BER^p based on real over-the-air data transmission. This method is illustrated by Fig. 3.2.3.

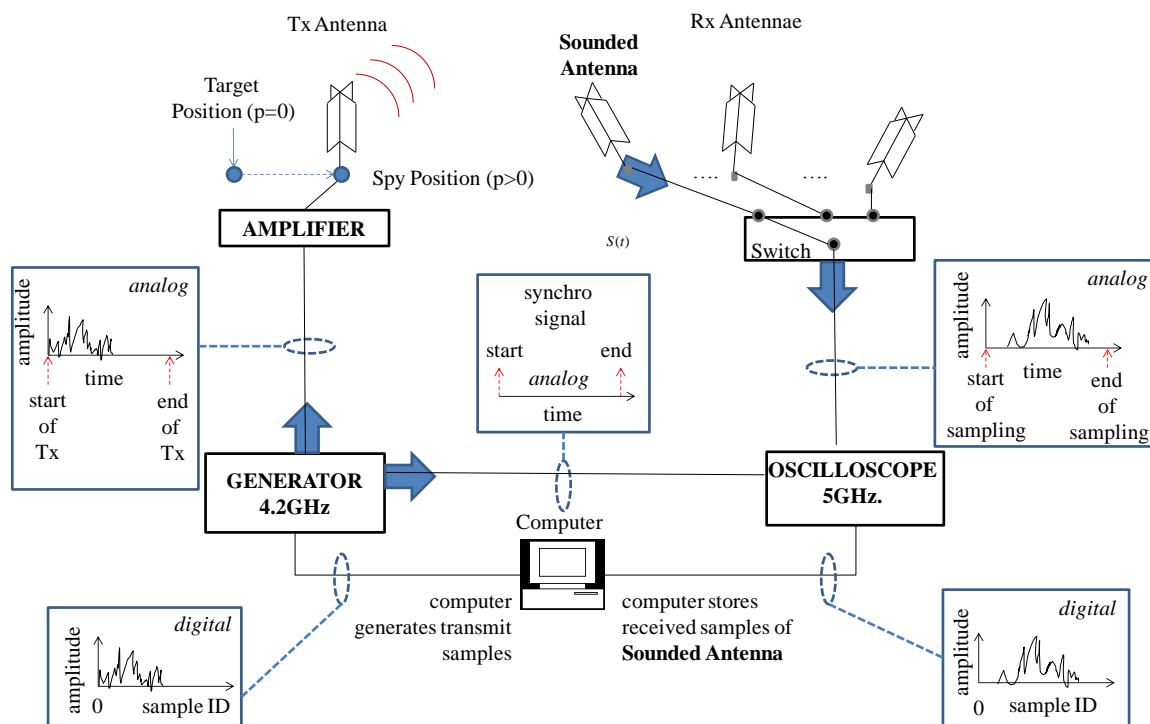


Fig. 3.2.3 Experimental Setup: focusing phase, for spy position p and antenna i

Our method only relies on one generator with sampling frequency F_G , 1 oscilloscope with sampling frequency F_O , 1 amplifier with gain \sqrt{T} , and one computer. The latter is in charge of emulating signal processing (both analog and digital processing) and monitoring the amplifier and the oscilloscope. The reciprocity of the channel is exploited: transmission from antenna i to antenna at position p , is replaced by transmission from antenna p to antenna i . Instead of using simultaneous transmission of multiple antennas, we process antennas successively, using a switch. Finally, instead of estimating the channel, computing the TR pre-filter and applying the pre-filter to the data, we first send the data through the wireless propagation channel, we store the received signal, and we transmit it in TR mode. TR is simply applied to both channel impulse response and data symbols, instead of channel alone.

Our method requires several successive steps depicted hereafter.

In a first phase (sub-section 3.2.3.2), the computer generates the data signal with sampling frequency F_G .

During a training phase (sub-section 3.2.3.3), which is repeated for every antenna i , the generator sends the same data signal over the air using the target antenna. Simultaneously, the oscilloscope acquires the signal received by antenna i . The computer then time inverses it, normalizes it, and finally stores it.

During a focusing phase (sub-section 3.2.3.4), which is reiterated for every antenna i , and every position p of the spying antenna, the signal stored for antenna i by the computer during the training phase, is sent over the air by the generator, through the spy antenna at position p . Simultaneously, the oscilloscope acquires the signal received by antenna i , this focused signal for antenna i and position p is stored by the computer.

During a combining phase (sub-section 3.2.3.5), the computer, combines over antennas i , the focused signals determined during the focusing phase for position p , and stores a unique focused signal for each position p .

Finally, for each position p , the computer post-processes the focused signal obtained after the combining phase, and performs synchronization (sub-section 3.2.3.6).

Finally, the demodulation, the Single Tap Receiver (sub-section 3.2.3.7) and the spy BER computation (sub-section 3.2.3.8) are performed by the computer, over sampled signals.

The BER^p metric measured using the methodology slightly differs from the one defined in sub-section 3.2.2. The methodology combines M measured signals corresponding to M antennas. Each measurement suffers from a different and independant receiver noise. The total receiver noise power after combination, is therefore proportional to the number of antennas M . However, this introduces a fix bias in SNR for all measured positions p , which could easily be corrected by transmitting at M times higher power. In other terms, this bias does not change the relative difference between the power received at one position (for instance the target position) and the power received at any other position in space.

3.2.3.2 Data Signal

The computer generates data bits d_j 's and associated symbols a_n 's and b_n 's, as described in sub-section 3.2.2. In addition, the following N_1 'guard symbols' are preceding the sequence of data symbols:

$$a_n = b_n = 0, \text{ for } -(N_1 - 1) \leq n < 0.$$

Eq. 3.2.7

The following N_2 ‘guard symbols’ are following sequence of data symbols:

$$a_n = b_n = 0, \text{ for } 0 \leq n - N_u < N_2.$$

Eq. 3.2.8

Thus, contrary to sub-section 3.2.2, a_n and b_n symbols have a index denoted n belonging to the set $S_{symbols} = [-(N_1 - 1), (N_u + N_2 - 1)]$. This set of symbol indexes corresponds to a time interval S_{time} . This time interval corresponds to a set S_G of generator samples indexes. It also corresponds to a set S_0 of oscilloscope sample indexes.. $N_1 > 0$ is chosen so that most of the energy of the symbol $n = 0$ is captured, (i.e. $|f(t < -\frac{N_1}{B})| \ll |f(0)|$). As the generator and the oscilloscope are synchronized, they transmit and receive, respectively, during the same exact period. One must ensure that the oscilloscope entirely receives the signal sent by the generator, over-the-air even with propagation delay. Hence, $N_2 > 0$ is chosen so that $|h^{p,i}(t > \frac{N_2}{B})| \ll |h^{p,i}(t < \frac{N_2}{B})|$.

The computer emulates the following analog processing phases listed in sub-section 3.2.2: filtering by $f(t)$, carrier modulation, $m^i(t)$ pre-filtering. Analog signals are replaced by signals sampled at F_G , and digital instead of analog processing is applied. The computer computes the data samples r_k , for $k \in S_G$, and the normalized sample s_k as follows:

$$r_k = \sum_{l \in S_{symbols}} \left(a_n \cos\left(\frac{k}{F_G}\right) + b_n \sin\left(\frac{k}{F_G}\right) \right) f\left(\frac{k}{F_G} - \frac{n}{B}\right),$$

Eq. 3.2.9

$$s_k = \frac{r_k}{\max_{l \in S_G} (|r_l|)}.$$

Eq. 3.2.10

3.2.3.3 Training of antenna i

This training procedure is described for a given antenna i . The generator transmits the following amplified analog signal $u(t)$ from the target position ($p = 0$), with $t \in S_{time}$:

$$u(t) = \sqrt{\Gamma} \sum_{k \in S_G} s_k y(F_G t - k),$$

Eq. 3.2.11

where, s_k has been defined in Eq. 3.2.10. and $y(t) = 1$ if $0 \leq t < 1$, $t = 0$ otherwise. Simultaneously, the oscilloscope, switched over antenna i , receives the analog signal $v^{0,i}(t)$ after propagation through the wireless channel $h^{0,i}$, with $t \in S_{time}$:

$$v^{0,i}(t) = (h^{0,i} * u)(t). \quad \text{Eq. 3.2.12}$$

The oscilloscope samples $w_k^{0,i}$ of $v^{0,i}(t)$, with $k \in S_O$, are given by:

$$w_k^{0,i} = v^{0,i}\left(\frac{k}{F_O}\right) + x_k^{0,i}, \quad \text{Eq. 3.2.13}$$

where $x_k^{0,i}$ is the sampled thermal noise. The $w_k^{0,i}$ coefficients are sent to the computer, and converted into samples $y_k^{0,i}$ with sampling frequency F_G . For $k \in S_G$:

$$y_k^{0,i} = \frac{1}{2}(x_{k1}^{0,i} + x_{k1+1}^{0,i}), \quad \text{Eq. 3.2.14}$$

with $k1 \in S_O$ such that:

$$\frac{k1}{F_O} \leq \frac{k}{F_G} < \frac{k1+1}{F_O}. \quad \text{Eq. 3.2.15}$$

The computer performs time inversion and normalization to obtain $S_k^{0,i}$.

$$S_k^{0,i} = \frac{y_{N\frac{F_O}{B}-1-k}^{0,i}}{\max_{l \in S_G}(|y_l^{0,i}|)}. \quad \text{Eq. 3.2.16}$$

The $S_k^{0,i}$'s are in fact samples (with the sampling frequency F_G) of the signal that 'would be' transmitted from antenna i to focus the data towards the position $p = 0$, in a 'real TR experiment'.

3.2.3.4 Focusing phase for antenna i and position p

This focusing procedure is described for a given antenna i and a given position p . The generator and the amplifier send the following analog signal over the air, for $t \in S_{time}$:

$$U^{0,i}(t) = \sqrt{\Gamma} \sum_{k=1}^{N_G} S_k^{0,i} y(F_G t - k),$$

Eq. 3.2.17

where $\sqrt{\Gamma}$ is a normalising factor. Simultaneously, the oscilloscope receives $V^{p,i}(t)$ at antenna i after propagation through wireless channel $h^{p,i}$, with $t \in S_{time}$:

$$V^{p,i}(t) = (h^{p,i} * U^{0,i})(t).$$

Eq. 3.2.18

The oscilloscope samples $W_k^{p,i}$ of $V^{p,i}(t)$, with $k \in S_O$, are:

$$W_k^{p,i} = V^{p,i}\left(\frac{k}{F_O}\right) + X_k^{p,i},$$

Eq. 3.2.19

where $X_k^{p,i}$ is the sampled thermal noise. The computer converts the sampling frequency from F_O to F_G :

$$Y_k^{p,i} = \frac{1}{2}(W_{k1}^{p,i} + W_{k1+1}^{p,i}), k \in S_G.$$

Eq. 3.2.20

such that:

$$\frac{k1}{F_O} \leq \frac{k}{F_G} < \frac{k1+1}{F_O}.$$

Eq. 3.2.21

The $Y_k^{p,i}$'s are in fact samples (with the sampling frequency F_G) of the signal which would be received after propagation of the $S_k^{0,i}$'s from antenna i to position p .

3.2.3.5 Combined focused signal for position p

The computer combines the $Y_k^{p,i}$ samples of focused signals of each antenna i . The resulting unique focused sampled signal γ_k^p , ($k \in S_G$) for position p , and its time inverse, ξ_k^p , are:

$$\gamma_k^p = \sum_{i=0}^{M-1} Y_k^{p,i},$$

Eq. 3.2.22

Eq. 3.2.23

$$\xi_k^p = \gamma_{N_{FG}-1-k}^p.$$

The y_k^p 's are in fact samples of the signal that would be received at position p if each antenna i where transmitting its $S_k^{0,i}$'s simultaneously. In y_k^p , the sequence of data symbols is inversed in time. ξ_k^p is the inverse in time of y_k^p , and is therefore the signal to be used for demodulation.

3.2.3.6 Emulating perfect synchronisation at the receiver

The focused signal ξ_k^p measured experimentally is delayed compared to the initial transmit signal s_k defined in Eq. 3.1.9 and Eq. 3.2.10, due to propagation. This propagation delay is unknown, and has to be estimated experimentally, by the computer. To study the confidentiality of the communication, we make sure that the achieved BER is not limited by the synchronization phase. To achieve ideal delay estimation, the entire sequence of reference symbols s_k is used to determine the propagation delay $k_{synchronro}^p$ in generator samples (this method is of course not applicable in a real system.):

Eq. 3.2.24

$$k_{synchronro}^p = Arg\{l, max_l(\sum_{i=0}^{M-1} \xi_k^p s_{k+l})\}.$$

The synchronized signal λ_k^p , with $(k - k_{synchronro}^p) \in S_G$ is defined as follows:

Eq. 3.2.25

$$\lambda_k^p = \xi_{k-k_{synchronro}^p}^p.$$

3.2.3.7 Demodulation for position number p , single tap receiver

The computer emulates the analog demodulation by the following digital processing, with $(k - k_{synchronro}^p) \in S_G$:

Eq. 3.2.26

$$\omega_k^p = \lambda_k^p \cos\left(2\pi F_C \frac{k}{F_G}\right),$$

Eq. 3.2.27

$$\vartheta_k^p = \lambda_k^p \sin\left(2\pi F_C \frac{k}{F_G}\right).$$

The computer emulates the analog filtering and the sampling (single tap receiver). The symbols, with $n \in S_{symbols}$ are:

$$p'_n = \sum_{(l-k_{synchro}) \in S_G} \omega_l^p f\left(\frac{l}{F_G} - \frac{n}{B}\right). \quad \text{Eq. 3.2.28}$$

$$q'_n = \sum_{(l-k_{synchro}) \in S_G} \vartheta_k^p f\left(\frac{l}{F_G} - \frac{n}{B}\right). \quad \text{Eq. 3.2.29}$$

Then the computer extracts the useful symbols \hat{a}_n^p and \hat{b}_n^p :

$$\hat{a}_n^p = p'_{N_1+n} \text{ for } 0 \leq n < N_u. \quad \text{Eq. 3.2.30}$$

$$\hat{b}_n^p = q'_{N_1+n} \text{ for } 0 \leq n < N_u. \quad \text{Eq. 3.2.31}$$

The required normalization of the received signal, before de-mapping to compensate for focusing and propagation, is unknown. The normalization has to be estimated experimentally. As for synchronization, in order to achieve ideal normalization estimation, we use the entire sequence as a reference. The optimum normalization ζ^p is found as follows:

$$\zeta^p = \text{Arg} \left\{ c, \min_{\zeta} \left(\sum_{n=0}^{N-1} (\hat{a}_n^p - a_n)^2 + (\hat{b}_n^p - b_n)^2 \right) \right\}. \quad \text{Eq. 3.2.32}$$

The estimated symbols are then normalized before being de-mapped, for $0 \leq n < N_u$, the computer updates \hat{a}_n^p and \hat{b}_n^p :

$$\hat{a}_n^p = \zeta^p \hat{a}_n^p. \quad \text{Eq. 3.2.33}$$

$$\hat{b}_n^p = \zeta^p \hat{b}_n^p. \quad \text{Eq. 3.2.34}$$

3.2.3.8 BER evaluation for position p

The same method as for the system described in sub-section 3.2.2 is used to evaluate BER^p .

3.2.4 Measurements results

BER^p has been assessed using the experimental methodology described in sub-section 3.2.3, with a measurement setup illustrated in the Fig. 3.2.2. The following parameters were used: $B = 30$ MHz, $F_C = 1$ GHz (this corresponds to a wavelength of 30 cm), $F_G = 4.2$ GHz, $F_O = 5$ GHz, $\beta = 0.22$. The constellation was size $C = 256$, 256QAM mapping and de-mapping was implemented in the computer. The BER^p measurements have been performed in a room with $M = 16$ distributed antennas, and along four axes (P1, P2, P3, and P4). BER^p is plotted in Fig. 3.2.4 as a function of the spy-to-target distance. The spy-to-target receive power ratio is plotted in Fig. 3.2.5. While the spy BER and power measurements are precise (low error on y-axis), the measurements of the positions of antennas are “noisy”. Indeed, antennas where moved manually using un-precise carriages. We estimate that there is a $+2/-2$ cm error on the distances reported on these figures (x-axis). This explains the “not smooth” aspect of the curves.

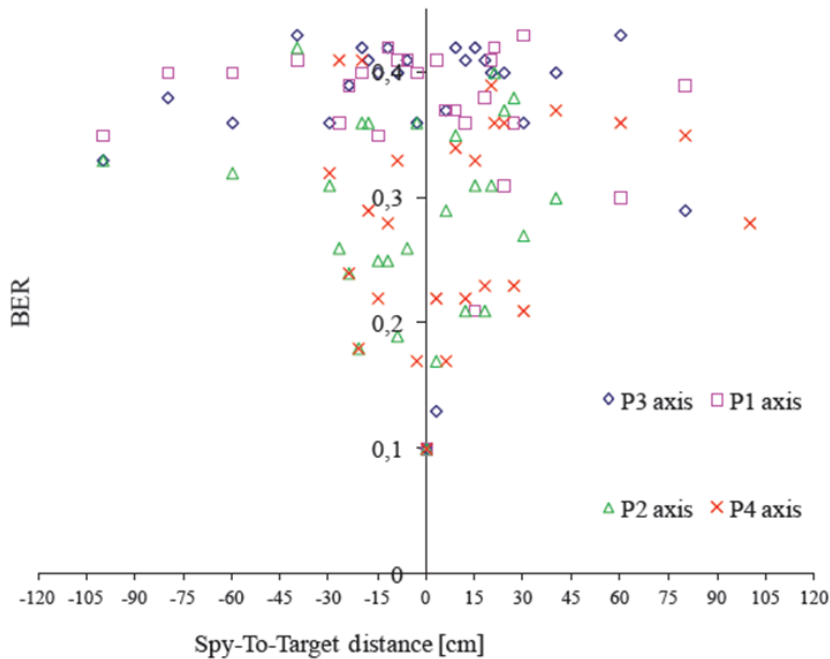


Fig. 3.2.4 Spy BER

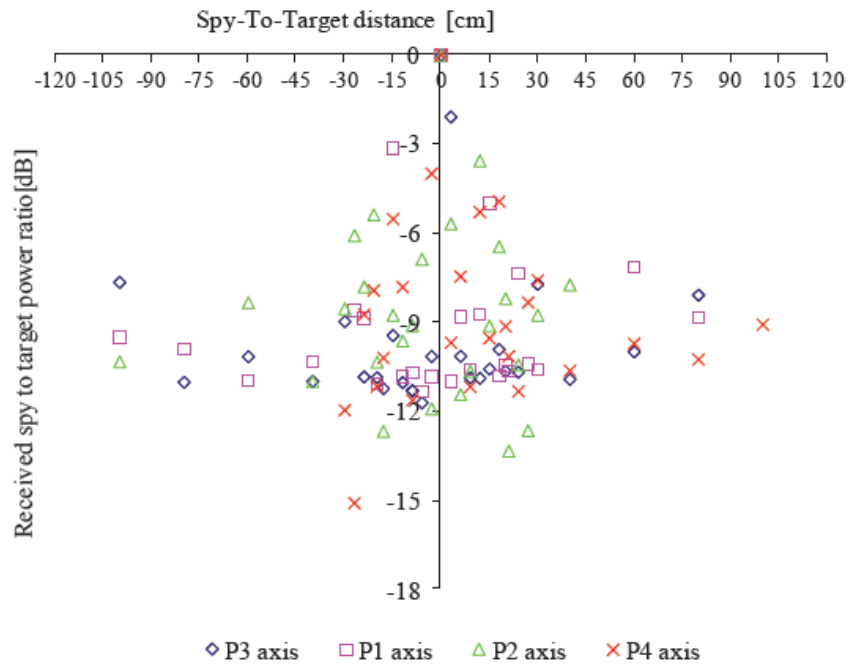


Fig. 3.2.5 Spy to target received power ratio[dB]

Nevertheless, even with these measurement impairments, even in conditions which are not favourable to focusing (with a bandwidth as low as 30 MHz, and even with a large amount of antennas being in LOS conditions), the measurements, strongly show a BER “sink” and a power “bell”, and confirm the confidentiality advantages given by TR technique, in addition to green aspects.

3.2.5 Conclusion

We have characterized the confidentiality of a time reversal communication system in indoor, through an experimental measurement of the BER achieved by a spy antenna nearby the target antenna. The measurements clearly show a spy BER “sink” centred on the target. This study also shows, that in indoor, with a spectrum typical of mobile networks (30MHz at 1GHz), 256 QAM and 240Mbits/s can be achieved with a single tap receiver, thanks to 16 transmits antennas using time reversal.

Chapter 4 - Design of enablers for time reversal focusing in challenging scenarios which are typical from mobile networks

Previous works mentioned in sub-section 2.4, show that the support of time reversal in mobile networks is still a challenge. The support of FDD mode (the dominant duplex mode in Europe) and the support of high velocities is a challenge. We present new techniques, which address both problems.

4.1 Frequency division duplex time reversal (FDD TR)

4.1.1 Introduction

As explained in section 2, TR is advantageous for low complexity and green communications in TDD mode. ‘1bit Time reversal’ (1Bit TR) [65] is a variant of TR, which has been proposed for FDD mode [67]. In this variant, the receiver estimates the channel and uses a very basic quantization and coding scheme to feed back this channel to the transmitter: the sign of the real part and the sign of the imaginary part of the channel impulse response is fed back for every tap. As for TR, 1bit TR enables to multiplex users, and even has better spatial focusing properties [63][64]. In parallel, general approaches to perform MIMO pre-coding in FDD, with unquantized and uncoded feedback have been explored. For instance, in [93], the receiver estimates the downlink channel and feeds it back to the transmitter directly without “digitization”, quantization nor coding. Simultaneously, it sends uplink pilots. In [95], to perform blind beamforming in FDD, the same approach is used, with a slight difference that the time inversion of the downlink channel is fed back. In both [93], and [95], the transmitter estimates the uplink channel, and estimates an equivalent channel, that would be due to propagation through the downlink and the uplink channels successively. Then, a highly complex phase is necessary, to estimate the downlink channel by de-scrambling the equivalent channel estimate using the uplink channel estimate. In the end, for both schemes, pre-coding is performed on the downlink channel only.

In this study, going further in the directions pointed by above mentioned works, we propose a new scheme called ‘FDD time reversal’ (FDD TR) to enable focusing in FDD mode, with a low complexity scheme. TR technique is simply applied to the equivalent channel due to propagation through the downlink and uplink channels successively. Thus, the proposed scheme does not need to de-scramble the downlink and uplink channels. FDD TR is compared to the one obtained with 1bit TR, and pure TR, in terms of throughput and overhead, for a 16×2 MIMO system. The performance evaluation methodology is based on post receiver SINR and capacity formulas, and takes into account inter-symbol interference and multi-stream interference, as in [45]. Winner II MIMO propagation channel

models [86] for indoor, accounting for spatial correlation of antennas at the transmitter and the receiver sides are used.

Sub-section 4.1.2 sets the system model. Sub-section 4.1.3 provides the methodology for post receiver SINR and capacity computation. Sub-section 4.1.4 analyses the overhead. Sub-section 4.1.5 gives our simulation results. Sub-section 4.1.6 concludes this study.

4.1.2 System description

Sub-section 4.1.2.1 lists the notations used throughout this study. Sub-section 4.1.2.2 provides an overview of the system model. Sub-section 4.1.2.3 recalls Time reversal pre-filter, sub-section 4.1.2.5 and sub-section 4.1.2.4 is a reminder of 1bit time reversal pre-filter, and sub-section 4.1.2.5 presents FDD Time reversal.

4.1.2.1 Notations

In this study, we use ‘mathematical notations for single carrier transmissions studies’.

Additionally, we define the following notations, only valid for this study: $g_{i,j,k}$ is the gain of the channel between the transmit antenna i and the receive antenna j on the uplink direction (from the receive antenna j and the transmit antenna i).

4.1.2.2 System Overview

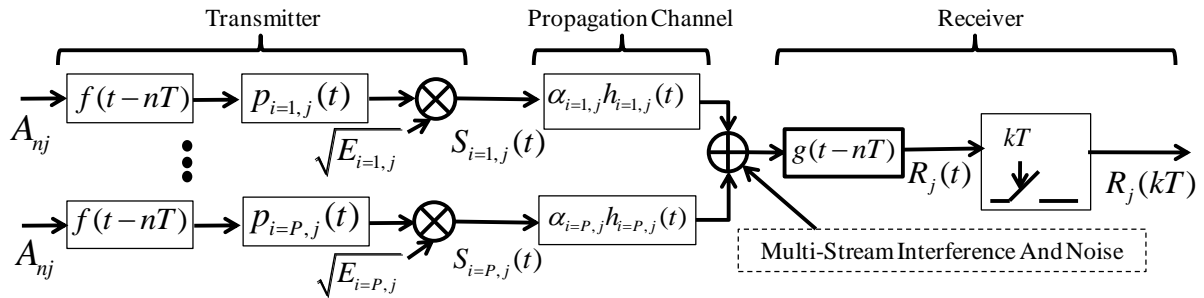


Fig. 4.1.1 System Model

Fig. 4.1.1 illustrates our system model. A downlink Communication between a transmitter with P antennas and N receive antennas is considered. We use the same notations and system model as in the study described in section 3.1.

4.1.2.3 TR pre-filter

The transmitter acquires the TR pre-filter in two steps. In a first phase, the transmitter sends pilots, the receiver estimates downlink channel $h_{i,j}(t)$ perfectly. In a second phase, the receiver feeds $h_{i,j}(t)$ back to the transmitter. The TR pre-filter is modelled as in section 3.1.

4.1.2.4 1Bit TR pre-filter

The transmitter acquires the TR pre-filter in two steps. In a first phase, the transmitter sends pilots. The receiver perfectly estimates $a_{i,j}(t)$:

$$a_{i,j}(t) = h_{i,j}^*(-t). \tag{Eq. 4.1.1}$$

In a second phase, the receiver feeds $a_{i,j}(t)$ back to the transmitter. Then, the transmitter builds the 1bit TR pre-filter as presented in section 3.1.

4.1.2.5 FDD TR pre-filter

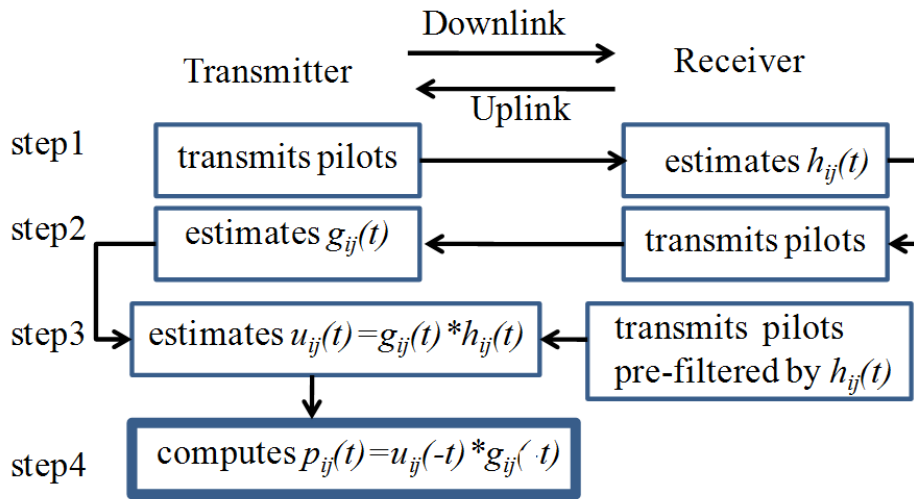


Fig. 4.1.2 FDD TR scheme

The third pre-filter, is the FDD TR pre-filter. Several steps are needed for the transmitter to acquire the FDD TR pre-filter. Fig. 4.1.2 illustrates FDD TR. During Step 1, the receiver sends pilots. The transmitter estimates the uplink channel $g_{i,j}(t)$. During Step 2, the transmitter sends pilots. The receiver estimates the downlink channel $h_{i,j}(t)$. During Step 3: the receiver sends pilots, which are pre-filtered by $h_{i,j}(t)$, which has been estimated at step 1. The pilots are received by the transmitter through an equivalent channel $u_{i,j}(t)$:

$$u_{i,j}(t) = g_{i,j}(t) * h_{i,j}(t). \tag{Eq. 4.1.2}$$

The transmitter estimates $u_{i,j}(t)$ perfectly. Step 4: the transmitter builds the FDD pre-filter $p_{i,j}(t)$:

Eq. 4.1.3

$$p_{i,j}(t) = g_{i,j}(t) * \frac{u_{i,j}^*(-t)}{\sqrt{\mu_{i,j}}},$$

where $\mu_{i,j}$ is a normalizing factor. Eq. 4.1.3 is equivalent to

Eq. 4.1.4

$$p_{i,j}(t) = h_{i,j}^*(-t) * g_{i,j}^*(-t) * \frac{g_{i,j}(t)}{\sqrt{\mu_{i,j}}},$$

Eq. 4.1.5

$$p_{i,j}(t) = \frac{\sum_{k,l,l'}^M h_{i,j,k}^* g_{i,j,l}^* g_{i,j,l'} \delta(-t - \tau_k - \tau_l + \tau_{l'})}{\sqrt{\mu_{i,j}}}.$$

If instantaneous normalization is applied, then we set:

Eq. 4.1.6

$$\mu_{ij} = \sqrt{\sum_{k,l,l'}^M |h_{i,j,k}^* g_{i,j,l}^* g_{i,j,l'}|^2}.$$

If average normalization is applied, then we set:

Eq. 4.1.7

$$\mu_{ij} = E \left[|p_{i,j}(t)|^2 \right] = 1 + \sum_{k=1}^M \sigma_{i,j,k}^4.$$

where $\sigma_{i,j,k}^4 = E[|g_{i,j,k}|^4]$.

Note that, $p_{i,j}(t)$ can be obtained through a process that is slightly longer but easier for interpretation.

First an estimate of the downlink channel $h_{i,j}(t)$ can be obtained by equalising the combined channel

$h_{i,j}(t) * g_{i,j}(t)$ by the time inverse of the uplink channel $\frac{g_{i,j}^*(-t)}{\sqrt{\mu_{i,j}}}$. The result of this estimation is

$h_{i,j}(t) * g_{i,j}(t) * \frac{g_{i,j}^*(-t)}{\sqrt{\mu_{i,j}}}$. Then, this time inverse of the estimation of the downlink channel $h_{i,j}(t)$ can

be used as a prefilter. This prefilter is therefore, given by $h_{i,j}^*(-t) * g_{i,j}^*(-t) * \frac{g_{i,j}(t)}{\sqrt{\mu_{i,j}}}$. One can recog-

nise the expression of $p_{i,j}(t)$ in Eq. 4.1.4.

4.1.3 Post receiver SINR computation

To compute the SINR formula, using the same assumptions and the same models as in section 3.1.

The SINR formula for TR and 1 bit TR are given in section 3.1.

For FDD TR, the signal sampled at $t = KT$ is given by:

$$R_j(KT) = \frac{A_{K,j}}{\mu_{i,j}} \sum_{i=1}^P \alpha_{i,j} \sqrt{E_{i,j}} \sum_{k,k',l,l'=1}^M h_{i,j,k} h_{i,j,k'}^* g_{i,j,l} g_{i,j,l'}^* \rho_f(\tau_{k,k'} + \tau_{l,l'}) + \sum_{n \neq K} \frac{A_{n,j}}{\mu_{i,j}} \sum_{i=1}^P \alpha_{i,j} \sqrt{E_{i,j}} \sum_{k,k',l,l'=1}^M h_{i,j,k} h_{i,j,k'}^* g_{i,j,l} g_{i,j,l'}^* \rho_f((K-n)T + \tau_{k,k'} + \tau_{l,l'}) + \sum_{j' \neq j} \sum_n \frac{A_{n,j'}}{\mu_{i,j'}} \sum_{i=1}^P \alpha_{i,j'} \sqrt{E_{i,j'}} \sum_{k,k',l,l'=1}^M h_{i,j,k} h_{i,j,k'}^* g_{i,j,l} g_{i,j,l'}^* \rho_f((K-n)T + \tau_{k,k'} + \tau_{l,l'}). \quad \text{Eq. 4.1.8}$$

Assuming that multi-stream interference and inter-symbol interference are Gaussian and independent, the expression of the post receiver SINR of user j can be derived as:

$$SINR_j = \frac{Pu_j}{Pisi_j + Pi_j + P_N} \quad \text{Eq. 4.1.9}$$

where Pu_j is the useful power, $Pisi_j$ is the inter-symbol interference power, Pi_j is the multi-stream interference and P_N is the noise power. $P_N = FN_0/T$ where F is the receiver noise figure. For FDD TR, the following equations apply.

$$Pu_j = \left| \sum_{i=1}^P \alpha_{i,j} \frac{\sqrt{E_{i,j}}}{\mu_{i,j}} \sum_{k,k'=1}^M h_{i,j,k} h_{i,j,k'}^* g_{i,j,l} g_{i,j,l'}^* \rho_f(\tau_{k,k'} + \tau_{l,l'}) \right|^2, \quad \text{Eq. 4.1.10}$$

$$Pisi_j = \sum_{n \neq 0} \left| \sum_{i=1}^P \alpha_{i,j} \frac{\sqrt{E_{i,j}}}{\mu_{i,j}} \sum_{k,k'=1}^M h_{i,j,k} h_{i,j,k'}^* g_{i,j,l} g_{i,j,l'}^* \rho_f(nT + \tau_{k,k'} + \tau_{l,l'}) \right|^2, \quad \text{Eq. 4.1.11}$$

Eq. 4.1.12

$$P_{i_j} = \sum_{j' \neq j} \sum_n \left| \sum_{i=1}^P \alpha_{i,j} \frac{\sqrt{E_{i,j'}}}{\mu_{i,j'}} \sum_{k,k',l,l'=1}^M h_{i,j,k} h_{i,j',k'}^* g_{i,j',l} g_{i,j,l'}^* \rho_f(nT + \tau_{k,k'} + \tau_{l,l'}) \right|^2.$$

Finally, the expression of the throughput T_j achieved by the receive antenna j is given by:

Eq. 4.1.13

$$T_j = \frac{\log(1 + \text{SINR}_j)}{T \log(2)}.$$

4.1.4 Feedback analysis

For TR based on perfect channel knowledge we do not consider practical feedback. For 1bit TR, for each couple of transmit antenna i and receive antenna j , we assume that the receiver reports 1bit for $\text{sign}(\Re(h_{ij}(nT)))$, and 1bit for $\text{sign}(\Im(h_{ij}(nT)))$, for $n = 0$ to $\lceil \tau_M/T \rceil$. Thus, the transmitter reports $2(\lceil \tau_M/T \rceil + 1)$ bits for each (i, j) pair. Assuming QPSK and a coding rate of 1/2, i.e. assuming a spectral efficiency of 1bit per symbol duration, the feedback requires $2(\lceil \tau_M/T \rceil + 1)$ symbols to transmit $2(\lceil \tau_M/T \rceil + 1)$ bits. For FDD TR, we assume that pilots are simply a single pulse of symbol duration. For each couple of transmit antenna i and receive antenna j , the transmitter sends a single pulse which is measured over a $\lceil \tau_M/T \rceil$ window by the receiver, during step 1. During step 3, a pre-filtered pulse is sent over $\lceil \tau_M/T \rceil$ symbols, which are measured over $\lceil 2\tau_M/T \rceil$. However, assuming an exponential decay of the power delay profile, it is sufficient to measure the combined channel over $\lceil \tau_M/T \rceil$. Therefore, the time that must be reserved for feedback is $2\lceil \tau_M/T \rceil$ symbols. The difference between the two schemes is that 1bit TR requires coding of $2(\lceil \tau_M/T \rceil + 1)$ bits and transmitting during $2(\lceil \tau_M/T \rceil + 1)$ symbols, while FDD TR does not require the coding of any information, and only requires transmitting during two periods of $\lceil \tau_M/T \rceil$ symbols.

4.1.5 Simulation results

In this sub-section, we use the post receiver SINR formula Eq. 4.1.9 derived in sub-section 4.1.3 to compare the performance of TR, 1bit TR and FDD TR. We set $\alpha_{ij} = 1$. Let E be the transmit power, we define the transmit Signal-to-noise ratio SNR as:

$$SNR = ET/(FN_0).$$

4.1.5.1 32x1 and average normalisation

In this sub-section, a 32x1 system is considered, thus, $P = 32$, $N = 1$. Equal power is allocated to all transmit antennas, thus for every i , $E_{i1} = E/P$. Fading channel coefficients h_{ijk} are generated through simulation using equal Rayleigh Taps channel model, with 1, 2, 4 and 8 Taps. The fast fading channel is normalized, verifying (4). A large number of fading samples are generated, and for each sample, post receiver SINR is computed for various values of the SNR. Finally, the average over all samples of the SINR is plotted as a function of the SNR. Average normalization of the pre-filter, as defined in 4.1.2 and Eq. 4.1.7, has been applied. Thus, in average, the pre-filter power is 1, while it can vary from one fading sample, to the other. Fig. 4.1.3 and Fig. 4.1.6 (a-c) provide curves for TR, 1bit TR and FDD TR respectively, with 1, 2, 4 and 8 Taps respectively. As expected, except for 1 Tap, the SINR saturates at high SNR, due to Inter-Symbol Interference. In addition, pure TR outperforms 1bit TR. FDD TR performs slightly worse than 1 bit TR.

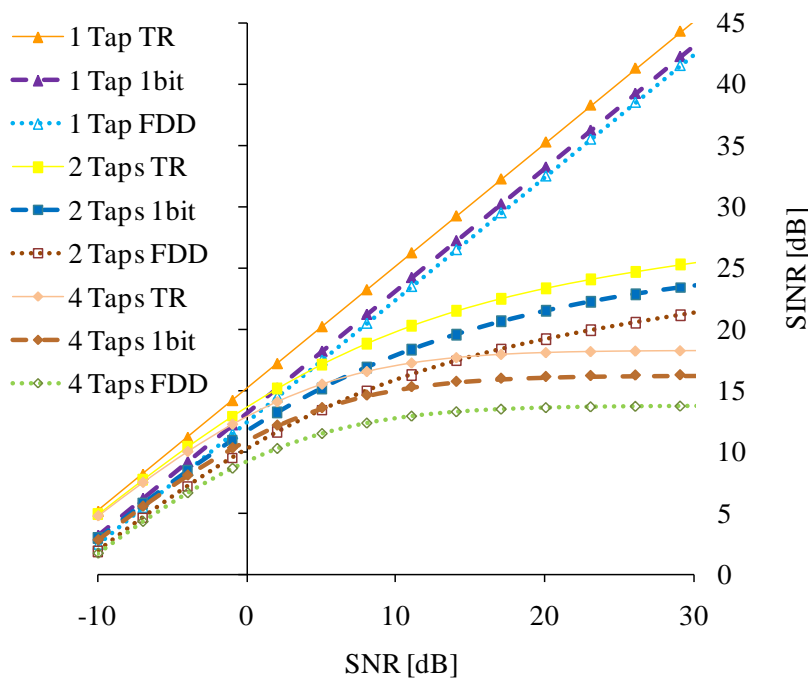


Fig. 4.1.3 32x1, M=1, 2 or 4 Tap(s)

Let us have a closer look at Fig. 4.1.3. First, let us recall that 1bit TR allocates the same power to all taps (in the prefilter). It therefore boosts lower power echoes and increases the inter-symbol interference. FDD TR uses an imperfect estimation of the downlink channel (as explained at the end of section 4.1.2.5). It therefore better reflects the relative powers of the taps, compared to 1bit TR, however not as well as the pure TR. This explains why at high SNR, in Fig. 4.1.3, TR outperforms FDD TR, which outperforms 1bit TR. This also explains why the difference between FDD TR and 1 bit TR is higher with large number of taps. Regarding, the difference between FDD TR and pure TR, it is not

due to inter-symbol interference, as we are considering a single tap channel. It is due to the power allocated to each transmit antenna. Indeed, in FDD TR, the power allocated to each transmit antenna is based on an imperfect estimation of the downlink channel amplitude.

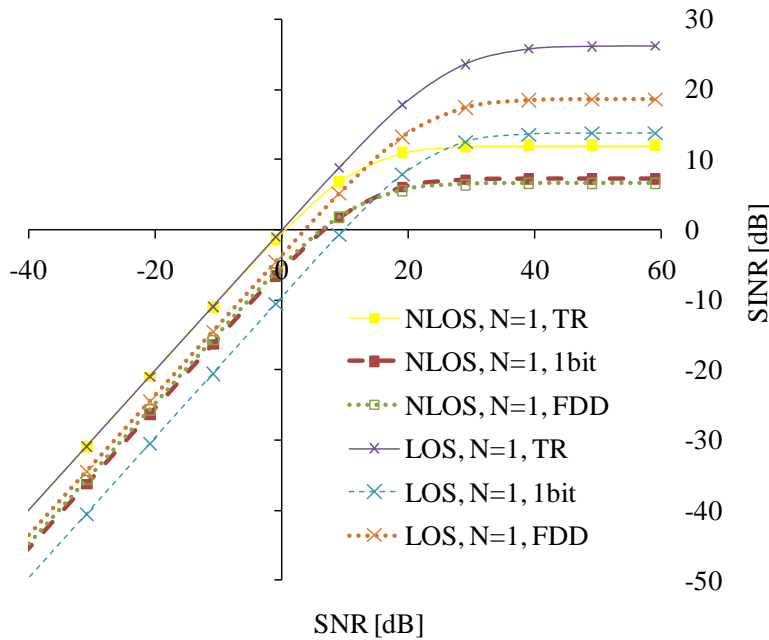


Fig. 4.1.4 32x1 Winner II

Let us have a closer look at Fig. 4.1.4. As already mentioned earlier, 1bit TR increases the amount of inter-symbol interference, compared to FDD TR and pure TR, by boosting low-power echoes in the prefilter. In the ‘LOS’ scenario simulated in Fig. 4.1.4, the channel has low power multiple echoes and a strong dominant LOS component. In such propagation conditions, 1bit TR strongly boosts low power echoes, strongly increases the inter-symbol interference, and therefore strongly degrades the performance. This explains why FDD TR outperforms 1bit TR in the ‘LOS’ scenario. In the ‘NLOS’ scenario simulated in Fig. 4.1.4, the multiple echoes are closer to each other in power value than they are in the ‘LOS’ scenario. In this case, the FDD and 1bit TR have similar performance. They are both outperformed by pure TR because they use an imperfect estimation of the downlink channel.

4.1.5.2 16x2 and Instantaneous Normalisation

In this sub-section, a 16x2 system and a 16x1 system are considered, thus, $P = 16$, $N = 1$ or $N = 2$. Equal power is allocated to all transmit antennas, thus for every i , $E_{i1} = E/(PN)$. Fading channel coefficient h_{ijk} 's are generated through simulation using Winner II indoor channel models. The NLOS and LOS ‘cluster delay line model’ for ‘indoor small office A1’ is used to generate fast fading, which is normalized as in 4.1.2. A linear array of 16 transmit antennas (spaced by half of the wavelength) and two receive antennas is simulated. Spatial correlation is taken into account. The bandwidth is 100MHz (corresponding to $T = 10^{-8}$ seconds). The carrier frequency is 2GHz. A large number of fading sam-

4.1 Frequency division duplex time reversal (FDD TR)

ples are generated, and for each sample, post receiver SINR is computed based on Eq. 4.1.9 and sum throughput over the receive antennas is computed based on Eq. 4.1.13 for various values of the SNR. Finally, the average over all samples of the sum throughput is plotted as a function of the SNR. Instantaneous normalization of the pre-filter, as defined in 4.1.2 and Eq. 4.1.6, has been applied, this time. Thus, the pre-filter power is constant and equal to 1, for each fading sample. We can notice that instantaneous normalization is more practical than average normalization. Fig. 4.1.4 and Fig. 4.1.7 (a)(b), illustrate the post receiver SINR for the 16x1 configuration. Fig. 4.1.5 and Fig. 4.1.8 (a-d), illustrate the post receiver sum throughput for the 16x2 configuration.

Again, as in the previous section, in the 16x1 case, it appears that FDD TR achieves the same performance than 1bit TR in NLOS conditions, and outperforms 1 bit TR in LOS conditions.

In the 16x2 case, where the transmitter focuses onto two receive antennas, in LOS conditions, 1bit TR outperforms TR. This is due to the fact that 1bit TR has better spatial focusing properties than TR especially in these propagation conditions. Indeed, in a LOS scenario, the channel has low power echoes and a dominant strong LOS component. Low power echoes arrive later (than the dominant LOS component) at the receive antenna, with a large angular spread. Thanks to their large angular spread, these low power echoes can help attaining a good spatial focusing, as long as their powers are sufficiently high. As 1bit TR boosts low power echoes it also improves the spatial focusing.

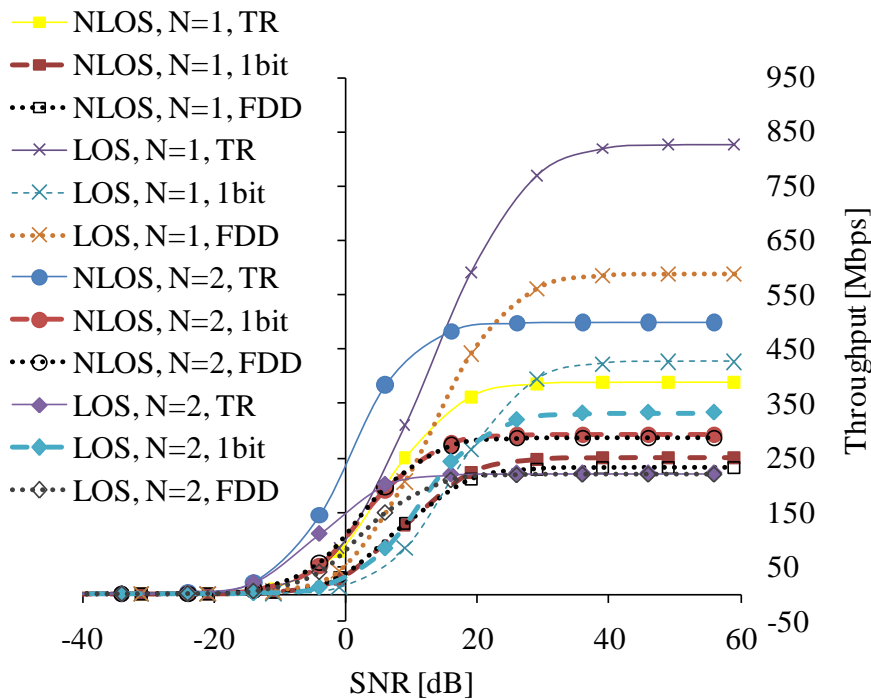
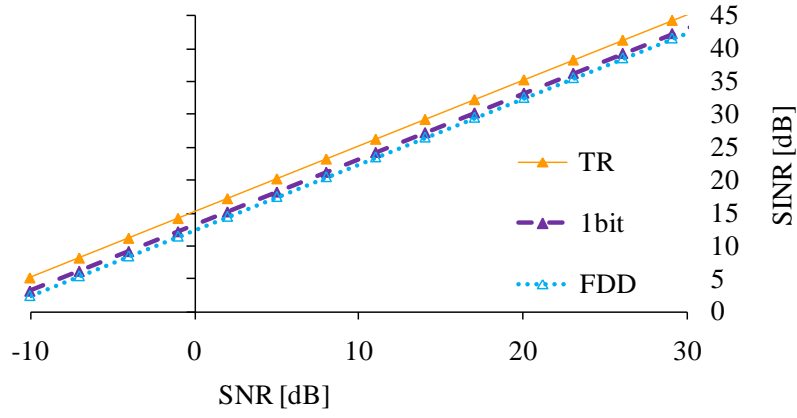
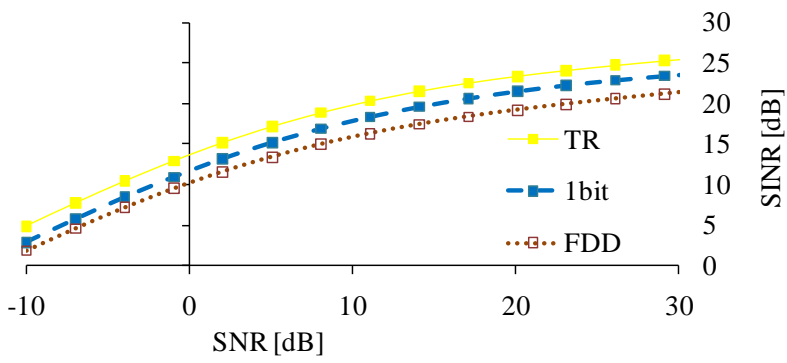


Fig. 4.1.5 16x2 Winner II

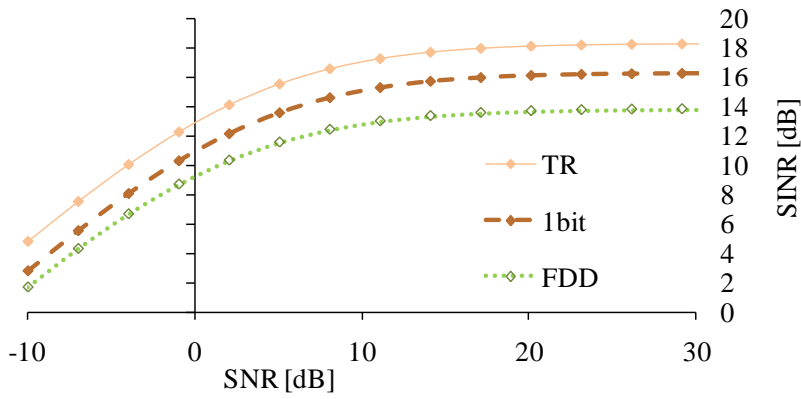
4.1 Frequency division duplex time reversal (FDD TR)



(a) 1 Tap

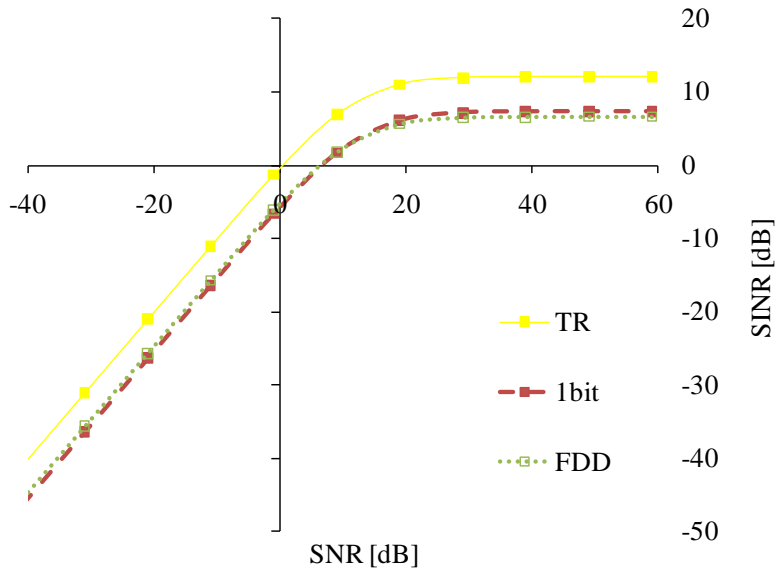


(b) 2 Taps

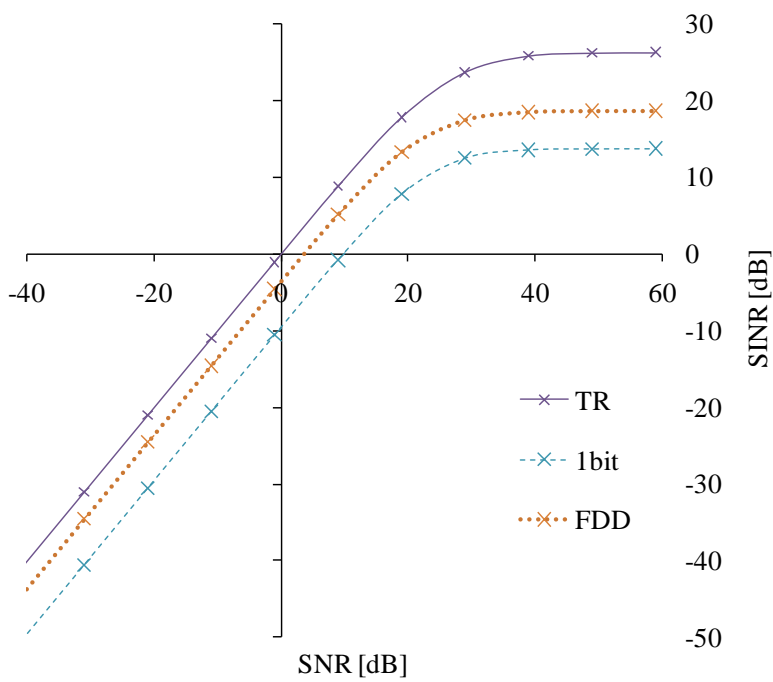


(c) 4 Taps

Fig. 4.1.6 16x1 M Tap



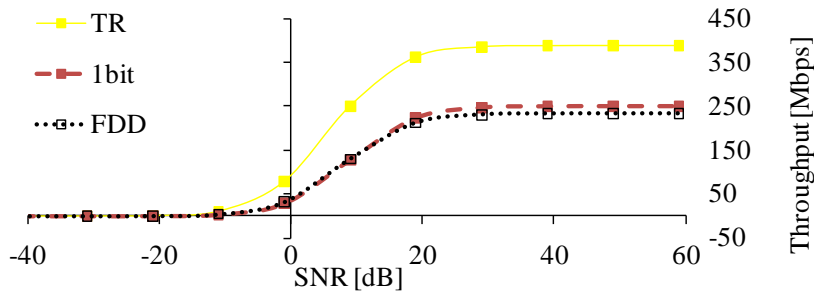
(a) NLOS



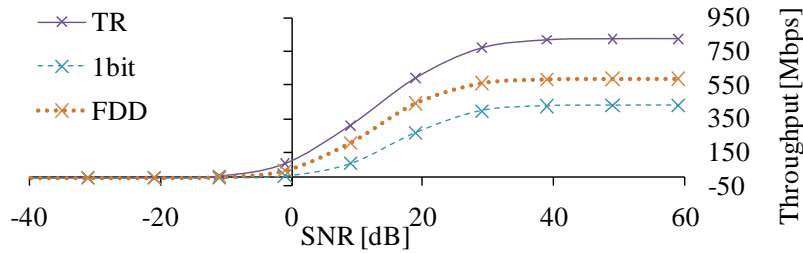
(b) LOS

Fig. 4.1.7 16x1 Winner II

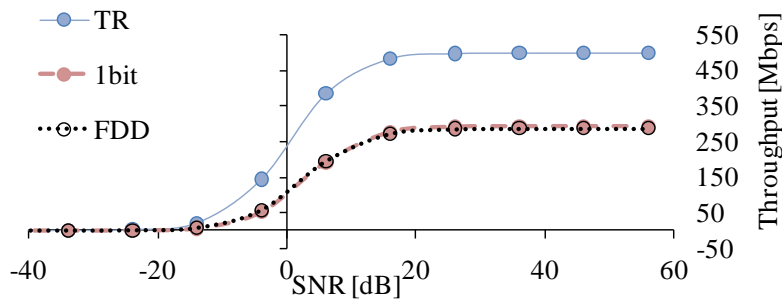
4.1 Frequency division duplex time reversal (FDD TR)



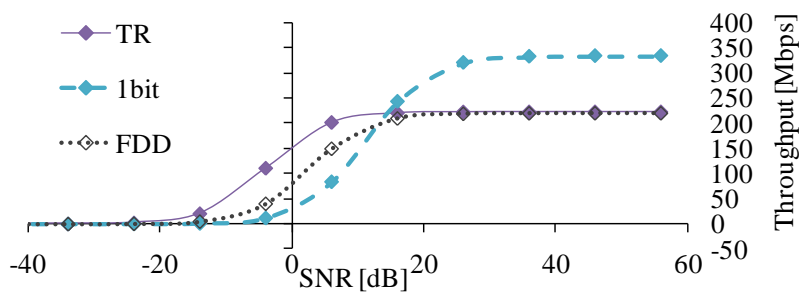
(a) NLOS, N=1



(b) LOS, N=1



(c) NLOS, N=2



(d) LOS, N=2

Fig. 4.1.8 16x2 Winner II

4.1.6 Conclusion

A new scheme, called FDD TR, based on unquantized and uncoded feedback. This scheme simply applies TR to the channel equivalent to propagation through the downlink and uplink channel successively. Assuming, instantaneous normalization of the pre-filtering, FDD TR outperforms 1bit TR in LOS conditions and achieves the same performance in NLOS conditions. In terms of overhead, FDD TR requires less overhead than 1bit TR.

4.2 Time reversal in mobility

4.2.1 Introduction

As explained in section 2, in TDD wireless communications, channel reciprocity and channel state information at the transmitter can be exploited by MISO techniques, such as MRT beamforming (equivalently TR) [8], to achieve a high performance, still with a low complexity [92]. Recent work has shown that very large antenna arrays at the base station have the potential to save energy without performance degradation [92][96][97]. The theoretical energy saving at the base station linearly increases with the number of uncorrelated transmit antennas [96][97], if the beamforming can be performed accurately. These “massive antenna configurations” are currently being studied for the future 5G networks [98].

In a conventional TDD, transmit beamforming system, which we will refer to as “Reference System” (RS), the mobile station sends pilots in the uplink, the base station acquires channel state information at the transmitter to predict the channel, and then computes beamforming weights. Shortly thereafter, the base station transmits data in the downlink using these weights. Thanks to the beamforming, a target SNR can be attained at a lower transmit power, as compared to the single-antenna case.

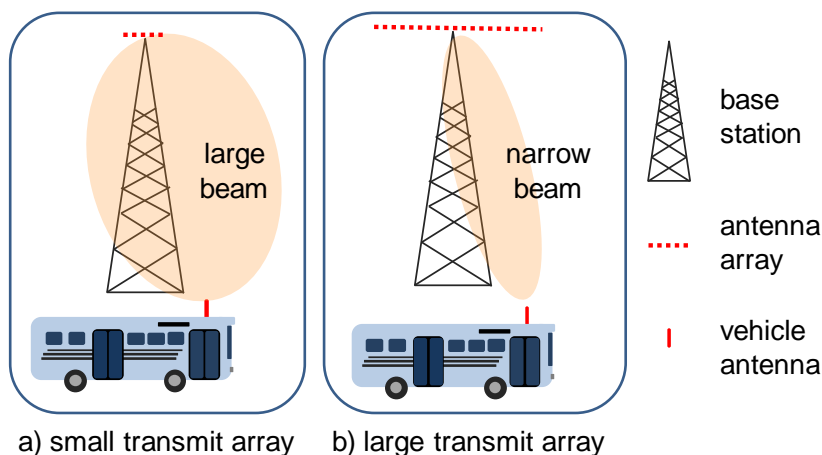


Fig. 4.2.1 Adaptive downlink beamforming towards a vehicle, LOS propagation scenario

There is a time delay between channel estimation and downlink transmission so the channel estimate becomes outdated for a moving terminal. If this time delay were short, it would be no major problem

in an ideal free space LOS propagation environment. An antenna array would then simply form a beam, as illustrated by Fig. 4.2.1. This beam would typically be much wider than the distance the vehicle travels from the time the channel is estimated to the time when the downlink transmission takes place. The transmit beam would then be slightly misplaced due to the time delay, but the receiver antenna on the vehicle would still be positioned well within the beam. In this case, the mispointing of the beam will not affect the performance of the system.

The situation is very different in the common case of a multipath fading environment, where NLOS propagation is significant. In this case, the result of the adaptive transmit beamforming does no longer look like a beam.

If we first consider the particular case where a single antenna at the base station is applying a MRT beamforming weight to its transmission, the net effect of reflections of scattering from multiple objects in the environment on the energy transmitted by an antenna can then be described by a standing wave pattern near the receiver antenna. This pattern has peaks separated by around half a carrier wavelength, as illustrated by Fig. 4.2.2 a. These peaks are in fact a main beam at the target receive antenna surrounded by side beams. In this SISO configuration, the main beam and the side beams have comparable strengths, and no beamforming gain is observed.

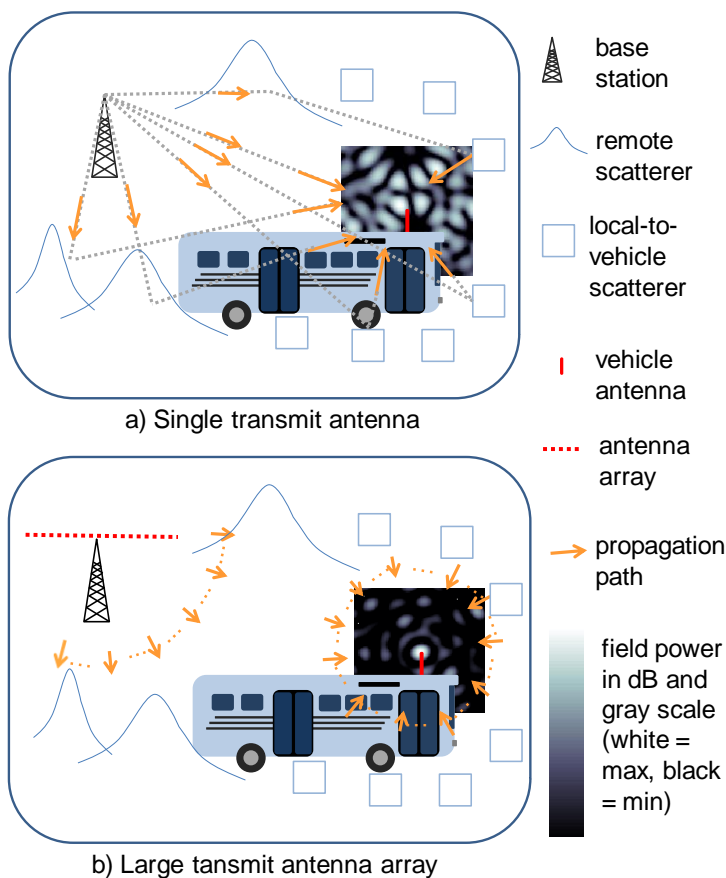


Fig. 4.2.2 Adaptive downlink beamforming towards a vehicle, NLOS propagation scenario.

As illustrated in Fig. 4.2.1, in the MISO case, the phenomenon described for the SISO case in a multipath environment will occur for the transmissions from all transmit antennas in an antenna array, as illustrated by Fig. 4.2.2-b. The MRT beamforming strives to adjust the phases of the signals from all transmit antennas so that the phases add constructively at the precise location of the receiver antenna. This does not result in a clean and regular narrow beam in the area of the target receiver. Instead, the system creates a strong main beam centred on the receiver antenna, surrounded by weak side beams spaced by half a wavelength on average. As a consequence, if the vehicle moves by only a fraction of a carrier wavelength between the time the channel is estimated and the instant when transmission takes place, the receive antenna is off the centre of the main beam. Beamforming mispointing now becomes a problem. Indeed, the signal-to-noise ratio and block error rate (BLER) targets are then not attained. In addition, the effect of mispointing is more severe when the base station antenna array is larger, as confirmed by studies conducted in [99].

Extrapolating previous channel samples using Wiener or Kalman prediction can improve the situation in some scenarios [100][101][102][103]. However, these techniques cannot reliably predict multipath fading channels by more than approximately 0.2-0.3 carrier wavelengths in space. This is inadequate at vehicular velocities for carrier wavelengths above 1 GHz [105][103].

The key challenge that motivates our present work is to develop methods that enable the use of precise channel state information at the transmitter also in such situations, with multipath fading channels rapidly varying in space. This would enable the use of the most advanced transmission models and techniques in our arsenal also for high data rate radio transmission to vehicles.

Recently, motivated by the problem of designing high-performance links to vehicular moving relays, the works [103][105] have introduced the new fundamental concept of “*Predictor Antenna*”. A predictor antenna is positioned on the roof of a vehicle and one or several separate receive antennas are aligned behind the predictor antenna. The vehicle is assumed to move through a stationary electromagnetic standing wave pattern. In other words, the base station creates a static electromagnetic field, and the vehicle simply moves through it. Due to this movement, receive antennas naturally replace the predictor antenna and see the same channel as the predictor antenna, but simply a bit later. Known pilot signals transmitted to the receiver from the predictor antenna can therefore be used to predict the channel of the receive antennas. This generic concept is an enabler for any technique based on channel state information at the transmitter. It is not restricted to Time division duplex and it is applicable to downlink and uplink. Further analysis and experimental validation of the concept with a vehicle in outdoor urban areas has been conducted in [105][107][108][109][109].

Recently, for the particular purpose of large MISO downlink beamforming in TDD, a closely related scheme called Separate Receive and Training Antennas (SRTA) described in the annex 7.2, has fur-

thermore been proposed to achieve high energy efficient wireless downlinks towards very fast moving vehicles. The vehicle roof has one predictor antenna at the front and several “Candidate Antennas” aligned behind. The predictor antenna sends pilots in the uplink and the base station computes beamforming weights. Among the candidate antennas, a “Receive Antenna”, responsible for data demodulation, is dynamically selected among the candidate antennas as a function of the vehicle speed. The TDD frame is also dynamically extended. The receive antenna is selected and the extended frame is computed to ensure that, during the downlink phase, the receive antenna is at the position that was previously occupied by the predictor antenna during the uplink phase. A somewhat similar scheme was proposed in [110]. There, antennas on the vehicle roof were transmitting successively to perform uplink beamforming from a roughly fixed position in space. Current standards support frame extensions with a time granularity of 1 ms. However, with such a coarse granularity, SRTA performance still suffers from residual beamforming mispointing (see details in the annex).

We here propose and investigate two ways to improve SRTA robustness.

- We first investigate a low complexity approach which consists in muting some transmit antennas to widen the beam when mispointing is too severe. Two schemes are studied, denoted the “border Switch Off Scheme” (BSOS) and the “Random Switch Off Scheme” (RSOS).
- We then explore a more complex approach, through the “Polynomial Interpolation” scheme, where all antennas at the vehicle are used as a Predictor Antenna Array, and all of them send uplink pilot symbols. Uplink measurements are collected from the transmission from all antennas during multiple periods, to obtain channel estimates over a dense pattern of positions in space. As these positions surround the position for which the channel must be predicted, polynomial interpolation can be used to provide an accurate estimate of the desired channel component.

Sub-section 4.2.2 presents our generic transmission model. Parameters which are specific to schemes are detailed in sub-section 4.2.3. Sub-section 4.2.4 gives an initial analysis, which is then validated and complemented by simulation results presented in sub-section 4.2.5. Sub-section 4.2.6 concludes the study. The following notations are used throughout the paper: $\vec{v} \in \mathbb{R}^3$ is a vector with Cartesian coordinates; if $u \in \mathbb{R}$, $[u]$ is the integer part of u ; if $u \in \mathbb{C}$, $|u|$ is its module; if $\vec{v} \in \mathbb{R}^3$, $\|\vec{v}\|$ is its norm. $[a, b[= \{x \in \mathbb{R} | a \leq x < b\}$.

4.2.2 Common system model

This sub-section presents common parameters and constrains for the proposed and investigated downlink transmit schemes.

We consider a downlink wireless backhaul link between a base station and a vehicle moving with a velocity vector \vec{v} and speed $v = \|\vec{v}\|$. All investigated schemes use MISO MRT beamforming weights based on channel state information at the transmitter, and target the same signal-to-noise ratio x_T . The required prediction horizon between the acquisition of the channel state information at the transmitter and the data transmission is at least t_0 , with t_0 being the minimum time required for processing at the base station.

4.2.2.1 Antennas and positions at different times

The base station has K transmit antenna(s), each with an index $k \in A_0$, with $A_0 = \{k \in \mathbb{N}, 0 \leq k < K\}$. A subset $A \subseteq A_0$ of K_a antenna(s) is active.

The vehicle has L antenna(s), each with an index $l \in \Lambda$, with $\Lambda = \{l \in \mathbb{N}, 0 \leq l < L\}$. Among these antennas,

- For simplicity of exposition, one antenna called the “receive antenna”, is of interest in the downlink. It is to receive a beamformed downlink transmission that is demodulated and decoded. Furthermore,
- P antenna(s), called “predictor antenna(s)”, each with an index $l \in \Pi$, with $\Pi = \{l \in \mathbb{N}, 0 \leq l < P\}$ is(are) responsible for sending pilots in the uplink.

Let l_a be the index of the receive antenna.

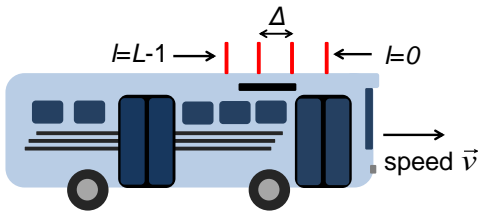


Fig. 4.2.3 Vehicle antennas

As illustrated by Fig. 4.2.3, the antennas of the vehicle are placed on the roof and are spaced by a distance Δ . The antenna positions are aligned with the vehicle direction of travel \vec{v} behind the front antenna (i.e. the antenna with index $l = 0$). Let \vec{n}_l^m and \vec{n}_l^t be the position vectors of the antenna number l at the specific times τ^m and t' (to be defined later on), respectively. We assume that the position vectors \vec{n}_l^m and \vec{n}_l^t satisfy the following conditions:

$$\vec{n}_l^t - \vec{n}_0^t = \vec{n}_l^m - \vec{n}_0^m = -l\Delta v^{-1}\vec{v}, \quad \text{Eq. 4.2.1}$$

$$\vec{n}_l^{t'} - \vec{n}_l^{t^m} = (t' - t^m)\vec{v}. \quad \text{Eq. 4.2.2}$$

We define $\vec{\alpha}$ as the position of the front antenna of the vehicle at time τ^0 . With this notation, we can write:

$$\vec{\alpha} = \vec{n}_0^0. \quad \text{Eq. 4.2.3}$$

We define $\vec{\varepsilon}$ as the position of the receive antenna (i.e. the antenna with index $l = l_a$) at time t' . With this notation, we can write:

$$\vec{\varepsilon} = \vec{n}_{l_a}^{t'}. \quad \text{Eq. 4.2.4}$$

4.2.2.2 Static Spatially Correlated Channel Model

The vehicle is assumed to be moving in a time-invariant and spatially correlated fading propagation channel, which will be further described in sub-section 4.2.5.1. This assumption has been verified experimentally in [105][107][108][109][109]. Measurement-based investigations [109] have shown that a very high correlation can be obtained between the propagation channel from/to two antennas on a vehicle that at different time instants move through the same position. In this study, we assume that the two channels seen by two antennas successively occupying the same position in space are exactly equal.

OFDM is assumed. Hence, for a given sub-carrier and OFDM symbol, the channel gain between base station antenna k and any antenna at position \vec{n} can be modeled by a complex coefficient $g_k(\vec{n})$.

4.2.2.3 Channel prediction and beamforming

We consider a TDD frame, with uplink and downlink periods $[-\tau^{UL}, 0[$ and $[0, \tau^{DL}[$, respectively.

Both the acquisition of the channel state information at the transmitter and the beamforming operation are performed on a per OFDM symbol and sub-carrier basis. For each transmitted downlink data symbol, sub-carrier and antenna k , the base station computes a beamforming weight based on one or several channel coefficient(s) measurement(s). Therefore, the base station applies two distinct beamformers to two consecutive symbols of the same frame.

Such a tight adaptation of the transmission to the current channel condition is useful for extremely high speeds or extremely large frames. However, it is un-necessarily complex for lower speeds. In practice, the frequency for the update of beamforming coefficients in the time domain and frequency domain would be optimized according to the channel coherence time and the channel coherence bandwidth, respectively.

It is assumed that for each sub-carrier, downlink data symbol and antenna, the same procedure is run. The following mathematical description is therefore valid for any sub-carrier, downlink data symbol and antenna number $k \in K_a$.

We consider the transmission of a downlink data symbol at time $t' \in [0, \tau^{DL}[$. The base station transmits the considered data symbol using the pre-computed prediction γ_k of the channel coefficient $g_k(\vec{e})$ from transmit antenna k . This prediction is used to send the data with the MRT beamforming [8][92] weight p_k . It equals the scaled complex conjugate of the predicted channel coefficient:

$$p_k = \gamma_k^* \sqrt{E}, \quad \text{Eq. 4.2.5}$$

where $E > 0$ is a transmit power scaling factor, equal for all antennas.

We constrain the prediction γ_k to be computed based on a set of channel measurement(s) C_k . C_k is defined as the set of measurements performed for each of the $P \geq 1$ predictor antenna(s) and at $M \geq 1$ different times during the uplink frame. By definition, C_k always contain $N_{meas} = \text{card}(C_k) = P \times M \geq 1$ measurements. We define $\tau^m \in [-\tau^{UL}, 0[$ as the measurement time number m , with $m \in \Gamma = \{m \in \mathbb{N}, 0 \leq m < M\}$. With this notation, $C_k = \{\hat{g}_k(\vec{n}_l^m) \mid m \in \Gamma, l \in \Pi\}$, where $\hat{g}_k(\vec{n}_l^m)$ is the measurement of $g_k(\vec{n}_l^m)$ performed by the base station for the predictor antenna number l at the time τ^m .

We define the prediction horizon δ^m associated with the measurement performed at time τ^m as the delay between

- the time t' when the prediction γ_k is used for the transmission of the considered data symbol and
- the time τ^m when the channel measurement is performed before being used for the prediction γ_k .

We constrain the prediction horizon δ^m to satisfy:

$$\delta^m = t' - \tau^m \geq t_0. \tag{Eq. 4.2.6}$$

Finally, we assume that measurements are perfect and noiseless:

$$\hat{g}_k(\bar{n}_l^m) = g_k(\bar{n}_l^m). \tag{Eq. 4.2.7}$$

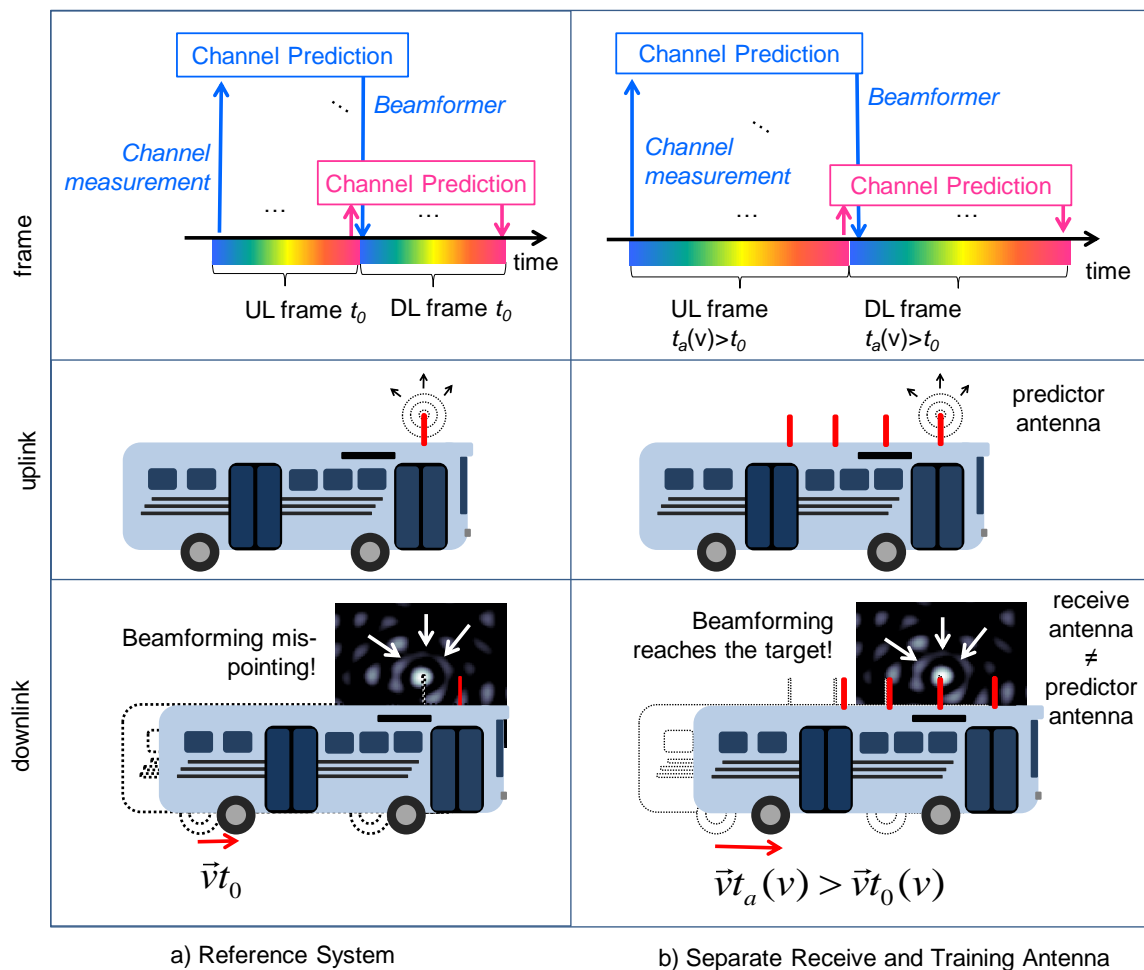


Fig. 4.2.4 RS and SRTA systems. Distinct beamformers are computed for distinct times during the downlink frame. Each beamformer is based on a distinct channel measurement performed during the uplink frame. All channel measurements go through the same procedure and undergo the same processing delay before being converted into beamformers. a) In the RS system, during the delay between the channel measurement and the data transmission, the vehicle moves by a displacement $\vec{v}t_0$. This causes beamforming mis-pointing to occur. b) In the SRTA system, during the during the delay between the channel measurement and the data transmission the vehicle moves by a displacement which is $\vec{v}t_a(v)$ compensated by the use of a predictor antenna which is distinct from the receive antenna. In this case, mispointing is avoided.

4.2.2.4 Signal-to-noise ratio and energy saving metrics

To save energy, the BS computes the required transmit power scaling factor E that is exactly necessary to attain a target signal-to-noise ratio x_T . Since $x_T N_0$ is the total received power per unit bandwidth,

$$x_T = \frac{|\sum_{k \in A} \gamma_k p_k|^2}{N_0} = \frac{E |\sum_{k \in A} |\gamma_k|^2|^2}{N_0}, \quad \text{Eq. 4.2.8}$$

where N_0 is the noise power per unit bandwidth at the receiver and where Eq. 4.2.5 was used in the last equality. The target transmit power scaling factor E is obtained from Eq. 4.2.8. as

$$E = x_T N_0 |\sum_{k \in A} |\gamma_k|^2|^{-2}. \quad \text{Eq. 4.2.9}$$

In current standards [112], the subcarrier spacing is large enough so that inter carrier interference can be neglected even for high speed. Therefore, the approximated achieved signal-to-noise ratio metric x is:

$$x = \frac{|\sum_{k \in A} g_k(\vec{\epsilon}) p_k|^2}{N_0} = \frac{E |\sum_{k \in A} g_k(\vec{\epsilon}) \gamma_k^*|^2}{N_0}. \quad \text{Eq. 4.2.10}$$

By inserting Eq. 4.2.9 into Eq. 4.2.10, we obtain:

$$x = x_T |\sum_{k \in A} g_k(\vec{\epsilon}) \gamma_k^*|^2 |\sum_{k \in A} |\gamma_k|^2|^{-2}. \quad \text{Eq. 4.2.11}$$

We define the energy saving metric e_S as the energy required by a SISO system divided by the energy required by the studied MISO system, for the same target signal-to-noise ratio x_T . This metric is a multiplicative factor. It measures how much less energy is consumed at the BS thanks to the use of a MISO system with a set A of base station antennas instead of a SISO system that uses only antenna $k = 0$. For instance, if $e_S = 2$, this then means that the BS uses twice less energy in MISO than in SISO. The required transmit power per unit bandwidth for a SISO system with one transmit antenna is, by Eq. 4.2.5 and Eq. 4.2.9, $|p_0|^2 = |\gamma_0|^2 E = |\gamma_0|^2 x_T N_0 |\gamma_0|^{-4} = x_T N_0 |\gamma_0|^{-2}$. For a MISO system with a set A of base station antennas, the required transmit power per unit bandwidth is $\sum_{k \in A} |p_k|^2 = (\sum_{k \in A} |\gamma_k|^2) E = (\sum_{k \in A} |\gamma_k|^2) x_T N_0 |\sum_{k \in A} |\gamma_k|^2|^{-2} = x_T N_0 |\sum_{k \in A} |\gamma_k|^2|^{-1}$. The attained energy saving for a MISO system therefore equals:

$$e_S = \frac{|p_0|^2}{\sum_{k \in A} |p_k|^2} = \sum_{k \in A} |\gamma_k / \gamma_0|^2. \quad \text{Eq. 4.2.12}$$

4.2.2.5 Beamforming mispointing effect

The signal-to-noise ratio metric x and the energy saving metric e_S depend on the channel estimate γ_k and the actual channel $g_k(\vec{\epsilon})$ only. If the prediction is accurate (i.e. if the channel estimate γ_k equals the actual channel $g_k(\vec{\epsilon})$), then Eq. 4.2.11 reduces to $x = x_T$, i.e. the signal-to-noise ratio target is met. Otherwise, beamforming mispointing occurs and the signal-to-noise ratio x is expected to be smaller than the target value x_T .

4.2.3 Systems specific models

The investigated schemes differ by the values of the parameters K_a , A_0 , M , P , L , τ^{UL} , τ^{DL} , δ^m , and l_a previously introduced in Sub-section 4.2.2, the prediction γ_k and the resulting performance metrics x and e_S .

4.2.3.1 Reference System (RS)

For RS, all antennas at the BS side are used. At the vehicle side, a single antenna is used both for prediction and for data reception. The UL/DL frames are set equal to a fixed value denoted t_0 . A single measurement from the PA is used for prediction, with a prediction horizon δ^0 between the channel estimation and the data transmission is equal to the frame duration.

Using the previously defined notations, the number of active antennas K_a equals K , the set of active antennas A is A_0 , the number of antennas on the vehicle L equals 1, the number of predictor antennas P equals 1, the index l_a of the receive antenna equals 0, the uplink/downlink frames durations are $\tau^{DL} = \tau^{UL} = t_0$, the number of measurement times M equals 1, the prediction horizon δ^0 between the channel estimation and the data transmission is $\delta^0 = t_0$. With these assumptions, Eq. 4.2.3 and Eq. 4.2.7, we use a simple extrapolation in time of the present channel estimate as channel predictor:

$$\gamma_k = g_k(\vec{\alpha}), \quad \text{Eq. 4.2.13}$$

The signal-to-noise ratio metric x and the energy saving metric e_S are then derived using Eq. 4.2.1-Eq. 4.2.6 and Eq. 4.2.10-Eq. 4.2.12:

$$x = \frac{|\sum_{k \in A_0} g_k(\vec{\alpha} + t_0 \vec{v}) g_k^*(\vec{\alpha})|^2}{|\sum_{k \in A_0} |g_k(\vec{\alpha})|^2|^2} x_T, \quad \text{Eq. 4.2.14}$$

$$e_S = \left| \sum_{k \in A_0} |g_k(\vec{\alpha})/g_0(\vec{\alpha})|^2 \right|^2. \quad \text{Eq. 4.2.15}$$

One can note that the signal-to-noise ratio metric x is speed-dependent whereas the energy saving metric e_S remains constant. At low speed, the signal-to-noise ratio is met whereas at high speed, mispointing occurs and we expect the signal-to-noise ratio to be below the target value x_T .

Fig. 4.2.4-a illustrates the RS operation and the resulting beamforming mispointing effect.

4.2.3.2 Separate Receive and Training Antennas (SRTA)

This sub-section briefly describes the SRTA scheme detailed in sub-section 7.2. As for RS, all transmit antennas are used, and the uplink/downlink frames are equal. Prediction relies on a single measurement from a single predictor antenna, with a prediction horizon equal to the frame duration. The base station and the vehicle are assumed to have a perfect estimate of the speed using e.g. the Global Positioning System (GPS).

As illustrated in Fig. 4.2.4, SRTA avoids mispointing by selecting dynamically, and according to speed, an extended frame and the receive antenna is selected among several candidate antennas located behind the predictor antenna, to ensure that the receive antenna is at the previous position of the predictor antenna.

As for RS, the number of active antennas K_a equals K , the set of active antennas A is A_0 , the number of predictor antennas P equals 1, the predictor antenna is the front antenna (with index $l=0$), the number of measurement times M equals 1.

Contrary to RS, the number of antennas on the vehicle L is strictly higher than 1, the frame duration $\tau^{DL} = \tau^{UL}$ and the corresponding prediction horizon δ^0 equal a speed-dependent function $t_a(v)$ which is always strictly higher than t_0 . The index of the receive antenna l_a equals a speed-dependent function $r_a(v)$.

The vehicle signals to the base station the antenna index $r_a(v)$ and the extended frame duration $t_a(v)$. $t_a(v)$ defines the new prediction horizon. $r_a(v)$ and $t_a(v)$ are selected by the vehicle to ensure that $\vec{\varepsilon} \approx \vec{\alpha}$.

In current standards [112], frames are adaptive by steps (such as sub-frames or slots) of constant size d . Sub-section 7.2 details the choices of $r_a(v)$, $t_a(v)$ and $\vec{\varepsilon}$ as functions of d :

$$r_a(v) = \min\{l \in \Lambda \mid [l\Delta(dv)^{-1}]d > t_0\}, \quad \text{Eq. 4.2.16}$$

$$t_a(v) = [r_a(v)\Delta v^{-1}d^{-1}]d, \quad \text{Eq. 4.2.17}$$

$$\rho(v) = [r_a(v)\Delta(dv)^{-1}]dv - r_a(v)\Delta, \quad \text{Eq. 4.2.18}$$

$$\vec{\varepsilon} = \vec{\alpha} + \rho(v)v^{-1}\vec{v}. \quad \text{Eq. 4.2.19}$$

The relation Eq. 4.2.17 above ensures that Eq. 4.2.13 is attained for speeds up to v_{max} , given by $v_{max}=(L-1)\Delta|t_0|^{-1}$. The prediction in this case is, as for RS: $\gamma_k = g_k(\vec{\alpha})$.

Finally, the signal-to-noise ratio metric x and the energy saving metric e_S are derived in as follows:

$$x = \frac{|\sum_{k \in A_0} g_k(\vec{\alpha} + \rho(v)v^{-1}\vec{v})g_k^*(\vec{\alpha})|^2}{|\sum_{k \in A_0} |g_k(\vec{\alpha})|^2|^2} x_T, \quad \text{Eq. 4.2.20}$$

$$e_S = \left| \sum_{k \in A_0} |g_k(\vec{\alpha})/g_0(\vec{\alpha})|^2 \right|^2. \quad \text{Eq. 4.2.21}$$

As for RS, the signal-to-noise ratio metric x is speed dependent and the energy saving metric e_S is constant.

For $v \in V$, (with $V = \{u = \Delta(dp)^{-1} \mid p \in \llbracket 1, L-1 \rrbracket\}$) the signal-to-noise ratio x equals the target value x_T and mispointing is canceled. In other words, at a discrete set of speeds belonging to V , the channel aging is “perfectly compensated”.

For $v \notin V$, due to the granularity d (see sub-section 7.2), the signal-to-noise ratio x is different from the target value x_T , and most of the time lower. In other words, a speed $v \notin V$ is a “non perfectly compensated” speed. In this case, the SRTA system suffers from a residual mispointing.

4.2.3.3 SRTA with Switch Off Scheme (SOS)

SOS is used on top of SRTA, to reduce the degradation in terms of signal-to-noise ratio and block error rate due to residual beamforming mispointing for the “non perfectly compensated” speeds identified in sub-section 4.2.3.2. SOS detects mispointing and switches off antennas at the base station with the aim to strengthen the side beams relatively to the main beam in the area of the target receiver.

As illustrated in Fig. 4.2.5, SOS does not cancel the residual mispointing, (i.e. the distance between the target beamforming position and the actual receive antenna position), however it reduces the signal-to-noise ratio degradation.

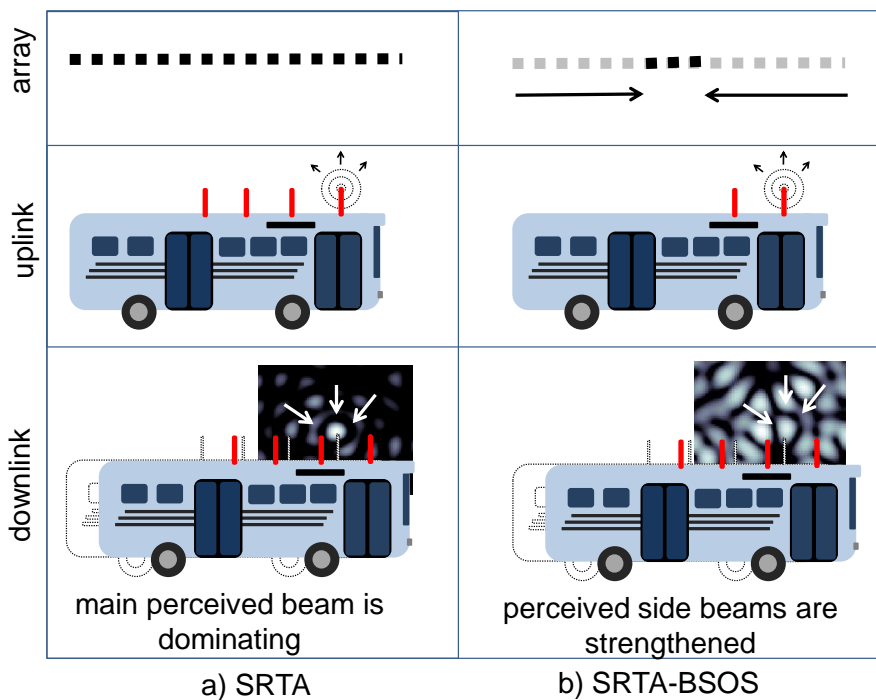


Fig. 4.2.5 SRTA and SRTA-BSOS systems. a) in SRTA system, residual beamforming mispointing occurs for the considered speed. The target antenna receives the data with a weak power. b) in the SRTA-BSOS system, multiple side lobes are strengthened to give more opportunities for the target antenna to receive the data with a high power.

SOS is a closed loop mechanism. Initially, SRTA is run with $K_a = K$ antennas. The vehicle assesses the achieved signal-to-noise ratio and compares it to a threshold (in our evaluations corresponding to a 20% block error rate). If the signal-to-noise ratio is lower than the threshold, then the vehicle sends a feedback message to the base station, the base station switches off half of its antennas ($K_a = K_a/2$) and updates A . Then, SRTA is run again, with the new K_a and A parameters. K_a is divided by 2, successively, until the signal-to-noise ratio threshold is exceeded. If the signal-to-noise ratio increases over a threshold, then antennas are added so the beam is narrowed. The achieved signal-to-noise and energy saving are obtained by using Eq. 4.2.20, Eq. 4.2.21 with A instead of A_0 :

$$x = \frac{|\sum_{k \in A} g_k(\vec{\alpha} + \rho(v)v^{-1}\vec{v})g_k^*(\vec{\alpha})|^2}{|\sum_{k \in A_0} |g_k(\vec{\alpha})|^2|^2} x_T, \quad \text{Eq. 4.2.22}$$

$$e_S = \left| \sum_{k \in A} |g_k(\vec{\alpha})/g_0(\vec{\alpha})|^2 \right|^2. \quad \text{Eq. 4.2.23}$$

Here, the energy saving metric e_S is lower than for SRTA when A is smaller than A_0 .

Two variants of the scheme are investigated:

- SRTA Random SOS (SRTA-RSOS), which reduces the number of utilized transmit antennas without giving any preference to specific antenna positions.
- SRTA-Border SOS (SRTA-BSOS), which removes the antenna elements at the outer parts of the linear array from use in transmission, and thus reduces the array aperture.

In a pure LOS propagation scenario, as illustrated in Fig. 4.2.1, the width of the transmit beam as perceived by the receiver decreases with the transmit array aperture. In this case, one should use SRTA-BSOS.

In a NLOS scenario, as illustrated in Fig. 4.2.2, the base station aperture as perceived by the receive antenna is no longer defined by its array size. Indeed, due to the scattering, the receive antenna sees rays arriving from many directions. In this case, there is no reason to switch off border antennas more than any other, and SRTA-RSOS might give similar or even better performance.

4.2.3.4 SRTA with Polynomial Interpolation (SRTA-PI)

As RS and SRTA, SRTA-PI uses $K_a = K$ transmit antennas at the base stations.

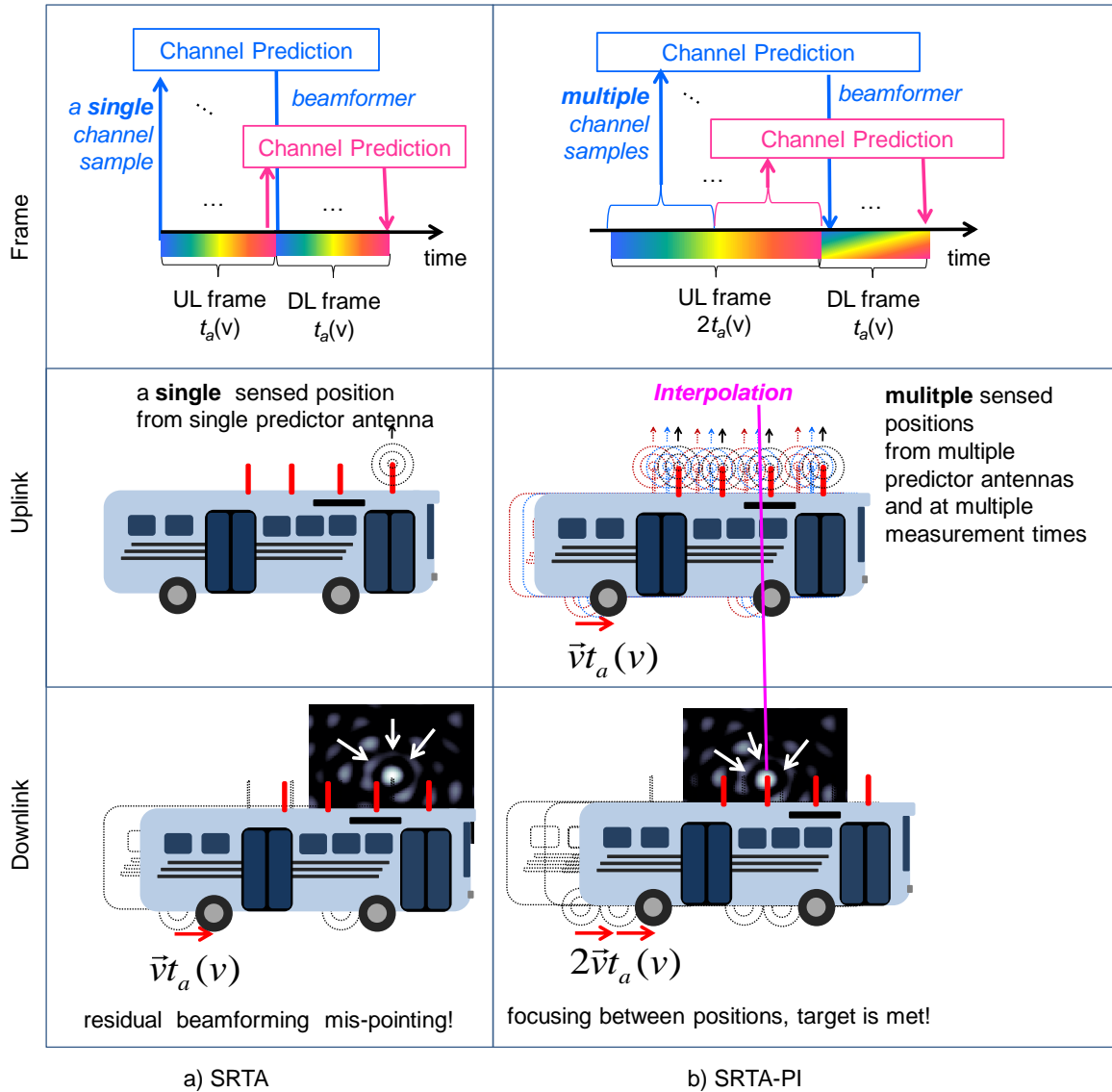


Fig. 4.2.6 SRTA and SRTA-PI systems. a) In SRTA system, for the considered speed, residual beamforming mis-pointing occurs and the beamformer ‘misses’ the receive antenna (the first antenna behind the front antenna). b) in the SRTA-PI system, several channel measurements collected over a duration of $t_a(v)$, and coming from several predictor antennas are collected and interpolated to predict the channel and beamform over the exact position of the new receive antenna (the second antenna behind the front antenna).

As illustrated by Fig. 4.2.6, SRTA-PI is based on SRTA, and mitigates mispointing by focusing “between” several “sensed” positions of the predictor antennas instead of focusing “over” a single position. As illustrated in Fig. 4.2.7, multiple measurements are collected by multiple predictor antennas, at multiple specific measurement times to obtain a dense pattern of measurements in space. Then, polynomial interpolation is applied to these measurements to predict the channel at the future position of the receive antenna. Contrary to all the previous discussed schemes, the number of measurement times M , the number of vehicle L and predictor antennas P are all strictly higher than 1.

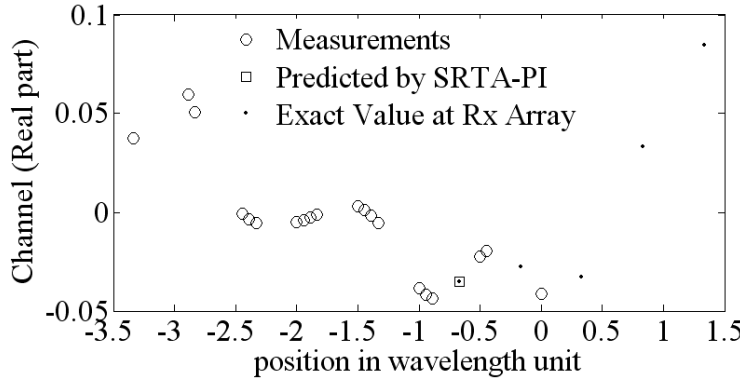


Fig. 4.2.7 SRTA-PI, one channel realization at 240kmph. The real part of the channel measurements, cumulated over predictor antennas and measurement times, are plotted. Each measurement is plotted as a function of the corresponding sensed position in space. The exact values of the channel coefficients of five antennas of the vehicles at the data transmission time are also plotted. One can observe that the channel predicted for the 5th antenna obtained by interpolation of the measurements, perfectly matches the exact value.

As for all previous presented schemes, we keep the constrain of having exactly the same procedure being applied per data symbol and sub-carrier, with the same prediction horizon. To that aim we impose the downlink frame duration to be half the uplink frame duration: $\tau^{DL}=0.5 \tau^{UL}$. As illustrated by Fig. 4.2.6, all data symbols go through the same procedure. Though this procedure involves several distinct measurement times τ^m and several associated distinct prediction horizons $\delta^m = t' - \tau^m$, we constrain the prediction horizon δ^m to be the same for any t' . As illustrated by Fig. 4.2.6, the prediction is based on measurements collected during τ^{DL} seconds and at least τ^{DL} seconds before beamforming is considered. The prediction horizon δ^m therefore varies between τ^{DL} and $2\tau^{DL}$.

As for SRTA, the downlink frame duration is extended compared to the RS frame: $\tau^{DL}=t_a(v)>t_0$. The extended frame duration $t_a(v)$ and the index $r_a(v)$ are computed using Eq. 4.2.16, Eq. 4.2.17. The index l_a of the receive antenna is then derived as follows:

$$l_a = r_a(v) + 1. \tag{Eq. 4.2.24}$$

The set C_k of channel measurements is defined as follows. The measurement $\hat{g}_k(\overline{n}_t^m)$ performed at time τ^m belongs to the set C_k if and only if it satisfies the following conditions:

$$\begin{aligned} \delta^m &= t_a(v) + d.p, p \in \mathbb{N} \text{ and} \\ \delta^m &\leq 2t_a(v). \end{aligned} \tag{Eq. 4.2.25}$$

The polynomial interpolation is performed as follows. For each channel measurement $\hat{g}_k(\overline{n}_l^m)$ belonging to C_k , the base station stores the couple constituted of the channel measurement $\hat{g}_k(\overline{n}_l^m)$ and the corresponding “sensed” position n_l^m (where $n_l^m \in \mathbb{R}$ is the scalar coordinate corresponding to \overline{n}_l^m , along the vehicle short term linear trajectory). Then, the relations Eq. 4.2.17 to Eq. 4.2.19 are used to predict the position $\vec{\varepsilon}$ (and its equivalent scalar coordinate ε) of the selected receive antenna. Finally, the base station performs polynomial interpolation over the stored couples, with the position ε and channel γ_k as the input and output of the interpolation operation, respectively.

One can note that Eq. 4.2.25 is feasible for all data symbols, i.e. for all $t' \in [0, \tau^{DL}]$, if τ^{UL} satisfies :

$$\tau^{UL} = 2\tau^{DL} = 2t_a(v). \quad \text{Eq. 4.2.26}$$

In other terms, the uplink frame needs to be twice larger than the downlink frame to ensure an identical processing and performance for all symbols of the downlink frame.

The relation Eq. 4.2.24 guarantees that the position $\vec{\varepsilon}$ is between at least two stored “sensed” positions. This enables the system to avoid extrapolation, which is less reliable than interpolation.

The number N_{meas} of measurements involved in the prediction of one channel coefficient is given by:

$$N_{meas} = L[t_a(v)d^{-1}] \geq L. \quad \text{Eq. 4.2.27}$$

Polynomial interpolation is performed for the real and imaginary parts of the channel separately, with order $N_{meas} - 1$. This number of measurements N_{meas} is a critical parameter as the complexity of the polynomial interpolation increases with it. On one hand, the measurements used for one channel prediction are collected during the duration $t_a(v)$. On the other hand, the duration $t_a(v)$ increases with the speed, due to Eq. 4.2.17. As a consequence, the number of measurements N_{meas} increases when the speed decreases. Consequently, at low v , where SRTA is already sufficient (see sub-section 4.2.3.2), the SRTA-PI scheme is the most complex.

To avoid un-necessary complexity, we therefore trigger polynomial interpolation for speeds larger than a predefined threshold v_{PI} . For speeds lower than v_{PI} , SRTA will be used instead.

The signal-to-noise ratio metric x and the energy saving metric e_S are derived using equations Eq. 4.2.11, 4.2.12, and using the prediction γ_k obtained after polynomial interpolation.

4.2.4 Initial comparison of the studied schemes

Parameter	RS	SRTA	SRTA BSOS/RSOS	SRTA-PI
τ^{DL}	t_0	$t_a(v) > t_0$		
δ^m	t_0	$t_a(v)$		$\in [t_a(v), 2t_a(v)]$
τ^{UL}/τ^{DL}	1		2	
K_a	K		$\leq K$	K
L	1	> 1		
l_a	0	$r_a(v)$		$r_a(v) + 1$
P	1		L	
M	1		> 1	
N_{meas}	1		$\geq L$	
Best x	4	3	2	1
Best e_S	1	1	2	1
Most Simple	1	2	3	4

Table 4.2.1 Parameters and expected ordering

Table 4.2.1 gives an overview of the values of the parameters and an initial comparison, based on the mathematical expressions given in sub-section 4.2.3, such as Eq. 4.2.14, Eq. 4.2.15, Eq. 4.2.20 and Eq. 4.2.21.

Regarding the prediction horizon δ^m , all SRTA schemes outperform RS by allowing higher values, thanks to the extended and speed-dependent downlink frame $t_a(v)$ (defined by Eq. 4.2.17) which exceeds the RS fixed value t_0 .

Regarding energy efficiency, the two SOS schemes may use a lower number K_a of active antennas, and are then expected to save less energy than RS and SRTA schemes.

Regarding the complexity, SRTA is more complex than RS as it implies the dynamic adaptation of the frame duration and the indexes of the predictor and the receive antenna. The SRTA-BSOS and SRTA-RSOS schemes are slightly more complex as they adapt the transmit array size to the speed. SRTA-PI which performs polynomial interpolation of $N_{meas} > 1$ measurements collected for multiple predictor antennas ($P > 1$) at multiple times ($M > 1$) is probably the most complex of all the studied schemes.

Regarding the robustness to speed of the achieved signal-to-noise ratio and the block error rate, RS should be the worst scheme as it will always suffer from beamforming mispointing. SRTA cancels

mispointing for “perfectly compensated speeds” only, and should therefore be the 2nd best scheme. SOS schemes enhance SRTA for “non perfectly compensated” speeds, and should be the 3rd bests. Finally, SRTA-PI completely cancels mispointing for all speeds and should hence be the best of all schemes.

4.2.5 Performance comparison

4.2.5.1 Simulation assumptions and methodology

The following simulation assumptions are used: $t_0 = 2\text{ms}$ [112]; the carrier frequency f_0 is 2GHz; the wavelength is $\lambda = c/f_0$; where $c = 3 \cdot 10^8$ m/s is the speed of light; the base station has a linear array with $K = 64$ antennas separated by 0.5λ . In SRTA and SRTA-BSOS/RSOS the vehicle has $L = 4$ antennas separated by Δ , with $\Delta = 0.5\lambda$. For SRTA-PI, $L = 5$. The time step for frame extension is $d = 1$ ms, which is feasible in current standards [112]. It is also used for SRTA-PI measurements selection in Eq. 4.2.25. The vehicle speed v ranges from 0 to 300kmph. The target SNR is $x_T = 15.5$ dB, which corresponds to a target BLER of 0.01 for 64QAM with code rate 3/4. $v_{PI} = 50$ kmph is chosen to trigger PI, for SRTA-PI.

In all studied systems, the same procedure, with the same prediction horizon(s), is applied to perform the transmission of any downlink data symbol over any sub-carrier. We therefore model and assess the performance of the studied systems on a single downlink data symbol and sub-carrier basis. A large number of downlink data symbols are simulated. The performance is assessed for each symbol, and the final result is averaged over all symbols.

For each simulated data symbol, channel coefficients for the uplink channel measurement and for the downlink data transmission phases, are generated in a random manner. Although these channel coefficients are random, they are correlated in the space and time domains. The angle giving the direction of the base station antenna array and the angle of the vector \vec{v} are generated randomly and are uniformly distributed between 0 and 2π . The position vector \vec{a} is also generated randomly. All other positions are deduced from \vec{a} and \vec{v} . Channel coefficients are then generated using a spatially correlated Ricean channel model with a LOS to total power ratio factor R which is either equal to 0 or 0.8. $R = 0$ corresponds to NLOS. For $R = 0.8$, the channel is dominated by the LOS component. We apply the method used to generate space-time correlated propagation channel coefficients for a scattering environment in sub-section 7.2 to our particular scenario. The propagation channel is modeled as a sum of the contributions of several planar waves. Each planar wave (or ray) is characterized by a random complex amplitude, a random angle of departure and a random angle of arrival (with angles uniformly distributed between 0 and 2π).

For each simulated data symbol, the following metrics are computed for various values of the speed v : the downlink frame duration τ^{DL} , the selected receive antenna index l_a , the number of active antennas K_a , the signal-to-noise ratio metric x and the energy saving metric e_s . As the simulations are performed on a data symbol basis, only the data symbol error rate can be derived in a straight forward manner from the signal-to-noise ratio. However, in this study, we will assume that all the data symbols within a data block are likely to be received with the same signal-to-noise ratio even for very high speed. Although the channel certainly differs from one data symbol to the other at high speed, the “width” of the beam and the corresponding mispointing is similar from one data symbol to the other, and mainly depends on the number of transmit antennas and the Ricean channel parameter R . In this study, we will therefore deduce the block error rate (or the block error probability) from the signal-to-noise ratio x using results stored in Table 4.2.2 based on link level simulations with constant channels and additive white Gaussian noise.

All the previously listed metrics are stored for each simulated data symbol and each speed v , and then averaged over data symbols, and plotted as a function of speed v .

SNR	14.5	15.0	15.5	15.7	16.0
BLER	1.0	0.8205	0.0125	0.0028	0.000001

Table 4.2.2 BLER For 64 QAM, rate $\frac{3}{4}$, Turbo code, with block length of 6000 bits

4.2.5.2 Robustness and energy efficiency

In this sub-section, simulations use a pure NLOS channel.

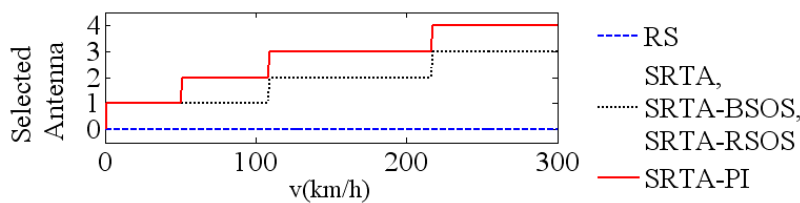


Fig. 4.2.8 Selected antennas

Fig. 4.2.8 illustrates the index l_a of the selected receive antenna as a function of v . RS only uses a single antenna, therefore $l_a=0$. As discussed in Sub-section 4.2.3.3, the SRTA and SRTA-RSOS/BSOS schemes share the same value. As explained in Sub-section 4.2.3.4, SRTA-PI uses a farther antenna than SRTA to avoid extrapolation. As expected, the receive antenna is selected farther behind the predictor antenna to compensate higher speeds.

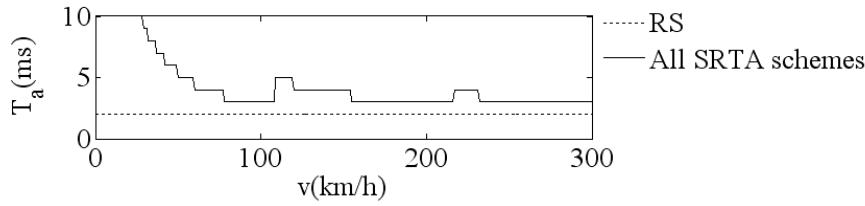


Fig. 4.2.9 Extended frame versus speed

Fig. 4.2.9 illustrates the downlink frame duration $t_a(v)$ as a function of the speed v . As explained in 4.2.4, all SRTA schemes use the same value, which decreases with speed but is always strictly higher than t_0 , thus higher than for RS.

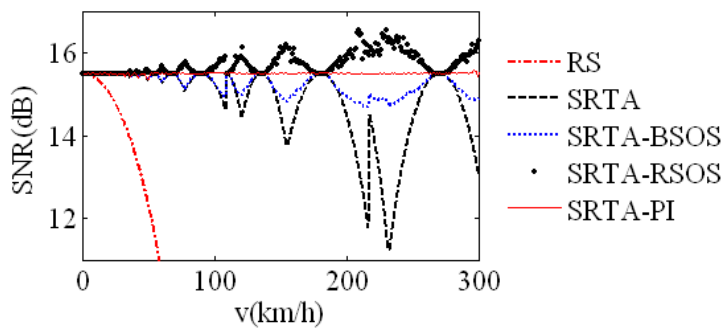


Fig. 4.2.10 SNR versus speed

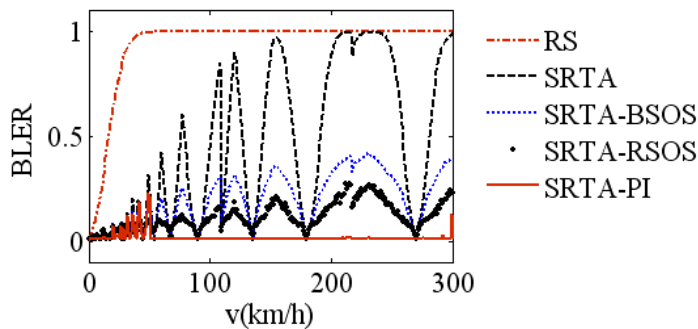


Fig. 4.2.11 BLER versus speed

Fig. 4.2.10 and Fig. 4.2.11 illustrate the signal-to-noise ratio and the block error rate as a function of the speed v , respectively. With RS, the performance degrades strongly for speeds larger than 50 kmph, reaching a block error rate of 1. Note in Table 4.2.2 that the block error rate is a sensitive function of the attained signal-to-noise ratio. As explained in Sub-section 4.2.3, SRTA is efficient for “perfectly compensated” speeds but not “non perfectly compensated” speeds. SRTA-BSOS/RSOS better handles “non perfectly compensated” speeds by reducing degradation in terms of signal-to-noise ratio and block error rate. RSOS outperforms BSOS as an irregular pattern of switched-off transmit antennas creates a tapering [113] effect.

Fig. 4.2.12 and Fig. 4.2.13 illustrate the number of active transmit antennas K_a and the corresponding energy saving e_s as a function of the speed v , respectively. RS and SRTA use all antennas and achieve

the maximum energy saving. For “perfectly compensated” speeds, SRTA-BSOS/RSOS behave like SRTA, whereas for “non perfectly compensated” speeds, $K_a < K$ antennas are used and less energy is saved. In other words, SOS schemes sacrifices energy saving to get better robustness of the block error rate against speed.

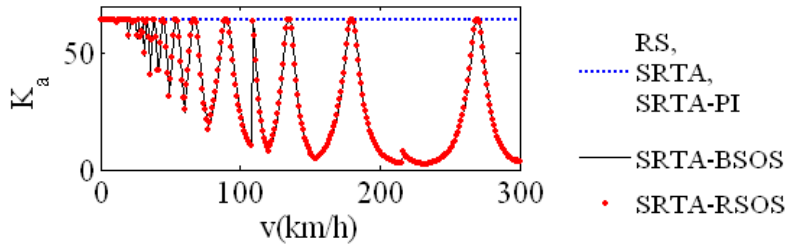


Fig. 4.2.12 Transmit active antennas versus speed

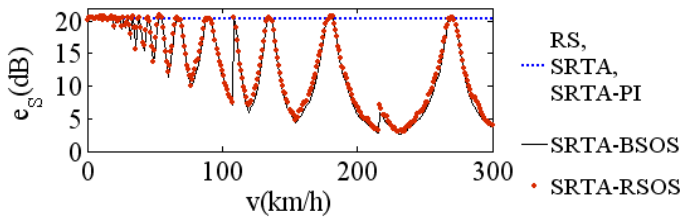


Fig. 4.2.13 Energy saving versus speed

As illustrated by Fig. 4.2.10 to Fig. 4.2.13, SRTA-PI perfectly compensates all speeds larger than $v_{PI}=50\text{kmph}$, and still with maximum energy saving. For lower speeds, the polynomial interpolation is not triggered (as specified in 4.2.3.4), as SRTA is sufficient. SRTA-PI therefore outperforms SRTA-RSOS with respect to energy saving and robustness.

These simulation results confirm the ordering identified in Sub-section 4.2.4.

4.2.5.3 Impact of the channel (LOS versus NLOS propagation)

In this sub-section simulations are run with $R=0.8$, i.e. with a dominating LOS component. Comparing Fig. 4.2.14 to Fig. 4.2.11 shows that the RS and SRTA schemes undergo a stronger mispointing effect in NLOS (Fig. 4.2.11) than in LOS (Fig. 4.2.14). This is not surprising, as it has been shown that scattering increases spatial focusing of Time reversal beamforming [20] which is similar to MRT beamforming[88]. Indeed, scatterers surrounding the transmit and the receive antenna arrays virtually increase the apertures of these arrays. As a consequence, the focused beam is more narrow.

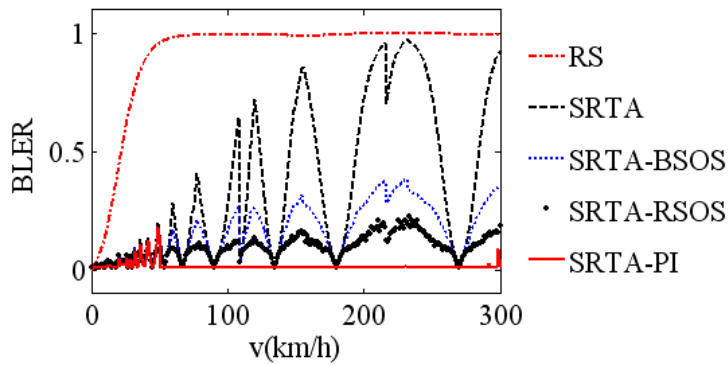


Fig. 4.2.14 BLER versus speed, strong LOS

4.2.6 Conclusion

In this study, we proposed three new schemes to improve the Separate Receive and Training Antenna technique to provide more robust energy efficient wireless downlink data transmission towards antennas upon very fast moving vehicles. The two first schemes, the “Border Switch Off Scheme” and the “Random Switch Off Scheme” simply switch off transmit antennas to widen the beam when beam-forming mispointing is too severe. They slightly improve robustness but reduce the energy savings. The third “Polynomial Interpolation” scheme is robust to all speeds up to 300 kmph and achieves maximum energy saving. This latter scheme relies on a Predictor Antennas Array and Polynomial Interpolation over multiple measurement samples. Ongoing studies focus on reducing its complexity, while keeping its ability to perfectly control the block error rate at any speed.

Chapter 5 - Design of new communication schemes and applications based on time reversal for mobile networks

In this chapter, we propose new communication techniques (sub-section 5.1, 5.2, and 5.4) or new applications for mobile networks other than wireless communications (sub-section 5.3). In all these proposed systems, TR plays a prevalent role.

5.1 Receive Antenna Shift Keying for time reversal wireless communications

5.1.1 Introduction

The concern for energy consumption in wireless networks is growing, and first studies show that a large part of the consumption comes from the power amplifier [89]. Systems operating at low output power, in the low SNR region, are becoming popular. As explained in section 2, TR [11] appears to be a candidate technique for low SNR systems.

All studies previously mentioned in section 3 on TR rely on a conventional phase and amplitude modulation (PAM), and show that at high SNR, the inter-symbol interference prevents from using high order PAM with a simple single tap receiver. Alternatively, [114] introduced a new modulation technique, called spatial modulation (SM) or space shift keying (SSK). In this scheme, at least two transmit antennas are necessary. During one symbol period, a single antenna among all transmit antennas is activated. The index of the transmit antenna codes for an information, i.e. a mapping rule exists that relates the index of the transmit antenna to a sequence of bits. The receiver must determine the transmit antenna index to recover the sequence of bits. In this scheme, the transmit signal is not using any phase and amplitude modulation. In [115][116][117], channel coding is added to SSK scheme and the gain in capacity of the proposed scheme over PAM is evaluated. However, with these techniques, only one antenna is allowed to transmit. Thus, these techniques cannot benefit from the beam-forming gain.

In this study, we propose a new scheme, called receive antenna shift keying (RASK) that enables to use high order modulations with time reversal and single tap receivers. We consider a communication involving several antennas at the transmitter and several antennas at the receiver. TR or 1bit TR are used at the transmitter, to focus energy on one receive antenna from the receive antenna array. Contrary to [115][116][117], all transmit antennas are active and focus toward a single target receive antenna. The index of the target receive antenna (instead of the transmit antenna) is coding for information.

This can be viewed as spatial modulation at the receiver side instead of the transmitter side. Sub-section 5.1.2 introduces the concept of RASK with a simple example. Sub-section 5.1.3 sets our generic system model and provides the analytical expression of the output of the Single Tap Receiver for any pre-filtering and modulation scheme, under a target peak receiver SNR constrain. Sub-section 5.1.4 describes PAM and RASK modulations and associated detection methods. Sub-section 5.1.5 compares the performance of 16QAM and RASK, for the TR and 1bit TR pre-filters, using the formula from 5.1.3. Sub-section 5.1.6 concludes this study. The Annex recalls the expressions of the TR and 1bit TR pre-filters and expresses the target peak receive SNR constrain.

In this study, we use ‘mathematical notations for single carrier transmissions studies’. Additionally, we define the following additional notations valid for this study only:

- J_n is the index of the target antenna at data symbol period n , in the spatial modulation scheme;
- $b_{n,k}$ is the bit number k coded by the spatial modulation symbol number n ;
- $R_j(t)$ is the signal received at antenna j ;
- $U_j(t)$ is the useful part of the signal received at antenna j ;
- $V_j(t)$ is the inter-symbol interference part of the signal received at antenna j ;
- $W_j(t)$ is the multi-stream interference part of the signal received at antenna j .

5.1.2 Introduction to receive antenna shift keying

To introduce the concept of RASK, this sub-section briefly describes, the example (illustrated in Fig. 5.1.1) of the transmission of the sequence of bits 111000010110. A communication between a transmitter and a receiver with $N = 16$ antennas is considered. The channel impulse is assumed to be known at the transmitter. The number of bits that can be sent within one symbol duration is $B = \log_2(N) = 4$. RASK requires the following 6 steps. During step1, the sequence is segmented in smaller binary sequences of B bits $b_{11}b_{12}b_{13}b_{14} = 1110$, $b_{21}b_{22}b_{23}b_{24} = 0001$ and $b_{31}b_{32}b_{33}b_{34} = 0110$ which will be sent during symbol period 1, 2 and 3, respectively. Then, for each symbol period n , steps 2, 3, 4 and 5 are executed successively. In step 2, the transmitter determines J_n as the integer coded by $b_{n1}b_{n2}b_{n3}b_{n4}$. Therefore, $J_1 = 15$, $J_2 = 2$ and $J_3 = 7$. In step 3, the transmitter performs TR pre-filtering and focuses toward the antenna having J_n as index. In step 4, the receiver detects the antenna \hat{J}_n among all its N antennas. A potential error on \hat{J}_n is caused by Inter-Symbol Interference, unperfect spatial focusing and noise. In step 5, the receiver converts \hat{J}_n into a sequence of bits

$\hat{b}_{n1}\hat{b}_{n2}\hat{b}_{n3}\hat{b}_{n4}$ which will content errors if \hat{J}_n is erroneous. Finally, in step 6, the receiver concatenates the small binary sequences of the 3 successive symbols.

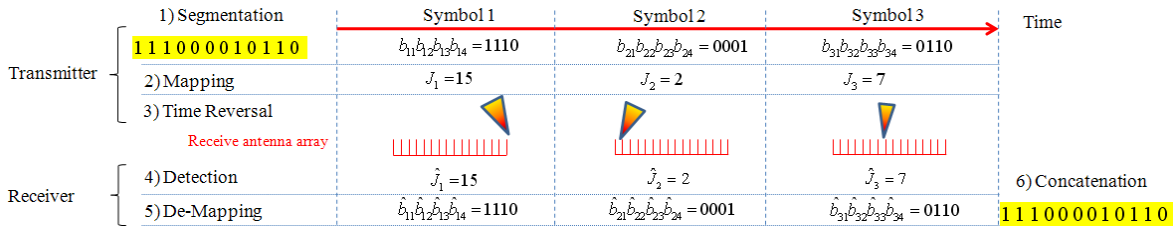


Fig. 5.1.1 Example of RASK with 16 receive antennas and 3 symbol periods

5.1.3 Generic system model and expression of the output of the single tap receiver

This sub-section provides a generic description of our system model. It also provides an analytical expression of the Single Tap Receiver output, which is valid for any TR pre-filtering and modulation technique, and which will be used for performance assessment in 5.1.5. Fig. 5.1.2 illustrates our system model for PAM and RASK.

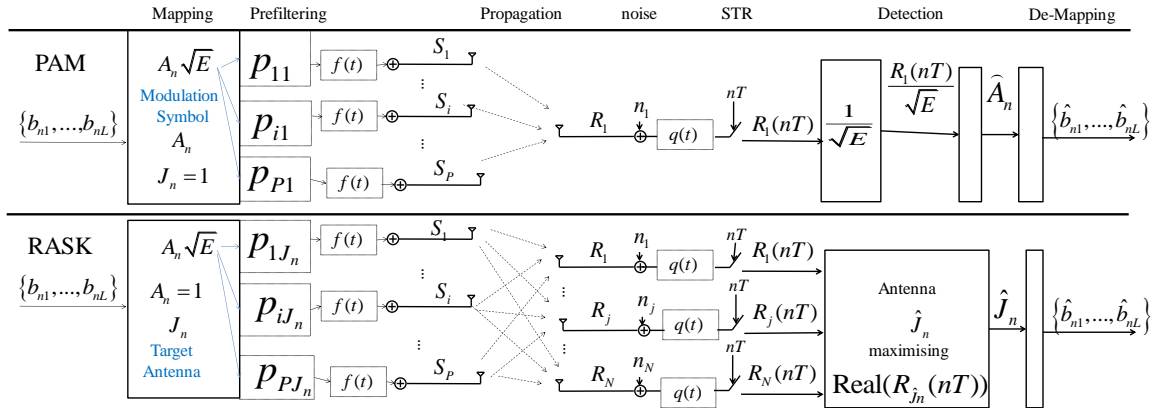


Fig. 5.1.2 System Model for PAM and RASK

A communication between a transmitter with P antennas and a receiver with N antennas is considered, with $N = 1$ for PAM and $N > 1$ for RASK. During the n^{th} symbol period, the transmitter focuses a modulation symbol A_n onto receive antenna J_n . For PAM, $J_n = 1$ and A_n is variable, while for RASK J_n is variable and $A_n = 1$. These two parameters will be further described in sub-section 5.1.4. In all cases, A_n must verify:

$$\max_n [|A_n|^2] = 1. \tag{Eq. 5.1.1}$$

Assuming per transmit antenna and per user pre-filtering $p_{ij}(t)$, equal power allocation per antenna, and a total energy of E , the expression of the signal transmitted by antenna i is:

Eq. 5.1.2

$$S_i(t) = \sqrt{\frac{E}{P}} \sum_n A_n f(t - nT) * p_{iJ_n}(t),$$

where T is the symbol period and $f(t)$ is a pulse shape filter occupying a bandwidth of $1/T$ and verifying

Eq. 5.1.3

$$\frac{1}{T} \int_{-\infty}^{+\infty} |f(t)|^2 dt = 1.$$

The fast fading channel impulse response $h_{ij}(t)$ between transmit antenna i and receive antenna j is modelled with K taps, and has the following expression:

Eq. 5.1.4

$$h_{ij}(t) = \sum_{k=1}^K h_{ijk} \delta(t - \tau_k),$$

where h_{ijk} and τ_k are the gain and the delay of the k^{th} tap, respectively. The fast fading channel coefficients h_{ijk} vary due to mobility. However in average, the power is assumed to be equal to 1:

Eq. 5.1.5

$$E \left[\sum_{k=1}^K |h_{ijk}|^2 \right] = 1.$$

The pre-filter $p_{iJ_n}(t)$ (which is either the TR prefilter or the 1bit TR prefilter as both defined in section 3.1) is a K -tap pre-filter with inversed time delays compared to h_{iJ_n} , which meets a target peak receive SNR value SNR_{rx} (defined in the Annex) and which focuses a signal towards receive antenna J_n :

Eq. 5.1.6

$$p_{iJ_n}(t) = \sum_{k=1}^K p_{iJ_n k} \delta(-t - \tau_k).$$

The signal received at antenna j , and filtered by $q(t)$ is:

Eq. 5.1.7

$$R_j(t) = \left(\left(\sum_{i=1}^P \alpha_{ij} S_i * h_{ij} + n_j \right) * q \right) (t).$$

where α_{ij} is the path loss gain, $n_j(t)$ is an additive white gaussian noise process of zero mean and spectral density N_0 , and $q(t)$ is matched to $f(t)$, i.e.,

Eq. 5.1.8

$$q(t) = f^*(-t).$$

We assume perfect synchronization, at the receiver. The output of the single tap receiver of antenna j , sampled at time $t = nT$ has the following expression (derived from Eq. 5.1.2, Eq. 5.1.4, Eq. 5.1.6 and Eq. 5.1.7):

Eq. 5.1.9

$$R_j(nT) = U_j(nT) + V_j(nT) + W_j(nT),$$

where,

Eq. 5.1.10

$$U_j(nT) = \sqrt{E} A_n \zeta_{j,l=0},$$

Eq. 5.1.11

$$V_j(nT) = \sqrt{E} \sum_{l=-K}^K A_{n-l} \zeta_{jl},$$

Eq. 5.1.12

$$W_j(nT) = n_j(nT)q(0),$$

with ζ_{jl} as defined below for every j and l :

Eq. 5.1.13

$$\zeta_{jl} = \sum_{i=1}^P \alpha_{ij} \sqrt{\frac{1}{P}} \sum_{k,k'=1}^K h_{ijk} p_{iJ_n k'} \rho_f(lT + \tau_{kk'}).$$

With these notations, $U_{J_n}(nT)$ and $V_{J_n}(nT)$ are the useful signal and the inter-symbol interference signal, respectively, received at the target antenna J_n . For $j \neq J_n$ (hence for RASK only), $U_j(nT) +$

$V_j(nT)$ is the unwanted signal received at the antenna j . For any antenna j , $W_j(nT)$ is the sampled noise.

5.1.4 PAM and RASK Modulation Schemes

This sub-section specifies the computation of the modulation symbol A_n and the target receive antenna index J_n during the n^{th} symbol period. In this sub-section, we consider the transmission of a binary sequence $B_n = \{b_{n1} \dots b_{nB}\}$ of B bits taking values in $\{0,1\}$. The mapping of B_n onto J_n and A_n , the detection and de-mapping methods, are described hereafter. \hat{A}_n , \hat{J}_n and $\hat{B}_n = \{\hat{b}_{n1} \dots \hat{b}_{nB}\}$ are the estimates of A_n , J_n and B_n , respectively.

5.1.4.1 PAM modulation

For PAM, the transmitter always focuses towards the same target receive antenna, i.e., $N = 1$ and $J_n = 1$. A_n is variable.

At the transmitter side, B_n is mapped onto A_n which is a PAM symbol verifying (Eq. 5.1.1) with 2^B as constellation size. 16QAM is used if $B = 4$, and 64QAM is used if $B = 6$.

At the receiver side, \sqrt{E} is estimated based on received pilots. The output of the Single Tap Receiver $R_1(nT)$ is used to detect \hat{A}_n . \hat{A}_n is simply the nearest PAM symbol from $R_1(nT)/\sqrt{E}$, in Euclidian distance. Finally, \hat{A}_n is converted into \hat{B}_n using 16QAM or 64QAM de-mapping.

5.1.4.2 RASK modulation

For RASK, we set $N = 2^B$ and $A_n = 1$. Fig. 5.1.2 illustrates RASK for a given symbol period n . J_n is variable this time.

At the transmitter side, J_n is computed as follows:

$$J_n = \sum_{k=1}^B b_{nk} 2^{k-1} + 1. \tag{Eq. 5.1.14}$$

At the receiver side, the output $R_j(nT)$ of the Single Tap Receiver of each antenna j is stored. Then, \hat{J}_n is determined very simply. \hat{J}_n is simply the index belonging to $[1: N]$ verifying:

$$\forall j \in [1: N], \text{Real}(R_j(nT)) \leq \text{Real}(R_{\hat{J}_n}(nT)). \tag{Eq. 5.1.15}$$

Finally, \hat{B}_n is de-mapped. It is simply the sequence verifying:

$$\hat{J}_n = \sum_{k=1}^B \hat{b}_{nk} 2^{k-1} + 1.$$

Eq. 5.1.16

5.1.5 Simulation Results

The performance of the system described in sub-section 5.1.3, is evaluated through BER versus SNR_{rx} curves (where SNR_{rx} is introduced in sub-section 5.1.3 and defined in the Annex), for various pre-filters and modulations. The performance evaluation methodology is depicted hereafter. For a given SNR_{rx} value, samples of fast fading channel are generated through simulation. For each channel sample, random bits are generated, and segmented into sequences of B bits as described in 5.1.3. Each sequence is mapped onto a modulation symbol and a target antenna according to sub-section 5.1.4. The output of the Single Tap Receiver is computed using Eq. 5.1.9 and pre-filtering coefficients defined in the Annex. These output values are then processed according to the detection and de-mapping methods described in sub-section 5.1.4. The resulting detected bits are compared to the original bits and the BER is computed.

Simulation assumptions are listed hereafter. We consider $B=4$ bits per symbol, and compare 16QAM to 16RASK. The receive antenna array size is $N=1$ for 16QAM and $N = 2^B=16$ for 16RASK. Both TR and 1bit TR are implemented. $P=1, 2, 4, 8, 16, 64$ transmit antennas are simulated. Channels $K = 1$ tap and with $K =15$ taps, are simulated. For each i and j we set $\alpha_{ij}=1$. Fast fading coefficients h_{ijk} are generated through simulation as complex random independent and identically distributed variables with Rayleigh distribution, equal average power and verifying Eq. 5.1.5. Thus, the channel is un-correlated in time and space. The filter $f(t)$ is the square raised root cosine filter with roll-off factor of 0.22. Finally, we generate a sufficient number of bits to measure raw BER values (down to 10^{-2}) which are typical in packet based wireless systems [118].

Fig. 5.1.3 illustrates the performance of 16QAM and 16RASK, with TR pre-filter and $K = 1$ tap. In the case of 16QAM, there is no inter-symbol interference. Indeed, Eq. 5.1.11 becomes $V_1(nT) = 0$. As a consequence, the BER depends on the useful signal $U_1(nT)$ and the noise $W_1(nT)$, i.e. on SNR_{rx} , which is fixed in Eq. 5.1.18 and does not depend on P . As the BER versus SNR_{rx} curve is the same for all P values, for the comfort of the reader, we only represent the $P = 1$ curve for 16QAM. Regarding 16RASK, though the inter-symbol interference on the target antenna J_n is also null (i.e. $V_{J_n}(nT) = 0$), the unwanted signal $U_j(nT) + V_j(nT)$ on antennas $j \neq J_n$ is non null. Increasing P enhances the

spatial focusing and lowers the unwanted signals. Consequently, the RASK detector performance is better when P increases. Indeed, 16RASK outperforms 16QAM when $P \geq 16$.

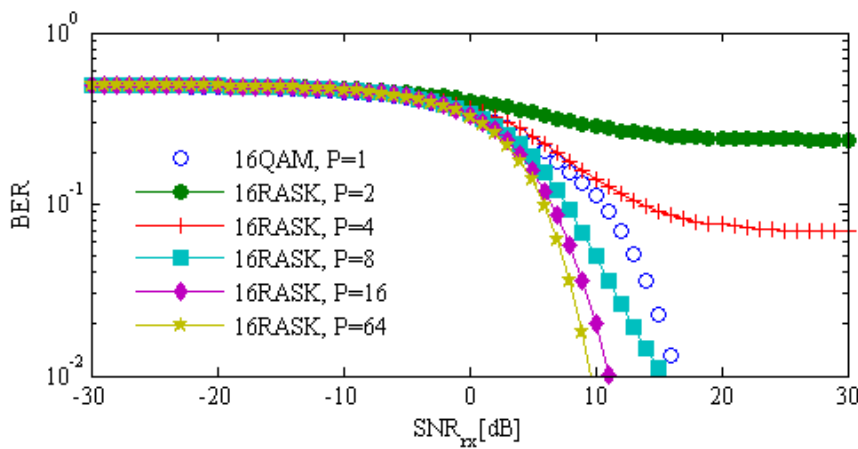


Fig. 5.1.3 TR, $K=1\text{tap}$, $P=1, 2, 4, 8, 16$ or 64 transmit antennas

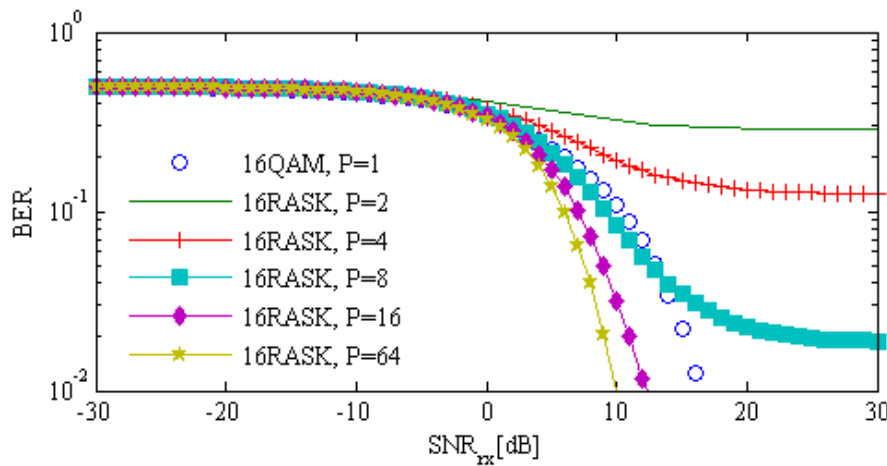


Fig. 5.1.4 1bit TR, $K=1\text{tap}$, $P=1, 2, 4, 8, 16$ or 64 transmit antennas

In Fig. 5.1.4, the same observations made with pure TR can be made with 1bit TR. However, a slight degradation, relatively to TR, is observed. As a 1tap channel is simulated, the difference is not due to inter-symbol interference in the time domain, and is purely due to spatial focusing properties. The 1bit TR allocates the same power to all transmit antennas. Under the same sum transmit power constrain, it therefore delivers less power at the target, compared to the pure TR. It therefore explains that pure TR outperforms 1bit TR.

Fig. 5.1.5 and Fig. 5.1.6 are the equivalent of Fig. 5.1.3 and Fig. 5.1.4 respectively. This time, K is set to 15 instead of 1, and consequently, 16QAM curves for all values of P are plotted. With such strong multi-path, Inter Symbol Interference V_{J_n} (nT) is non null and is impacting both 16QAM and 16RASK. We can observe that 16RASK outperforms 16QAM in this case. The 16RASK detection which relies on spatial focusing is more robust to Inter Symbol Interference than the 16QAM detection.

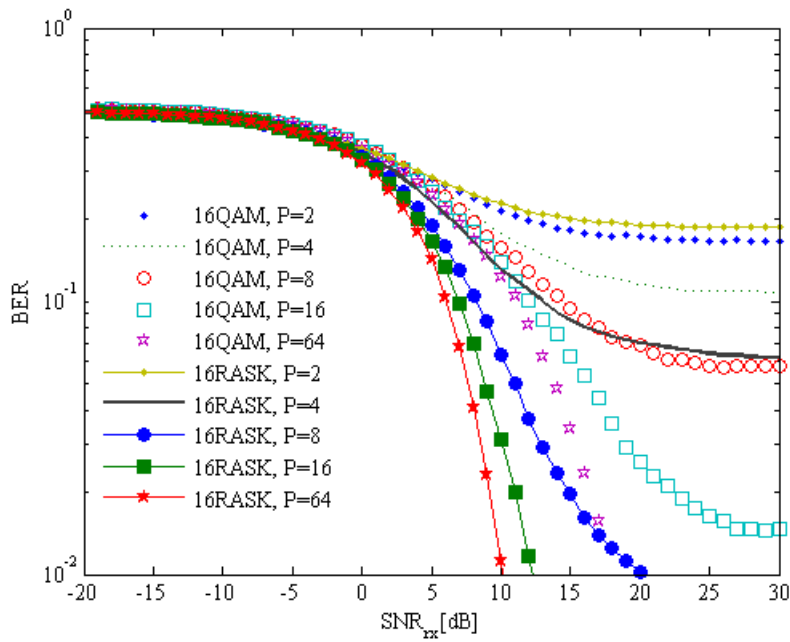


Fig. 5.1.5 TR, $K=15$ taps, $P=1, 2, 4, 8, 16$ or 64 transmit antennas

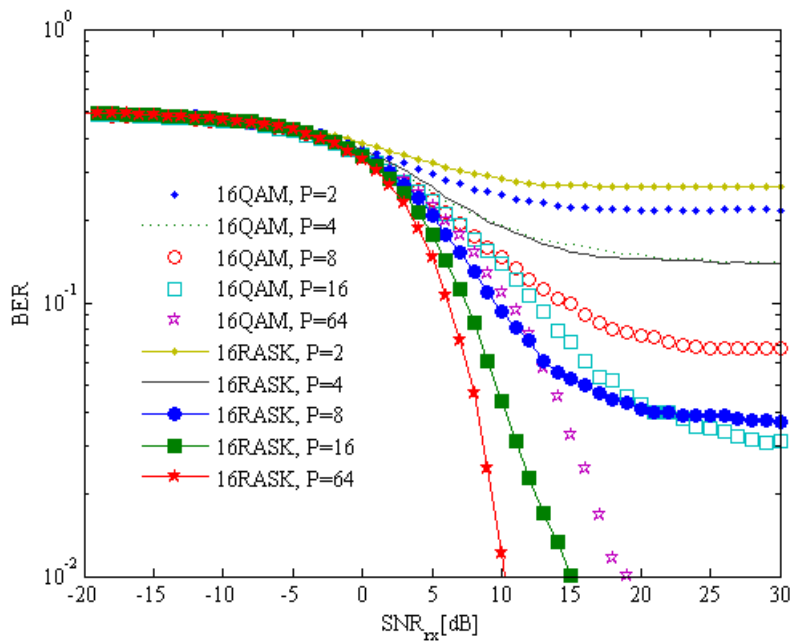


Fig. 5.1.6 1bit TR, $K=15$ taps, $P=1, 2, 4, 8, 16$ or 64 transmit antennas

Again, the same observations made with pure TR can be made with 1bit TR. And again, pure TR outperforms 1bit TR. This is due to two reasons. The first reason is that, due to the strong level of multipath the level inter-symbol interference is dramatically increased for 1bit TR compared to pure TR. The second reason is that the simulated multipath is based on a Rayleigh model: all the echoes have similar power values (no strong dominant component). Hence, 1bit TR cannot even exploit its ability to boost low power echoes to improve spatial focusing.

5.1.6 Conclusion

A new scheme, called RASK has been proposed to reach higher spectral efficiency with Time reversal pre-filters, while keeping the low complexity of single tap receivers. Contrary to PAM, RASK focuses a symbol with a constant phase and amplitude on a changing target receive antenna. Information bits are mapped onto a target receive antenna index instead of a phase and amplitude. Simulations show that in 16RASK scheme, the detection of the target receive antenna is more robust to inter-symbol interference than the symbol detection in 16QAM. Indeed, 16RASK outperforms 16QAM for large transmit antennas arrays or under strong multipath channels.

5.1.7 Annex

In this sub-section, the pre-filtering coefficients $p_{iJ_n k}$ are specified for a given J_n and A_n . We first define the peak receive SNR, SNR_{rx} , as follows:

$$SNR_{rx} = \frac{\max_n [|U_{J_n}(nT)|^2]}{E [|W_{J_n}(nT)|^2]} \tag{Eq. 5.1.17}$$

Normalizing factors λ_{J_n} ensuring $\zeta_{J_n, l=0} = 1$ will be computed to guaranty that SNR_{rx} meets the following target:

$$SNR_{rx} = \frac{E}{N_0} \tag{Eq. 5.1.18}$$

Indeed, if $\zeta_{j_0} = 1$, then Eq. 5.1.12 will lead to:

$$U_{J_n}(nT) = \sqrt{E} A_n \tag{Eq. 5.1.19}$$

By replacing Eq. 5.1.19 in Eq. 5.1.17 we obtain:

$$SNR_{rx} = \frac{E}{N_0} \max_{n,j} [|A_{nj}|^2] \tag{Eq. 5.1.20}$$

Due to Eq. 5.1.1, Eq. 5.1.20 will become equivalent to Eq. 5.1.18, as desired. The p_{ijk} coefficients are updated periodically to track the variations of the fast fading coefficients h_{ijk} . Two pre-filters based on

the inversed channel impulse response are considered: TR and 1bit TR namely. In the case of TDD, channel reciprocity is assumed and perfect channel knowledge is supposed to be available at the transmitter. Pure TR pre-filter is therefore used. For each transmit antenna i and each channel tap k , $p_{iJ_n k}$ and λ_{J_n} have:

$$p_{iJ_n k} = \frac{h_{iJ_n k}^*}{\lambda_{J_n}}, \quad \text{Eq. 5.1.21}$$

$$\lambda_{J_n} = \sqrt{\frac{1}{P}} \sum_{i=1}^P \alpha_{iJ_n} \sum_{k,k'=1}^K h_{iJ_n k} h_{iJ_n k'}^* \rho_f(\tau_{kk'}). \quad \text{Eq. 5.1.22}$$

In the case of FDD, 1bit TR is used and the coefficients are assumed to be computed and reported by the receiver. For each transmit antenna i and each tap k , $p_{iJ_n k}$ and λ_{J_n} have the following expressions, with y as defined in sub-section 5.1.1.:

$$p_{iJ_n k} = \frac{y(h_{iJ_n k}^*)}{\lambda_{J_n}}, \quad \text{Eq. 5.1.23}$$

$$\lambda_{J_n} = \sqrt{1/P} \sum_{i=1}^P \alpha_{iJ_n} \sum_{k,k'=1}^K h_{iJ_n k} y(h_{iJ_n k}^*) \rho_f(\tau_{kk'}). \quad \text{Eq. 5.1.24}$$

5.2 “Make-It-Real” precoders for MIMO OFDM/OQAM without inter carrier interference

5.2.1 Introduction

Low complexity MIMO precoders for OFDM, such as MRT [8] and MMSE precoders [10] enable to multiplex data streams in the spatial domain, without breaking OFDM orthogonality in the frequency domain. Though these precoders do provide a spectral efficiency gain thanks to spatial multiplexing, one can further enhance the system performance by using MIMO OFDM receivers that reduce or cancel the inter stream interference [120][121].

OFDM/OQAM is a multi-carrier transmission mode [122][123] which is more spectrally efficient than OFDM as it does not require cyclic prefix. Unfortunately, spatial multiplexing in OFDM/OQAM with traditional MRT and MMSE precoders break the orthogonality in the frequency domain, and introduce inter-carrier interference, in addition to inter stream interference. It therefore requires receivers which are able to mitigate the inter-carrier interference [124][125], and which are therefore more complex than conventional MIMO OFDM receivers.

ZF precoders [126] do achieve orthogonality in both the frequency and the spatial domains and can therefore be used safely with OFDM/OQAM. However, at low SNR, or when the MIMO channel matrix is not well conditioned, ZF performance becomes very poor [126]. For OFDM at least, and for low SNR ZF, is outperformed by MRT precoder, and for low to medium SNR, ZF precoder is outperformed by MMSE precoder [10].

Alternatively, new transmit filters [127][128] especially designed for OFDM/OQAM can achieve optimum performance, in MISO configuration. However, these filters are highly complex and still introduce inter-carrier interference.

This study proposes a new family of low complexity precoders, for OFDM/OQAM, called “Make-It-Real”(MIR) Precoders to achieve better performance than ZF precoder. MIR MRT and MIR MMSE precoders are obtained by performing a slight modification of the traditional MRT and MMSE precoders. MIR precoders are designed so that the equivalent channel, after precoding and wireless propagation, is “made real”, and the OFDM/OQAM orthogonality in the frequency domain is conserved.

The paper is organized as follows. Sub-section 5.2.2 presents our system model. Sub-section 5.2.3 presents MRT, MMSE and ZF traditional precoders for MIMO OFDM, and MIR MRT, MIR MMSE, and ZF precoders for OFDM/OQAM. Sub-section 5.2.4 presents our performance evaluation methodology.

Sub-section 5.2.5 presents simulation results and compares MIMO OFDM with MRT, MMSE, ZF precoders to MIMO OFDM/OQAM with MIR MRT, MIR MMSE and ZF precoders under various SNR conditions. Sub-section 5.2.6 concludes this study.

The following notations are used throughout this study:

- $\mathbf{a}^{(l)} \in \mathbb{C}^{N \times 1}$ is the vector of N data symbols sent during symbol period n on sub-carrier l ;
- $\mathbf{b}^{(l)} \in \mathbb{C}^{N \times 1}$ is the vector of signals received over the N receive antennas on sub-carrier l ;
- c is the spectral efficiency without guard time taken into account;
- C is the spectral efficiency with guard time taken into account;
- $f_n^{(l)} \in \mathbb{R}^+$ is the spectral efficiency of data stream n on sub-carrier l ;
- $g_n^{(l)} \in \mathbb{R}^+$ is the truncated spectral efficiency of data stream n on sub-carrier l ;
- g^{min} is the minimum spectral efficiency;
- g^{max} is the maximum spectral efficiency;
- $\mathbf{H}^{(l)} \in \mathbb{C}^{N \times M}$ is the MIMO channel matrix on sub-carrier l ;
- $\mathbf{H}_{n,m}^{(l)}$ is the complex channel gain between receive antenna n and transmit antenna m , on sub-carrier l ;
- $\mathbf{k}^{(l)} \in \mathbb{R}^{N \times 1}$ the vector of N real data symbols are sent over even periods of duration $0.5T_u$ on sub-carrier l ;
- l is the sub-carrier index;
- L is the number of sub-carriers;
- m is the transmit antenna index;
- M is the number of transmit antennas;
- n is the data symbol index;
- N is the number of receive antennas;

- $\mathbf{R}^{(l)} \in \mathbb{C}^{N \times N}$ is the equivalent channel, after precoding and propagation through the wireless MIMO channel on sub-carrier l ;
- $\mathbf{R}^{(l),real} \in \mathbb{R}^{N \times N}$ is the real extraction of $\mathbf{R}^{(l)}$;
- $\mathbf{R}^{(l),imag} \in \mathbb{R}^{N \times N}$ is the imaginary extraction of $\mathbf{R}^{(l)}$;
- SNR is the transmit signal-to-noise power;
- $s_n^{(l)} \in \mathbb{R}^+$ is the signal-to-noise ratio of data stream n on sub-carrier l ;
- $\mathbf{s}^{(l)} \in \mathbb{R}^{N \times 1}$ is the inter-carrier interference term on sub-carrier l ;
- T_s is the overall duration of the OFDM symbol;
- T_u is the useful symbol duration;
- T_g is the guard time duration;
- $\mathbf{u}^{(l)} \in \mathbb{C}^{N \times 1}$ the vector of the receivers complex noise samples of the N receive antennas;
- $\mathbf{v}^{(l)} \in \mathbb{C}^{N \times 1}$ is the vector of the N data demodulated symbols received over the N receive antennas;
- $\mathbf{W}^{(l)} \in \mathbb{C}^{M \times N}$ is the precoding matrix on sub-carrier l ;
- $\mathbf{x}^{(l)} \in \mathbb{R}^{N \times 1}$ is the vector of N real data symbol are sent during odd periods of duration $0.5T_u$ on sub-carrier l ;
- $\mathbf{y}^{(l)} \in \mathbb{R}^{N \times N}$ is the real part of the received vector of data symbols;
- $\mathbf{z}^{(l)} \in \mathbb{R}^{N \times 1}$ is the inter-carrier interference term on sub-carrier l ;
- $\gamma \in \mathbb{R}^+$ is a normalising factor;
- λ^{data} is the average power of data symbols;
- λ^{noise} is the noise power; on sub-carrier l ;

5.2.2 System model

This sub-section presents our system model. Sub-section 5.2.2.1 describes the common framework for MIMO OFDM and MIMO OFDM/OQAM, and for any precoders. Sub-sections 5.2.2.2 and 5.2.2.3 describe MIMO OFDM and MIMO OFDM/OQAM specificities, respectively. Sub-section 5.2.2.4 defines common metrics.

5.2.2.1 Common framework

We consider a MIMO wireless communication between a transmitter with M antennas and a receiver with N antennas. A multi-carrier transmission with L sub-carriers is used. We denote T_s the overall duration of the OFDM symbol. T_u and T_g denote the useful symbol and guard time durations, respectively. The wireless propagation channel between the transmitter and the receiver is flat over each sub-carrier. We also assume that MIMO precoding and AMC is performed on a sub-carrier basis. In this case, one can study each sub-carrier independently. All equations in sub-section 5.2.2 are valid for any sub-carrier l . The MIMO propagation channel can be modeled by a complex matrix $\mathbf{H}^{(l)}$. $\mathbf{H}_{nm}^{(l)}$ is the complex channel gain between receive antenna n and transmit antenna m . Spatial multiplexing of N data streams is performed at the transmitter using a precoding matrix $\mathbf{W}^{(l)}$ which is computed based on perfect CSIT (which is possible in Time division duplex mode for instance). To allow for a fair comparison between various precoders, $\mathbf{W}^{(l)}$ is always designed to verify:

$$\|\mathbf{W}^{(l)}\| = 1. \quad \text{Eq. 5.2.1}$$

During one OFDM symbol duration, for each data stream n , a complex data symbol $\mathbf{a}_n^{(l)}$ is sent over each transmit antenna m , with the precoding weight $\mathbf{W}_{mn}^{(l)}$. Equal average power per data stream, is assumed, and \mathbf{a}_n^l 's are assumed to be complex independent identically distributed (iid) random variables with power $\lambda^{data} = E[|\mathbf{a}_n^{(l)}|^2]$. We denote by $\mathbf{u}^{(l)}$ the vector of the receivers complex noise samples of the N receive antennas. $\mathbf{u}_n^{(l)}$ are assumed to be complex iid gaussian random variables with power $\lambda^{noise} = E[|\mathbf{u}_n^{(l)}|^2]$. We denote $\mathbf{R}^{(l)}$ the equivalent channel, after precoding and propagation through the wireless MIMO channel:

$$\mathbf{R}^{(l)} = \mathbf{H}^{(l)}\mathbf{W}^{(l)}. \quad \text{Eq. 5.2.2}$$

5.2.2.2 MIMO OFDM specificities

For OFDM, the guard time is non null: $T_g > 0$. Using notations of Sub-section 5.2.2.1, one can derive the expression of the vector $\mathbf{b}^{(l)}$ of the N data symbols received over the N receive antennas as follows:

$$\mathbf{b}^{(l)} = \mathbf{H}^{(l)} \mathbf{W}^{(l)} \mathbf{a}^{(l)} + \mathbf{u}^{(l)} = \mathbf{R}^{(l)} \mathbf{a}^{(l)} + \mathbf{u}^{(l)} \quad \text{Eq. 5.2.3}$$

For any data stream n , $\mathbf{R}_{nn}^{(l)}$ and $\mathbf{R}_{n,m}^{(l)}$, with $m \neq n$ are the weighting factors of the useful signal and interference components between streams m and n , respectively. However, this interference, is purely spatial, and comes from the same sub-carrier l . In other words, though spatial multiplexing does introduce inter stream interference, it does not break the orthogonality of OFDM in the frequency domain. Some practical implementations of advanced receivers exist that cancel inter stream interference alone [120][121].

5.2.2.3 MIMO OFDM/OQAM specificities and condition of orthogonality in the frequency domain

For OFDM/OQAM, the guard time is null: $T_g = 0$. This sub-section summarizes the principles of MIMO OFDM/OQAM [122][123][124][125]. Using notations in Sub-section 5.2.2.1, one can decompose the data symbol $\mathbf{a}_n^{(l)}$ into real and imaginary part:

$$\mathbf{a}_n^{(l)} = \mathbf{x}_n^{(l)} + J \cdot \mathbf{k}_n^{(l)}. \quad \text{Eq. 5.2.4}$$

$\mathbf{x}_n^{(l)}$ real data symbols are sent during odd periods of duration $0.5T_u$ while $\mathbf{k}_n^{(l)}$ real data symbols are sent over even periods of duration $0.5T_u$. For the comfort of the reader, we will write the equations for $\mathbf{x}_n^{(l)}$ only, as the same equations apply for $\mathbf{k}_n^{(l)}$. For each data stream n , $\mathbf{x}_n^{(l)}$ is sent over each transmit antenna m , with the precoding weight $\mathbf{W}_{mn}^{(l)}$. The MIMO OFDM/OQAM transmitter architecture is illustrated in Fig. 5.2.1.

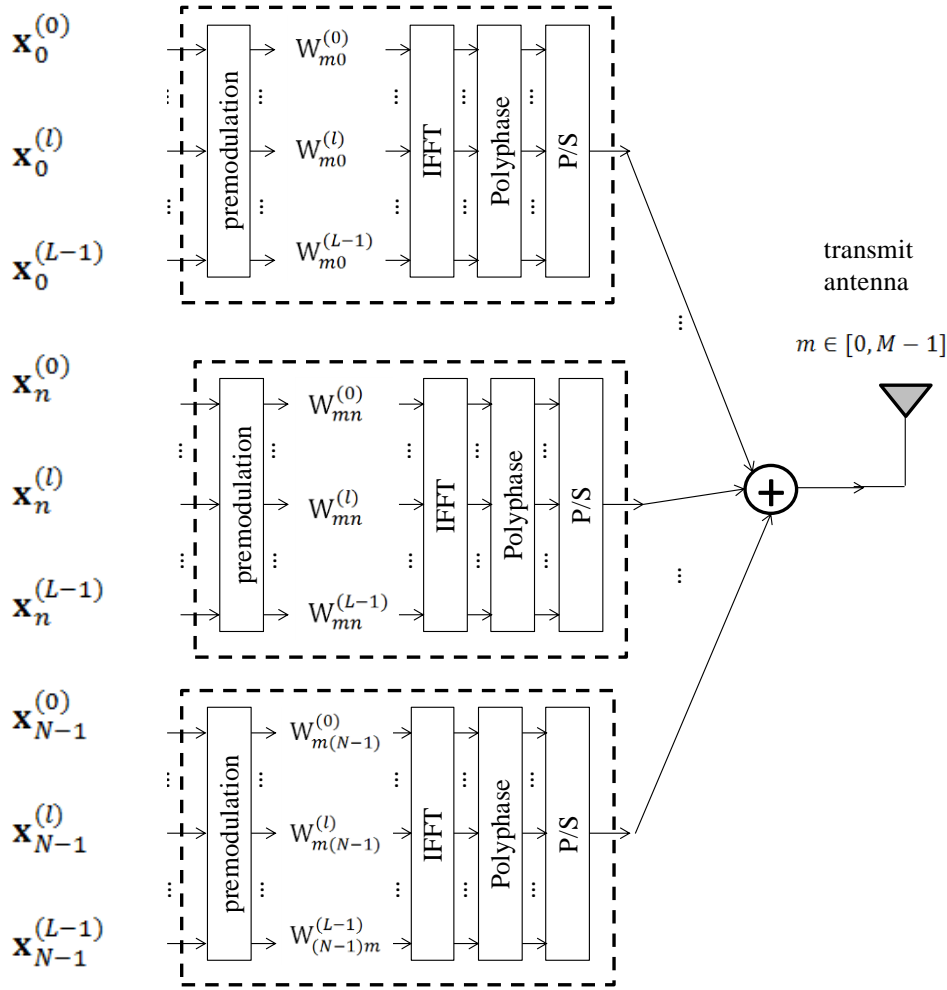


Fig. 5.2.1 MIR Precoder OFDM/OQAM Transmitter architecture

Based on [122][123], and assuming that the channel $\mathbf{H}^{(l)}$ is constant in time and flat over a few contiguous sub-carriers, the vector $\mathbf{v}^{(l)}$ of the N data demodulated symbols received over the N receive antennas can be written as:

$$\mathbf{v}^{(l)} = \mathbf{H}^{(l)} \mathbf{W}^{(l)} (\mathbf{x}^{(l)} + J \cdot \mathbf{z}^{(l)}) + \mathbf{s}^{(l)} + \mathbf{u}^{(l)}, \quad \text{Eq. 5.2.5}$$

where $\mathbf{z}^{(l)}$ and $\mathbf{s}^{(l)}$ are two inter-carrier interference terms. $\mathbf{z}^{(l)}$ is a purely real containing terms $\mathbf{x}^{(p)}$ from sub-carriers $p \neq l$ with low $|p - l|$ values, whereas $\mathbf{s}^{(l)}$ contains terms $\mathbf{x}^{(p)}$ from sub-carriers $p \neq l$ with large $|p - l|$ values. According to [123], if the prototype filter of OFDM/OQAM is designed to be well localized in time and frequency, $\mathbf{s}^{(l)}$ can be neglected and equation Eq. 5.2.5 can be simplified into:

$$\mathbf{v}^{(l)} = \mathbf{H}^{(l)} \mathbf{W}^{(l)} (\mathbf{x}^{(l)} + J \cdot \mathbf{z}^{(l)}) + \mathbf{u}^{(l)}, \quad \text{Eq. 5.2.6}$$

where $\mathbf{z}^{(l)}$ is a purely real inter-carrier interference term due to OFDM/OQAM modulation. In other terms, $\mathbf{z}^{(l)}$ contains terms $\mathbf{x}^{(p)}$ from sub-carriers $p \neq l$. The MIMO OFDM/OQAM receiver architecture is illustrated in Fig. 5.2.2.

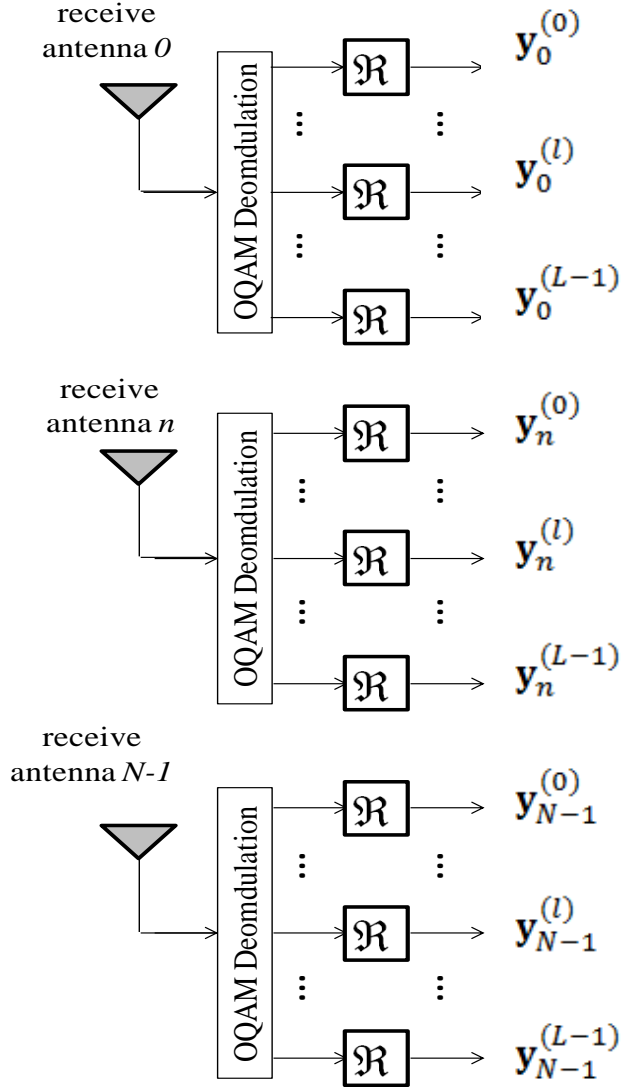


Fig. 5.2.2 OFDM/OQAM Receiver architecture

Using, as in [122], a very simple receiver which only needs to extract the real part of the demodulated signals, we get the vector $\mathbf{y}^{(l)}$:

$$\mathbf{y}^{(l)} = \Re(\mathbf{v}^{(l)}). \quad \text{Eq. 5.2.7}$$

Using Eq. 5.2.2 and Eq. 5.2.6, one can re-write Eq. 5.2.7 as follows:

$$\mathbf{y}^{(l)} = \Re \left(\mathbf{R}^{(l)} \left(\mathbf{x}^{(l)} + J. \left(\mathbf{z}^{(l)} \right) \right) + \mathbf{u}^{(l)} \right). \quad \text{Eq. 5.2.8}$$

Additionally, $\mathbf{R}^{(l)}$ can be decomposed as follows:

$$\mathbf{R}^{(l)} = \mathbf{R}^{(l),real} + J. \mathbf{R}^{(l),imag}. \quad \text{Eq. 5.2.9}$$

where, $\mathbf{R}^{(l),real}$ and $\mathbf{R}^{(l),imag}$, are two real matrices. We can then distinguish two different cases. $\mathbf{R}^{(l)}$ can be either complex or real.

If $\mathbf{R}^{(l)}$ is complex, then $\mathbf{R}^{(l),imag} \neq 0$, and (8) becomes equivalent to:

$$\mathbf{y}^{(l)} = \mathbf{R}^{(l),real} \mathbf{x}^{(l)} - \mathbf{R}^{(l),imag} \mathbf{z}^{(l)} + \Re(\mathbf{u}^{(l)}). \quad \text{Eq. 5.2.10}$$

$\mathbf{y}^{(l)}$ suffers from an inter-carrier interference term $\mathbf{R}^{(l),imag} \mathbf{z}^{(l)}$ which has to be deleted at the receiver side, using algorithms which are more complex than for OFDM [124][125][126][127].

On the contrary, if $\mathbf{R}^{(l)}$ is real, then $\mathbf{R}^{(l),imag} = 0$, $\mathbf{R}^{(l)} = \mathbf{R}^{(l),real}$, and Eq. 5.2.10 becomes equivalent to:

$$\mathbf{y}^{(l)} = \mathbf{R}^{(l)} \mathbf{x}^{(l)} + \Re(\mathbf{u}^{(l)}). \quad \text{Eq. 5.2.11}$$

This equation, is very similar to Eq. 5.2.3. Thus, $\mathbf{y}^{(l)}$ only suffers from inter stream interference just like for MIMO OFDM. MIMO OFDM receivers [120][121] can directly be used for the MIMO OFDM/OQAM.

In this study, only MIMO OFDM/OQAM precoders for which ensure that $\mathbf{R}^{(l)}$ real are studied.

5.2.2.4 Common Performance Metrics

First of all, one can notice that \mathbf{x}_n^l has a power of $0.5\lambda^{data}$ and that $\Re(\mathbf{u}^{(l)})$ has a power of $0.5\lambda^{noise}$. For both OFDM and OFDM/OQAM systems, the Signal-to-noise ratio SNR is therefore:

$$SNR = \frac{\lambda^{data}}{\lambda^{noise}}. \quad \text{Eq. 5.2.12}$$

As we want to focus on the precoder design, for both OFDM and OFDM/OQAM modulation schemes, we consider a basic receiver (without interference cancellation and without interference mitigation). In this case, the expression of the Signal-to-interference-and-noise ratio s_n^l of data stream n and sub-carrier l is simply given by:

$$s_n^{(l)} = \frac{|\mathbf{R}_{nn}^{(l)}|^2}{\sum_{p=0}^{N-1} |\mathbf{R}_{np}^{(l)}|^2 + SNR^{-1}}. \quad \text{Eq. 5.2.13}$$

Assuming AMC, the achievable peak spectral efficiency $f_n^{(l)}$ in bits/s/Hz of data stream n and sub-carrier l is then given by:

$$f_n^{(l)} = \log_2(1 + s_n^{(l)}). \quad \text{Eq. 5.2.14}$$

For practical Modulation and Coding Schemes (MCS), $f_n^{(l)}$ takes integer values. The corresponding spectral efficiency is therefore bounded. We denote it by $g_n^{(l)}$, it lies between g^{min} and g^{max} . The bounded spectral efficiency is denoted $g_n^{(l)}$. To obtain statistical results, one may generate several samples of $\mathbf{H}^{(l)}$, sum $g_n^{(l)}$ over data streams, average the result over sub-carriers and over samples. In this case, the system peak spectral efficiency c is given by:

$$c = \frac{1}{L} E \left[\sum_{l=0}^{L-1} \sum_{n=0}^{N-1} g_n^{(l)} \right]. \quad \text{Eq. 5.2.15}$$

The peak spectral efficiency does not account for the guard interval. Hence, one must also evaluate the spectral efficiency C defined by:

$$C = \frac{T_u}{T_s} c. \quad \text{Eq. 5.2.16}$$

5.2.3 Precoders

This sub-section defines the studied precoders $\mathbf{W}^{(l)}$ and the corresponding equivalent channel $\mathbf{R}^{(l)}$. For the comfort of the reader, and just in this sub-section, we will use \mathbf{H} , \mathbf{R} and \mathbf{W} notations instead of $\mathbf{H}^{(l)}$, $\mathbf{R}^{(l)}$ and $\mathbf{W}^{(l)}$. In each sub-section, $\gamma \in \mathbb{R}^+$ is a normalizing factor ensuring that Eq. 5.2.1 is veri-

fied. A “Make-It-Real” precoder \mathbf{W} is built very simply, based on the equivalent channel \mathbf{R} of a traditional “inspiring” precoder:

$$\mathbf{W} = \gamma \mathbf{H}^H (\mathbf{H}\mathbf{H}^H)^{-1} \Re(\mathbf{R}) \quad \text{Eq. 5.2.17}$$

The resulting equivalent channel is $\Re(\mathbf{R})$ instead of \mathbf{R} and is therefore “made real”. According to subsection 5.2.2.3, the orthogonality of OFDM/OQAM is thus not broken in the frequency domain. Also, \mathbf{W} is expected to benefit from its traditional “inspiring” precoder.

5.2.3.1 MRT Precoder for OFDM

MRT precoder is extremely simple, and is known to be better at low SNR [8]:

$$\mathbf{W} = \gamma \mathbf{H}^H. \quad \text{Eq. 5.2.18}$$

5.2.3.2 MMSE Precoder for OFDM

MMSE [10] requires the knowledge of SNR at the transmitter. It is known to outperform ZF precoder at medium and low SNRs.

$$\mathbf{W} = \gamma \mathbf{H}^H (\text{SNR}^{-1} \mathbf{I} + \mathbf{H}\mathbf{H}^H)^{-1}. \quad \text{Eq. 5.2.19}$$

5.2.3.3 ZF Precoder for OFDM and OFDM/OQAM

ZF precoder [10] inverses the channel, it can therefore be used for both MIMO OFDM and MIMO OFDM/OQAM.

$$\mathbf{W} = \gamma \mathbf{H}^H (\mathbf{H}\mathbf{H}^H)^{-1}. \quad \text{Eq. 5.2.20}$$

5.2.3.4 MIR MRT Precoder for OFDM/OQAM

$$\mathbf{W} = \gamma \mathbf{H}^H (\mathbf{H}\mathbf{H}^H)^{-1} \Re(\mathbf{H}\mathbf{H}^H). \quad \text{Eq. 5.2.21}$$

5.2.3.5 MIR MMSE Precoder for OFDM/OQAM

$$\mathbf{W} = \gamma \mathbf{H}^H (\mathbf{H}\mathbf{H}^H)^{-1} \Re(\mathbf{H}\mathbf{H}^H (SNR^{-1} \mathbf{I} + \mathbf{H}\mathbf{H}^H)^{-1}). \quad \text{Eq. 5.2.22}$$

5.2.3.6 Regularity of the MIR precoders matrices

It might often happen that $\mathbf{H}^H (\mathbf{H}\mathbf{H}^H)^{-1}$ has a weak regularity. However, the MIR precoders themselves will most of the time have good regularity properties. Let λ_{low} and λ_{high} be the lowest and highest singular values of the matrix $\mathbf{H}\mathbf{H}^H$, respectively. Even though λ_{low} and λ_{high} may be very different, the singular values of $(\mathbf{H}\mathbf{H}^H)^{-1} \Re(\mathbf{H}\mathbf{H}^H)$ are much closer to each other. As a consequence, the MIR MRT precoder, most of the time, has good regularity properties. Similarly, the same conclusions can be derived for the MIR MMSE precoder.

5.2.4 Performance evaluation methodology

The SNR value is fixed. $g^{min} = 1$ bits/s/Hz, which corresponds to the practical MCS QPSK with coding rate $1/2$, and $g^{max} = 6$ bits/s/Hz, which corresponds to the practical MCS 64QAM with coding rate 1. A large number of random and independent channel samples \mathbf{H}_{nm}^l are generated through simulations according to a Rayleigh distribution law. The channel is normalized so that: $\frac{1}{N \times M} \|\mathbf{H}^{(l)}\|^2 = 1$. For each sample, and each sub-carrier l , the precoders $\mathbf{W}^{(l)}$, is computed based on $\mathbf{H}^{(l)}$ using formulas defined in Sub-section 5.2.3. The peak spectral efficiency $c_{ofdm}^{zf}, c_{ofdm}^{mrt}, c_{ofdm}^{mmse}, c_{oqam}^{zf}, c_{oqam}^{mirmrt}, c_{oqam}^{mirmmse}$ are then deduced for MIMO OFDM with ZF, MRT and MMSE precoders, and MIMO OFDM/OQAM with ZF, MIR MRT, MIR MMSE precoders, respectively, using formula Eq. 5.2.15. One can notice that $c_{oqam,zf} = c_{ofdm,zf}$. To account for the guard interval, the spectral efficiency $C_{ofdm}^{zf}, C_{ofdm}^{mrt}, C_{ofdm}^{mmse}, C_{oqam}^{zf}, C_{oqam}^{mirmrt}, C_{oqam}^{mirmmse}$ are also computed according to formula Eq. 5.2.16, with $\frac{T_u}{T_s^{OFDM}} = 0.75$ (as in WiMAX [129]) and $\frac{T_u}{T_s^{OQAM}} = 1$.

5.2.5 Results

In this sub-section, the number of transmit and receive antennas is equal to $N = M = 8$. Due to the way \mathbf{H}^l is generated, $N = M$ ensures that $\mathbf{H}^{(l)} (\mathbf{H}^{(l)})^H$ is invertible.

5.2.5.1 Peak Spectral Efficiency

Fig. 5.2.3 plots $c_{ofdm}^{zf} = c_{oqam}^{zf}, c_{ofdm}^{mrt}, c_{ofdm}^{mmse}, c_{oqam}^{mirmrt}, c_{oqam}^{mirmmse}$ as a function of SNR.

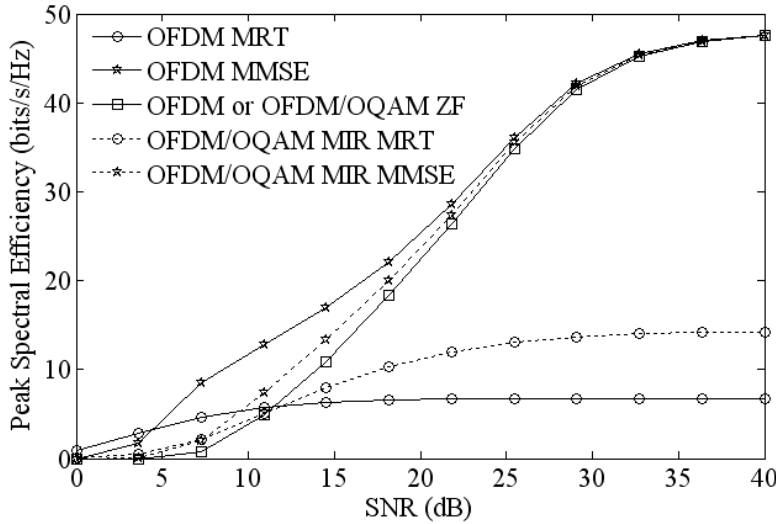


Fig. 5.2.3 Peak spectral efficiencies, 8x8 MIMO

For MIMO OFDM, the well known behavior of MRT, ZF and MMSE precoders are observed: MRT is the best solution at low SNR, ZF at high SNR, and MMSE for all SNRs. MMSE tends towards ZF at very high SNR and towards MRT at very low SNR (the integer and bounded values of g^{min} and g^{max} prevent from having exact same performance).

For MIMO OFDM/OQAM, the behavior of MIR MRT, MIR MMSE and ZF precoders is very similar to the one of MRT, MMSE and ZF precoders for MIMO OFDM. This confirms the interest of designing new precoders such as MIR MRT and MIR MMSE precoders for OFDM/OQAM, as they do outperform ZF precoder at low SNR.

When comparing MRT OFDM and MIR MRT OFDM/OQAM, one can observe that the first solution is better at low SNR while the second solution is better at high SNR. This is due to the fact that MRT equivalent channel R^l has real coefficients on its diagonal. Therefore, MIR MRT equivalent channel has the same diagonal than MRT equivalent channel but has lower out of diagonal terms (and thus lower interference). As a consequence MIR MRT is a little bit closer to ZF than MRT is. Therefore, as ZF, MIR MRT outperforms MRT at high SNR and is outperformed by MRT at low SNR.

When comparing MMSE OFDM and MIR MMSE OFDM/OQAM, one can observe that the first solution always outperforms the second one, because it is perfectly adapted to the noise level.

5.2.5.2 Spectral Efficiency (Accounting for Guard Interval)

Fig. 5.2.3 does not provide a fair comparison between MIMO OFDM and MIMO OFDM/OQAM as it does not account for the guard interval of OFDM. We therefore plot $C^{ofdm,zf}$, C_{ofdm}^{zf} , C_{ofdm}^{mrt} , C_{ofdm}^{mmse} , C_{oqam}^{zf} , C_{oqam}^{mirmrt} , $C_{oqam}^{mirmmse}$ in Fig. 5.2.4, as a function of SNR. This time, in many SNR conditions, MIMO OFDM/OQAM outperforms MIMO OFDM. Indeed, For SNR values between 15 and 25 dB,

in particular, we observe that $C_{oqam}^{mirmrt} > C_{ofdm}^{mrt}$, $C_{oqam}^{mirmmse} > C_{ofdm}^{mmse}$ and also that $C_{oqam}^{mirmmse}$ is better than all solutions. This confirms the interest in designing new precoders for MIMO OFDM/OQAM, as better performance can be achieved than with MIMO OFDM, at least when a large guard interval is necessary for OFDM, and under the assumption that the OFDM/OQAM prototype filter is properly localized in time and frequency to verify Eq. 5.2.6.

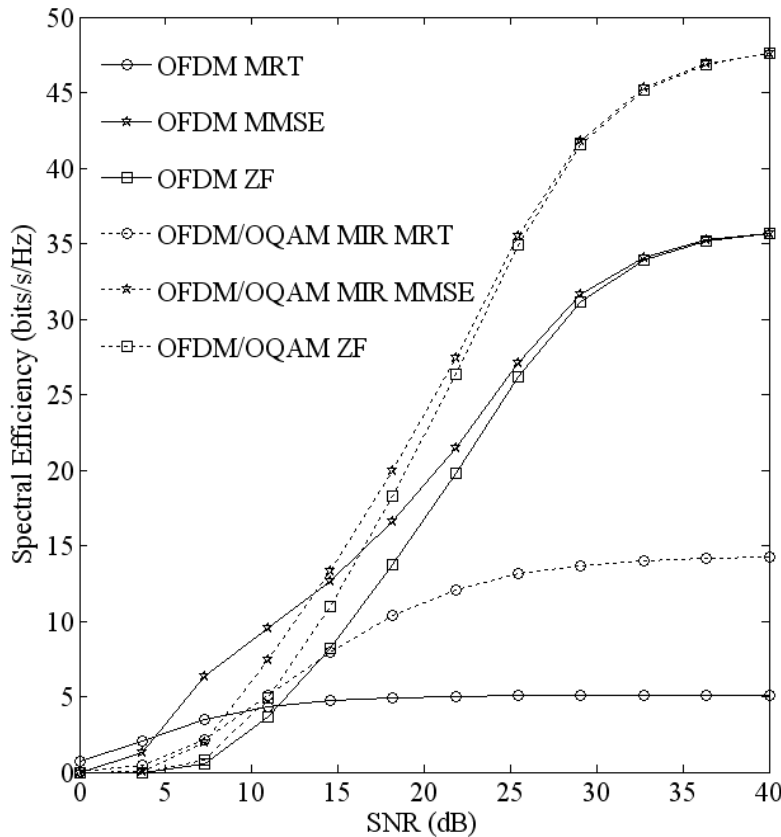


Fig. 5.2.4 Spectral efficiencies with $\frac{T_u}{T_s^{OFDM}} = 0.75$ and $\frac{T_u}{T_s^{OQAM}} = 1$, 8x8 MIMO

5.2.6 Conclusion

New precoders, called MIR MRT and MIR MMSE precoders, based on traditional MRT and MMSE precoders have been proposed to perform data multiplexing in the spatial domain for OFDM/OQAM. They are designed so that the equivalent channel after precoding and wireless propagation is "made real". As a consequence, a low complexity receiver, simply extracting the real part of the received signal, is enough to de-multiplex data streams without suffering from inter-carrier interference. Only inter-data streams interference, as for an OFDM system remains. First performance evaluation studies show that MIR MRT and MIR MMSE precoders do behave like MRT and MMSE precoders. Finally, when the ratio between the useful symbol duration and the total OFDM symbol duration is 0.75, OFDM/OQAM with MIR MMSE precoder outperforms all MIMO OFDM solutions, in many SNR

conditions. Further studies are needed to assess the performance of MIR precoders by simulations including the effective impact of some given OFDM/OQAM filters.

5.3 Time reversal for ant trails in wireless networks

5.3.1 Introduction

This study proposes to use standard wireless networks to guide robots along unknown itineraries which have been previously taken by human or robotic explorers. The paper tackles the problem of navigation and exploration, in the particular and challenging context of complex environments without maps.

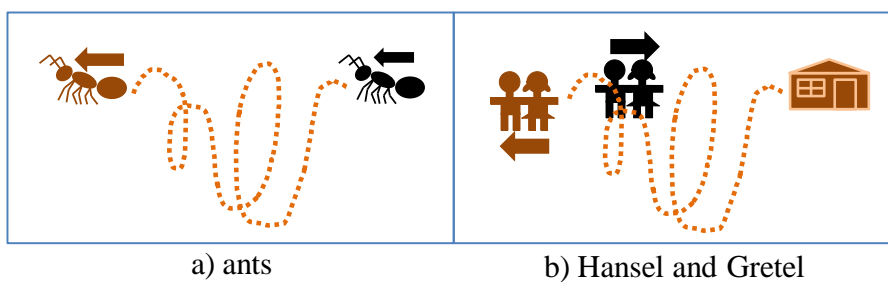


Fig. 5.3.1 two examples of ‘exploration-followed-by-navigation’ process

Fig. 5.3.1 illustrates two well known examples of such ‘exploration-followed-by-navigation’ procedure. The first example comes from nature [130]. A first ant leaves a pheromone trail along its path, during its research for food. Later on, another ant follows the pheromone trail to reach the food. The second example comes from child literature [131]. During the day, Hansel and Gretel explore the forest and leave white pebbles along their path. When the night falls, the children follow the path of pebbles shining under the moonlight, and find their way back to home. In both examples, a two-step procedure is performed: during an exploration phase, a moving ‘explorer’ marks his itinerary with beacons (either pheromones or white pebbles); later on, during a navigation phase, a ‘navigator’ follows the path of beacons, either in the forward or backward direction. We stress that no map of the environment is necessary.

In [132], robots mimic ants by generating and detecting odors. However, due to the persistence of odors, this solution does not seem practicable. In [133], a human deploys a network of telecommunicating nodes along the desired trajectory. Later on, the nodes are activated remotely to broadcast a wireless beacon, one after the other. Attracted by the beacon the robot moves from one node to the other. As the nodes must be deployed again for each new trajectory, this solution is not practicable either. Alternative solutions such as in [134][135] allow for the deployment of nodes in arbitrary locations. This time, all nodes send beacons. The ‘navigator’ analyses the delay of the signal received from each node and deduces its position relatively to the nodes, using a triangularization method. The ‘navigator’ uses a map of the environment, with the recorded positions of the nodes and the desired

trajectory, to deduce its own position and guide himself along the trajectory. The drawback of such technique is that a map is required. Also, highly complex triangularization techniques are required to cope with complex environments undergoing strong multi-path, such as indoor.

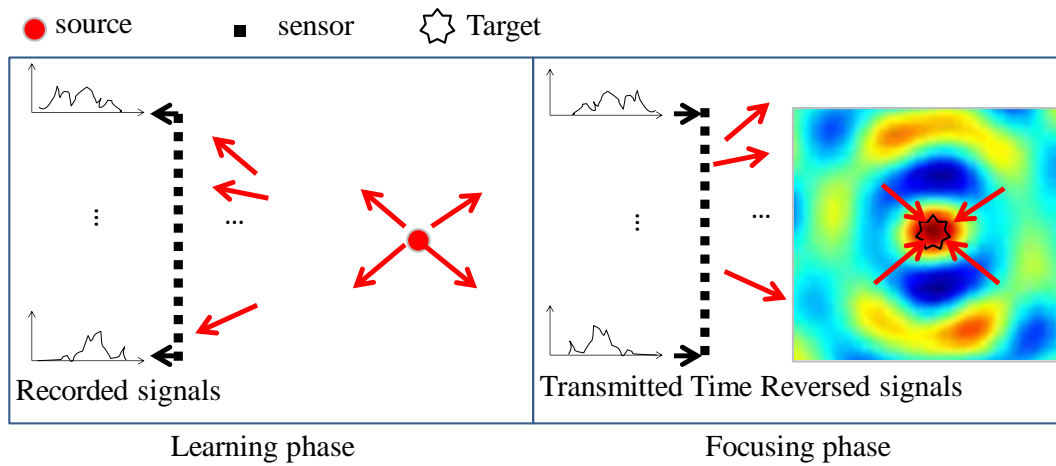


Fig. 5.3.2 Time reversal focusing

Recently, [136] has proposed to replace physical kilometer markers on the railway tracks to facilitate tracks maintenance, by virtual electromagnetic beacons which are created by radio transmitters placed outside the railway. TR is used to generate the focused beacons. As explained in section 2 and as illustrated in Fig. 5.3.2, during a learning phase, a source sends an ultrasound pulse and a network of sensors records the received signals; during the focusing phase, the network of sensors plays the recorded signals time reversely. The resulting wave propagates back to the source with a high power at the source: space-time focusing is obtained. As explained in section 2, MRT beamforming, applied to a multi-carrier waveform such as OFDM, is a variant of Time reversal focusing, at the sub-carrier level.

In this study, we propose a new scheme, called ‘time reversal for Ant Trails’ (TRAT). As in [134] [135], it relies on a network of arbitrarily deployed nodes. Similarly to [133], beacons are placed along the considered trajectory of the ‘explorer’ to guide the ‘navigator’. As in [136], these beacons are ‘virtual’ and generated by distant nodes thanks to Time reversal focusing technique. Finally, to ensure that TRAT is compatible with wireless standards using OFDM [137][112], Maximum Ratio Transmission, as a variant of Time reversal, is used on a sub-set of sub-carriers [85].

The paper is organized as follows. Sub-section 5.3.2 describes the proposed system. Sub-section 5.3.3 gives the performance evaluation methodology. Sub-section 5.3.4 provides some simulation results. Sub-section 5.3.5 concludes this study.

The following notations are used throughout this study:

- $c = 3 \times 10^8$ m/s is the speed of light;

- $\vec{\mathbf{d}}^n$ is the displacement vector of the navigator at the iteration number n ;
- D_{max} is the maximum distance reached by the navigator without being lost;
- D_{lost} is the distance for which P_{lost} is ensured;
- f_0 is the considered sub-carriers average frequency;
- $f_{0,ref}$ is the carrier frequency of the reference simulated scenario;
- $\mathbf{F}^n \in \mathbb{C}^{N_{rx} \times N_{tx}}$ be the channel matrix between the network node and the ‘navigator’;
- $\vec{\mathbf{m}}^j$ is the position vector of the navigator antenna j relatively to the ‘navigator’ position;
- j is the navigator antenna index;
- k is the network antenna index;
- l^n is the index of the navigator antenna being detected;
- L is the length of the labyrinth in meters;
- n is the iteration (or beacon) index;
- n_{max} is the number of iterations for which the navigator is considered as lost;
- N_{beacon} is the number of beacons;
- N_{MPC} is the number of multipath components;
- $N_{MPC,ref}$ is the number of multipath components of the reference simulated scenario;
- N_{run} is the number of simulation runs;
- N_{rx} is the number of receive antennas;
- $N_{rx,ref}$ is the number of receive antennas of the reference simulated scenario;
- N_{traj} is the number of trajectories;
- N_{tx} is the number of transmit antennas;
- $N_{tx,ref}$ is the number of transmit antennas of the reference simulated scenario;

- P_{lost} is the target probability of being lost;
- \mathbf{p}^n is the MRT beamformer at iteration number n ;
- S is the side of the square grid in which sensing is performed;
- $\mathbf{s}^n \in \mathbb{C}^{N_{rx} \times N_{tx}}$ is the equivalent channel after precoding and propagation;
- $\vec{\mathbf{u}} = (1,0,0)$;
- $\vec{\mathbf{v}} = (0,1,0)$;
- $\vec{\mathbf{z}}^n$ as the position of the ‘explorer’ at the iteration number n , it is also the beacon number n ;
- $\vec{\mathbf{z}}^n$ is the position of the ‘navigator’ at iteration number n ;
- \mathbf{h}_k^n is the channel between the antenna of the ‘explorer’ and the antenna number k of the network, at the iteration number n ;
- $x_{t,r}$ is the value of D_{max} for the trajectory number t and the simulation run r ;
- β is the angle of the linear trajectory;
- δ is the inter-beacon spacing in meters;
- δ_{ref} is inter-beacon spacing in meters of the reference simulated scenario;
- $\gamma_k^{n,l}$ is the amplitude of departure of the multipath component number l for network antenna k and iteration number n ;
- $\gamma_k^{m,l}$ is the amplitude of arrival of the multipath component number l for network antenna k and iteration number n ;
- $\theta_k^{n,l}$ is the angle of departure of the multipath component number l for network antenna k and iteration number n ;
- $\eta(x_{t,r}, D) = 1$ if $x_{t,r} < D$ and $\eta(x_{t,r}, D) = 0$ otherwise;
- λ is the wavelength;
- $\lambda_{0,ref}$ is the wavelength of the reference simulated scenario;

- $\sigma_{\gamma_k^{n,l}}$ is the variance of $\gamma_k^{n,l}$;
- $\sigma_{\gamma_k^{m,l}}$ is the variance of $\gamma_k^{m,l}$.

5.3.2 System model

5.3.2.1 Overall System Description

We consider a bi-directional wireless communication between a network equipped with N_{tx} antennas, and two devices: the ‘explorer’ and the ‘navigator’. The antennas of the network have fixed arbitrary positions and can be either co-located or distributed. The ‘explorer’ has one antenna, whereas the ‘navigator’ has N_{rx} receive antennas. OFDM is considered, and a sub-set of contiguous sub-carriers is used. The propagation channel between each transmit antenna and each receive antenna (either from the ‘navigator’ or the ‘explorer’) is assumed to be flat in frequency over the considered sub-carriers, and is therefore modeled as a complex coefficient. We define f_0 as the considered sub-carriers average frequency. $\lambda = c/f_0$ is the corresponding wavelength, with $c = 3 \times 10^8$ m/s being the speed of light. The ‘explorer’ receive antenna number j has a fixed position vector \vec{m}^j relatively to the ‘navigator’ position \vec{z} . Both the ‘navigator’ and the ‘explorer’ are moving.

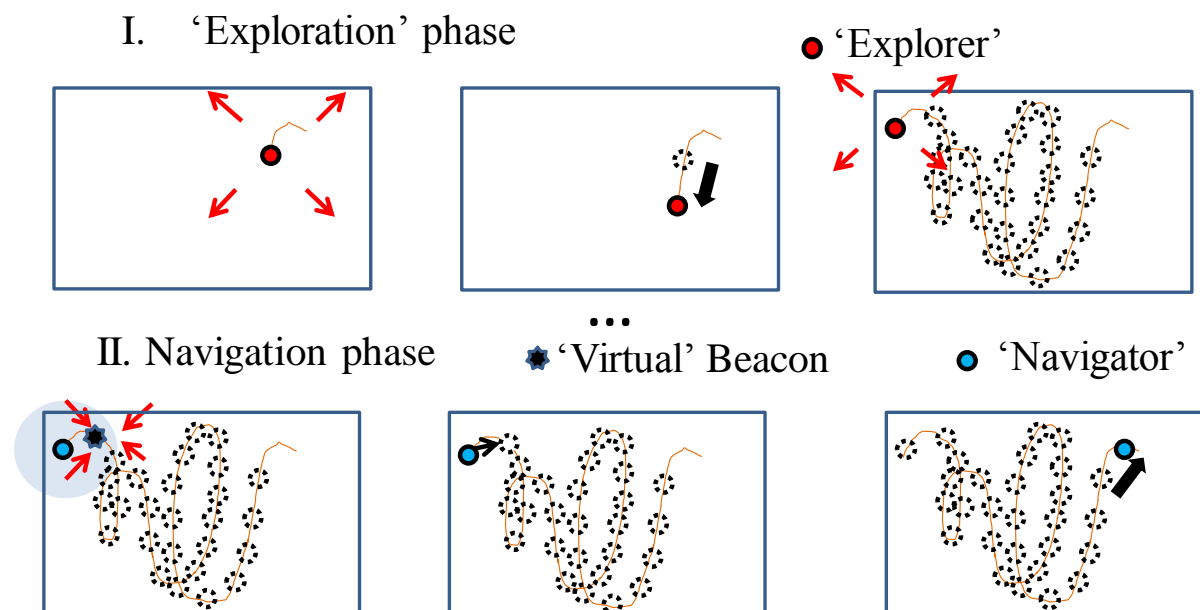


Fig. 5.3.3 TRAT procedure

As illustrated in Fig. 5.3.3, the TRAT scheme consists of two phases. During the ‘exploration’ phase, the trajectory of the moving ‘explorer’ is recorded by the network, under the shape of received beacons. During the ‘guided-navigation’ phase, the ‘navigator’ follows the path of ‘virtual’ beacons generated by the network based on the previously recorded trajectory.

5.3.2.2 Exploration phase

During the ‘exploration’ phase, the ‘explorer’ moves from an ‘start’ position to an unknown ‘destination’ position, and sends a wireless beacon, iteratively. Let N_{beacon} be the total number of iterations. By its definition, N_{beacon} is therefore also the number of beacons. For the iteration number n , based on the received beacon number n , the network perfectly estimates \mathbf{h}^n which is defined as follows: \mathbf{h}_k^n is the channel between the antenna of the ‘explorer’ and the antenna number k of the network, at the iteration number n . We denote $\vec{\mathbf{z}}^n$ as the position of the ‘explorer’ at the iteration number n . As $\vec{\mathbf{z}}^n$ is unknown, the network records \mathbf{h}^n instead, to have a picture of the exploratory trajectory.

5.3.2.3 Guided-navigation phase

During the navigation phase, the following procedure is performed, iteratively. During the iteration number n , the network generates the ‘virtual’ beacon number n , which is a focused signal centered over position $\vec{\mathbf{z}}^n$. As the network does know $\vec{\mathbf{z}}^n$, it simply transmits a wireless beacon pre-coded by the MRT beamformer \mathbf{p}^n , given by: $\mathbf{p}^n = (\mathbf{h}^n)^H$. The ‘navigator’ uses its antennas to estimate the location of the ‘virtual’ beacon relatively to its own position. Let \mathbf{F}^n be the channel matrix between the network node and the ‘navigator’. \mathbf{F}_{jk}^n is the channel between the antenna number k of the network and the ‘navigator’ antenna number j . The ‘virtual’ beacon is received at the ‘navigator’ through the equivalent channel \mathbf{s}^n given by [8]: $\mathbf{s}^n = \mathbf{F}^n \mathbf{p}^n$. The ‘navigator’ perfectly estimates \mathbf{s}^n based on the received beacon, and then, determines the antenna l^n , among all its antennas, which maximizes the received power: $l^n = \arg(\max_l |\mathbf{s}^n|^2)$. Let us define $\vec{\mathbf{z}}^n$ as the current position vector of the ‘navigator’. The ‘navigator’ moves himself by a vector of displacement $\vec{\mathbf{d}}^n = \vec{\mathbf{m}}^{l^n}$. Therefore, its new position $\vec{\mathbf{z}}^{n+1}$ is given by: $\vec{\mathbf{z}}^{n+1} = \vec{\mathbf{z}}^n + \vec{\mathbf{d}}^n$. Finally, the ‘navigator’ sends a message to the network, asking for the ‘virtual’ beacon number $n + 1$.

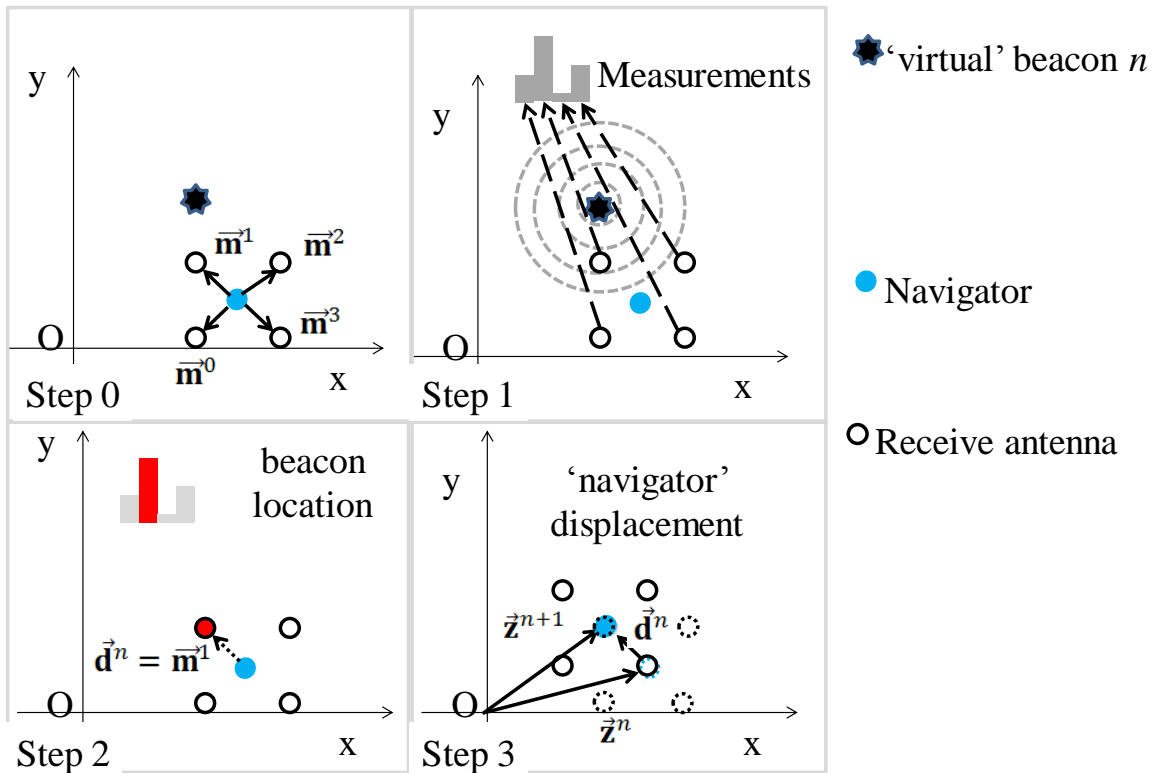


Fig. 5.3.4 'Navigation' phase

This iterative procedure, is run either in increasing (like ants) or de-creasing (like Hansel & Gretel) order of n , until the destination is reached. We stress that neither the network, nor the 'explorer' or the 'navigator' need to know the absolute positions \vec{z}^n or \vec{z}^{n+1} . Fig. 5.3.4 illustrates the 'navigation' phase. One must notice that the inter-beacon spacing and the receive array size should be chosen 'smaller' than the focusing area (which is around half a wavelength large).

5.3.2.4 Lost 'navigator' criterium

If at iteration number n_{max} , the 'navigator' gets farther than one wavelength from its target 'virtual' beacon, i.e. $\|\vec{z}^{n_{max}} - \vec{z}^{n_{max}}\| > \lambda$, we consider that the navigator is 'lost', and the system behavior is no longer modeled.

5.3.2.5 Emulating a dense pattern of 'virtual' receive antennas

A dense pattern of receive antennas in space is desirable to detect the 'virtual' beacon with precision. However, the coupling effect prevents using such arrays of antennas. We propose to use a small set of antennas spaced by at least half a wavelength to avoid coupling. These physical antennas are moved mechanically to emulate N_{rx} very close 'virtual' antennas. In this case, the coefficients of the vector \mathbf{s}^n are acquired sequentially, in time instead of simultaneously, according to a 'scanning' method, which is either 'Grid-based' or 'Rotation-based'. In the grid-based scanning method, a single physical antenna is moved to occupy a regular grid of positions in a square of side S . $\sqrt{N_{rx}}$ is the number of

lines and columns of the grid. In the rotation-based scanning method, two physical antennas separated by a distance S , are mechanically and regularly rotated $N_{rx}/2$ times around an axis. On one hand, if $S \gg \lambda$, a huge N_{rx} is needed to achieve a high spatial density, and the resulting ‘navigation’ procedure is complex. On the other hand, if $S \ll \lambda$, the ‘virtual’ beacon risks to be out of the scanned area. We therefore choose $S = 0.5\lambda$ as a trade-off between complexity and efficiency. The ‘virtual’ antenna positions are illustrated in Fig. 5.3.5 for $S = 0.5\lambda$, and a few several values of N_{rx} .

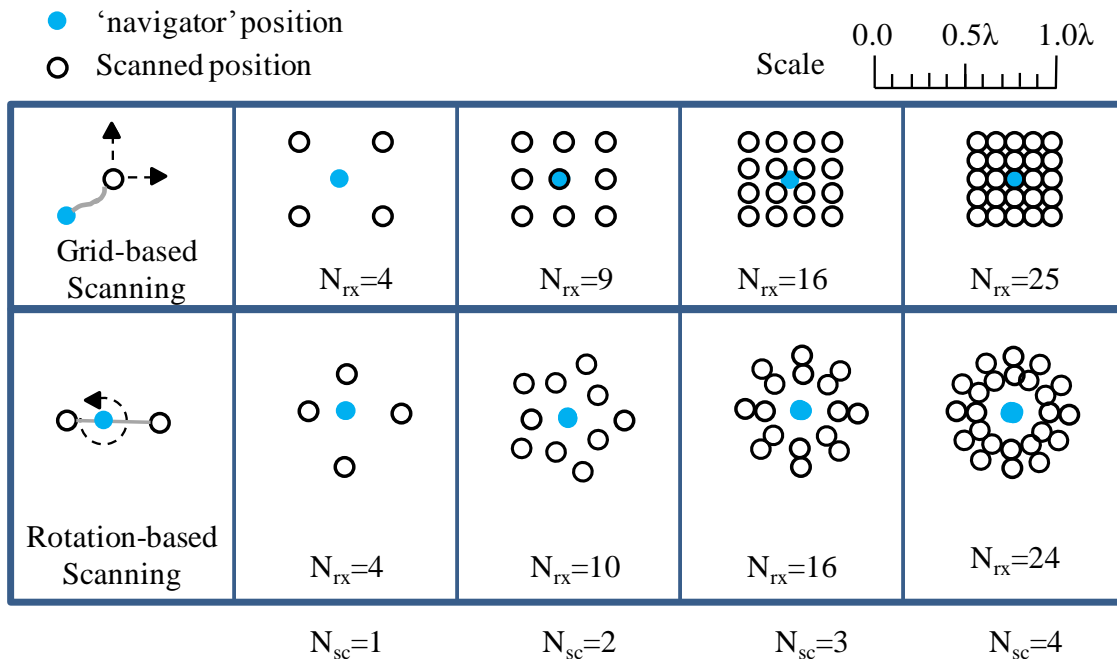


Fig. 5.3.5 Positions of ‘virtual’ antennas depending on the scanning method

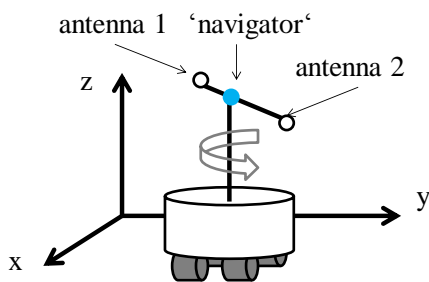


Fig. 5.3.6 Example of implementation of the rotation-based scanning

Fig. 5.3.6 illustrates a potential implementation of the ‘navigator’: a mobile robot with a rotating couple of antennas.

5.3.3 Performance evaluation methodology

This sub-section, we describe the performance evaluation methodology.

5.3.3.1 Random spatially correlated channel model with static scatterers

We use a simplified version of the channel model in [86] for wireless fixed and mobile networks with random scatterers. We assume that the ‘navigator’ and the ‘explorer’ move in the same environment, with the same static scatterers. The channel between two antennas is therefore a function of the positions of the antennas. Also, we assume the ‘navigator’ and the ‘explorer’ to move on a plan and 2-dimensional propagation is modeled.

Let us consider the iteration number n of the exploration procedure. The channel \mathbf{h}_k^n (which is the channel between the network antenna k and the ‘explorer’) is modeled as a sum of N_{MPC} Multi-Path Components (MPC), each corresponding to one scatterer. The MPC number l is a plane wave, with the angle $\theta_k^{n,l}$ and the amplitude $\gamma_k^{n,l}$ at the departure, and the angle $\theta_k^{\prime n,l}$ and the amplitude $\gamma_k^{\prime n,l}$ at the arrival. $\theta_k^{n,l}$, $\theta_k^{\prime n,l}$, $\gamma_k^{n,l}$ and $\gamma_k^{\prime n,l}$ are independent and random variables. They vary from one scatterer to the other, and from one antenna to the other. This ensures that antennas are un-correlated at the network side, which is a good assumption for a distributed antenna system or a highly complex environment like indoor, with strong multi-path and NLOS propagation. These parameters also vary from one iteration to the other, even in the case of close iterations. This assumption is used, as fully spatially correlated channels over long distances (such as a trajectory) is still a research topic [138]. $\theta_k^{n,l}$ and $\theta_k^{\prime n,l}$ are uniformly distributed between 0 and 2π . $\gamma_k^{n,l}$ and $\gamma_k^{\prime n,l}$ are complex gaussian variables, with average powers $\sigma_{\gamma_k^{n,l}} = \sigma_{\gamma_k^{\prime n,l}} = N_{MPC}^{-1}$. Therefore, the channel is normalized.

Let us consider the iteration number n of the navigation procedure. Assuming planar waves, the channel between the antenna number k of the network and the receive antenna number j of the ‘navigator’, is given by: $\mathbf{h}_k^n = \sum_{l=1}^{N_{MPC}} \gamma_k^{n,l} \gamma_k^{\prime n,l} e^{j\theta_k^{n,l}} e^{j\theta_k^{\prime n,l}} e^{j2\pi(\lambda^{-1} \vec{\mathbf{m}}^j \cdot \vec{\mathbf{w}}_k^{n,l})}$, where, $\vec{\mathbf{w}}_k^{n,l} = \cos(\theta_k^{n,l}) \vec{\mathbf{u}} + \sin(\theta_k^{n,l}) \vec{\mathbf{v}}$, $\vec{\mathbf{u}} = (1,0,0)$ and $\vec{\mathbf{v}} = (0,1,0)$. The channel \mathbf{F}_{kj}^n between the antenna j of the ‘navigator’ and the antenna k of the network is then deduced from the position $\vec{\mathbf{z}}^n$ of the ‘virtual’ beacon number n and the position $\vec{\mathbf{z}}^{\prime n}$ of the ‘navigator’ as follows:

$$\mathbf{F}_{kj}^n = \sum_{l=1}^{N_{MPC}} \gamma_k^{n,l} \gamma_k^{\prime n,l} e^{j\theta_k^{n,l}} e^{j\theta_k^{\prime n,l}} e^{j2\pi(\lambda^{-1}(\vec{\mathbf{m}}^j + \vec{\mathbf{z}}^{\prime n} - \vec{\mathbf{z}}^n) \cdot \vec{\mathbf{w}}_k^{n,l})}.$$

The term $(\vec{\mathbf{m}}^j + \vec{\mathbf{z}}^{\prime n} - \vec{\mathbf{z}}^n) \cdot \vec{\mathbf{w}}_k^{n,l}$ models the spatial correlation. For instance, the channels \mathbf{F}_{kj}^n and $\mathbf{F}_{k j'}^n$ sensed by antennas j and j' , respectively, have close values if the antennas are close in space, i.e. if $\vec{\mathbf{m}}^j \approx \vec{\mathbf{m}}^{j'}$. Similarly, if the position $\vec{\mathbf{z}}^{\prime n}$ of the ‘navigator’ and the position $\vec{\mathbf{z}}^n$ of the ‘virtual’ beacon are close in space, the channel \mathbf{F}_{kj}^n sensed during the navigation is close to the channel \mathbf{h}_k^n recorded during the exploration. This model which is valid only if the ‘navigator’ is in the vicinity of the ‘virtu-

al' beacon is suited for the purpose of the TRAT assessment, as we only model what happens before the 'navigator' gets lost (as explained in sub-section 5.3.2.4).

5.3.3.2 Description of one simulation run and D_{\max} metric

The TRAT system is tested by simulation. First, the equation of the trajectory is defined, with its length L . The explorer is assumed to move with a constant speed, by steps of δ (in meters). For each iteration number n , the position $\vec{\mathbf{z}}^n$ is computed based on δ and the equation of the trajectory, according to the exploration procedure described in sub-section 5.3.2. Then, for each n , the random parameters $\theta_k^{n,l}$, $\theta'_k{}^{n,l}$, $\gamma_k^{n,l}$ and $\gamma'_k{}^{n,l}$ are drawn and the channel \mathbf{h}^n is derived, according to sub-section 5.3.3.1. In a second phase, for each iteration number n , the channels \mathbf{F}^n are computed, according to sub-section 5.3.3.1, and $\vec{\mathbf{z}}^n$ is computed using the 'navigation' procedure described in 5.3.2.

If at $n = n_{\max}$, the 'navigator' gets lost (according to the criteria defined in 5.3.2), the simulation is stopped, and the current position of the 'navigator' $\vec{\mathbf{z}}^{n_{\max}}$ is recorded as the 'navigator' destination and compared to the desired destination. Also, the distance $D_{\max} = n_{\max}\delta$ is stored.

5.3.4 Simulation results

This sub-section presents simulation results obtained with the methodology described in sub-section 5.3.3. As explained in sub-section 5.3.2.3, the inter-beacon spacing and the receiver array size must be smaller than the focusing area to ensure a successful navigation. We therefore expect the TRAT performance to strongly depend on the parameters δ , N_{tx} , N_{rx} , λ and N_{MPC} .

5.3.4.1 Study on one labyrinth type trajectory

In this sub-section, the 'labyrinth-type' trajectory described in Fig. 5.3.7, is studied to provide an intuitive illustration of the effect of various parameters on the TRAT system performance.

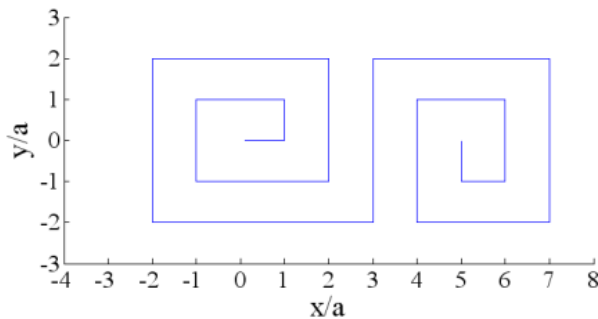


Fig. 5.3.7 Labyrinth-type trajectory, with total $L=49a$

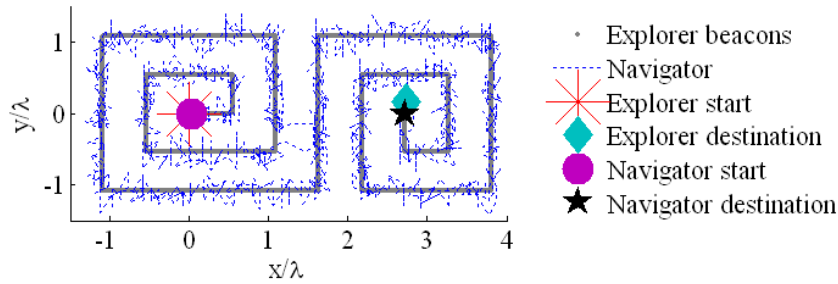


Fig. 5.3.8 Reference simulation

A reference simulation is run, with the following parameters: the length of the labyrinth is $L=10$ meters, the carrier frequency is $f_{0,ref} = 800$ MHz, the wavelength is $\lambda_{0,ref} = 37.5$ centimeters, the inter-beacon separation is $\delta_{ref} = 0.025 \times \lambda_{0,ref}$, the number of transmit antennas of the network is $N_{tx,ref} = 10$, the number of multi-path components is $N_{MPC,ref} = 10$ and the ‘navigator’ uses rotation-based scanning with $N_{rx,ref} = 24$ virtual receive antennas. The result of the simulation is given in Fig. 5.3.8. The ‘navigator’ is guided successfully from the starting point to the destination, erratically though. The erratic behavior is due to the fact that the inter-beacon spacing is chosen much smaller than the ‘navigator’ displacements. On one hand beacons are spaced by $\delta_{ref} = 0.025$ wavelengths. On the other hand, receive antennas are spaced by 0.2 to 0.7 wavelengths (as illustrated in Fig. 5.3.6 for the rotation-based scanning with $N_{rx} = 24$ antennas) and thus generate displacements of the same size. As the ratio between the displacements and the inter-beacon spacing is in the order of 10 to 30, the ‘navigator’ tends to stay around the same area.

In next simulations, all parameters except one are kept equal to the values set for the reference simulation. We will therefore visualize the impact of one parameter at a time.

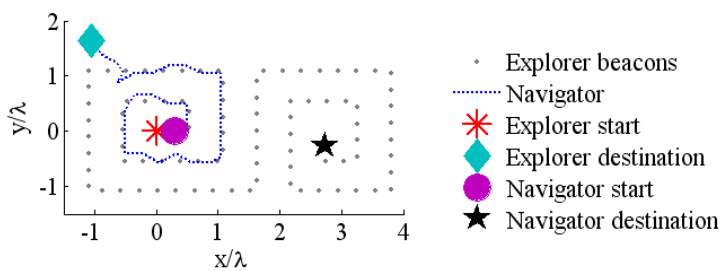


Fig. 5.3.9 $\delta = 0.3 > \delta_{ref}$

Fig. 5.3.9, illustrates a simulation run with a larger inter-beacon spacing $\delta = 0.3 > \delta_{ref}$. The trajectory of the ‘navigator’ is no longer erratic, as δ is in the order of magnitude of the ‘displacement’. However, the risk of having a ‘virtual’ beacon out of the area scanned by the ‘navigator’ is greater, and the ‘navigator’ gets lost. We conclude that the smaller δ the better.

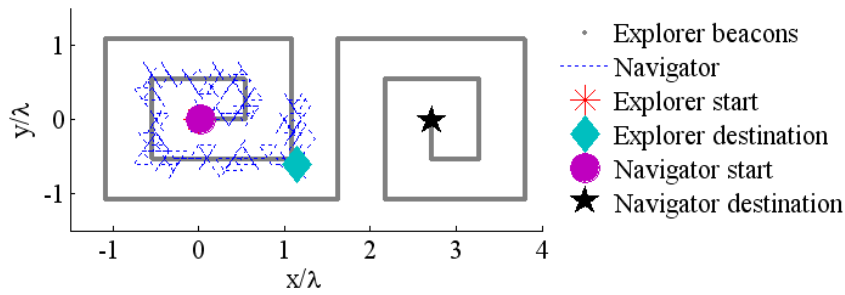


Fig. 5.3.10 $N_{rx} = 4 < N_{rx,ref}$

Fig. 5.3.10, illustrates a simulation run with a lower number of receive antennas $N_{rx} = 4 < N_{rx,ref}$. As illustrated in Fig. 5.3.6, the spatial density of the scanning is low. As a consequence, the precision of the navigation is lower and the ‘navigator’ gets lost. We conclude that the larger N_{rx} the better.

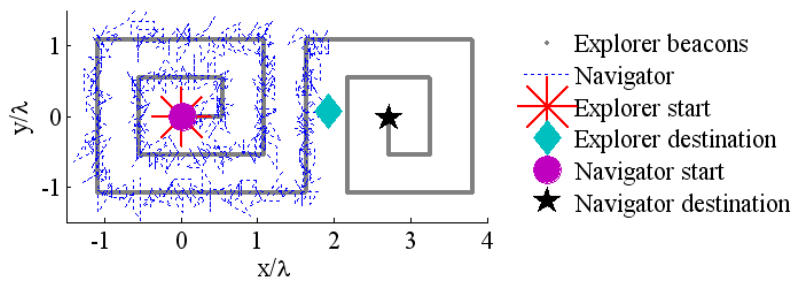


Fig. 5.3.11 $N_{tx} = 6 < N_{tx,ref}$

Fig. 5.3.11, illustrates a simulation run with a lower number of transmit antennas $N_{tx} = 6 < N_{tx,ref}$. It is well known that the spatial focusing quality increases with N_{tx} . Decreasing N_{tx} therefore increases side lobes in space, and the risk for the ‘navigator’ to move get in the wrong direction. As a consequence, the ‘navigator’ gets lost before the destination. We conclude that the greater N_{tx} , the better (assuming perfect CSIT).

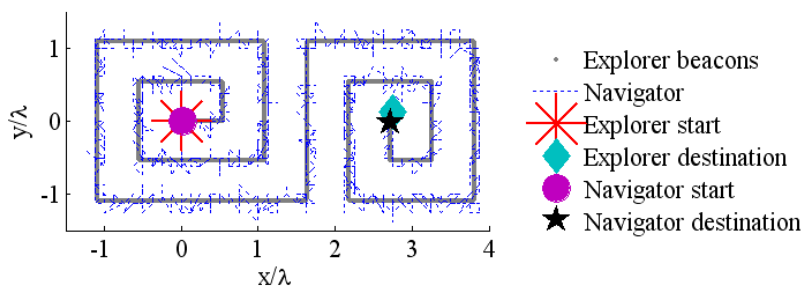


Fig. 5.3.12 Scanning: grid-based instead of rotation-based

Fig. 5.3.12, illustrates a simulation run with grid-based scanning and $N_{rx} = 25$ instead of rotation-based scanning with $N_{rx} = 24$. As the spatial density is similar, the ‘navigator’ is successfully guided to the destination, with a slightly different path though.

Fig. 5.3.13, illustrates the result of a simulation run with a higher carrier frequency $f_0 = 5\text{GHz} > f_{0,ref}$. This corresponds to a wavelength of $\lambda = 6\text{cm}$. As the size of the focusing area depends on the wave-

length, the inter-beacon spacing and the inter-antenna spacing are reduced accordingly. We keep $\delta/\lambda = \delta_{ref}/\lambda_{0,ref} = 0.025$ and $S/\lambda = 0.5$. As a consequence, the ‘navigator’ path is much closer to the trajectory which still has a length of $L = 10$ meters. Surprisingly, the performance is degraded by smaller wavelength and the smaller inter-beacon spacing and the smaller scanned area. Actually, this new configuration increases the number of iterations $N_{beacons}$ for the entire trajectory. As at each iteration there is the same risk to get lost as in the reference simulation, increasing $N_{beacons}$, also increases the probability of getting lost before destination.

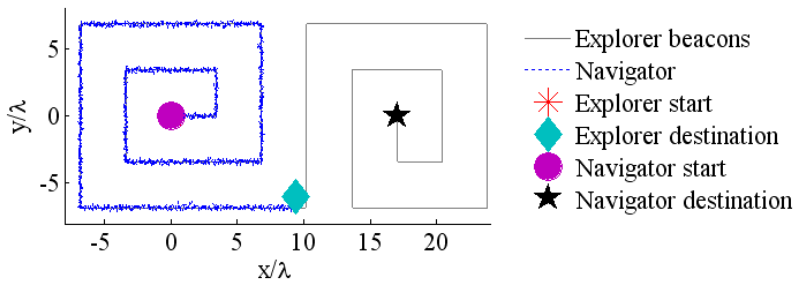


Fig. 5.3.13 $f_0 = 5GHz > f_{0,ref}$

5.3.4.2 A more statistical study on the labyrinth type trajectory

The channel is generated randomly (through parameters $\theta_k^{n,l}$, $\theta_k^{m,l}$, $\gamma_k^{n,l}$). Hence, a statistical study of the performance requires a large number N_{run} of independent simulations, with different random values. For each simulation, the D_{max} value is collected, and then statistics over the N_{run} simulations are performed. The cumulative density function (cdf) of D_{max} is defined as the probability of $D_{max} < x$. It is computed as the ratio of the number of runs with $D_{max} < x$ divided by N_{run} . Simulations are run with following the parameters: $L=200$ meters, all other parameters are the same as for the reference simulation. A first set of simulations are run, with four different values of N_{tx} . The cdf of D_{max} is plotted in the Fig. 5.3.14, and confirms the well known advantage of using a large N_{tx} to create well focused ‘virtual’ beacons. Another set of simulations are run, with different values of N_{MPC} . The cdf of D_{max} is plotted in Fig. 5.3.15, and illustrates the well known property of time reversal of exploiting strong multi-path for better spatial focusing. Therefore, the larger N_{MPC} , the better.

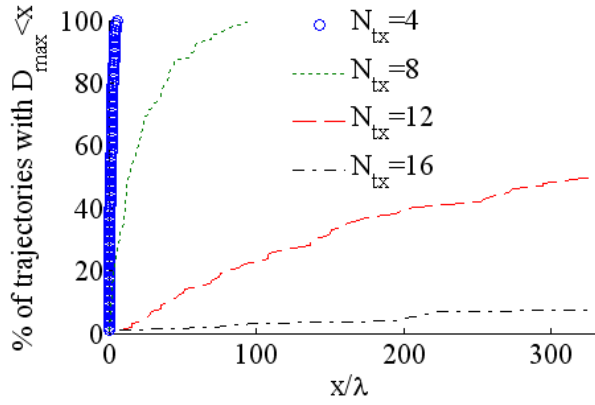


Fig. 5.3.14 CDF of D_{max} with $N_{MPC} = N_{MPC,ref}$ and varying N_{tx}

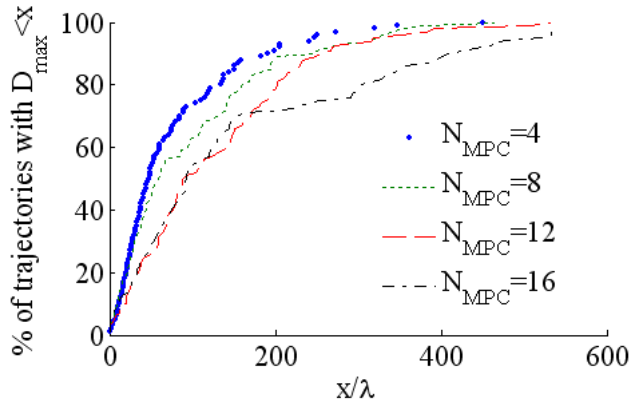


Fig. 5.3.15 CDF of D_{max} with $N_{tx} = N_{tx,ref}$ and varying N_{MPC}

5.3.4.3 Performance metrics for statistical study

In this sub-section, linear trajectories starting at coordinate $(0,0,0)$ and ending at coordinate $L(\cos(\beta), \sin(\beta), 0)$, with $0 \leq \beta < 2\pi$. To obtain more statistical results than with the labyrinth-type trajectory, we propose to assess the proposed scheme over a large number N_{traj} of linear trajectories with different β values. For each trajectory, N_{run} independent simulations are run, and the D_{max} metric is collected. We denote $x_{t,r}$ as the value of D_{max} for the trajectory number t and the simulation run r . The probability of being lost at distance D is given by:

$$\Gamma(D) = (N_{run}N_{traj})^{-1} \sum_{t=0}^{N_{traj}-1} \sum_{r=0}^{N_{run}-1} \eta(x_{t,r}, D),$$

where $\eta(x_{t,r}, D) = 1$ if $x_{t,r} < D$ and $\eta(x_{t,r}, D) = 0$ otherwise. Let P_{lost} be a target probability of being lost. Let D_{lost} be the distance for which P_{lost} is ensured. D_{lost} is given by:

$$D_{lost} = \arg_D(\Gamma(D) = P_{lost}).$$

Simulations are run with a trajectory length is $L=10$ meters and the same parameters as for the reference simulation. A first set of simulations is run with grid-based scanning, and is illustrated in Fig. 5.3.16, for various target P_{lost} and N_{rx} values. As expected, larger distances D_{lost} are reached, but only

with larger probabilities P_{lost} of being lost. Also, large N_{rx} (high spatial density of the scanning) increase the scheme performance. The same set of simulations, is run again, with the rotation-based scanning instead of the grid-based scanning, and is illustrated in Fig. 5.3.17. The grid-based scanning slightly outperforms the rotation-based scanning, probably thanks to its more homogeneous pattern.

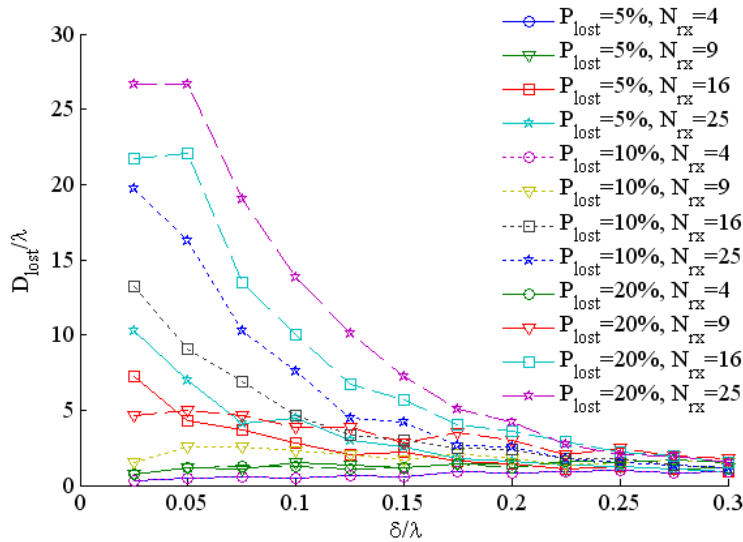


Fig. 5.3.16 Grid-based scanning

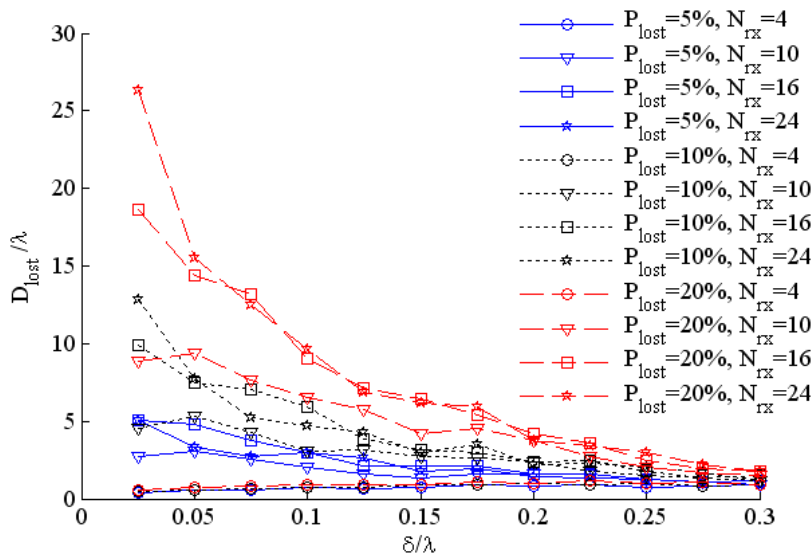


Fig. 5.3.17 Rotation-based scanning

5.3.5 Conclusion

In this study, we introduce a new protocol for wireless networks, called Time reversal for Ant Trails which mimics ants by using electromagnetic ‘virtual’ beacons generated by Time reversal focusing instead of pheromones. During an ‘exploration’ phase, a moving ‘explorer’ regularly sends wireless beacons, which are used by the network to record the trajectory of the ‘explorer’ under the shape of a bank of successive estimates of the propagation channel. Later on, during the ‘navigation’ phase, the network guides a ‘navigator’ with ‘virtual’ electromagnetic beacons generated by Time reversal based

on the recorded channels. The ‘navigator’ locates the beacon and moves towards it, by scanning its close environment. Simulations show that for a given trajectory, the performance of the proposed scheme increases with the quality of the focusing (obtained either with a large number of transmit antennas or strong multi-path), with the precision of the scanning, and decreases with the inter-beacon spacing and the carrier frequency. Further studies will include experimental assessments, more realistic channel models, the analysis of the required signaling and information storage capacity. Finally, the use of large spectrums to obtain better and more robust spatial focusing will be studied.

5.3.6 Details

In this sub-section, we provide the computation of $\vec{\mathbf{m}}^j$. For the grid-based scanning, we set $j = v + u$ with $0 \leq v < \sqrt{N_{rx}} - 1$ and $0 \leq u < \sqrt{N_{rx}} - 1$ and $\vec{\mathbf{m}}^{j=v+u} = S(-\frac{1}{2} + \frac{(v-1)}{\sqrt{N_{rx}-1}}, -\frac{1}{2} + \frac{(u-1)}{\sqrt{N_{rx}-1}} 0)$. For the rotation-based scanning, we define $j = 2v$, with $0 \leq v < N_{rx}/2 - 1$, $\alpha_v = 2\pi v/(N_{rx}/2)$, $\vec{\mathbf{m}}^{j=2v} = 0.2S(\cos(\alpha_v + \pi), \sin(\alpha_v + \pi), 0)$ and $\vec{\mathbf{m}}^{j=2v+1} = 0.3S(\cos(\alpha_v), \sin(\alpha_v), 0)$. Except for $N_{rx} = 4$, where we use a rotation by $\pi/2$.

5.4 Discrete Fourier transform based spatial multiplexing and MRT for millimetre wave large MIMO

5.4.1 Introduction

An air interface such as the 60GHz WIFI standard [139][140][141], can provide throughputs of several Gigabits per second in indoor, by using millimeter-waves (mm-waves). Recent investigations, as illustrated by Fig. 5.4.1, propose to extend the use of mm-waves to the outdoor mesh networks [142][143][144] or to 5G networks [145], for both the direct link and the backhaul link.

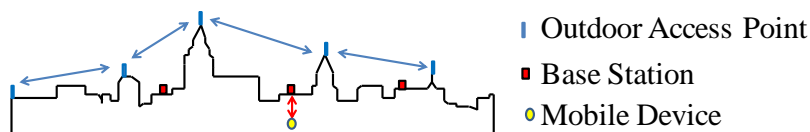


Fig. 5.4.1 Example of outdoor wireless meshed network

The well known MIMO spatial multiplexing techniques, enable to improve the spectral efficiency of a wireless link, by using several antennas at the transmitter and the receiver, provided that the rank of the MIMO channel is large enough[146]. For millimeter waves, a rank much higher than 1 can be achieved even in LOS conditions, as long as the spacing between antennas of the same array is chosen large enough compared to the transmitter-receiver distance (which is typically of tens to a few hundreds of meters) and the wavelength. For instance, in [147], the diffraction theory in optics is used to compute the inter-antenna spacing which ensures that the angular separability of antennas of the transmit array and the angular resolution of the receiver array are equal. The computed inter-antenna spacing is a function of the distance between the transmitter and receiver and of the wavelength. It en-

sure that the MIMO channel is well conditioned. It thus allows the use of low complexity spatial multiplexing schemes such as the ZF [148], the MMSE [10] or the MRT [8] precoders. Similar observations have been made in [149] for short-range communications exploiting the spherical wave.

One could extend the approach of [147] to the mm-waves and the large MIMO systems, which exploit hundreds of antennas to reach huge energy savings [96]. However, in practice, it seems difficult to deploy arrays with the inter-antenna spacing optimized for each possible distance between transmitters and receivers, and for each carrier frequency. If, contrary to what is shown in [9], the inter-antenna spacing is arbitrarily chosen, then the MIMO channel has a great risk to be ill conditioned. Singular value decomposition could be applied [150][151] to determine the number of data streams to be sent, assuming that CSIT and the receiver CSIR. However, in large MIMO systems, the complexity of the processing rapidly grows with the number of antennas, at both the receiver and the transceiver [96]. We acknowledge that for backhauling in the outdoor, the complexity is not an issue, because the channel is static or slowly varies. Indeed, in this case, the SVD processing can be done with a slow update rate. However, in cellular networks [145], where a frequent and fast update is required, low complexity schemes are preferable.

In this study, we propose a new low complexity system for large MIMO mm-wave communications, with arbitrary inter-antenna spacing. This technique, called Discrete Fourier Transform based spatial multiplexing with maximum ratio transmission (DFT-SM-MRT) combines two techniques:

- DFT based Spatial Multiplexing (DFT-SM) ;
- MRT beamforming (equivalently TR on a sub-carrier basis).

The DFT-SM scheme uses an inverse Discrete Fourier Transform (IDFT) performed in the spatial domain [152][153] at the transmitter, and a Discrete Fourier Transform (DFT) also in the spatial domain, at the receiver. When the DFT-SM scheme is used with linear arrays, the data streams are mapped onto beams of various angles of departures [152][153] which are then detected at the receiver side, by beams with various angles of arrivals. When the DFT-SM scheme is used with circular arrays, data streams are mapped onto vortices with various orbital angular momentums [154]. The DFT-SM scheme is better suited for arrays being aligned according to Fig. 5.4.2 and Fig. 5.4.3, for linear and circular arrays, respectively. The authors of [153] have in fact demonstrated that the DFT-SM achieves the SVD performance, if the circular arrays are perfectly aligned. Also, based on a spherical wave channel model, [149] has shown that the alignment of linear arrays provide better conditions for spatial multiplexing in LOS conditions. In practice, slight misalignments (which are expected to reduce the number of streams which can be spatially multiplexed) cannot be avoided. We therefore introduce

the MRT precoder based on CSIT, in order to pre-equalize the channel [10] and compensate for misalignments.



Fig. 5.4.2 DFT-SM for aligned linear arrays

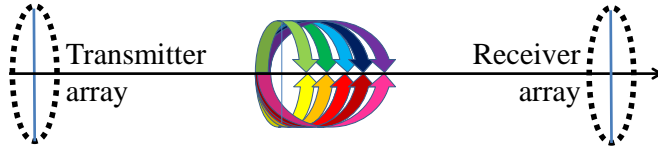


Fig. 5.4.3 DFT-SM for aligned circular arrays

This study is organized as follows. Sub-section 5.4.2 introduces the common system model, sub-section 5.4.3 presents the SVD, DFT-SM, DFT-SM-MRT schemes and a fourth scheme called “DFT-SM-MRT filtered”. Sub-section 5.4.4 presents the performance evaluation methodology. Sub-section 5.4.5 presents some numerical results and sub-section 5.4.6 concludes this study. The following notations are used throughout this study: A^H is the transpose conjugate of A . $E[|\cdot|^2]$ is the expectation operation. A^{DFT} and A^{IDFT} are the butler matrices corresponding to the DFT and IDFT operation respectively [156][157].

The following notations are used for this study:

- $\mathbf{a} \in \mathbb{C}^{N \times 1}$ is the vector of N complex data symbols;
- $\mathbf{a}' \in \mathbb{C}^{N_a \times 1}$ is the vector of N complex data symbols for active data streams;
- \mathbf{A}^{IFT} is the butler matrix for the DFT
- \mathbf{A}^{IDFT} is the butler matrix for the inverse DFT
- A is the common aperture of the transmitter and the receiver;
- $\mathbf{b} \in \mathbb{C}^{N \times 1}$ is the vector of N received complex data symbols;
- c is the speed of light;
- D is the transmitter-receiver distance;
- f is the carrier frequency;
- $g(\cdot)$ is the path loss law as a function of the transmitter-receiver distance;

- F_i is the noise figure;
- $\mathbf{H} \in \mathbb{C}^{N \times N}$ is the channel matrix;
- $\mathbf{M} \in \mathbb{C}^{N \times N}$ is a matrix;
- m is the 'physical metric';
- N is the number of transmit antennas;
- N_a is the number of active data streams;
- N_o is the thermal noise power spectral density;
- $\mathbf{P} \in \mathbb{C}^{N \times N}$ is the precoding matrix;
- $\mathbf{P}' \in \mathbb{C}^{N \times N_a}$ is the truncated precoding matrix;
- P_{data} is the average power of data symbols;
- P_{noise} is the average noise power;
- $\mathbf{Q} \in \mathbb{C}^{N \times N}$ is a decoding matrix;
- $\mathbf{Q}' \in \mathbb{C}^{N_a \times N}$ is the truncated decoding matrix;
- r is the coefficient of reflection;
- R is the radius of the circular array or half of the length of the linear array;
- T_{symbol} is the symbol duration;
- $\mathbf{U} \in \mathbb{C}^{N \times N}$ is the result of the SVD;
- $\mathbf{V} \in \mathbb{C}^{N \times N}$ is the result of the SVD;
- $\mathbf{w} \in \mathbb{C}^{N \times 1}$ is the vector of N complex noise samples;
- x_n is the SINR of the data stream number n ;
- α is the oxygen loss;
- γ is a normalising factor;

- γ' is a normalising factor;
- δ_{nq} is the distance between the transmit antenna q and the receive antenna n ;
- δ'_{nq} is the distance between the virtual source corresponding to the reflection of antenna q and the receive antenna n ;
- δ_z is a translation along the z -axis;
- $\mathbf{\Delta} \in \mathbb{C}^{N \times N}$ is the result of the SVD;
- ϑ_x is the angle of rotation around the x -axis;
- ϑ_y is the angle of rotation around the y -axis;
- ϑ_z is the angle of rotation around the z -axis;
- $\mathbf{\Gamma} \in \mathbb{C}^{N \times N}$ is the equivalent channel;
- $\mathbf{\Gamma}' \in \mathbb{C}^{N_a \times N_a}$ is the truncated equivalent matrix;
- λ is the wavelength;
- $\Lambda(N)$ is the ratio of the complexity scaling laws of the proposed scheme versus the SVD;
- $\Lambda_1(N)$ is the complexity scaling law for FFT;
- $\Lambda_2(N)$ is the complexity scaling law for SVD;
- ρ is a normalising factor;
- Φ_n is the truncated spectral efficiency of data stream n ;
- φ_n is the spectral efficiency of data stream n ;
- φ_{min} is the minimum spectral efficiency;
- φ_{max} is maximum spectral efficiency.
- ρ is a normalising factor;
- ρ' is a normalising factor.

5.4.2 Common system model

5.4.2.1 System description

A wireless link between a transmitter and a receiver, both having an identical array of N antennas, is considered. In this study, we restrict our analysis to a narrowband single carrier transmission, and we therefore consider the channel as being flat in the frequency domain. The results of the paper could easily be extended to the wideband multi-carrier scenario, by considering each sub-carrier, independently. Indeed, the 60GHz WIFI standard is based on orthogonal frequency division multiplex (OFDM) [139][140][141].

Assuming flat fading, one can model the MIMO propagation channel by a complex $N \times N$ matrix \mathbf{H} . The TDD mode is considered, and CSIT and CSIR are assumed to be perfectly known. The transmitter sends a vector \mathbf{a} of N complex data symbols with an average power $P_{data} = E[\frac{1}{N} \sum_{n=0}^{N-1} |\mathbf{a}_n|^2]$. The power is equally shared between data streams. The transmitter multiplexes data streams by multiplying to the vector \mathbf{a} with the precoding matrix $\rho \mathbf{P}$, where ρ is a normalizing factor ensuring that $\sum_{n=0}^{N-1} \sum_{p=0}^{N-1} |\rho \mathbf{P}_{np}|^2 = 1$. The receiver de-multiplexes the data streams by applying the decoding matrix $\gamma \mathbf{Q}$, with γ being a normalizing factor ensuring that $\sum_{p=0}^{N-1} |\gamma \mathbf{Q}_{np}|^2 = 1, \forall n$. Let \mathbf{w} be the vector of the additive white Gaussian noise samples at the N receive antennas, with average power $P_{noise} = E[|\mathbf{w}_p|^2]$. With these notations, the expression of the vector \mathbf{b} of the N received complex data symbols is given by:

$$\mathbf{b} = \mathbf{\Gamma} \mathbf{a} + \gamma \mathbf{Q} \mathbf{w}, \quad \text{Eq. 5.4.1}$$

where, $\mathbf{\Gamma}$ is the equivalent channel defined by:

$$\mathbf{\Gamma} = \rho \gamma \mathbf{Q} \mathbf{H} \mathbf{P}. \quad \text{Eq. 5.4.2}$$

5.4.2.2 Performance metrics

Based on the diffraction theory, we expect the performance to increase with the following ‘‘physical metric’’ m :

$$m = \frac{R^2}{\lambda D}, \quad \text{Eq. 5.4.3}$$

where, R is the radius of the circular array or half of the length of the linear array, λ is the wavelength and D is the transmitter-receiver distance. In fact, m is simply proportional to the ratio of the transmit array maximum angular separation A/D (i.e. the angle between the two antennas located at the array borders, thus separated by A , and viewed from a distance D [9]) over the receive array maximum resolution λ/A (i.e. the smallest angle between two objects that the receiver is able to resolve with an aperture A [9]), where A is the common aperture of the transmitter and the receiver (with $A = 2R$). We expect that a scheme (either SVD, DFT-SM or DFT-SM-MRT) tested with the same number of antennas and the same value of m but with different combinations of R , D and λ values, and therefore different values of inter-antenna spacing, may result in a similar performance.

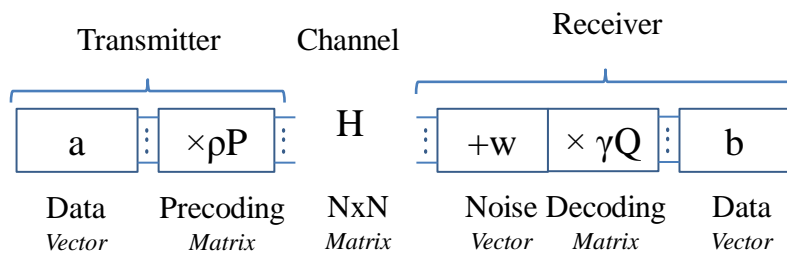


Fig. 5.4.4 System model

All the following performance metrics (defined hereafter) will be assessed as a function of the physical metric m : the SINR x_n and the spectral efficiency Φ_n of data stream n and the number of active data streams N_a . The data symbols and the noise samples are considered to be independent Gaussian variables with zero mean. The same assumption is taken for the interference which is supposed to be a large sum of independent variables. With these assumptions, and based on Eq. 5.4.1, one can derive the following SINR expression for x_n :

$$x_n = \frac{|\Gamma_{nn}|^2 P_{data}}{P_{noise} + \sum_{q=0, q \neq n}^{N-1} |\Gamma_{nq}|^2 P_{data}} \quad \text{Eq. 5.4.4}$$

Per sub-carrier and per data stream Adaptive modulation and coding is assumed. φ_{min} and φ_{max} are the minimum and maximum spectral efficiencies, achievable with practical modulation and coding schemes. We set $\varphi_n = \log_2(1 + x_n)$. The expression of Φ_n is given by: $\Phi_n = \varphi_n$ if $\varphi_{min} \leq \varphi_n \leq \varphi_{max}$, $\Phi_n = 0$ if $\varphi_n < \varphi_{min}$, and $\Phi_n = \varphi_{max}$ if $\varphi_n > \varphi_{max}$.

If $\Phi_n = 0$, the stream n is considered 'inactive', if $\Phi_n > 0$, the stream n is considered 'active'. N_a is the number of active streams. The inactive streams are sent, consuming power and creating interference. This is sub-optimal, of course. Ideally, a reduced and optimum set of data streams (after an exhaustive search over all possible combinations of streams) would be selected, at the cost of extra

complexity. However, the main objective of the study is to see the potential benefit of the precoders/decoders alone, without smart power allocation and stream selection.

5.4.3 Studied systems

This sub-section presents the specific expressions of the \mathbf{P} , \mathbf{Q} and $\mathbf{\Gamma}$ matrices introduced in sub-section 5.4.2 for the SVD, DFT-SM, DFT-SM-MRT and ‘‘DFT-SM-MRT filtered’’ schemes. We here define the matrix \mathbf{M} by: $\mathbf{M} = \mathbf{H}\mathbf{H}^H$. We recall that the expression of the MRT precoder is \mathbf{H}^H [8].

5.4.3.1 SVD

In the studied SVD scheme, the data stream n is mapped onto the n^{th} singular value of \mathbf{M} . The SVD of \mathbf{M} is given by $\mathbf{M} = \mathbf{U}\mathbf{\Delta}\mathbf{V}$, where \mathbf{U} and \mathbf{V} are unitary matrices and $\mathbf{\Delta}$ is a diagonal matrix with the singular values as coefficients. The expressions of \mathbf{P} , \mathbf{Q} and $\mathbf{\Gamma}$ are given by: $\mathbf{P} = \mathbf{H}^H\mathbf{V}^H$; $\mathbf{Q} = \mathbf{U}^H$ and $\mathbf{\Gamma} = \rho\gamma\mathbf{\Delta}$. \mathbf{H} is a square matrix, therefore one could simply make the SVD of \mathbf{H} and use the following equality to simplify the system: $\mathbf{V} = \mathbf{U}^H$. However, we prefer to study the SVD of \mathbf{M} , as it has the advantage to be applicable to non-square MIMO matrices.

5.4.3.2 DFT-SM

The expressions of \mathbf{P} , \mathbf{Q} and $\mathbf{\Gamma}$ are given by: $\mathbf{P} = \mathbf{A}^{IDFT}$; $\mathbf{Q} = \mathbf{A}^{DFT}$ and $\mathbf{\Gamma} = \rho\gamma\mathbf{A}^{IDFT}\mathbf{H}\mathbf{A}^{DFT}$; where \mathbf{A}^{IDFT} and \mathbf{A}^{DFT} , are the butler matrices for the inverse DFT and the DFT, respectively.

5.4.3.3 DFT-SM-MRT

The expressions of \mathbf{P} and \mathbf{Q} and $\mathbf{\Gamma}$ are therefore given by: $\mathbf{P} = \mathbf{H}^H\mathbf{A}^{IDFT}$; $\mathbf{Q} = \mathbf{A}^{DFT}$ and $\mathbf{\Gamma} = \rho\gamma\mathbf{A}^{DFT}\mathbf{M}\mathbf{A}^{IDFT}$.

5.4.3.4 DFT-SM-MRT filtered

In the ‘‘DFT-SM-MRT filtered’’ scheme, the system computes the expected spectral efficiency for the DFT-SM-MRT in a first step. Then, it determines which streams are not useful to be transmitted (inactive streams), and thus only transmits the other streams (active streams). In this case, the model presented in II must be slightly modified: \mathbf{a} , \mathbf{P} , \mathbf{Q} and $\mathbf{\Gamma}$ are replaced by \mathbf{a}' of size N_a , with $E[\frac{1}{N_a}\sum_{n=0}^{N_a-1}|\mathbf{a}'_n|^2]$, \mathbf{P}' of size $N \times N_a$, \mathbf{Q}' of size $N_a \times N$ and $\mathbf{\Gamma}'$ of size $N_a \times N_a$. \mathbf{P}' and \mathbf{Q}' only include the lines of \mathbf{P} and the column of \mathbf{Q} , respectively, which correspond to active streams and $\mathbf{\Gamma}' = \rho'\gamma'\mathbf{Q}'\mathbf{H}\mathbf{P}'$. ρ' and γ' are set to ensure that $\sum_{n=0}^{N-1}\sum_{p=0}^{N_a-1}|\rho'\mathbf{P}'_{np}|^2 = 1$ and $\sum_{n=0}^{N_a-1}\sum_{p=0}^{N-1}|\gamma'\mathbf{Q}'_{np}|^2 = 1$. The SINR expression x'_n is then computed using Eq. 5.4.4, with $\mathbf{\Gamma}'$ and N_a instead of $\mathbf{\Gamma}$ and N , and for active streams only. Finally, Φ_n is updated with x'_n instead of x_n , using the same method as in sub-section 5.4.2.1. This scheme suppresses the interference created by inactive

streams over active streams, by simply muting inactive streams. We do not propose filtering for SVD as it is already orthogonal. We do not propose it for DFT-SM either, as it is expected to deliver almost no active data streams in the misalignment conditions.

5.4.3.5 Basic Complexity Comparison

This sub-section gives a first complexity analysis of the studied schemes, for large values of the number N of antennas.

First of all, the complexity at the transmitter side is estimated. MRT needs a matrix transposition, a matrix conjugation and a matrix multiplication. Compared to MRT, DFT-SM-MRT requires an additional DFT. Compared to MRT, the studied SVD scheme needs an additional SVD. According to [156][157], the complexity of the FFT scales with $\Lambda_1(N) = N\log_2(N)$, and the complexity of SVD scales with $\Lambda_2(N) = N^3$. We define the complexity ratio $\Lambda(N)$ between the SVD and the DFT-SM-MRT schemes as: $\Lambda(N) = \frac{\Lambda_2(N)}{\Lambda_1(N)} = \frac{N^2}{\log_2(N)}$. Fig. 5.4.5 plots $\Lambda(N)$ as a function of the number of antennas N , and shows that $\Lambda(N)$ becomes tremendous for large MIMO systems ($N > 100$).

Now, on the receiver side, MRT needs no particular operation. DFT-SM-MRT and SVD schemes need the same operations as for the transmitter side, and therefore have the same complexity ratio.

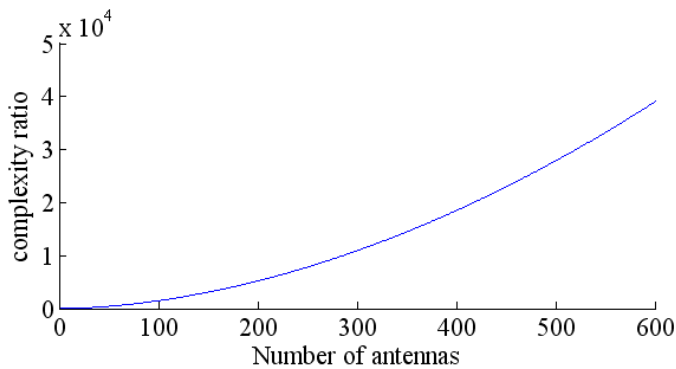


Fig. 5.4.5 Complexity ratio versus number of antennas

To conclude, at first sight, SVD is much more complex than DFT-SM-MRT especially for large MIMO systems. Computations based on low complexity implementations of the SVD would be needed for a more fair comparison.

5.4.4 Performance evaluation methodology

5.4.4.1 Main assumptions

The number of antennas N is fixed to 512.

The system carrier frequency f is varied. The wavelength λ is given by: $\lambda = c/f$, where c is the speed of light.

Regarding the MCS, QPSK with coding rate $\frac{1}{2}$ is chosen as the lowest MCS, corresponding to $\varphi_{min} = 1\text{bits/s/Hz}$, and 64 QAM with coding rate 1 is chosen as the maximum MCS, corresponding to $\varphi_{max} = 6\text{bits/s/Hz}$.

As we are considering a single carrier transmission, the value of the power spectral density (in watts per Hz, or watts \times seconds) is used instead of the power (in watts) for P_{data} and P_{noise} . P_{data} is chosen equal to $20\text{dBm} \times T_{symbol}$, with $T_{symbol} = 800$ ns, which corresponds to a typical value for 60GHz standards [139][140][141] and $P_{noise} = F_i N_o$, where N_o is the thermal noise power spectral density and F_i is the noise figure. $N_o = -174\text{dBm/Hz}$ and $F_i = 5\text{dB}$.

5.4.4.2 Misaligned arrays

As already stated in II, the transmit antenna array and the receive antenna array are identical, and have N elements. Linear arrays of lengths $2R$ and circular arrays of radius R are tested, to ensure they have the same aperture: $A = 2R$. The positions of the transmitter and the receiver arrays are determined using a two step approach. In a first step, they are “aligned”: i.e. they are set perpendicular to the y -axis, centered over the y -axis and separated by the distance D . In the linear case, the arrays are set parallel to the z -axis. In a second step, a translation by δ_z along the z -axis is applied to the receive array, and rotations by the angles ϑ_x , ϑ_y and ϑ_z around the x -axis, y -axis and z -axis, respectively, are applied to the transmit array. Circular and linear arrays are illustrated in Fig. 5.4.6 and Fig. 5.4.7 respectively.

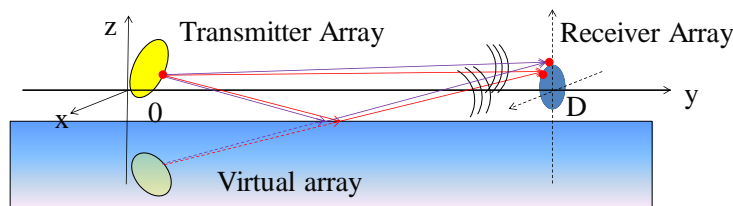


Fig. 5.4.6 Model for translated, rotated circular array with reflection

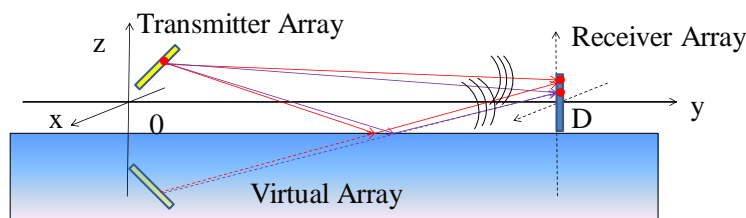


Fig. 5.4.7 Model for translated, rotated linear array with reflection

5.4.4.3 Channel Model

The MIMO channel H is generated using a ray tracing propagation model. One infinite and perfectly flat reflector (illustrated by Fig. 5.4.6 and Fig. 5.4.7) is considered. It is orthogonal to the z -axis and its

coordinate is: $z = -R$. A virtual source, defined as the symmetrical image of the array through the surface, is used to model the perfect reflection. This could be, for instance, a basic model for a roof top. A reflection coefficient r is applied. The path loss between the transmit antenna n and the receive antenna q is given by [142][143][144]:

$$g(\delta_{nq}) = \left(\frac{\lambda}{4\pi\delta_{nq}} \right)^2 10^{-0.1 \times \alpha \times \left(\frac{\delta_{nq}}{1000} \right)}.$$

where α is the oxygen loss, δ_{nq} is the distance between the transmit antenna q and the receive antenna n . Let δ'_{nq} be the distance between the virtual source corresponding to the reflection of antenna q and the receive antenna n . The same equation can be used with δ'_{nq} instead of δ_{nq} . The channel coefficient H_{nq} is therefore:

$$H_{nq} = \sqrt{g(\delta_{nq})} e^{j2\pi \frac{\delta_{nq}}{\lambda}} + r \sqrt{g(\delta'_{nq})} e^{j2\pi \frac{\delta'_{nq}}{\lambda}}.$$

5.4.4.4 Testing various configurations

In order to make the study with arbitrary inter-antenna spacings (with respect to the transmitter-receiver distance, and the wavelength), all possible combinations of the following values for the frequency, the radius and the transmitter-receiver distance, are tested: f between 10 and 100GHz; R between 0.4 and 3 meters and D between 10 and 100 meters.

For each combination, the physical parameter m is computed using Eq. 5.4.3 and the metrics N_a and Φ_n are computed using the equations in sub-section 5.4.2 and the matrices defined in 5.4.3.

All possible combinations of the following values for the rotation, the translation and the reflection are tested: ϑ_x, ϑ_y and ϑ_z between 0 and 0.2 radians ($\sim 11^\circ$), δ_z between 0 and 20cm, $r = 0$ (no reflection) or $r = 1$ (reflection).

5.4.5 Results

All simulation results are plotted as a function of the physical parameter m , with values between 0 and 40. Points with m beyond 40 correspond to huge arrays being very close to each other, compared to the wavelength. Such configurations are likely to be more rare than configurations with $m < 40$. Also, in those configurations, the SVD performance saturates due to the fixed number of antennas $N = 512$. In other terms, the channel becomes close to full rank, and low complexity precoders or decoders such

as ZF, MMSE or even MRT may suffice. Here are two examples of scenarios corresponding to $m = 40$: $R = 3\text{m}$, $D = 45\text{m}$ and $f = 60\text{GHz}$, or $R = 3\text{m}$, $D = 75\text{m}$ and $f = 100\text{GHz}$.

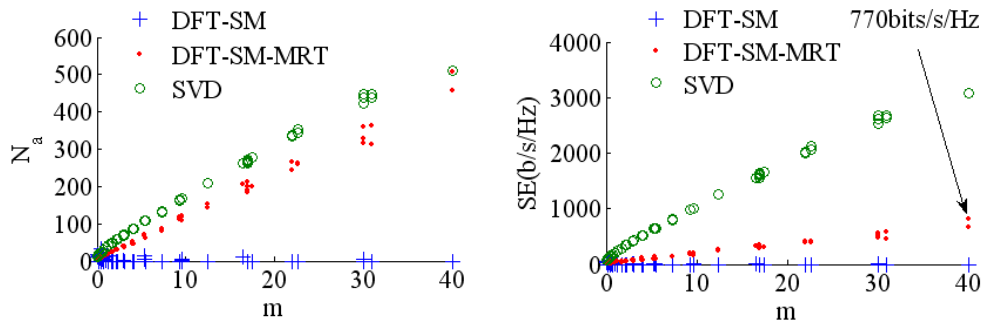


Fig. 5.4.8 Circular array, translation effect only

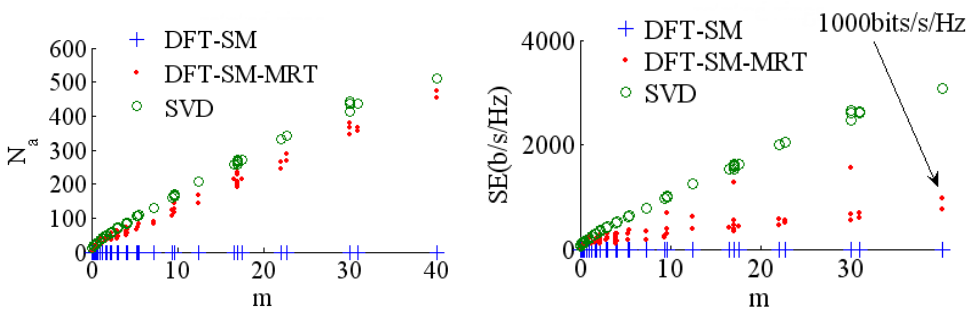


Fig. 5.4.9 Circular array, rotation effect only

Fig. 5.4.8 illustrates the number of active streams N_a and the spectral efficiency Φ_n as a function of the physical parameter m , for SVD, DFT-SM and DFT-SM-MRT, when only translation is activated ($\vartheta_x = \vartheta_y = \vartheta_z = r = 0$, and $\delta_z \geq 0$). Fig. 5.4.9 illustrates the impact of rotation alone, ($\delta_z = r = 0$, $\vartheta_x \geq 0$, $\vartheta_y \geq 0$, and $\vartheta_z \geq 0$). As expected, for all schemes, the performance mainly depends on m . One can observe that DFT-SM fails to deliver active streams due to the slight misalignment induced by either the translation or the rotation, whereas DFT-SM-MRT delivers almost the same number of active streams as SVD. Regarding the spectral efficiency, DFT-SM-MRT reaches around one third of the SVD performance.

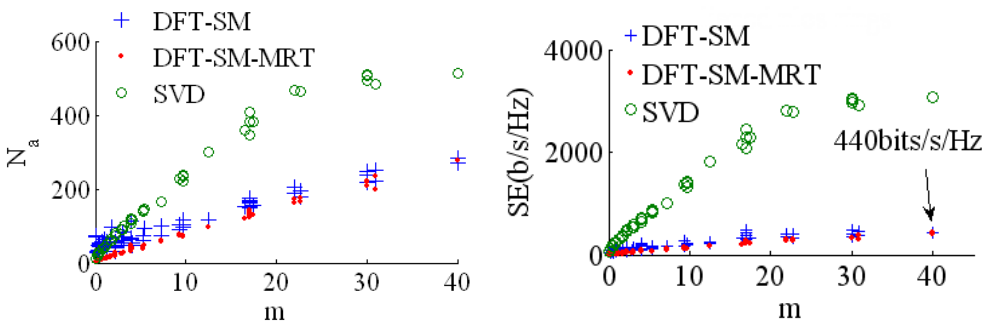


Fig. 5.4.10 Circular array, reflection effect only

Fig. 5.4.10 illustrates the impact of the reflector alone, ($\vartheta_x = \vartheta_y = \vartheta_z = \delta_z = 0$, and $r = 1$). This time, the transmitter and the receiver are perfectly aligned, and one reflector creates an additional path

in the propagation channel. DFT-SM alone is already robust to the multi-path, and DFT-SM-MRT does not bring additional gain, because the alignment is already perfect.

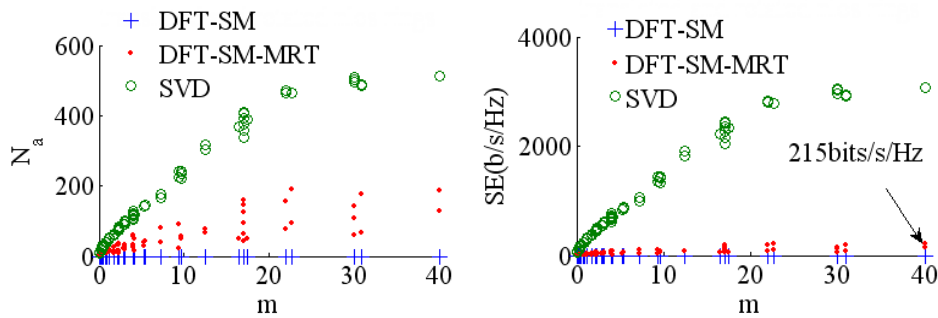


Fig. 5.4.11 Circular array, rotation, translation and reflection effects

Fig. 5.4.11 illustrates the combined effect of misalignment and reflection. Again, due to the misalignment, and contrary to DFT-SM-MRT, DFT-SM performance collapses.

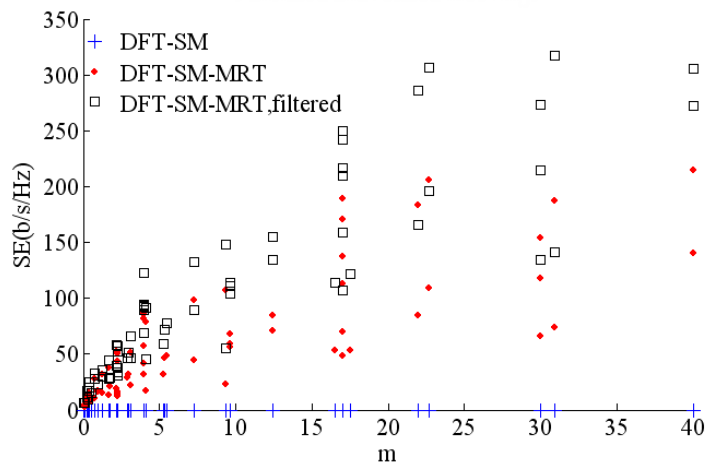


Fig. 5.4.12 Circular array, rotation, translation and reflection (Zoom)

Fig. 5.4.12 is a zoom of Fig. 5.4.11 with “DFT-SM-MRT filtered” scheme added. The filtered scheme, slightly improves the performance by muting non active streams, and by reducing the level of interference over active streams. We recall that filtering is not proposed for SVD which is already orthogonal. It is not implemented for DFT-SM either, due to the very low number of active data streams.

The same analysis as was shown from Fig. 5.4.8 to Fig. 5.4.12, can be made for the linear case, with Fig. 5.4.13 to Fig. 5.4.17. However, the linear array is much more sensitive to rotation than to translation. Also, when comparing Fig. 5.4.12 and Fig. 5.4.17, one can observe that the circular array outperforms the linear array for the same value of the physical parameter. Hence, even though DFT-SM-MRT adapts to m as SVD does, without requiring an optimised antenna spacing with respect to m , it still clearly needs some particular antenna array “shapes”.

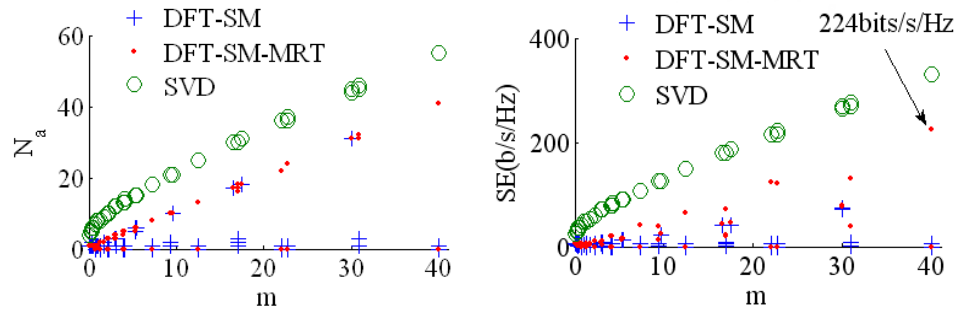


Fig. 5.4.13 Linear array, translation effect only

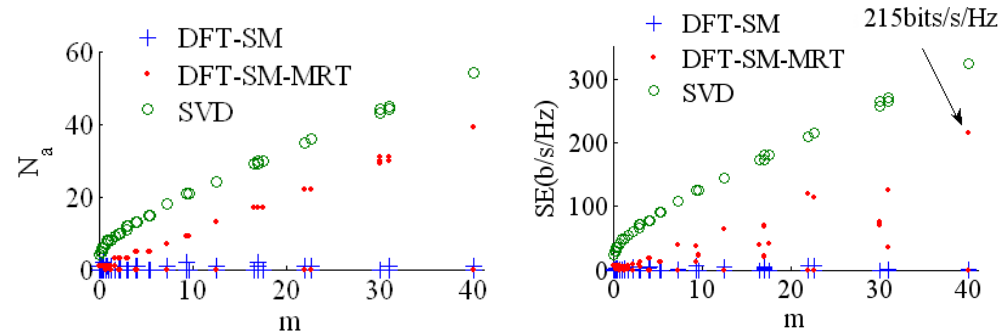


Fig. 5.4.14 Linear array, rotation effect only

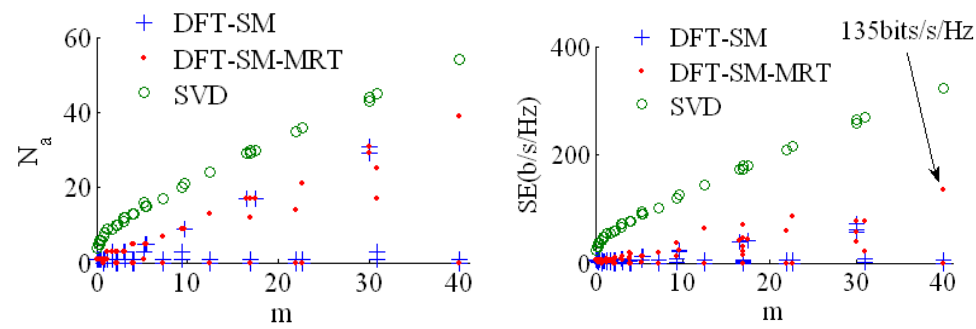


Fig. 5.4.15 Linear array, reflection effect only

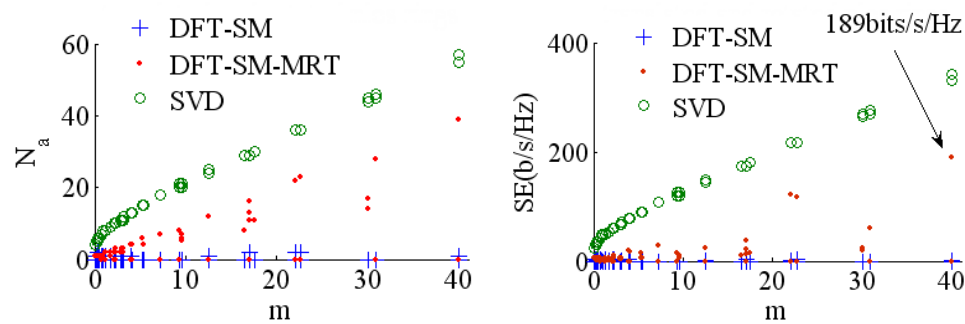


Fig. 5.4.16 Linear array, translation, rotation and reflection effects

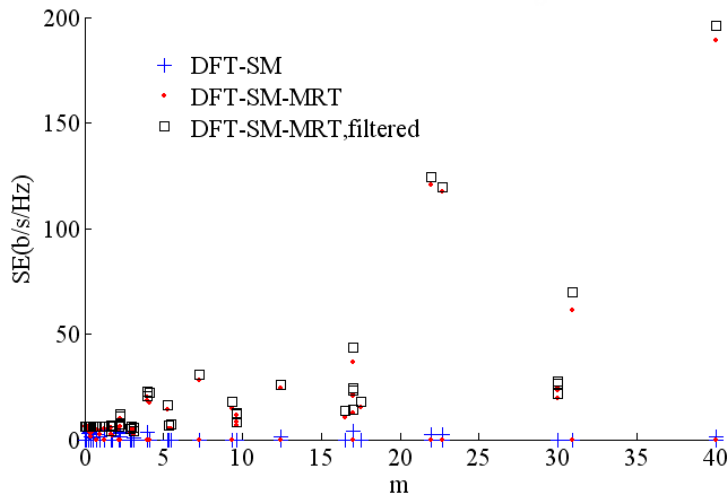


Fig. 5.4.17 Linear array, translation, rotation and reflection effects (Zoom)

Table 5.4.1. summarizes the spectral efficiencies achieved by DFT-SM-MRT at $m=40$. Depending on the scenario, DFT-SM-MRT achieves hundreds of bits/s/Hz. In comparison with SVD, DFT-SM-MRT achieves 1/3 to 1/14 of SVD performance, with a complexity which is around $\Lambda(N)^{-1} = 3.10^{-5}$ times lower, for the considered number of antennas ($N=512$).

Effects	DFT-SM-MRT spectral efficiency (bits/s/Hz)		Ratio between DFT-SM-MRT and SVD spectral efficiencies	
	Circular Array	Linear Array	Circular Array	Linear Array
Translation	770	224	>1/3	~3/4
Rotation	1000	215	~1/3	~5/7
Reflection	440	135	>1/7	~4/9
All	215	189	>1/14	~5/8

Table 5.4.1 DFT-SM-MRT performance at $m=40$

To conclude this sub-section, DFT-SM-MRT provides high spectral efficiency without inter-antenna spacing optimization with respect to the distance, and is robust to misalignment plus one reflector.

5.4.6 Conclusion

This study introduces a new low complexity scheme for large MIMO millimeter-wave communications where the MIMO matrix is likely to be ill conditioned if the antenna separation is not optimized as a function of the transmitter-receiver distance. The proposed scheme, called DFT based spatial multiplexing with MRT, combines IDFT and MRT precoders at the transmitter and DFT decoder at the receiver. At first sight, the system has a much lower complexity than singular value decomposition, which is the chosen reference solution for ill conditioned MIMO. Simulations with a simple ray trac-

ing model and one perfectly flat reflector show that the proposed scheme achieves a very high spectral efficiency and is robust to slight misalignment. Additionally, it has been shown that the circular array outperforms the linear array. Future work will therefore focus on performance assessment with more realistic propagation channel models, on the design of new arrays shapes, and on some more precise complexity analysis.

Chapter 6 - Conclusion and future works

6.1 Conclusions

Time reversal is a space-time filtering technique that provides focusing in the time and the spatial domain. It can be implemented with single-carrier modulation by using distinct matched filters per transmit antenna. It can also be implemented with multi-carrier modulation by using distinct maximum ratio transmission beamformers per sub-carrier.

Time reversal has been clearly identified by previous works to be beneficial for ultrawideband communications by lowering the cost of the receivers. Thanks to our simulations and experiments, it is now a bit clearer that even for bands and spectrums typical for mobile networks, time reversal space-time focusing can deliver high throughput to low cost devices also in indoor mobile networks (such as femto/small cell networks).

Most of previous works on time reversal considered the best-case scenario: time division duplex mode and static environment. In mobile networks, two challenging scenarios are often met: frequency division duplex mode and fast moving connected car. Thanks to our work on new enablers, it seems a bit more possible to benefit from TR advantages even in these challenging scenarios. In frequency division duplex mode, a low cost device can still be used. In high mobility, the maximum ratio transmission beamforming gain can still be exploited to save energy at the network side.

Most of previous works focus on using time reversal in wireless networks for data communication using single carrier modulation or OFDM. We also propose new communication schemes with alternative modulations (spatial modulation or OFDM/OQAM), new deployment scenarios (massive multiple input multiple output systems for wireless backhaul in ultra dense networks) and new applications apart from data transmission (guidance and navigation) based on time reversal focusing.

6.2 Future works

During all the aforementioned studies, it appeared that the quality of the space-time focusing property of time reversal strongly depends on the propagation, but also on the design of antennas. In our future works, we will therefore try to have a ‘cross antenna-environment-signal processing’ design approach, more systematically.

For instance, in [162], section 7.2, we have very recently shown that massive antenna arrays facing each other in near to line of sight exhibit huge degrees of freedom, if a sufficiently high carrier frequency is selected. They can potentially convey hundreds of data streams in parallel, multiplexed in

the spatial domain. This very early results show that by integrating antenna arrays in urban architecture and objects, and exploiting the natural geometries one can provide huge data rates. Going further, we have seen in in chapter 5.4, that for some shapes and some particular geometries, the near to optimum schemes can be very simple. In another example of study presented in [163], we propose a new and low complexity space-time block coding scheme for OFDM/OQAM MIMO systems which exploits near line-of-sight propagation to lower the complexity of the system. In the future, we will therefore try to optimize together the following three elements:

- the geometries of antenna arrays so that they can be imbedded in urban architecture or objects;
- the deployment scenarios of these antennas so that huge degrees of freedom with low complexity can be met;
- the signal processing schemes so that the best performance is obtained.

One can also explore alternatives to antenna arrays. In [164] for instance, we start to take into account multipoint antennas instead of antenna arrays, to perform time reversal focusing. More works will follow on this kind of antennas, as they have the advantage to be more compact than antenna arrays. They mainly provide diversity in the angular domain. They are therefore good candidates for connected objects.

Annex

7.1 Details on OFDM/OQAM with time reversal

The figure below illustrates an OFDM/OQAM modulator and its associated demodulator.

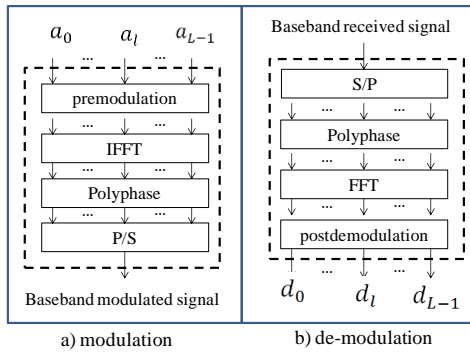


Fig. 7.1.1 OFDM/OQAM modulator and de-modulator

Fig. 7.1.2 illustrates the architecture of a transmitter that implements TR in the time domain. The figure is drawn for an OFDM/OQAM waveform. However, it is valid for any multi-carrier transmission scheme. In this figure, $W_n^{(l,p)}$ is the data symbol transmitted over the sub-carrier number l , which is intended to the receive antenna n during the OFDM or OFDM/OQAM symbol number p . $h_{n,M}(t)$ is the impulse response of the propagation channel between the receive antenna number n and the transmit antenna number m , with $0 \leq n < N - 1$ and $0 \leq m < M - 1$. $\hat{h}_{n,M}(t)$ is the estimate of $h_{n,M}(t)$.

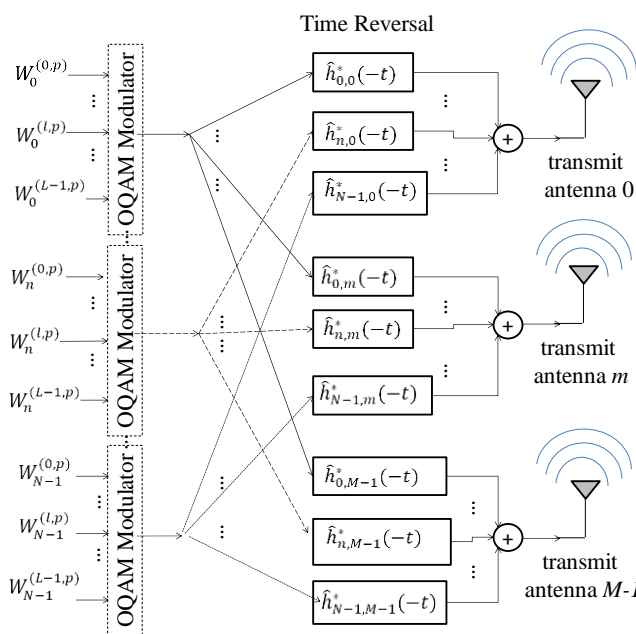


Fig. 7.1.2 Transmitter architecture, TR implementation

Fig.7.1.3 below illustrates the architecture of a transceiver that implements TR in the frequency domain, i.e. using MRT beamformer on a sub-carrier basis. The figure is drawn for an OFDM/OQAM waveform. However, it is valid for any multi-carrier transmission scheme. In this figure, $W_n^{(l,p)}$ is the data symbol transmitted over the sub-carrier number l , which is intended to the receive antenna n during the OFDM or OFDM/OQAM symbol number p . $H_{n,M}^{(l)}$ is the coefficient of the propagation channel between the receive antenna number n and the transmit antenna number m , on sub-carrier number l , with $0 \leq n < N - 1$, $0 \leq m < M - 1$ and $0 \leq l < L - 1$. $\hat{H}_{n,M}^{(l)}$ is the estimate of $h_{n,M}(t)$.

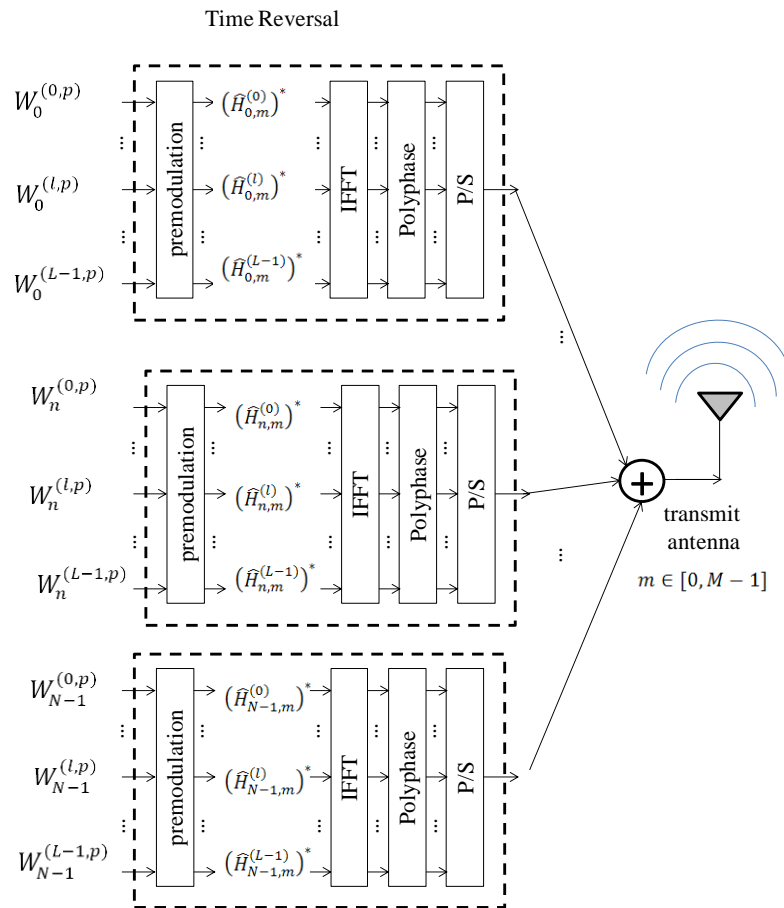


Fig. 7.1.3 Transmitter architecture, Maximum Ratio Transmission implementation

7.2 Details on separate receive and training antenna system

7.2.1 Introduction

Multiple antenna techniques are well known for their beneficial effect on wireless communications. Among them, beamforming based on CSIT is often proposed, in MISO systems, to maximize the received SINR, and the DL throughput. More recently, large MISO systems have become popular, as they increase the beamforming gain simply by using larger transmit antennas arrays at the base station [srta1][95][srta2][158][srta3].

For such large systems, that we will latter call Reference Systems (RS), the Channel State Information feedback necessary in FDD mode is heavier. Hence, TDD is a better option. Classically, in TDD, during the training phase, the mobile station (MS) sends pilots, which are used by the base station to perform UL channel estimation, CSIT acquisition and beamforming weights computation. During the data transmission phase, the base station transmits data in the downlink (DL) using the beamformer weights and a high SINR is finally achieved at the mobile station. The theoretical beamforming gain, i.e. the SINR gain, increases with the number of transmit antennas [srta1][95][srta2] [158] [srta3][srta7][srta8][92].

The mentioned beamforming gain is achievable for low speed mobile station. However, in the case of high speed mobile station, the propagation channel changes during the delay between the training phase and the data transmission phase, causing the CSIT to be outdated. In other terms, the beamforming scheme “misses” its moving target and the beamforming gain is degraded [srta4][159][srta8] [92]. Moreover, this degradation worsens with the number of transmit antennas.

For the particular case of high speed trains, works in [srta5][srta6][160][160] have experimented route-tracking beamforming. Contrary to approaches in [srta1][95][srta2] [158] [srta3], the base station does not use CSIT. Instead, it dynamically rotates the beam of a directive antenna towards the vehicle, based on its current position. The position is estimated by the vehicle GPS and fed back to the base station. In this case, the base station does not “miss” its target as the beam is large. However, as no CSIT is available, the achieved beamforming gain and spectral efficiency are very low.

In this study, we propose a new scheme called Separate Receive and Training Antennas (SRTA), to achieve high beamforming gain thanks to a large transmit antenna array, even with a high speed moving vehicle. As for RS, this technique is based on TDD, beamforming and CSIT. Nevertheless, contrary to RS where a user has a single antenna, in our scheme, the vehicle is equipped with several antennas playing different roles: a “Training Antenna” (TA), several “Candidate Antennas” (CAs), and among the CAs, a particular antenna, called the “Receive Antenna” (RA). In SRTA, the TA is responsible for sending UL pilots during the training phase, and the RA is responsible for data demodulation, during the data transmission phase, while in RS, the same antenna plays the two roles. In SRTA, the RA is dynamically selected among the CAs as a function of the vehicle speed. The delay between training and data transmission is also dynamically adapted to the vehicle speed. More precisely, the RA and the frame duration are computed to ensure that, during the data transmission phase, the RA is exactly at the position that was previously occupied by the TA during the training phase. The important advantage of SRTA is that the frame duration is extended for higher speeds.

The paper is organized as follows. In Sub-section 7.2.27.2.2 we present our generic system model. Specific parameters of the RS and the SRTA are detailed in sub-section 4.2.3 and 7.2.4 respectively. In

particular, the differences in the SINR expressions are highlighted. Sub-section 4.2.5 is a performance comparison. Sub-section 7.2.6 concludes this study.

The following notations are used: $k, l, p, v, K, L, P \in \mathbb{N}$. $\tau, t, t_0, t_s, v, \Delta, x_T, N_0 \in \mathbb{R}$; $t_a, t_{a,d}: \mathbb{R} \rightarrow \mathbb{R}$; $l_a, l_{a,d}, l_{a,d}: \mathbb{R} \rightarrow \llbracket 1, L - 1 \rrbracket$; $g_k, \hat{g}_k: \mathbb{R}^3 \rightarrow \mathbb{C}$; $p_k \in \mathbb{C}$. $n, n', m, m', \vec{v} \in \mathbb{R}^3$ are Cartesian coordinates; if $u \in \mathbb{R}$, $[u]$ is the integer part of u ; if $u \in \mathbb{C}$, $|u|$ is its module; if $\vec{v} \in \mathbb{R}^3$, $\|\vec{v}\|$ is its norm.

7.2.2 Generic system model

This sub-section presents common elements of RS and SRTA. For both systems, the beamforming scheme will be the MRT which was demonstrated to offer MISO SVD performance [92].

A wireless DL transmission between a base station with K transmit antennas and a moving vehicle is considered. The vehicle velocity vector is \vec{v} and $v = \|\vec{v}\|$. In SRTA, the vehicle has one TA and several CAs, the CAs include the RA, and the RA is different from the TA. In RS, there is only one antenna on the vehicle, thus the TA and the RA are the same antenna.

Spatially correlated flat fading channel is assumed. Hence, the propagation channel between any antenna $k \in [0, K - 1]$ of the base station and any position m of any antenna of the vehicle is a complex coefficient, and is denoted $g_k(m)$.

TDD mode is considered, with an equal UL and DL frame duration τ . The system symbol duration is t_s . One frame is divided in symbols of duration t_s . Each data symbol sent by the base station at time $t' \in [\tau, 2\tau[$ during the data transmission phase described in sub-section B, uses beamforming weights previously determined at time $t \in [0, \tau[$, during the training phase, described in sub-section A, with:

$$t' = t + \tau. \quad \text{Eq. 7.2.1}$$

τ is thus also the delay between the training phase and the data transmission phase, for any data symbol. For the sake of clarity, we use simple notations to describe positions of the vehicle moving antennas. We simply denote n and n' as the positions of the TA at time t and t' respectively, and m and m' the positions of the RA at time t and t' , respectively. The channel between the TA and the transmit antenna k at time t is thus $g_k(n)$, and the channel between the RA and the transmit antenna k at time t' is $g_k(m')$.

For a first analysis we assume than the latency impact of base station acquiring precise vehicle speed information is neglected because not varying very quickly compared to the channel coherence time.

7.2.2.1 Training Phase

At time t , the TA sends pilots from its current position n , the base station determines the estimate $\hat{g}_k(n)$ of $g_k(n)$ for each transmit antenna k and computes the maximum ratio transmission beamforming weight p_k :

$$p_k = \hat{g}_k^*(n). \quad \text{Eq. 7.2.2}$$

The base station computes the power allocation E verifying:

$$x_T = EN_0^{-1} \left| \sum_{k=1}^K p_k \hat{g}_k(n) \right|^2, \quad \text{Eq. 7.2.3}$$

where N_0 is the noise power and x_T is a target SNR. Using Eq. 7.2.2 and 7.2.3, the base station deduces E :

$$E = x_T N_0 \left| \sum_{k=1}^K |\hat{g}_k(n)|^2 \right|^{-2}. \quad \text{Eq. 7.2.4}$$

7.2.2.2 Data Transmission

At time t' , the base station sends data with the power allocation E and the weights p_k stored at time t . Thus, both RS and SRTA send the same signal with the same power.

7.2.2.3 Received SNR expression

The expression of the receive SNR $x_{\tau\bar{v}}$ is given by:

$$x_{\tau\bar{v}} = EN_0^{-1} \left| \sum_{k=1}^K g_k(m') p_k \right|^2. \quad \text{Eq. 7.2.5}$$

By replacing E by 7.2.4 and p_k by 7.2.2, in 7.2.5, and by assuming perfect channel estimation ($\hat{g}_k(n) = g_k(n)$), one obtains:

$$x_{\tau\bar{v}} = \left| \sum_{k=1}^K g_k(m') g_k(n)^* \right|^2 \left| \sum_{k=1}^K |g_k(n)|^2 \right|^{-2} x_T. \quad \text{Eq. 7.2.6}$$

7.2.3 Classical MISO or Reference System (RS)

τ has a fixed value:

$$\tau = t_0. \quad \text{Eq. 7.2.7}$$

The vehicle has only one antenna. The TA is also the RA. Hence, we have $m = n$, $m' = n'$, and,

$$m' = n + t_0 \vec{v}. \quad \text{Eq. 7.2.8}$$

Consequently, Eq. 7.2.6 becomes:

$$x_{t_0 \vec{v}} = \left| \sum_{k=1}^K g_k(n + t_0 \vec{v}) g_k(n)^* \right|^2 \left| \sum_{k=1}^K |g_k(n)|^2 \right|^{-2} x_T. \quad \text{Eq. 7.2.9}$$

If $t_0 \vec{v} = \vec{0}$ (no delay or mobility), the target SNR is met:

$$x_{t_0 \vec{v}} = x_T. \quad \text{Eq. 7.2.10}$$

If $t_0 \vec{v} \neq 0$, (delay or mobility), the target SNR is not met:

$$x_{t_0 \vec{v}} \leq x_T. \quad \text{Eq. 7.2.11}$$

Hence, due to the frame duration t_0 and the velocity \vec{v} , the data is received out of the beamforming target position. As a consequence, the SNR is lower and the BLER is larger, than expected. $x_{t_0 \vec{v}}$ decreases when t_0 increases. Thus, the smallest value of t_0 that does not create too much overhead (due to the additional guard time after the DL frame), must be chosen. Nevertheless, and as confirmed by simulation results presented in sub-section V.B, for MRT precoding, the greater the number of transmit antenna at base station, the greater the theoretical target SNR, but the lower $x_{t_0 \vec{v}}$ when $t_0 \vec{v} \neq 0$. And moreover, for a given number of transmit antennas and a frame duration t_0 , the higher \vec{v} , the lower $x_{t_0 \vec{v}}$.

7.2.4 Separate receive and training antennas (SRTA)

7.2.4.1 Concept

Fig. 7.2.1 a) and b) illustrate the vehicle antenna(s) for RS and SRTA, assuming the same velocity \vec{v} .

In SRTA, the vehicle has L antennas with indexes $l \in [0, L - 1]$, fixed on its roof, and regularly spaced by Δ . In addition to the TA (with index $l = 0$), $L - 1$ CAs (with indexes $l \in [1, L - 1]$) are used. The antennas are fixed on the vehicle in such a way that they are always aligned with the vehicle velocity vector. Let n_l be the position of CA l , at time t and n'_l its position at time t' . n_l and n'_l verify:

$$\overrightarrow{n'_l n'} = \overrightarrow{n_l n} = l\Delta v^{-1} \vec{v}, \quad \text{Eq. 7.2.12}$$

$$n'_l - n' = n_l - n = -l\Delta v^{-1} \vec{v}. \quad \text{Eq. 7.2.13}$$

A vehicle with such antennas is illustrated in Fig. 7.2.2.

We assume that L and Δ are designed large enough to verify:

$$v < (L - 1)\Delta \|t_0\|^{-1}. \quad \text{Eq. 7.2.14}$$

We assume that the base station and the vehicle have a precise estimation of v (based on GPS for instance). The base station and the vehicle jointly select the RA among CAs (i.e. the index $l_a(v)$), and an extended frame duration (i.e. $\tau = t_a(v)$) adapted to the speed v according to:

$$l_a(v) = \min\{l \in \llbracket 1, L - 1 \rrbracket \mid l\Delta v^{-1} > t_0\}. \quad \text{Eq. 7.2.15}$$

$$t_a(v) = l_a(v)\Delta v^{-1}. \quad \text{Eq. 7.2.16}$$

Due to Eq. 7.2.14, $l_a(v)$ does exist and Eq. 7.2.15 and Eq. 7.2.16 leads to:

$$t_a(v) > t_0. \quad \text{Eq. 7.2.17}$$

The data symbol is received by antenna $l_a(v)$ at position m' :

$$m' = n'_{l_a(v)} = n_{l_a(v)} + t_a(v)\vec{v}. \quad \text{Eq. 7.2.18}$$

Additionally, due to Eq. 7.2.14, $n_{l_a(v)}$ has the following expression:

$$n_{l_a(v)} = n - l_a(v)\Delta v^{-1}\vec{v}. \quad \text{Eq. 7.2.19}$$

By replacing $n_{l_a(v)}$ by Eq. 7.2.20 in Eq. 7.2.19, one obtains:

$$m' = n + (t_a(v)v - l_a(v)\Delta)v^{-1}\vec{v}. \quad \text{Eq. 7.2.20}$$

By replacing $t_a(v)$ by Eq. 7.2.16 in Eq. 7.2.20, one obtains:

$$m' = n. \quad \text{Eq. 7.2.21}$$

As a consequence, Eq. 7.2.6 becomes equivalent to:

$$x_{t_a(v)\vec{v}} = x_T. \quad \text{Eq. 7.2.22}$$

In other terms, at time $t' = t + t_a(v)$, the RA is exactly at the position that was previously occupied by the TA at time t , and the target SNR is met. The couple $(l_a(v), t_a(v))$ perfectly compensates the vehicle velocity \vec{v} by applying a frame duration $t_a(v)$ larger than t_0 .

7.2.4.2 Practical Implementation

In practice, the frame duration is adapted with a limited granularity d , i.e. a given time step. For instance, $d = t_s$ or several t_s . Based on Eq. 7.2.15, Eq. 7.2.16 and Eq. 7.2.20, the RA index $l_{a,d}(v)$, the extended frame duration $t_{a,d}(v)$ and the position of the RA m' expressions are thus given by:

$$l_{a,d}(v) = \min\{ l \in \llbracket 0, L - 1 \rrbracket \mid [l\Delta(dv)^{-1}]d > t_0 \}, \quad \text{Eq. 7.2.23}$$

$$t_{a,d}(v) = [l_{a,d}(v)\Delta v^{-1}d^{-1}]d, \quad \text{Eq. 7.2.24}$$

$$m' = n + \rho_d(v)v^{-1}\vec{v}, \quad \text{Eq. 7.2.25}$$

where, $\rho_d(v)$ is the distance between the beamformer target position and the RA, due to d and v :

$$\rho_d(v) = [l_{a,d}(v)\Delta(dv)^{-1}]dv - l_a(v)\Delta. \tag{Eq. 7.2.26}$$

and finally, the achieved SNR $x_{t_{a,d}(v)\vec{v}}$ is given by:

$$x_{t_{a,d}(v)\vec{v}} = \frac{|\sum_{i=1}^M g_k(n+\rho_d(v)v^{-1}\vec{v})g_k^*(n)|^2}{|\sum_{k=1}^K |g_k(n)|^2} x_T. \tag{Eq. 7.2.27}$$

Some values of v are noticeable. The BLER target is achieved for speed values $v = a_p$, with $p \in \llbracket 1, L - 1 \rrbracket$, defined by:

$$a_p = \Delta(dp)^{-1}. \tag{Eq. 7.2.28}$$

Indeed, $\rho_d(a_p) = 0$. For other values of v , $x_{t_{a,d}(v)\vec{v}}$ gets nearer to the target value, when the granularity d is better:

$$\lim_{d \rightarrow 0} \rho_d(v) = 0. \tag{Eq. 7.2.29}$$

$$\lim_{d \rightarrow 0} x_{t_{a,d}(v)\vec{v}} = x_T. \tag{Eq. 7.2.30}$$

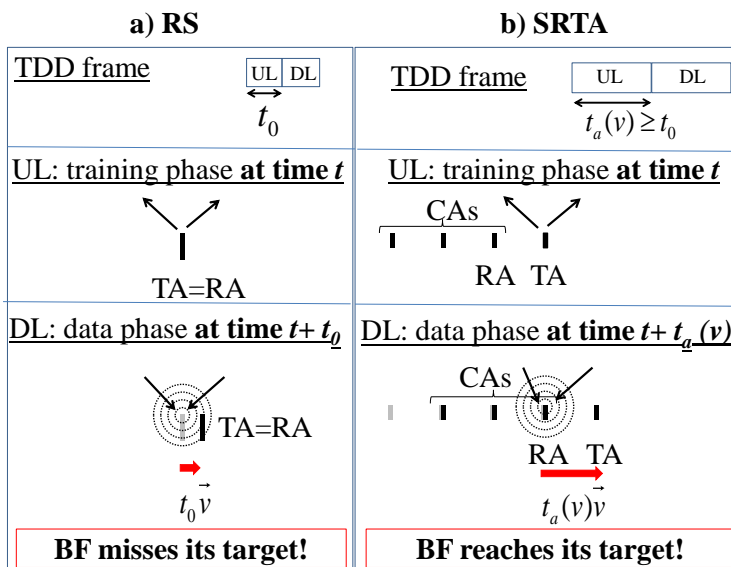


Fig. 7.2.1 Vehicle antenna(s) for RS and SRTA systems

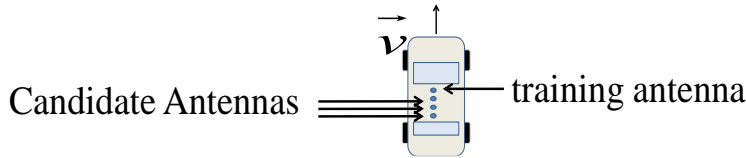


Fig. 7.2.2 Vehicle Antennas in SRTA

7.2.5 Performance evaluation

This sub-section compares RS and SRTA performance, based on simulations.

7.2.5.1 Simulation assumptions and methodology

The following assumptions are used: $t_0=2\text{ms}$; the carrier frequency f_0 is 2GHz; the wavelength is $\lambda = c/f_0$; where $c=3\cdot 10^8$ m/s is the light speed; the base station has $K=4, 8, 16, 64$ antennas aligned and separated by 0.5λ . In SRTA, the vehicle has $L=4$ antennas separated by Δ , where $\Delta = 0.5\lambda$. Various values of the granularity are tested: $d=1, 0.5, 0.2, 0.1\text{ms}$. The vehicle speed v ranges from 0 to 300kmph. The couples $(t_{a,d}(v), l_{a,d}(v))$ are computed using equations Eq. 7.2.23 and Eq. 7.2.24. The target SNR is $x_T=15.5$ dB, which corresponds to a target BLER of 0.01 for 64QAM with code rate 3/4.

A large number of random events are generated by simulation. For each event, the angle of the transmit antenna array and the angle of the vector \vec{v} are generated randomly and are uniformly distributed between 0 and 2π . The TA position n is dropped randomly. $\rho_d(v)$ is computed using Eq. 7.2.26. The coefficients $g_k(n), g_k(n + t_0\vec{v}), g_k(n + \rho_d(v)v^{-1}\vec{v})$ are generated and computed using a spatially correlated propagation channel model. Then, the formulas Eq. 7.2.9 and Eq. 7.2.27 are applied to derive the SNR $x_{t_0\vec{v}}$ for RS and the SNR $x_{t_{a,d}(v)\vec{v}}$ for SRTA. The corresponding BLERs are computed using the look up table below. The achieved SNRs, BLERs, are averaged over all events, and plotted as a function of speed v , for each d value, for both RS and SRTA schemes.

SNR	14.5	15.0	15.5	15.7	16.0
BLER	1.0	0.8205	0.0125	0.0028	0.000001

Table 7.2.1 Look Up Table

Two types of channel models are tested: the theoretical ‘‘Random Channel Model’’ and the Winner II Channel Models which are based on measurements.

The ‘‘Random Channel Model’’ generates 100 rays with equal amplitudes, random phases (uniformly distributed between 0 and 2π), and random angles of arrival and departures (uniformly distributed between 0 and 2π radians) to compute $g_0(n)$. The coefficients $g_k(n + t_0\vec{v}), g_k(n + \rho_d(v)v^{-1}\vec{v})$ are

deduced by using the same rays and by computing additional phases offsets using geometrical rules. Thus, coefficients are spatially correlated.

The Winner II Cluster Delay Line Models are used to generate spatially correlated coefficients with more realistic angle of arrivals, angles of departures and power delay profiles: C1 (Suburban Macro cell) in LOS and NLOS. These models consider a system bandwidth of 100MHz and are not flat fading channel models. Thus some computations are required to use equations (26) and (27).

More precisely, for one given random event, a number of rays with amplitudes, phases, angles arrivals, departures and delays are generated using the Winner II model to build the channel impulse response $h_{0,n+t_0\vec{v}}(r)$ (where r is the time) of the channel between transmit antenna $k = 0$ and position n . The impulse response $h_{k,n+t_0\vec{v}}(r)$ of the channel between transmit antenna k and position $n + t_0\vec{v}$, and the impulse response $h_{k,n+\rho_d(v)v^{-1}\vec{v}}(r)$ of the channel between antenna k and position $n + \rho_d(v)v^{-1}\vec{v}$ are deduced using the same initial rays, with additional phases offsets computed by applying geometric rules. Thus, spatial correlation is modeled.

Then, for each impulse response, the corresponding frequency response is obtained by Fast Fourier Transform operation: $H_{0,n+t_0\vec{v}}(f)$, $H_{k,n+t_0\vec{v}}(f)$, and $H_{k,n+\rho_d(v)v^{-1}\vec{v}}(f)$, where f is the frequency. Finally, Orthogonal Frequency Division Multiplex (OFDM) is assumed, and equations (26) and (27) are applied to each sub-carrier f independently, with $g_k(n) = H_{0,n+t_0\vec{v}}(f)$, $g_k(n + t_0\vec{v}) = H_{k,n+t_0\vec{v}}(f)$ and $g_k(n + \rho_d(v)v^{-1}\vec{v}) = H_{k,n+\rho_d(v)v^{-1}\vec{v}}(f)$.

7.2.5.2 Sensitivity to speed of classical large MISO systems (RS) with MRT

Fig. 7.2.3 and Fig. 7.2.4 illustrate the performance of RS, classical MISO with MRT precoding over the Random Channel Model. These curves serve as reference to evaluate the expected gains of SRTA. As analyzed in or MISO systems, with $K = 16$ or 64 , the SNR and BLER strongly but obviously degrade with v . The potential theoretical gain of large MISO system is not well exploited because of the vehicle movement. Fig. 7.2.5 to Fig. 7.2.6 compare RS and SRTA over the Random Channel Model, for $K = 64$. With the best granularity ($d = 0.1ms$), SRTA largely outperforms classical systems with a BLER lower than 0.1 for 0-300kmph, while for RS BLER is near to 1 for speeds larger than 25kmph. The particular speed values defined by Eq. 7.2.28 (which meet the target SNR and BLER) and the impact of the granularity expressed in Eq. 7.2.29 and Eq. 7.2.30 can easily be observed.

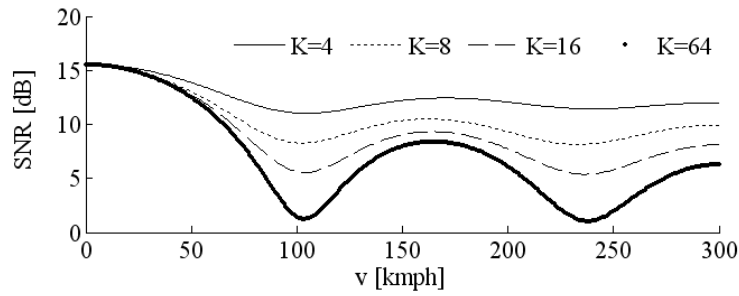


Fig. 7.2.3 Impact of number of transmit antennas K and vehicle speed v on SNR , for classical (RS) scheme

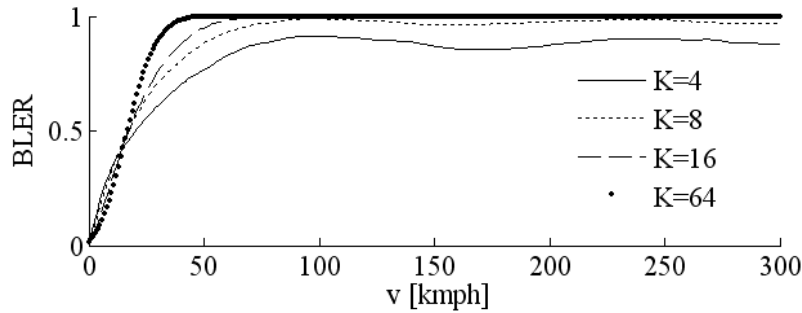


Fig. 7.2.4 Impact of number of transmit antennas K and vehicle speed v on BLER for classical (RS) scheme

7.2.5.3 SRTA versus RS over random channel model

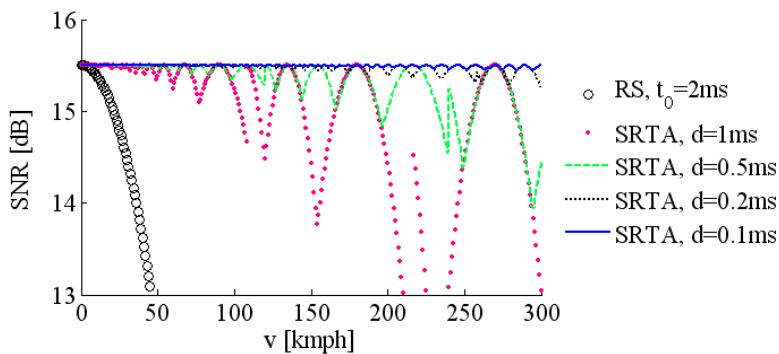


Fig. 7.2.5 Impact of vehicle speed v on SNR , for classical (RS) and SRTA schemes, for $K=64$, over random channel model

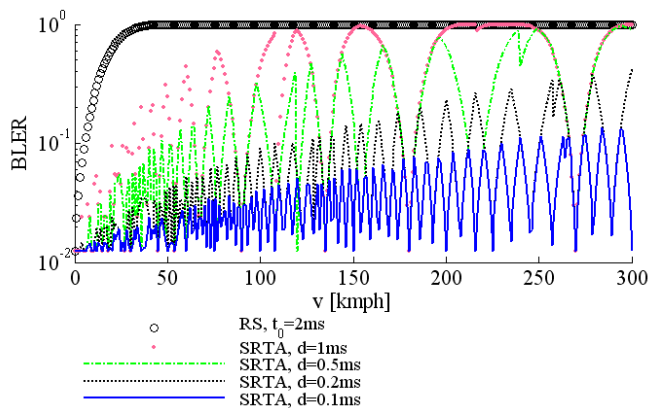


Fig. 7.2.6 Impact of v on BLER for classical (RS) and SRTA with different d values, for $K=64$, over random channel model

The SRTA also needs to calculate the required frame duration $t_{a,d}(v)$. The different values of $t_{a,d}$ are plotted in Fig. 7.2.7 over random channel model as a function of v . If we consider $10ms$ as the largest frame duration, for large speeds higher than $25kmph$, $t_0 < t_{a,d}(v) < 10ms$. Nevertheless, for $v < 25kmph$, one may prefer RS with t_0 , instead of SRTA with large $t_{a,d}(v)$ values.

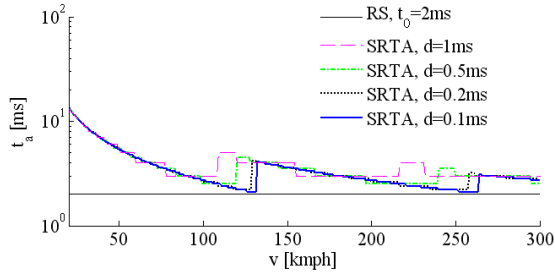


Fig. 7.2.7 Adaptive Frame Duration vs vehicle speed v

Fig. 7.2.8 presents the index $l_{a,d}$ of the CA that is therefore chosen as RA when the speed increases. To compensate the moving of the vehicle at speed between 0 to $300kmph$, SRTA was carried out with $L = 4$ antennas. We can see that in order compensate a speed between 0 to $120kmph$ and between 0 to $250kmph$, $L = 2$ and $L = 3$, respectively, are enough.

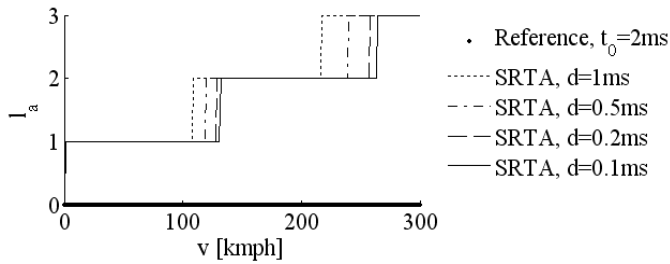


Fig. 7.2.8 Receive Antenna index versus vehicle speed v

7.2.5.4 SRTA versus RS, Winner II channel models

Fig. 7.2.9 compares RS and SRTA, for Winner II models, for $K = 16$ and $d = 0.1ms$. The achieved BLER is kept below 0.1 with SRTA, even at $300kmph$, while it is 1 for speeds larger than $50kmph$ for RS. $l_{a,d}(v)$ and $t_{a,d}(v)$ do not depend on the channel, and are thus not plotted again for Winner II. As expected, beamforming is more sensitive to speed in NLOS than in LOS.

7.2.6 Conclusion

A new and quite simple scheme called SRTA is proposed, to perform beamforming with large MISO systems towards high speed vehicles in TDD. SRTA has been compared to RS, a traditional beamforming system, using simulations based on Winner II spatially correlated channel models, and assuming a target BLER of 0.01 . SRTA BLER is lower than 0.1 even at $300kmph$, while RS BLER is 1 for speeds larger than $50kmph$. This improvement is obtained for a large MISO system (16 transmit antennas), without power increase, and thanks to an extended and optimized frame duration.

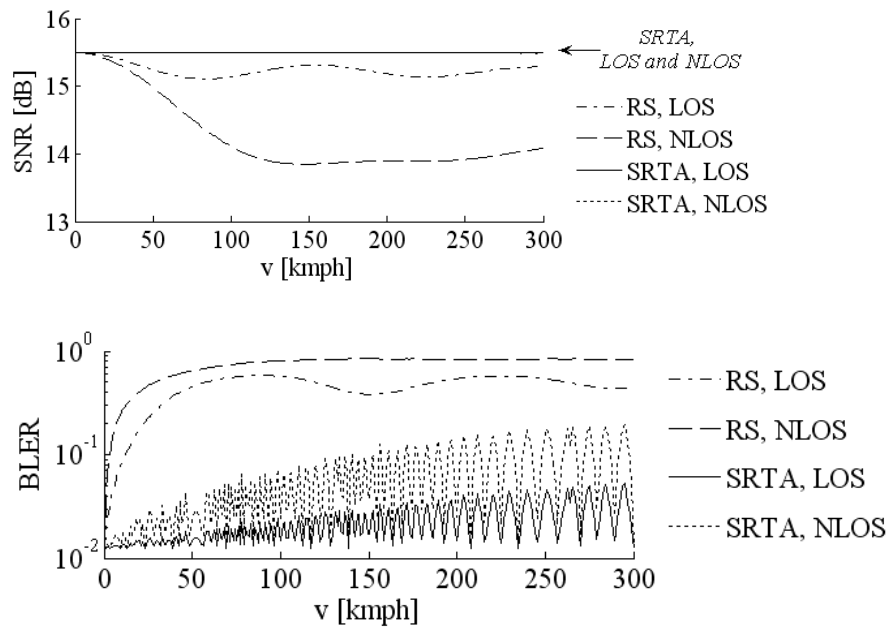


Fig. 7.2.9 Results with Winner II C1 Channel Models

References

- [1] Bogert, B.P., "Demonstration of Delay Distortion Correction by Time-Reversal Techniques," *IRE Transactions on Communications Systems*, vol.5, no.3, pp.2,7, December 1957.
- [2] Turin, G.L., "An introduction to matched filters," *IRE Transactions on Information Theory*, vol.6, no.3, pp.311,329, June 1960.
- [3] Turin, G.L., "An introduction to digital matched filters," *Proc. IEEE*, vol.64, no.7, pp.1092,1112, July 1976.
- [4] Turin, G.L., "Introduction to spread-spectrum antimultipath techniques and their application to urban digital radio," *Proceedings of the IEEE*, vol.68, no.3, pp.328,353, March 1980.
- [5] Price, R.; Green, P.E., "A Communication Technique for Multipath Channels," *Proceedings of the IRE*, vol.46, no.3, pp.555,570, March 1958.
- [6] Kumar, R.V.R., "Development of a CDMA system with RAKE receiver for the third generation wireless communication systems," in *Proc. 2002 IEEE International Conference on Personal Wireless Communications*, pp.309,313, 15-17 Dec. 2002.
- [7] Van Veen, B.D.; Buckley, K.M., "Beamforming: a versatile approach to spatial filtering," *IEEE ASSP Magazine*, vol.5, no.2, pp.4,24, April 1988.
- [8] Lo, T. K Y, "Maximum ratio transmission," *IEEE Transactions on Communications*, vol.47, no.10, pp.1458,1461, Oct 1999.
- [9] Rao, B.D.; Ming Yan, "Performance of maximal ratio transmission with two receive antennas," in *Proc. Conference Record of the Thirty-Fifth Asilomar Conference on Signals, Systems and Computers, 2001*, vol.2, pp.980,983, 4-7 Nov. 2001.
- [10] Sampath, H.; Stoica, P.; Paulraj, A., "Generalized linear precoder and decoder design for MIMO channels using the weighted MMSE criterion," *IEEE Transactions on Communications*, vol.49, no.12, pp.2198-2206, Dec 2001.
- [11] Fink, M., « Time reversed Acoustics », *Physics Today*, 20, p.34-40, Mars 97.
- [12] Derode, A.; Roux, P. and Fink, M.; "Robust Acoustic Time reversal With High Order Multiple Scattering," *Phys. Rev. Letters*, vol. 75, pp. 4206-4209, 1995.
- [13] Altman, C.; Schatzberg, A.; Suchy, K., "Symmetry transformations and time reversal of currents and fields in bounded (Bi)anisotropic media," *IEEE Transactions on Antennas and Propagation*, vol.32, no.11, pp.1204,1210, Nov 1984.
- [14] Altman, C.; Suchy, K., "Spatial mapping and time reversal in magnetized compressible media," *IEEE Transactions on Antennas and Propagation*, vol.34, no.11, pp.1294,1299, Nov 1986.
- [15] Tanter, M.; Thomas J.-L. and Fink, M.; "Comparison between time reversal focusing in absorbing medium and inverse filtering", in *Proc.1997 IEEE Ultrasonic Symposium*.
- [16] Tanter, M.; Aubry, J.-F.; Gerber, J.; Thomas, J.-L.; Fink, M.; "Optimal focusing by spatio-temporal inverse filter. I Basic Principles". *J. Acoustic Soc. Am.* July 2001.
- [17] Simon, S. H.; "Communication In a Disordered World", *Physics Today*, September 2001.
- [18] Moustakas, A. L.; Baranger, H. U.; Balents, L.; Sengupta, A. M. ; Simon, S. H.; "Communication Through a Diffusive Medium: Coherence and Capacity", *Science*, 14 January 2000.
- [19] "Characterization of space-time focusing in time-reversed random fields" Oestges, C.; Kim, A.D.; Papanicolaou, G.; Paulraj, A.J.; *IEEE Transactions on Antennas and Propagation*, Volume 53, Issue 1, Part 2, Jan. 2005 Page(s):283 – 293.
- [20] Derode, A.; Tourin, A.; de Rosny, J.; Tanter, M.; Yon, S.; Fink, M.; "Taking Advantage of Multiple Scattering to Communicate with Time-Reversal Antennas" *Physical Review Letters* 2003, 90 (1), pp 014301-1-014301-4.
- [21] Edelmann, G. F.; Akal, T.; Hodgkiss, W. S.; Kim, S.; Kuperman, W. A. and Song, H. C. ; "An Initial Demonstration of Underwater Acoustic Communications Using Time reversal," *IEEE J. of Oceanic Eng.*, vol. 27, no. 3, pp. 602-609, 2002.
- [22] Emami, M.; Lee F. and Paulraj, A.; "Communications through High Delay Spread x Bandwidth (HDB) Channels: Opportunities and Challenges," in *Proc. Workshop on Time-Reversal Communications in Richly Scattering Environments*, Stanford University, October 18, 2004, AIM.
- [23] Oestges, C. ; Hansen, J.; Emami, S. M. ; Kim, A. D.; Papanicolaou, G. and Paulraj, A. J. ; "Time reversal Techniques for Broadband Wireless Communication Systems," in *Proc. European Microwave Conference (Workshop)*, Amsterdam, The Netherlands, pp. 49-66, Oct 2004.

-
- [24] Lienard, M.; Degauque, P.; Degardin, V.; Vin, I., "Focusing Gain Model of Time-Reversed Signals in Dense Multipath Channels," in *Proc. IEEE Antennas and Wireless Propagation Letters*, vol.11, no., pp.1064,1067, 2012.
- [25] Terchoune, H.; Lautru, D.; Gati, A.; Man-Fai Wong; Wiart, J.; Hanna, V.F., "Investigation of space-time focusing of time reversal using FDTD," in *Proc. IEEE MTT-S International Microwave Symposium Digest, 2009. MTT '09*. pp.273,276, 7-12 June 2009.
- [26] Ziade, Y.; Wong, M.-F.; Wiart, J., "Reverberation chamber and Indoor measurements for time reversal application," in *Proc. IEEE 2008 Antennas and Propagation Society International Symposium*,. pp.1,4, 5-11 July 2008.
- [27] Emami, S. M.; Hansen, J. A.; Kim, D. ; Papanicolaou, G.; Paulraj, A. J.; Cheung, D. and Prettie, C. ;"Predicted time reversal performance in wireless communications using channel measurements," *IEEE Communications Letters*, 2004.
- [28] Pajusco, P.; Pagani, P., "On the Use of Uniform Circular Arrays for Characterizing UWB Time reversal," *IEEE Transactions on Antennas and Propagation*, vol.57, no.1, pp.102,109, Jan. 2009.
- [29] Pajusco, P.; Pagani, P., "Comparison of Two Time reversal Schemes using Circular UWB Measurements," in *Proc. IEEE 18th International Symposium on Personal, Indoor and Mobile Radio Communications, 2007. PIMRC 2007*. pp.1,5, 3-7 Sept. 2007.
- [30] Pajusco, P.; Pagani, P., "Characterization of UWB time reversal using circular array measurements," in *Proc. 2007 European Conference on Wireless Technologies*, pp.102,105, 8-10 Oct. 2007.
- [31] Naqvi, I.H.; Aleem, S. A.; Usman, O.; Ali, S. B.; Besnier, P.; Zein, G.E., "Robustness of a time reversal system: From ultra-wide to narrow bandwidths," in *Proc. 2012 IEEE Wireless Communications and Networking Conference (WCNC)*, pp.37,41, 1-4 April 2012.
- [32] Khalegi, A.; "Measurement and Analysis of Ultra-Wideband Time reversal for Indoor Propagation Channels," in *Wireless Pers. Commun.*, May. 2009.
- [33] Monsef, F.; Cozza, A.; Abboud, L.; "Effectiveness of Time-Reversal technique for UWB wireless communications in standard indoor environments," in *Proceedings 2010 ICECom Conference*, pp.1-4, 20-23 Sept. 2010.
- [34] El-Sallabi, H.; Kyritsi, P.; Paulraj, A.; Papanicolaou, G., "Experimental Investigation on Time reversal Precoding for Space-Time Focusing in Wireless Communications," in *Proc. IEEE Transactions on Instrumentation and Measurement*, vol.59, no.6, pp.1537-1543, June 2010.
- [35] Bellens, F.; Quitin, F.; Dricot, J.-M.; Horlin, F.; Benlarbi-Delai, A.; De Doncker, P., "Performance evaluation of time reversal in intra-vehicular environment," in *Proceedings of the 5th European Conference on Antennas and Propagation (EUCAP)*, pp.206-210, 11-15 April 2011.
- [36] Zhou, C.; Guo, N. and Qiu, R. C.; "Time-Reversed Ultra-wideband (UWB) Multiple Input Multiple Output (MIMO) Based on Measured Spatial Channels", *IEEE Transactions on vehicular technology*, vol. 58, no. 6, July 2009.
- [37] Khaleghi, A. ; El Zein, G.; Naqvi, I. H.; "Demonstration of Time-Reversal in Indoor Ultra-Wideband Communication: Time Domain Measurement", *IEEE ISWCS*, 2007.
- [38] Dou, J.-H.; Yang, X.-S.; Chen, J.; Wang, B.-Z.; "Performance analysis of Time-reversed ultra-wideband indoor channel by simulation," in *Proc. 2010 International Conference on Microwave and Millimeter Wave Technology (ICMMT)*, pp.1424-1427, 8-11 May 2010.
- [39] Qiu, R.C., "A Theory of Time-Reversed Impulse Multiple-Input Multiple-Output (MIMO) for Ultra-Wideband (UWB) Communications," in *Proc. 2006 IEEE 2006 International Conference on Ultra-Wideband*, pp.587-592, 24-27 Sept. 2006.
- [40] Qiu, R.C.; Zhou, C.; Guo, N.; Zhang, J.Q.; "Time reversal With MISO for Ultrawideband Communications: Experimental Results", *Antennas and Wireless Propagation Letters* Volume 5, Issue 1, Dec. 2006 pp:269-273.
- [41] Song, Y.; Guo, N.; Qiu, R.C.; "Implementation of UWB MIMO Time-reversal Radio Testbed," *IEEE Antennas and Wireless Propagation Letters*, no.99, pp.1, 0.
- [42] Ziade, Y.; Wiart, J., "Data transmission using time reversal technique - Results of reverberating chamber measurements," in *Proc. 2013 Third International Conference on Communications and Information Technology (ICCIT)*, pp.356,360, 19-21 June 2013.
- [43] Dezfooluyan, A.; Weiner, A.M., "Experimental test-bed for studying ultrawideband wireless multiple-input single-output Time reversal using optical delay lines," in *Proc. 2012 Conference on Lasers and Electro-Optics (CLEO)*, pp.1,2, 6-11 May 2012.
- [44] Song, Y.; Guo, N.; Hu, Z. and Qiu, R. C.; "FPGA Based UWB MISO Time-Reversal System Design and Implementation" in *Proceedings of 2010 IEEE International Conference on Ultra-Wideband (ICUWB2010)*.
- [45] Ben Cheikh Battikh, D.; Kelif, J.-M.; Abdallah, F.A.; Phan-Huy, D.-T., "Time reversal outage probability for wideband indoor wireless communications," in *Proc. 2010 IEEE 21st International Symposium on Personal Indoor and Mobile Radio Communications (PIMRC)*, pp.999-1003, 26-30 Sept. 2010.

-
- [46] [Dubois10] Dubois, T.; Crussière, M.; Hélar, M., "On the use of Time reversal for digital communications with non-impulsive waveforms," in *Proc. 2010 4th International Conference on Signal Processing and Communication Systems (ICSPCS)*, pp.1-6, 13-15 Dec. 2010.
- [47] Lerosey, G.; de Rosny, J.; Tourin, A.; Fink, M.; "Focusing Beyond the Diffraction Limit with Far-Field Time reversal" *Science*, Vol 315, 1120-1122, Feb 2007
- [48] [spy6] Hoydis, J.; Kobayashi, M.; Debbah, M.; "Green Small-Cell Networks," *IEEE Vehicular Technology Magazine*, vol.6, no.1, pp.37-43, March 2011.
- [49] Jungnickel, V.; Manolakis, K.; Zirwas, W.; Panzner, B.; Braun, V.; Lossow, M.; Sternad, M.; Apelfrojd, R.; Svensson, T., "The role of small cells, coordinated multipoint, and massive MIMO in 5G," *IEEE Communications Magazine*, vol.52, no.5, pp.44,51, May 2014.
- [50] Emami, M.; Vu, M.; Hansen, J.; Paulraj, A.J.; Papanicolaou, G.; "Matched filtering with rate back-off for low complexity communications in very large delay spread channels," in *Proc. Conference Record of the Thirty-Eighth Asilomar Conference on Signals, Systems and Computers, 2004*, Vol.1, pp. 218,222, 7-10 Nov. 2004.
- [51] Nguyen, H. T.; Kyritsi, P.; Eggers, P.C.F.; "Time reversal technique for multi-user wireless communication with single tap receiver", in *Proc. 16th IST Mobile and Wireless Communications Summit, 2007*, 1-5 July 2007 Page(s):1 – 5.
- [52] Nguyen, H. T.; Kovacs, I. Z. and Eggers, P. C. F.; "A Time reversal Transmission Approach for multiuser UWB Communications," *IEEE Trans. on Ant. and Prop.*, vol. 54, no. 11, pp. 3216-3224, Nov. 2006.
- [53] Fu, H.; Crussière, M.; Hélar, M., "Partial Channel Overlay in Moderate-Scale MIMO Systems Using WH Precoded OFDM", in *Proc. International Conference on Telecommunications (ICT) 2014*, Lisbon, 5 - 7 May 2014, pp.16,21.
- [54] Fu, H.; Crussière, M.; Hélar, M., "Spectral efficiency optimization in overlapping channels using TR-MISO systems," in *Proc. IEEE Wireless Communications and Networking Conference (WCNC)*, Shanghai, 7-10 April 2013, pp.3770,3775.
- [55] El Din, S.A.; El-Hadidy, M.; Kaiser, T., "Realistic time reversal and spatial beamforming: An interference mitigation approach," in *Proceedings of the 5th European Conference on Antennas and Propagation (EUCAP)*, pp.3104,3108, 11-15 April 2011.
- [56] Han, F.; Yang, Y.-H.; Wang, B.; Wu, Y.; Liu, K.J.R., "Time-Reversal Division Multiple Access in Multi-Path Channels," in *Proc. 2011 IEEE Global Telecommunications Conference (GLOBECOM 2011)*, pp.1,5, 5-9 Dec. 2011.
- [57] Yang, Y.-H.; Wang, B.; Lin, W.S.; Liu, K.J.R., "Near-Optimal Waveform Design for Sum Rate Optimization in Time-Reversal Multiuser Downlink Systems," *IEEE Transactions on Wireless Communications*, vol.12, no.1, pp.346,357, January 2013.
- [58] Panaitopol, D.; Fiorina, J.; Di Benedetto, M.-G.; "Trade-off between the number of fingers in the prefilter and in the rake receiver in time reversal IR-UWB" in *Proc. IEEE International Conference on Ultra-Wideband, 2009 (ICUWB 2009)*, 9-11 Sept. 2009 Page(s):819 - 823.
- [59] Strohmer, T.; Emami, M.; Hansen, J.; Papanicolaou, G. and Arogyaswami, P.J.; "Application of Time-Reversal with MMSE Equalizer to UWB Communications", in *Proc. IEEE Global Telecommunications Conference (GlobeCom)*, Vol. 5, December 2004, Page(s): 3123 – 3127.
- [60] Nguyen, H.; Zhao, Z.; Zheng, F.; Kaiser, T.; "On the MSI mitigation for MIMO UWB time reversal systems" in *Proc. IEEE International Conference on Ultra-Wideband, 2009 (ICUWB 2009)*, 9-11 Sept. 2009 Page(s):295 - 299.
- [61] Gomes, J.; Barroso, V.; "Doppler compensation in underwater channels using time-reversal arrays" in *Proc. 2003 IEEE International Conference Acoustics, Speech, and Signal Processing (ICASSP '03)*, Page(s):V - 81-4 vol.5.
- [62] Nguyen, H.T.; Andersen, J.B.; Pedersen, G.F.; Kyritsi, P.; Eggers, P.; "A measurement based investigation on the potential use of time reversal in wireless communications," *IEEE Transactions on Wireless Communications*, Vol 5, No 8, pp 2242- 2252. Aug. 2006.
- [63] Nguyen, H. T.; Andersen, J. B. and Pedersen, G. F.; "The Potential Use of Time reversal Techniques in Multiple Element Antenna Systems", *IEEE Communication Letters*, vol 9, no. 1, january, 2005.
- [64] Chen, Y.; Yang, Y.-H.; Han, F.; Liu, K.J.R., "Time-Reversal Wideband Communications," *IEEE Signal Processing Letters*, vol.20, no.12, pp.1219,1222, Dec. 2013.
- [65] Derode, A.; Tourin, A.; Fink, M.; "Ultrasonic pulse compression with one bit time reversal through multiple scattering," in *J. Acoust. Soc. Am.* 85, 1999, vol. (9), pp. 6343-6352.
- [66] Kyritsi, P.; Eggers, P. and Oprea, A.; "MISO time reversal and time compression," in *URSI Internatl. Symp. on Electromag. Theory*, May 2004.
- [67] Kyritsi, P.; Papanicolaou, G. "One-bit Time reversal for WLAN Applications" in *Proc. IEEE PIMRC 2005*, 11-14 Sept 2005, Vol.1, pp: 532-536.

- [68] Nguyen, H.T. "On the performance of one bit time reversal for multi-user wireless communications", in *Proc. IEEE ISWCS*, Trondheim, Norway 2007, pp: 672-676.
- [69] Nguyen, H. T.; "Partial one bit time reversal for UWB impulse radio multi-user communications", in *Proc. Second International Conference on Communications and Electronics*, 2008, 4-6 June 2008 Page(s):246 – 251.
- [70] Yoon, M.; Lee, C., "A quantized TR prefilter for indoor wireless communication system with channel estimation error," in *Proc. 2013 International Conference on ICT Convergence (ICTC)*, pp.207,211, 14-16 Oct. 2013
- [71] Barton, R.J.; Zheng, R., "Order-Optimal Data Aggregation in Regular Wireless Sensor Networks," *IEEE Transactions on Information Theory*, vol.56, no.11, pp.5811-5821.
- [72] Ben Halima, S.; Hélar, M.; Phan-Huy, D.-T.; "New Coordination and Resource Allocation Schemes for Uniform Rate in Femtocell Networks," in *Proc. 2011 IEEE 73rd Vehicular Technology Conference (VTC Spring)*, pp.1,5, 15-18 May 2011.
- [73] Wang, B.; Wu, Y.; Han, F.; Yang, Y.-H.; Liu, K.J.R., "Green Wireless Communications: A Time-Reversal Paradigm," *IEEE Journal on Selected Areas in Communications*, vol.29, no.8, pp.1698-1710, September 2011.
- [74] Bouzigues, M.-A.; Siaud, I.; Ulmer-Moll, A.-M.; Hélar, M., "On the use of time-reversal for packet switching in green communications," in *Proc. 2013 IEEE 9th International Conference on Wireless and Mobile Computing, Networking and Communications (WiMob)*, pp.22,27, 7-9 Oct. 2013.
- [75] Bouzigues, M.-A.; Siaud, I.; Helard, M.; Ulmer-Moll, A.-M., "Turn Back the Clock: Time reversal for Green Radio Communications," *IEEE Vehicular Technology Magazine*, vol.8, no.1, pp.49,56, March 2013.
- [76] Mawlawi, B.; Bastug, E.; Nerguizian, C.; Azarian, S.; Debbah, M., "Non-invasive green small cell network," in *Proc. 2012 Conference Record of the Forty Sixth Asilomar Conference on Signals, Systems and Computers (ASILOMAR)*, pp.68,73, 4-7 Nov. 2012.
- [77] Li, D.; Hong, J.-S.; Wang, B.-Z.; "Improving Anti-Detection/Interception Performance for Wireless Sensor Network Based on Time-Reversal Technology," in *Proc. 5th International Conference on Wireless Communications, Networking and Mobile Computing, 2009 (WiCom '09)*, pp.1,4, 24-26 Sept. 2009.
- [78] Shao, W.; Liu, X.; Wang, B.-Z.; "Analysis of time reversed electromagnetic wave propagation with FDTD method," in *Proc. 2010 International Conference on Microwave and Millimeter Wave Technology (ICMMT)*, pp.1164,1166, 8-11 May 2010.
- [79] Punnoose, R.J.; Counsil, D.; Young, D., "Focusing a radio signal and simultaneously nulling it at another location using time-reversal: Experimental results," in *Proc. 2012 MILITARY COMMUNICATIONS CONFERENCE, 2012 - MILCOM*, pp.1,6, Oct. 29 2012-Nov. 1 2012.
- [80] Chen, Y.; Han, F.; Yang, Y.-H.; Ma, H.; Han, Y.; Jiang, C.; Lai, H.-Q.; Claffey, D.; Safar, Z.; Liu, K.J.R., "Time-Reversal Wireless Paradigm for Green Internet of Things: An Overview," *IEEE Internet of Things Journal*, vol.1, no.1, pp.81,98, Feb. 2014.
- [81] Gomes, J.; Barroso, V.; "Time-reversed OFDM communication in underwater channels" in *Proc. 2004 IEEE 5th Workshop on Signal Processing Advances in Wireless Communications*, 11-14 July 2004 Page(s):626 – 630.
- [82] Wang, Y.; Coon, J.; "Full Rate Orthogonal Space-Time Block Coding in OFDM Transmission Using Time reversal" in *Proc. IEEE Wireless Communications and Networking Conference, 2009 (WCNC 2009)*, 5-8 April 2009 Page(s):1 – 6.
- [83] Dubois, T.; Crussière, M.; Hélar, M., "On the use of Time reversal for digital communications with non-impulsive waveforms," in *Proc. 2010 4th International Conference on Signal Processing and Communication Systems (ICSPCS)*, pp.1-6, 13-15 Dec. 2010.
- [84] Dubois, T.; Hélar, M. and Crussière, M., "Time reversal and OFDM combination: Guard Interval design, dimensioning and synchronisation aspects", *WRF29*, Berlin 23-25 octobre 2012.
- [85] Dubois, T. ; Hélar, M ; Crussière, M. ; Germond, C., "Performance of time reversal precoding technique for MISO-OFDM systems", *EURASIP 2014*.
- [86] [duboisLargeMiso]Dubois, T.; Helard, M.; Crussiere, M.; Maaz, I., "Time reversal applied to large MISO-OFDM systems," in *Proc. IEEE 24th International Symposium on Personal Indoor and Mobile Radio Communications (PIMRC) 2013*, London, 8-11 Sept. 2013, pp.896,901.
- [87] Dubois, T. ; Hélar, M. ; Siohan, P. ; Crussière ; M., Jahan, B., "Efficient MISO system combining Time reversal and OFDM/OQAM", in *Proc. European Wireless (EW) 2014*, 14 - 16 May 2014, Barcelone, Spain.
- [88] T. Dubois, *PHD thesis*, 25th march 2013, INSA IETR, « Application du Retournement Temporel aux systèmes multi-porteuses : propriétés et performances ».
- [89] Blume, O.; Zeller, D.; Barth, U.; "Approaches to energy efficient wireless access networks," in *Proc. 2010 4th International Symposium on Communications, Control and Signal Processing (ISCCSP)*, pp.1-5, 3-5 March 2010.

-
- [90] Xio, S. Q.; Chen, J.; Wang, B.-Z. and Liu, X. F. ;“A Numerical Study on Time reversal Electromagnetic Wave For Indoor Ultra-Wideband Signal Transmission,” *Progress in Electromagnetics Research, PIER 77*, pp. 329-342, 2007.
- [91] IST-4-027756 WINNER II D1.1.2 V1.2 “WINNER II Channel Models”, available at <https://www.ist-winner.org>.
- [92] Paulraj, A. ; Nabar, R.; Gore, D.; “Introduction to Space-Time Wireless Communications”, *Cambridge Univeristy Press*, 2003.
- [93] Samardzija, D.; Mandayam, N., "Unquantized and uncoded channel state information feedback on wireless channels [mobile radio applications]," in *Proc. 2005 IEEE Wireless Communications and Networking Conference*, vol.2, no., pp. 1059- 1065 Vol. 2, 13-17 March 2005.
- [94] Dahl, T.; Kirkebo, J.E., "Blind beamforming in frequency division duplex MISO systems based on time reversal mirrors," in *Proc. 2005 IEEE 6th Workshop on Signal Processing Advances in Wireless Communications*, pp. 640- 644, 5-8 June 2005.
- [95] Mohammed, S.K. ; Chockalingam, A. and Sundar Rajan, B.; "A low-complexity precoder for large multiuser MISO systems," in *Proc. IEEE Vehicular Technology Conference, 2008*, pp.797-801, 11-14 May 2008.
- [96] Yang, H. and Marzetta, T.L.; "Performance of conjugate and zero-forcing beamforming in large-scale antenna systems," *IEEE Journal on Selected Areas in Communications*, vol.31, no.2, pp.172, Feb. 2013.
- [97] Wagner, S.; Couillet, R. ; Debbah, M. and Slock, D.; "Large system analysis of linear precoding in correlated MISO broadcast channels under limited feedback," *IEEE Transactions on Information Theory*, vol.58, no.7, pp.4509-4537, July 2012.
- [98] Osseiran, A.; Braun, V.; Hidekazu, T.; Marsch, P.; Schotten, H.; Tullberg, H.; Uusitalo, M.A.; Schellman, M., "The foundation of the mobile and wireless communications system for 2020 and beyond: Challenges, enablers and technology solutions," in *Proc. 2013 IEEE 77th Vehicular Technology Conference (VTC Spring)*, pp.1,5, 2-5 June 2013.
- [99] Truong, K.T.; Heath, R.W., "Effects of channel aging in massive MIMO systems," *Journal of Communications and Networks*, vol.15, no.4, pp.338,351, Aug. 2013.
- [100]Ekman, T.; Ahlén, A. and Sternad, M.; “Unbiased power prediction on Rayleigh fading channels,” in *Proc. IEEE Vehicular Technology Conference, VTC2002-Fall*, Vancouver, Canada, Sept. 2002.
- [101]Ekman, T.; Prediction of Mobile Radio Channels: Modeling and Design. *Ph.D Thesis, Signals and Systems, Uppsala University, 2002*. Available: <http://www.signal.uu.se/Publications/pdf/a023.pdf>
- [102]Duel-Hallen, A.; “Fading channel prediction for mobile radio adaptive transmission systems,” in *Proceedings of the IEEE*, vol. 95, no. 12, pp. 2299-213, December 2007.
- [103]Aronsson, D. ;Channel Estimation and Prediction for MIMO OFDM Systems: - Key Design and Performance Aspects of Kalman-based Algorithms. *Ph.D Thesis, Signals and Systems, Uppsala, University, March 2011*. <http://www.signal.uu.se/Publications/pdf/a112.pdf>.
- [104] Sternad, M.; Grieger, M.; Apelfröjd, R. ; Svensson, T.; Aronsson, D. and Belén Martínez, A.; "Using “predictor antennas” for long-range prediction of fast fading for moving relays," in *Proc. IEEE Wireless Communications and Networking Conference Workshops (WCNCW)*, pp.253-257, April 2012.
- [105]Sui; Vihriala, J. ; Papadogiannis, A.; Sternad, M.; Yang, W. and Svensson, T.; "Moving cells: a promising solution to boost performance for vehicular users," *IEEE Communications Magazine*, vol.51, no.6, pp., June 2013.
- [106]Belén Martínez, A. “Using "Predictor Antennas" for Long-Range Prediction of Fast Fading for Moving Relays”, MSc thesis at TU Dresden, August 20, 2012.
- [107]Jamaly, N.; Apelfröjd, R.; Belén Martínez, A.; Grieger, M.; Svensson, T. ; Sternad M. and Fettweis, G.; “Analysis and measurement of multiple antenna systems for fading channels prediction in moving relays,” in *Proc. European Conference on Antennas an Propagation, EuCAP 2014*, Hague, The Netherlands., April 6-11, 2014.
- [108]Grieger, M. and Fettweis, G.; "Field trial results on uplink joint detection for moving relays," in *Proc. 2012 IEEE 8th International Conference on Wireless and Mobile Computing, Networking and Communications (WiMob)*, pp.586,592, 8-10 Oct. 2012.
- [109]Wiklund, I.; “Channel Prediction for Moving Relays”, *MSc thesis at Uppsala University*, August 2012. Available: <http://uu.diva-portal.org/smash/record.jsf?pid=diva2:607338>,
- [110]Jamaly, N.; “Multiport Antenna Systems for Space-Time Wireless Communications”, *Ph.D. thesis*, Communication Systems Group Department of Signals and Systems Chalmers University of Technology, Gothenburg, Sweden 2013.
- [111]Zirwas, W.; Giebel, T. ; Rohling, H.; Schulz, E. and Eichinger, J. ; “CSI-estimation for cooperative antennas,” in *Proc. International OFDM Workshop*, Hamburg, Germany, September 2003.
- [112]3GPP; Technical Specification Group Radio Access Network; Evolved Universal Terrestrial Radio Access (E-UTRA), “Physical Channels and Modulation (Release 10)”, TS 36.211, December 2012.
- [113]Balanis, C.; *Antenna Theory: Analysis and Design*, 2nd Ed, Wiley, 1997.

-
- [114]Chau, Y.A.; Yu, S.-H.; "Space modulation on wireless fading channels," in *Proc. IEEE 54th Vehicular Technology Conference (VTC), 2001 Fall.*, vol.3, no., pp.1668-1671.
- [115]Jeganathan, J.; Ghrayeb, A.; Szczecinski, L.; Ceron, A.; "Space shift keying modulation for MIMO channels," *IEEE Transactions on Wireless Communications*, vol.8, no.7, pp.3692-3703, July 2009.
- [116]Di Renzo, M.; Haas, H.; "On the Performance of SSK Modulation over Multiple-Access Rayleigh Fading Channels," in *Proc. 2010 IEEE Global Telecommunications Conference on Communications (GLOBECOM 2010)*, pp.1-6, 6-10 Dec. 2010.
- [117]Mesleh, R.Y.; Haas, H.; Sinanovic, S.; Chang Wook Ahn; Sangboh Yun, "Spatial Modulation," *IEEE Transactions on Vehicular Technology*, vol.57, no.4, pp.2228-2241, July 2008.
- [118]Nokia, "Physical channel BER and Downlink Outer Loop Power Control," TSGR1#10(00)0113, TSG-RAN Working Group 1 meeting #10, Beijing, China 18-21 January 2000.
- [119]Jialing Li; I-Tai Lu; Enoch Lu, "Novel MMSE Precoder and Decoder Designs for Single-User MIMO Systems under General Power Constraints," in *Proc. 2010 IEEE 71st Vehicular Technology Conference (VTC 2010-Spring)*, pp.1-5, 16-19 May 2010.
- [120]Namboodiri, V.; Hong Liu; Spasojević, P., "Low complexity turbo equalization for mobile MIMO OFDM systems," in *Proc. 2011 International Conference on Communications and Signal Processing (ICCSP)*, pp.255-260, 10-12 Feb. 2011.
- [121]Ahmed, S.; Ratnarajah, T.; Sellathurai, M.; Cowan, C., "Iterative Receivers for MIMO-OFDM and Their Convergence Behavior," in *Proc. IEEE Transactions on Vehicular Technology*, vol.58, no.1, pp.461-468, Jan. 2009.
- [122]Siohan, P., Siclet, C. and Lacaille, N. ; "Analysis and design of OFDM/OQAM systems based on filterbank theory," *IEEE Transactions on Signal Processing*, vol. 50, no. 5, pp. 1170–1183, May 2002.
- [123]Lélé, C.; Javaudin, J.-P.; Legouable, R. ; Skrzypczak, A. and Siohan, P.; "Channel estimation methods for preamble-based OFDM/OQAM modulations," in *European wireless*, Apr. 2007.
- [124]El Tabach, M.; Javaudin, J.-P.; Hédard, M., "Spatial Data Multiplexing Over OFDM/OQAM Modulations," in *Proc. IEEE International Conference on Communications, 2007 (ICC '07)*, pp.4201-4206, 24-28 June 2007.
- [125]Zakaria, R.; Le Ruyet, D.; Bellanger, M., "Maximum likelihood detection in spatial multiplexing with FBMC," in *Proc. 2010 European Wireless Conference (EW)*, pp.1038-1041, 12-15 April 2010.
- [126]Yoo, T. and Goldsmith, A. ; "On the optimality of multiantenna broadcastscheduling using zero-forcing beamforming," *IEEE J. Sel. Areas Commun.*, vol. 24, no. 3, pp. 528–541, March 2006.
- [127]Caus, M.; Perez-Neira, A.I., "Transmit and receive filters for MISO FBMC systems subjected to power constraints," in *Proc. 2011 IEEE International Conference on Acoustics, Speech and Signal Processing (ICASSP)*, pp.2660,2663, 22-27 May 2011.
- [128]Caus, M.; Pérez-Neira, A.I., "Optimal MISO pre-equalization for filter bank based multicarrier systems," in *Proc. 2010 Conference Record of the Forty Fourth Asilomar Conference on Signals, Systems and Computers (ASILOMAR)*, pp.1521,1525, 7-10 Nov. 2010.
- [129]Bhattacharyya, B.; Misra, I.S.; Sanyal, S.K., "Optimization of error performance in a WiMAX transceiver using novel Adaptive Cyclic Prefix strategy," in *Proc. 2011 14th International Conference on Computer and Information Technology (ICCIT)*, pp.245-250, 22-24 Dec. 2011.
- [130]Dorigo, M.; Maniezzo, V.; Colomi, A., "Ant system: optimization by a colony of cooperating agents," *IEEE Trans. on Systems, Man, and Cybernetics, Part B: Cybernetics*, vol.26, no.1, pp.29,41, Feb 1996.
- [131]J. Grimm, W. Grimm, *Fairy Tales* (1812).
- [132]Russell, R. Andrew, "Ant trails - an example for robots to follow?," in *Proc. Proceedings. 1999 IEEE International Conference on Robotics and Automation*, vol.4, no., pp.2698,2703 vol.4, 1999.
- [133]Kuo, Y.-W.; Shr, H.-K.; Wu, M.-S.; "Wireless navigation system for a self-propelled car with a rotational directional antenna," in *Proc. 2013 10th IEEE International Conference on Control and Automation (ICCA)*, pp.623,627, 12-14 June 2013.
- [134]Bulusu, N.; Heidemann, J.; Estrin, D., "Adaptive beacon placement," in *Proc. 21st International Conference on Distributed Computing Systems*, pp.489,498, Apr 2001.
- [135]Fu, S.; Hou, Z.-G.; Yang, G., "An indoor navigation system for autonomous mobile robot using wireless sensor network," in *Proc. International Conference on Networking, Sensing and Control, 2009 (ICNSC '09)*, pp.227,232, 26-29 March 2009.
- [136]Fall, B.; Elbahhar, F.; Heddebaut, M.; Rivenq, A., "Time-Reversal UWB positioning beacon for railway application," in *Proc. 2012 International Conference on Indoor Positioning and Indoor Navigation (IPIN)*, pp.1,8, 13-15 Nov. 2012.

- [137] IEEE Std 802.11, Information Technology –Part 11: Wireless Lan MAC and PHY Specifications - First Edition, 1999-08-20.
- [138] Poutanen, J.; Haneda, K.; Lingfeng Liu; Oestges, C.; Tufvesson, F.; Vainikainen, P., "Parameterization of the COST 2100 MIMO channel model in indoor scenarios," in *Proc. Proceedings of the 5th European Conference on Antennas and Propagation*, pp.3606,3610, 11-15 April 2011.
- [139] Giannetti, F.; Luise, M. and Reggiannini, R., "Mobile and personal communications in the 60 GHz band: A survey," *Wireless Pers. Commun.*, vol. 10, no. 2, pp. 207–243, Jul. 1999.
- [140] Wireless LAN Medium Access Control (MAC) and Physical Layer (PHY). Specification, IEEE Standard, Supplement to Standard 802 Part 11: Wireless LAN, New York, NY, 1999.
- [141] Choi, C.-S.; Grass, E.; Piz, M.; Ehrig, M.; Marinkovic, M.; Kraemer, R. and Scheytt, C., "60-GHz OFDM systems for multi-gigabit wireless LAN applications", in *Proc. IEEE CCNC 2010*.
- [142] Mudumbai, R.; Singh, S.; Madhow, U.; "Medium Access Control for 60 GHz Outdoor Mesh Networks with Highly Directional Links," in *Proc. IEEE INFOCOM 2009*, pp.2871-2875, 19-25 April 2009.
- [143] Singh, S.; Mudumbai, R.; Madhow, U.; "Interference Analysis for Highly Directional 60-GHz Mesh Networks: The Case for Rethinking Medium Access Control," *IEEE/ACM Transactions on Networking*, vol.19, no.5, pp.1513-1527, Oct. 2011.
- [144] Singh, S.; Mudumbai, R.; Madhow, U.; "Distributed Coordination with Deaf Neighbors: Efficient Medium Access for 60 GHz Mesh Networks," in *Proc. IEEE INFOCOM*, pp.1-9, 14-19 March 2010.
- [145] Rappaport, T.S.; Shu Sun; Mayzus, R.; Hang Zhao; Azar, Y.; Wang, K.; Wong, G.N.; Schulz, J.K.; Samimi, M.; Gutierrez, F., "Millimeter Wave Mobile Communications for 5G Cellular: It Will Work!," *IEEE Access*, vol.1, pp.335,349, 2013.
- [146] Gesbert, D.; Shafi, M.; Da-shan Shiu; Smith, P.J.; Naguib, A.; "From theory to practice: an overview of MIMO space-time coded wireless systems," *IEEE Journal on Selected Areas in Communications*, vol.21, no.3, pp. 281- 302, April 2003.
- [147] Sheldon, C.; Torkildson, E.; Munkyo Seo; Yue, C.P.; Rodwell, M.; Madhow, U., "Spatial multiplexing over a LOS millimeter-wave MIMO link: A two-channel hardware demonstration at 1.2Gbps over 41m range," in *Proc. European Conference on Wireless Technology, 2008 (EuWiT 2008)*, pp.198,201, 27-28 Oct. 2008.
- [148] Yoo, T. and Goldsmith, A., "Optimality of zero-forcing beamforming with multiuser diversity," in *Proc. IEEE ICC*, pp:542-546, May 2005.
- [149] Jiang, J.-S.; Ingram, M.-A., "Spherical-wave model for short-range MIMO," *IEEE Transactions Communications*, vol.53, no.9, pp.1534,1541, Sept. 2005.
- [150] Raja, M.; Muthuchidambaranathan, P.; "BER performance of SVD-based transmit beamforming with various modulation techniques," in *Proc. 2010 International Conference on Industrial and Information Systems (ICIIS)*, pp.155-160, July 29 2010-Aug. 1 2010.
- [151] Wang, F.; Liu, X.; Bialkowski, M.E.; "Investigation into SVD Based Beamforming over Rician MIMO Channels," in *proc. WiCom '09. 5th International Conference on Wireless Communications, Networking and Mobile Computing*, pp.1-4, 24-26 Sept. 2009.
- [152] Kohno, R.; Choonsik Yim; Imai, H., "Array Antenna Beamforming Based On Estimation Of Arrival Angles Using DFT On Spatial Domain," *IEEE International Symposium on Personal, Indoor and Mobile Radio Communications*, pp.38,43, 23-25 Sep 1991.
- [153] Yang, D.; Yang, L.-L.; Hanzo, L., "DFT-Based Beamforming Weight-Vector Codebook Design for Spatially Correlated Channels in the Unitary Precoding Aided Multiuser Downlink" in *Proc. IEEE Int. Conf. Comm. 2010*, pp.1,5, 23-27 May 2010.
- [154] Edfors, O.; Johansson, A.J., "Is Orbital Angular Momentum (OAM) Based Radio Communication an Unexploited Area?," *IEEE Trans. on Antennas and Propagation*, vol.60, no.2, pp.1126,1131, Feb. 2012.
- [155] Irmer, R.; Droste, H.; Marsch, P.; Grieger, M.; Fettweis, G.; Brueck, S.; Mayer, H.-P.; Thiele, L.; Jungnickel, V.; "Coordinated multipoint: Concepts, performance, and field trial results," *IEEE Communications Magazine*, vol.49, no.2, pp.102-111, February 2011.
- [156] Duhamel, P. and Vetterli, M., 1990, "Fast Fourier transforms: a tutorial review and a state of the art", *Signal Processing* 19: 259–299.
- [157] Golub, G. H.; Van Loan, C. F. (1996). "Matrix Computations" (3rd ed.). Hopkins, J.
- [158] Wagner, S.; Slock, D.T.M.; "Weighted sum rate maximization of correlated MISO broadcast channels under linear precoding: A large system analysis," in *Proc. 2011 IEEE 12th International Workshop on Signal Processing Advances in Wireless Communications (SPAWC)*, pp.411-415, 26-29 June 2011.

-
- [159] Jose, J.; Ashikhmin, A.; Marzetta, T.L.; Vishwanath, S.; "Pilot Contamination and Precoding in Multi-Cell TDD Systems," *IEEE Transactions on Wireless Communications*, vol.10, no.8, pp.2640-2651, August 2011.
- [160] Wang, H.-H.; Hou, H.-A.; "Field trial and study of route-tracking beamforming over high-speed railway," *2011 14th International IEEE Conference on Intelligent Transportation Systems (ITSC)*, pp.2063-2067, 5-7 Oct. 2011.
- [161] Wang, H.-H.; Hou, H.-A.; "Experimental analysis of beamforming in high-speed railway communication," in *Proc. 2011 IEEE 22nd International Symposium on Personal Indoor and Mobile Radio Communications (PIMRC)*, pp.745-749, 11-14 Sept. 2011.
- [162] P. Baracca et al. "Final performance results and consolidated view on the most promising multi-node/multi-antenna transmission technologies" available at https://www.metis2020.com/wp-content/uploads/deliverables/METIS_D3.3_v1.pdf.
- [163] Phan-Huy, D.-T.; Siohan, P.; Héland, M., "Make-It-Real-And-Anticirculating Orthogonal Space-Time Coding for MIMO OFDM/OQAM", in *Proc. 2015 IEEE 16th International Workshop on Signal Processing Advances in Wireless Communications (SPAWC)*, June 2014.
- [164] Phan-Huy, D.-T.; Kokar, Y.; Sarrebourg d'Audeville, T.; Malhouroux Gaffet, N.; Pajusco, P.; Leray, C.; Gati, A.; Wiart, J., "On the human exposure to radio frequency radiations expected from future small connected objects", in *Proc. 2014 IEEE Global Telecommunications Conference (GLOBECOM)*, December 2014.

AVIS DU JURY SUR LA REPRODUCTION DE LA THESE SOUTENUE

Titre de la thèse:

Retournement temporel : application aux réseaux mobiles

Nom Prénom de l'auteur : PHAN HUY DINH THUY

Membres du jury :

- Madame LIENARD Martine
- Madame BAUDOIN Geneviève
- Madame HELARD Maryline
- Monsieur CRUSSIÈRE Matthieu
- Monsieur DE ROSNY Julien
- Madame BERBINEAU Marion
- Monsieur WIART Joe

Président du jury : *Marion BERBINEAU*

Date de la soutenance : 14 Décembre 2015

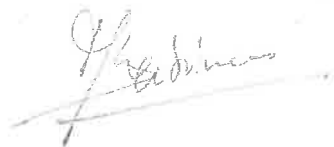
Reproduction de la these soutenue

Thèse pouvant être reproduite en l'état

~~Thèse pouvant être reproduite après corrections suggérées~~

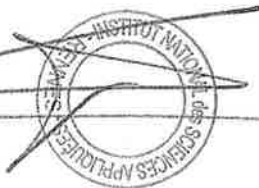
Fait à Rennes, le 14 Décembre 2015

Signature du président de jury



Le Directeur,

M'hamed DRISSI



Résumé

Cette thèse étudie la technique dite de 'Retournement Temporel' afin d'améliorer l'efficacité énergétique des futurs réseaux mobiles d'une part, et réduire le coût des futurs terminaux mobiles, d'autre part.

Le retournement temporel consiste à utiliser l'inverse temporel de la réponse impulsionnelle du canal de propagation entre un émetteur et un récepteur pour préfiltrer l'émission d'un signal de données. Avantagusement, le signal ainsi préfiltré est reçu avec une puissance renforcée (c'est la focalisation spatiale) et un écho principal qui est renforcé par rapport aux échos secondaires (c'est la compression temporelle). Lors d'une étape préalable d'apprentissage, l'émetteur estime le canal en mesurant un signal pilote provenant du récepteur. La focalisation spatio-temporelle n'est obtenue qu'à condition que la propagation demeure identique entre la phase d'apprentissage et la phase de transmission de données : c'est la condition de 'réciprocité du canal'.

De nombreux travaux montrent que la focalisation spatiale permet de réduire la puissance émise nécessaire pour atteindre une puissance cible au récepteur d'une part, et que la compression temporelle permet de réduire la complexité du récepteur nécessaire pour gérer l'effet des échos multiples, d'autre part.

Cependant, les études sur la réduction de la complexité du récepteur se limitent à l'ultra large bande. Des travaux de cette thèse (basés sur des simulations et des mesures expérimentales) montrent que pour des bandes de fréquences plus typiques des futurs réseaux mobiles (fréquence porteuse à 1GHz et spectre de 30 MHz à 100 MHz), grâce au retournement temporel, un récepteur simple et un signal mono-porteuse suffisent pour atteindre de hauts débits.

En outre, la condition de réciprocité du canal n'est pas vérifiée dans deux scénarios typiques des réseaux mobiles. Tout d'abord, dans la plupart des réseaux mobiles européens, le mode de duplex en fréquence est utilisé. Ce mode implique que l'émetteur et le récepteur communiquent l'un avec l'autre sur des fréquences porteuses distinctes, et donc à travers des canaux de propagations différents. De plus, lorsqu'on considère un récepteur sur un véhicule connecté en mouvement, l'émetteur et le récepteur communiquent l'un avec l'autre à des instants distincts, correspondant à des positions distinctes du véhicule, et donc à travers des canaux de propagations différents. Des travaux de cette thèse proposent des solutions pour obtenir la focalisation spatio-temporelle dans ces deux scénarios.

Enfin, des travaux de la thèse explorent la combinaison du retournement temporel avec d'autres techniques de traitement de signal récentes (la modulation spatiale, d'une part, et une nouvelle forme d'onde multi-porteuse, d'autre part), ou des scénarios de déploiement nouveaux (ondes millimétriques et très grands réseaux d'antennes pour inter-connecter les noeuds d'un réseau ultra dense) ou de nouvelles applications (guidage et navigation) envisageables pour les futurs réseaux mobiles.

Abstract

This thesis studies the time reversal technique to improve the energy efficiency of future mobile networks and reduce the cost of future mobile devices.

Time reversal technique consists in using the time inverse of the propagation channel impulse response (between a transceiver and a receiver) as a pre-filter. Such pre-filtered signal is received with a stronger power (this is spatial focusing) and with a strong main echo, relatively to secondary echoes (this is time compression). During a previous learning phase, the transceiver estimates the channel by measuring the pilot signal emitted by the receiver. Space-time focusing is obtained only at the condition that the propagation remains identical between the learning phase and the data transmission phase: this is the 'channel reciprocity' condition.

Numerous works show that spatial focusing allows for the reduction of the required transmit power for a given target received power, on the one hand, and that time compression allow for the reduction of the required complexity at the receiver side to handle multiple echoes, on the other hand.

However, studies on complexity reduction are limited to ultra wideband. Some works of this thesis (based on simulations and experimental measurements) show that, for bands which are more typical for future networks (a carrier frequency of 1GHz and a spectrum of 30 MHz to 100 MHz), thanks to time reversal, a simple receiver and a mono-carrier signal are sufficient to reach high data rates.

Moreover, the channel reciprocity condition is not verified in two scenarios which are typical from mobile networks. Firstly, in most European mobile networks, the frequency division duplex mode is used. This mode implies that the transceiver and the receiver communicate on distinct carriers, and therefore through different propagation channels. Secondly, when considering a receiver on a moving connected vehicle, the transceiver and the receiver communicate one with each other at distinct instants, corresponding to distinct positions of the vehicles, and therefore through different propagation channels. Some works of this thesis propose solutions to obtain space-time focusing for these two scenarios.

Finally, some works of this thesis explore the combination of time reversal with other recent signal processing techniques (spatial modulation, on the one hand, a new multi-carrier waveform, on the other hand), or new deployment scenarios (millimeter waves and large antenna arrays to inter-connect the nodes of an ultra dense network) or new applications (guidance and navigation) which can be envisaged for future mobile networks.